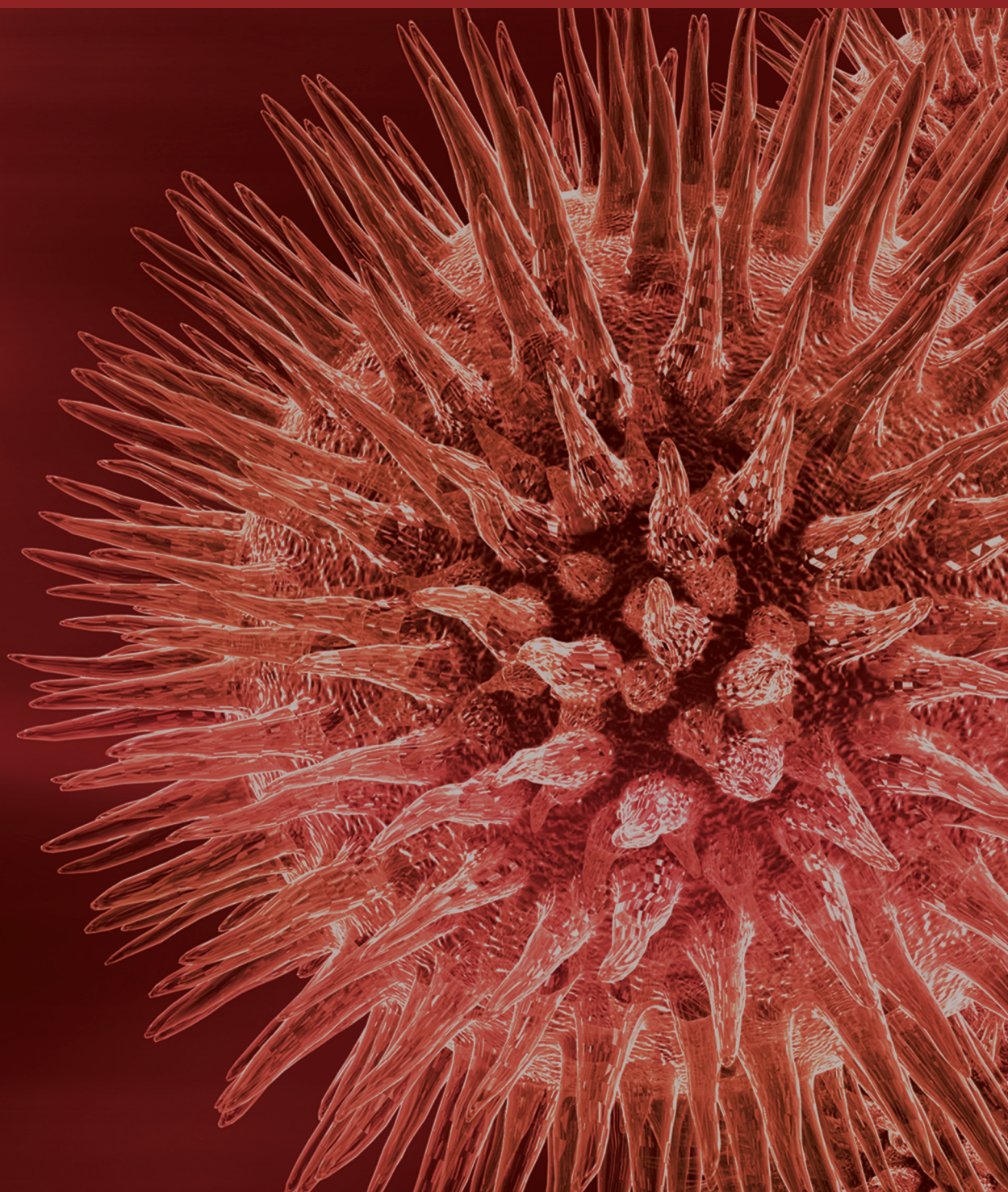


# **Bionanotechnology and Nanomedicine**

Guest Editors: P. Bryant Chase, Seunghun Hong, Alf Månsson,  
and Peng Xiong





---

# **Bionanotechnology and Nanomedicine**

Journal of Biomedicine and Biotechnology

---

## **Bionanotechnology and Nanomedicine**

Guest Editors: P. Bryant Chase, Seunghun Hong,  
Alf Månsson, and Peng Xiong



---

Copyright © 2012 Hindawi Publishing Corporation. All rights reserved.

This is a special issue published in “Journal of Biomedicine and Biotechnology.” All articles are open access articles distributed under the Creative Commons Attribution License, which permits unrestricted use, distribution, and reproduction in any medium, provided the original work is properly cited.



## Editorial Board

The editorial board of the journal is organized into sections that correspond to the subject areas covered by the journal.

### Agricultural Biotechnology

Ahmad Z. Abdullah, Malaysia	Ian Godwin, Australia	B. C. Saha, USA
Guihua H. Bai, USA	Hari B. Krishnan, USA	Mariam B. Sticklen, USA
Christopher P. Chanway, Canada	Carol A. Mallory-Smith, USA	Chiu-Chung Young, Taiwan
Ravindra N. Chibbar, Canada	Dennis P. Murr, Canada	
Adriana S. Franca, Brazil	Rodomiro Ortiz, Sweden	

### Animal Biotechnology

E. S. Chang, USA	Tosso Leeb, Switzerland	Lawrence B. Schook, USA
Bhanu P. Chowdhary, USA	James D. Murray, USA	Mari A. Smits, The Netherlands
Noelle E. Cockett, USA	Anita M. Oberbauer, USA	Leon Spicer, USA
Peter Dovc, Slovenia	Jorge A. Piedrahita, USA	J. Verstegen, USA
Scott C. Fahrenkrug, USA	Daniel Pomp, USA	Matthew B. Wheeler, USA
Dorian J. Garrick, USA	Kent M. Reed, USA	Kenneth L. White, USA
Thomas A. Hoagland, USA	Lawrence Reynolds, USA	

### Biochemistry

David Ronald Brown, UK	Hicham Fenniri, Canada	Wen-Hwa Lee, USA
Saulius Butenas, USA	Nick V. Grishin, USA	George Makhatadze, USA
Vittorio Calabrese, Italy	J. Guy Guillemette, Canada	Leonid Medved, USA
Miguel Castanho, Portugal	Paul W. Huber, USA	Susan A. Rotenberg, USA
Francis J. Castellino, USA	Chen-Hsiung Hung, Taiwan	Jason Shearer, USA
Roberta Chiaraluce, Italy	Maria Jerzykiewicz, Poland	Andrei Surguchov, USA
D. M. Clarke, Canada	Michael Kalafatis, USA	John B. Vincent, USA
Francesca Cutruzzolà, Italy	B. E. Kemp, Australia	Y. George Zheng, USA
Paul W. Doetsch, USA	Phillip E. Klebba, USA	

### Bioinformatics

T. Akutsu, Japan	Stavros J. Hamodrakas, Greece	Florencio Pazos, Spain
Miguel A. Andrade, Germany	Paul Harrison, USA	Zhirong Sun, China
Mark Y. Borodovsky, USA	George Karypis, USA	Ying Xu, USA
Rita Casadio, Italy	Jack A. Leunissen, The Netherlands	Alexander Zelikovsky, USA
Artem Cherkasov, Canada	Guohui Lin, Canada	Albert Zomaya, Australia
David Corne, UK	Satoru Miyano, Japan	
Sorin Draghici, USA	Zoran Obradovic, USA	



## Biophysics

Miguel Castanho, Portugal  
P. Bryant Chase, USA  
Kuo-Chen Chou, USA  
Rizwan Khan, India

Ali A. Khraibi, Saudi Arabia  
Rumiana Koynova, USA  
Serdar Kuyucak, Australia  
Jianjie Ma, USA

S. B. Petersen, Denmark  
Peter Schuck, USA  
Claudio M. Soares, Portugal

## Cell Biology

Omar Benzakour, France  
Sanford I. Bernstein, USA  
Phillip I. Bird, Australia  
Eric Bouhassira, USA  
Mohamed Boutjdir, USA  
Chung-Liang Chien, Taiwan  
Richard Gomer, USA  
Paul J. Higgins, USA  
Pavel Hozak, Czech Republic

Xudong Huang, USA  
Anton M. Jetten, USA  
Seamus J. Martin, Ireland  
Manuela Martins-Green, USA  
Shoichiro Ono, USA  
George Perry, USA  
M. Piacentini, Italy  
George E. Plopper, USA  
Lawrence Rothblum, USA

Michael Sheetz, USA  
James L. Sherley, USA  
G. S. Stein, USA  
Richard Tucker, USA  
Thomas van Groen, USA  
Andre Van Wijnen, USA  
Steve Winder, UK  
Chuanyue Wu, USA  
Bin-Xian Zhang, USA

## Genetics

Adewale Adeyinka, USA  
Claude Bagnis, France  
J. Birchler, USA  
Susan Blanton, USA  
Barry J. Byrne, USA  
R. Chakraborty, USA  
Domenico Coviello, Italy  
Sarah H. Elsea, USA  
Celina Janion, Poland

J. Spencer Johnston, USA  
M. Ilyas Kamboh, USA  
Feige Kaplan, Canada  
Manfred Kayser, The Netherlands  
Brynn Levy, USA  
Xiao Jiang Li, USA  
Thomas Liehr, Germany  
James M. Mason, USA  
Mohammed Rachidi, France

Raj S. Ramesar, South Africa  
Elliot D. Rosen, USA  
Dharambir K. Sanghera, USA  
Michael Schmid, Germany  
Markus Schuelke, Germany  
Wolfgang Arthur Schulz, Germany  
Jorge Sequeiros, Portugal  
Mouldy Sioud, Norway  
Rongjia Zhou, China

## Genomics

Vladimir Bajic, Saudi Arabia  
Margit Burmeister, USA  
Settara Chandrasekharappa, USA  
Yataro Daigo, Japan  
J. Spencer Johnston, USA

Vladimir Larionov, USA  
Thomas Lufkin, Singapore  
John L. McGregor, France  
John V. Moran, USA  
Yasushi Okazaki, Japan

Gopi K. Podila, USA  
Momiao Xiong, USA

## Editorial Board

The editorial board of the journal is organized into sections that correspond to the subject areas covered by the journal.

### Immunology

Hassan Alizadeh, USA  
Peter Bretscher, Canada  
Robert E. Cone, USA  
Terry L. Delovitch, Canada  
Anthony L. DeVico, USA  
Nick Di Girolamo, Australia  
Don Mark Estes, USA  
Soldano Ferrone, USA  
Jeffrey A. Frelinger, USA  
John Robert Gordon, Canada

James D. Gorham, USA  
Silvia Gregori, Italy  
Thomas Griffith, USA  
Young S. Hahn, USA  
Dorothy E. Lewis, USA  
Bradley W. McIntyre, USA  
R. Lee Mosley, USA  
Marija Mostarica-Stojković, Serbia  
Hans Konrad Muller, Australia  
Ali Ouaisi, France

Kanury V. S. Rao, India  
Yair Reisner, Israel  
Harry W. Schroeder, USA  
Wilhelm Schwaeble, UK  
Nilabh Shastri, USA  
Yufang Shi, China  
Piet Stinissen, Belgium  
Hannes Stockinger, Austria  
J. W. Tervaert, The Netherlands  
Graham R. Wallace, UK

### Microbial Biotechnology

Suraini Abd-Aziz, Malaysia  
Jozef Anné, Belgium  
Nuri Azbar, Turkey  
Yoav Bashan, Mexico  
Marco Bazzicalupo, Italy  
Hakan Bermek, Turkey  
Nico Boon, Belgium  
José Luis Campos, Spain  
Yinguang Chen, China  
Luca Simone Cocolin, Italy

Peter Coloe, Australia  
Daniele Daffonchio, Italy  
Han de Winde, The Netherlands  
Raf Dewil, Belgium  
José Domingos Fontana, Brazil  
Petros Gikas, Greece  
Tom Granstrom, Finland  
Ismail Kiran, Turkey  
Hongjuan Liu, China  
Yanhe Ma, China

Paula Loureiro Paulo, Brazil  
Bernd H A Rehm, New Zealand  
Alberto Reis, Portugal  
Muthuswamy Sathishkumar, Singapore  
Ramkrishna Sen, India  
Angela Sessitsch, Austria  
Ya-Jie Tang, China  
Orhan Yenigun, Turkey  
Eileen Hao Yu, United Kingdom

### Microbiology

D. Beighton, UK  
Steven R. Blanke, USA  
Stanley Brul, The Netherlands  
Isaac K. O. Cann, USA  
Stephen K. Farrand, USA  
Alain Filloux, UK

Gad Frankel, UK  
Roy Gross, Germany  
Hans-Peter Klenk, Germany  
Tanya Parish, UK  
Gopi K. Podila, USA  
Frederick D. Quinn, USA

Didier A. Raoult, France  
Isabel Sá-Correia, Portugal  
P. L. C. Small, USA  
Michael Thomm, Germany  
H. C. van der Mei, The Netherlands  
Schwan William, USA

### Molecular Biology

Rudi Beyaert, Belgium  
Michael Bustin, USA  
Douglas Cyr, USA  
K. Iatrou, Greece  
Lokesh Joshi, Ireland  
David W. Litchfield, Canada

Wuyuan Lu, USA  
Patrick Matthias, Switzerland  
John L. McGregor, France  
S. L. Mowbray, Sweden  
Elena Orlova, UK  
Yeon-Kyun Shin, USA

William S. Trimble, Canada  
Lisa Wiesmuller, Germany  
Masamitsu Yamaguchi, Japan

## Oncology

Colin Cooper, UK	Steve B. Jiang, USA	Allal Ouhtit, Oman
F. M. J. Debruyne, The Netherlands	Daehee Kang, Republic of Korea	Frank Pajonk, USA
Nathan Ames Ellis, USA	Abdul R. Khokhar, USA	Waldemar Priebe, USA
Dominic Fan, USA	Rakesh Kumar, USA	F. C. Schmitt, Portugal
Gary E. Gallick, USA	Macus Tien Kuo, USA	Sonshin Takao, Japan
Daila S. Gridley, USA	Eric W. Lam, UK	Ana Maria Tari, USA
Xin-yuan Guan, Hong Kong	Sue-Hwa Lin, USA	Henk G. Van Der Poel, The Netherlands
Anne Hamburger, USA	Kapil Mehta, USA	Haodong Xu, USA
Manoor Prakash Hande, Singapore	Orhan Nalcioğlu, USA	David J. Yang, USA
Beric Henderson, Australia	P. J. Oefner, Germany	

## Pharmacology

Abdel A. Abdel-Rahman, USA	Ayman El-Kadi, Canada	Kennerly S. Patrick, USA
M. Badr, USA	Jeffrey Hughes, USA	Vickram Ramkumar, USA
Stelvio M. Bandiera, Canada	Kazim Husain, USA	Michael J. Spinella, USA
Ronald E. Baynes, USA	Farhad Kamali, UK	Quadiri Timour, France
R. Keith Campbell, USA	Michael Kassiou, Australia	Todd W. Vanderah, USA
Hak-Kim Chan, Australia	Joseph J. McArdle, USA	Val J. Watts, USA
Michael D. Coleman, UK	Mark J. McKeage, New Zealand	David J. Waxman, USA
J. Descotes, France	Daniel T. Monaghan, USA	
Dobromir Dobrev, Germany	T. Narahashi, USA	

## Plant Biotechnology

Prem L. Bhalla, Australia	Metin Guru, Turkey	Yong Pyo Lim, Republic of Korea
J. R. Botella, Australia	H. M. Häggman, Finland	Gopi K. Podila, USA
Elvira Gonzalez De Mejia, USA	Liwen Jiang, Hong Kong	Ralf Reski, Germany
Shi-You Ding, USA	Pulugurtha Bharadwaja Kirti, India	Sudhir Kumar Sopory, India

## Toxicology

Michael Aschner, USA	Hartmut Jaeschke, USA	Qaisar Mahmood, Pakistan
Juergen Buenger, Germany	Youmin James Kang, USA	R. S. Tjeerdema, USA
Michael L. Cunningham, USA	M. Firoze Khan, USA	Kenneth Turteltaub, USA
Laurence D. Fechter, USA	Pascal Kintz, France	Brad Upham, USA



## Editorial Board

The editorial board of the journal is organized into sections that correspond to the subject areas covered by the journal.

### Virology

Nafees Ahmad, USA  
Edouard Cantin, USA  
Ellen Collisson, USA  
Kevin M. Coombs, Canada  
Norbert K. Herzog, USA  
Tom Hobman, Canada  
Shahid Jameel, India

Fred Kibenge, Canada  
Fenyong Liu, USA  
Éric Rassart, Canada  
Gerald G. Schumann, Germany  
Y.-C. Sung, Republic of Korea  
Gregory Tannock, Australia

Ralf Wagner, Germany  
Jianguo Wu, China  
Decheng Yang, Canada  
Jiing-Kuan Yee, USA  
Xueping Zhou, China  
Wen-Quan Zou, USA

# Contents

**Bionanotechnology and Nanomedicine**, P. Bryant Chase, Seunghun Hong, Alf Månsson, and Peng Xiong  
Volume 2012, Article ID 763967, 1 page

**Toward a Blended Ontology: Applying Knowledge Systems to Compare Therapeutic and Toxicological Nanoscale Domains**, Christopher M. Grulke, Michael-Rock Goldsmith, and Daniel A. Vallero  
Volume 2012, Article ID 308381, 9 pages

**Sarcomere Imaging by Quantum Dots for the Study of Cardiac Muscle Physiology**,  
Fuyu Kobirumaki-Shimozawa, Kotaro Oyama, Takahiro Serizawa, Akari Mizuno, Tatsuya Kagemoto,  
Togo Shimozawa, Shin'ichi Ishiwata, Satoshi Kurihara, and Norio Fukuda  
Volume 2012, Article ID 313814, 7 pages

**Self-Organization of Motor-Propelled Cytoskeletal Filaments at Topographically Defined Borders**,  
Alf Månsson, Richard Bunk, Mark Sundberg, and Lars Montelius  
Volume 2012, Article ID 647265, 10 pages

**Nanoparticulate Adjuvants and Delivery Systems for Allergen Immunotherapy**,  
Juliana De Souza Rebouas, Irene Esparza, Marta Ferrer, Mari'a Luisa Sanz, Juan Manuel Irache,  
and Carlos Gamazo  
Volume 2012, Article ID 474605, 13 pages

**Interaction between Pheromone and Its Receptor of the Fission Yeast *Schizosaccharomyces pombe* Examined by a Force Spectroscopy Study**, Shintaro Sasuga, Ryohei Abe, Osamu Nikaido, Shoichi Kiyosaki, Hiroshi Sekiguchi, Atsushi Ikai, and Toshiya Osada  
Volume 2012, Article ID 804793, 7 pages

**Micromechanical Thermal Assays of Ca<sup>2+</sup>-Regulated Thin-Filament Function and Modulation by Hypertrophic Cardiomyopathy Mutants of Human Cardiac Troponin**, Nicolas M. Brunet, Goran Mihajlović, Khaled Aledealat, Fang Wang, Peng Xiong, Stephan von Molnár, and P. Bryant Chase  
Volume 2012, Article ID 657523, 13 pages

**Detection of Target ssDNA Using a Microfabricated Hall Magnetometer with Correlated Optical Readout**, Steven M. Hira, Khaled Aledealat, Kan-Sheng Chen, Mark Field, Gerard J. Sullivan, P. Bryant Chase, Peng Xiong, Stephan von Molnár, and Geoffrey F. Strouse  
Volume 2012, Article ID 492730, 10 pages

**Electric-Field-Directed Self-Assembly of Active Enzyme-Nanoparticle Structures**,  
Alexander P. Hsiao and Michael J. Heller  
Volume 2012, Article ID 178487, 9 pages

**High-Resolution Whole-Mount *In Situ* Hybridization Using Quantum Dot Nanocrystals**,  
Andriani Ioannou, Iro Eleftheriou, Andrea Lubatti, Anna Charalambous, and Paris A. Skourides  
Volume 2012, Article ID 627602, 9 pages

## Editorial

# Bionanotechnology and Nanomedicine

**P. Bryant Chase,<sup>1</sup> Seunghun Hong,<sup>2</sup> Alf Månsson,<sup>3</sup> and Peng Xiong<sup>4</sup>**

<sup>1</sup> Department of Biological Science, The Florida State University, Tallahassee, FL 32306, USA

<sup>2</sup> Department of Physics and Astronomy, Seoul National University, Seoul 151-742, Republic of Korea

<sup>3</sup> School of Natural Sciences, Linnaeus University, SE-391 82 Kalmar, Sweden

<sup>4</sup> Department of Physics and Integrative NanoScience Institute, The Florida State University, Tallahassee, FL 32306, USA

Correspondence should be addressed to P. Bryant Chase, chase@bio.fsu.edu

Received 1 February 2012; Accepted 1 February 2012

Copyright © 2012 P. Bryant Chase et al. This is an open access article distributed under the Creative Commons Attribution License, which permits unrestricted use, distribution, and reproduction in any medium, provided the original work is properly cited.

This special issue contains contributions from the broad interdisciplinary fields of bionanotechnology and nanomedicine. Nanotechnology has great promise in biology and medicine. This includes new approaches to fundamental studies, improved methods for detection of protein or nucleic acid-based biomarkers of disease, and new ways to administer drugs or vaccines or enhancing their effects. The tools of nanotechnology provide new insights into mechanisms of normal biological functions and diseases. Novel nanotechnology-based imaging methods reveal structural and functional information at progressively higher levels of resolution, both in vitro, in cells and in organisms. Molecular components of biological systems on their own can be often viewed as nanoscale machines with functions that have been tuned through evolution and with design principles often based on self-assembly and self-organization phenomena. These biological nanomachines can be incorporated into micro- and nanofabricated devices, a merger that yields novel structures and functionalities.

that have applications to biology and/or medicine, and perspectives on development of these fields, combined with the promises and challenges that lie ahead. It is our hope that this special issue will not only provide insights but also stimulate new ideas and advances.

*P. Bryant Chase  
Seunghun Hong  
Alf Månsson  
Peng Xiong*

## Acknowledgments

The editors of this special issue on bionanotechnology and nanomedicine sincerely thank the authors for providing original research and review contributions that will be of interest to a broad array of nanoscience researchers as well as biologists and biomedical scientists who wish to explore recent developments in the “nano” arena. Their contributions describe novel insights into biology and medicine made possible by nanotechnology, new nanotechnology devices

## Research Article

# Toward a Blended Ontology: Applying Knowledge Systems to Compare Therapeutic and Toxicological Nanoscale Domains

**Christopher M. Grulke, Michael-Rock Goldsmith, and Daniel A. Vallero**

*National Exposure Research Laboratory, US Environmental Protection Agency, Research Triangle Park, NC 27711, USA*

Correspondence should be addressed to Daniel A. Vallero, [vallero.daniel@epa.gov](mailto:vallero.daniel@epa.gov)

Received 3 October 2011; Accepted 7 January 2012

Academic Editor: P. Bryant Chase

Copyright © 2012 Christopher M. Grulke et al. This is an open access article distributed under the Creative Commons Attribution License, which permits unrestricted use, distribution, and reproduction in any medium, provided the original work is properly cited.

Bionanomedicine and environmental research share need common terms and ontologies. This study applied knowledge systems, data mining, and bibliometrics used in nano-scale ADME research from 1991 to 2011. The prominence of nano-ADME in environmental research began to exceed the publication rate in medical research in 2006. That trend appears to continue as a result of the growing products in commerce using nanotechnology, that is, 5-fold growth in number of countries with nanomaterials research centers. Funding for this research virtually did not exist prior to 2002, whereas today both medical and environmental research is funded globally. Key nanoparticle research began with pharmacology and therapeutic drug-delivery and contrasting agents, but the advances have found utility in the environmental research community. As evidence ultrafine aerosols and aquatic colloids research increased 6-fold, indicating a new emphasis on environmental nanotoxicology. User-directed expert elicitation from the engineering and chemical/ADME domains can be combined with appropriate Boolean logic and queries to define the corpus of nanoparticle interest. The study combined pharmacological expertise and informatics to identify the corpus by building logical conclusions and observations. Publication records informatics can lead to an enhanced understanding the connectivity between fields, as well as overcoming the differences in ontology between the fields.

## 1. Introduction

The hazard of a chemical compound largely depends on its product formulation (i.e., an impregnated solid suspension versus a chemical solution). Recently, there has been much interest in the role that the size of a particle plays in chemical hazard and exposure potential [1], such as the degree to which very small particles cause greater chemical risk than larger particles with the same chemical composition. Both nanoparticles and derivative nanomaterials are pervasive and growing at a rate of over 243 new products per year worldwide. It is currently estimated that 1317 nanoproducts are manufactured by 587 companies in over 30 countries. These consumer products span several major categories (e.g., health and fitness, home and garden, automotive, food and beverage, crosscutting, electronics and computers, appliances, and goods for children) [2], yet their full impact on product life-cycle and human health still remains poorly understood due to a paucity of harmonized standards for safety, environmental impacts, and human health threats.

In fact, there is still some dispute over what should be deemed a nanoparticle [3]. Current standards in biomedicine and environmental contamination define nanoparticles as being <100 nm in at least one dimension. Whereas such dimensional thresholds between nanoscale and bulk materials are useful for research and scientific inquiry, they are not completely applicable to toxicology and risk assessment. When looking at a particle as a whole, its dimensions may not meet the above criteria for a nanoparticle while its construction may have important nanoscale variability that requires it be studied as a nanoparticle. As evidence, take a nanoparticle composite with two distinct compartments: surface and core. These particles may change in time and space, so that the core becomes the surface with time, as the original surface is degraded (e.g., during metabolism and environmental degradation). Such particles constituencies (i.e., surface versus core) are therefore key in determining efficacy and toxicity as a function of time and space, thereby validating the need for studying such a particle using



nanoscale techniques though its overall dimensions need not be <100 nm.

Setting the definition of a nanoparticle aside, the federal government of the United States has with the creation of the National Nanotechnology Initiative (NNI—see also: <http://www.nano.gov/>) identified a need for the organizational framework to coordinate nanorelated research efforts and domains among the federal agencies. The eight major research areas are the following: (1) fundamental nanoscale phenomena and processes, (2) nanomaterials, (3) devices and systems, (4) instrumentation and standards, (5) nanomanufacturing, (6) facilities and acquisitions, (7) environment, health, and safety, and (8) educational and societal dimensions. Interestingly, the most impactful fields of research appear to be aggregated under a single consolidated area: environment, health, and safety. This choice to aggregate such fields is one that should be scrutinized further.

In a sense, researchers advancing therapeutics investigate similar phenomena as researchers aiming to improve the understanding of environmental xenobiotics, but in opposite directions. That is, both assess and address the factors that govern the dose-response characteristic of the material and the risks presented by an agent, whether it is chemical, or physical. However, biomedicine is looking for ways to improve the efficacy of a substance while environmental toxicologists are searching for ways to prevent a xenobiotic from having biological effects.

According to the US Environmental Protection Agency's (EPA) white paper on nanotechnology, the primary research target for absorption, distribution, metabolism, and elimination (ADME) research of nanoparticles is ecological risk (i.e., mainly focused on nonhuman species). In addition, lessons learned from computational toxicology in other agencies such as the U.S. Food and Drug Administration (FDA) or on methods gleaned from natural or incidental particulate matter may prove to be useful to fill the data gaps for these emerging materials [5]. However, such hypotheses cannot be tested without first identifying the landscape of available research. Hence, informatics and other knowledge tools provide a means of assessing the growth, extent, and congruence of these research domains addressing nanomaterials.

Drug delivery concepts can, in theory, be applied to toxicology models, such as the need to keep a substance that is efficacious in certain tissue from reaching other tissues for which it is toxic (i.e., controlled dose, pharmacokinetics, or toxicokinetics). For example, liposomes are developed for drug delivery based on their ability to evade immune response and enabling bioavailability of the drug to the target site. Both the biomedical and environmental scientific communities are seeking better models for pharmacokinetic and dynamic (PBPK/PD) behavior of nanoparticles. These models should be built using the expertise of both contingents as the same ADME processes are in force. Further, emergent materials, including nanoparticles, have attracted considerable attention from scientists from the exposure and health hazards communities alike. The source of these emerging materials in products, and their overall environmental fate and transport, environmental degradation,

TABLE 1: Comparison table of critical factors at play in nanotoxicology versus toxicity of bulk material of identical composition (reproduced from: [4]).

Bulk properties	Nanoscale properties
Chemical composition	Structure (nanostructure)
Dose (mass concentration)	Particle concentration
Exposure route	Size distributions
Reactivity	Particle numbers
Conductivity	Aggregation/agglomeration
Morphology	Surface adsorb ability
Physical form	Surface area
Impurities	Surface charge
Solubility	Self-assembly
	Quantum effects

biodegradation, biological uptake and disposition, and effects remains poorly characterized [5].

Usually, the toxicity, ADME, and other hazards associated with chemical ingredients are a function of the physical composition of the substance. This means that the properties of both the surface and the substance core help to determine the chemical risk. For example, surface properties drive the mobility and toxicity of engineered nanomaterials/particle, but the makeup of the material construct that has been coated is also important. To this extent it has become more apparent that there are significantly more than the nine factors commonly used for bulk materials that affect nanomaterial ADME and toxicity. Some of these nanomaterial specific factors are listed in Table 1.

Chemical manufacturers, pharmaceutical companies, and environmental researchers all share interest in the characteristics of nanoparticles that may allow them to “hide” from physiological processes as they find their way to the target cells. For example, nanoparticles for drug delivery consist of various biological substances like albumin, gelatin, and phospholipids for liposomes, and abiotic substances, including various polymers and solid metal containing nanoparticles. The potential interaction of these nanoparticles with tissues and cells is under investigation, but there appears to be both great promise and concern, depending on whether the target is drug delivery or potential toxicity [1]. One aspect of more adequately addressing emerging concerns of nanomaterials is being able to properly characterize both their core and surface properties, variables that ultimately delineate many downstream phenomena found in biological systems that have remained elusive in public health and environmental characterization.

Reliable information is needed to determine whether a nanoparticle may provide benefits, risks, or, as is usually the case, both. In the analogous field of chemical characterization, a typical means of gaining such information is to compare a chemical to other chemicals with similar structures (known as quantitative structure activity relationships (QSAR)). Unfortunately, QSAR treatment of chemicals has its limitations. In order to estimate properties, there must be a sufficient amount of data regarding similar chemicals. More

importantly, QSAR cannot account for unique differences in even very similar compounds. For example, it is well known that chemicals with identical formulas, but with different configurations (e.g., enantiomers), may either be efficacious or toxic as ingredients in medicines. Likewise, chiral compounds with the same composition but different handedness [6] will have very different environmental persistence (e.g., the right-handed chiral may take years to biodegrade whereas the left-hand compound may degrade in a few weeks). While QSAR methods have shown some applicability in the field of nanoparticle characterization, they certainly are not a complete solution [7].

The typical means of gaining information about ADME, aside from developed QSAR models and other tools for predicting whether a bulk material or compound will present risks, is to conduct *in vitro*, *in vivo*, and, more recently, *in silico* experimental methods. *In vitro* studies may look at cellular activity in a petri dish whereas *in vivo* studies may expose rats to the chemical ingredient and observe effects. *In silico* studies employ computational methods such as genomic and proteomic studies, data mining, molecular modeling, and quantitative structure activity relationships. The pharmacokinetics/pharmacodynamics of a chemical or its modified progeny must be understood in order to determine how the particle and its components become bioavailable. Similarly, a variety of accelerated degradation studies can be performed on varied core-surface combinations by using biomimetics methods (i.e., lung-on-a-chip technology) and employing models tailored for nanomaterial characterization properties such as the chirally perturbed particle in a box model (CPPIB) [8] and other core-surface models. Subsequently, morphology size domain optimization can be completed via microscopy and chromatography specialists and methods. These studies fully integrate a variety of vital activities, research streams, and facilities to take on a major emerging challenge for this novel class of materials, from both a modeling and characterization perspective.

While the high degree of overlap in environmental, health, and safety nanoparticle research promotes the consolidation of the fields into one area, the differences in ontology between the fields is a significant impediment. Often, different terminology is used to describe similar phenomena or homonyms for different phenomena [9]. An example of the former is the terminology employed for very small particles (<100 nm diameter). Aerosol researchers call them ultra-fines. Nanotechnologists and material scientists call them nanoparticles. Aquatic biologists and chemists call them colloids. Soil scientists call them clay textures. An example of the latter is the “E” in ADME. Biomedical researchers usually consider it to be excretion whereas environmental toxicologists usually consider it to be elimination. Another example is the use of adsorption by physicists and engineers versus its use by ADME researchers.

Such ontological differences typically lead to greater segregation of researchers and reduce cross-field integration of similar research streams. Such segregation may lead to underutilization or slower incorporation of important discoveries made by specialists in either the health or the environmental specialty of nano research and thereby impede the

advancement of nanoscience. In this effort, we investigate the growth of nanoparticle ADME research using bibliometric techniques to visualize nature of growth, gaps in study, and the isolation of research streams in the hope that the pressing issues in the field can be identified leading to a cohesive and comprehensive body of nanoparticle ADME research.

## 2. Methods

**2.1. Corpus Selection.** To obtain a knowledge concerning the state of research in nanoparticle ADME, we sought to obtain the corpus of relevant peer-reviewed literature by searching two databases: the Web of Knowledge (WoK) and PubMed (<http://www.PubMed.org/>). These two databases provide a comprehensive collection of peer-reviewed literature citations related to nanoparticle ADME properties. Other databases containing unreviewed publications on the topic were omitted to ensure the integrity of the literature corpus.

Collecting the full set of the literature related to nanoparticle ADME research involved integration of several queries with Boolean logic. Thankfully, such logic is simple to form using the query engines available through the Web of Knowledge (WoK) advanced search interface and PubMed title filters. The primary limitation in accessing the appropriate articles was due to difference in the annotation of articles as being related to ADME. In order to collect a corpus that we felt covered the relevant literature space, we were forced to include several terms related to ADME, pharmacokinetic modeling, or degradation. The inclusion of nano-related terms and toxicity was more facile. The respective queries shown in Table 2 retrieved a total of 1802 and 630 references from WoK and PubMed.

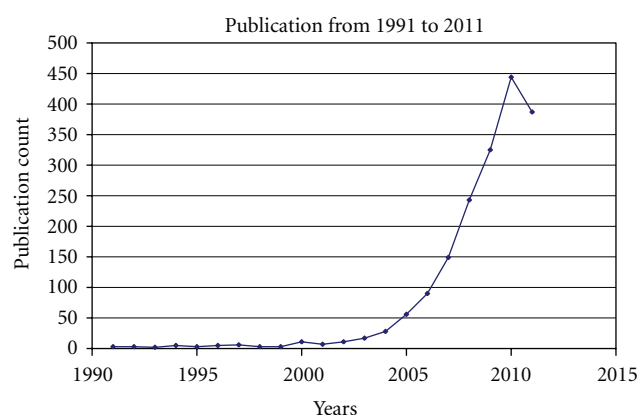
**2.2. Bibliometric Techniques.** Using the “Analyze Results” section of Web of Science (WoS) found within WoK (Web of Knowledge) various reports (related to WoS subject heading domains, authors, countries, dates, journal titles, etc.) were generated as a csv files for export into various graphing applications. For the sake of this paper, we have exported the reports related to histograms of (a) timeline, (b) WoS subject heading, (c) journal title, and (d) country of origin and have imported (b) and (d) into Many Eyes (<http://www.ManyEyes.com/>) to create a bubble-plot and a geographical map representation of the data, respectively. Graphs for (a) and (c) were generated in Excel (Microsoft) (see Figures 2–5).

Many Eyes is an open-access Web 2.0 data visualization (or visual analytics toolbox) provided and developed by IBM. We imported the domain-specific corpus of interest into Many Eyes and used the Phrase Net visualization option with Term 1 and Term 2 word structure map as an example (see Figure 6).

Exporting the WOS reference list (plus cited references) as a text file and importing into HistCite, we generated a “histiograph” or timeline that contains information of impact factor (circle size scaled to impact factor) as well as linkages between citations within the specific collection or corpus (see Figure 7).

TABLE 2: Queries used to obtain the studied literature corpus.

Database	Query	Record count
ISI's Web of Knowledge ( <a href="http://wokinfo.com/">http://wokinfo.com/</a> )	TI = (nano* OR nanotox*) AND TS = ((pharmacokinetic* OR toxicokinetic* OR disposition OR distribution OR ADME OR pbpk OR environment*)) AND TS = (toxic*) Timespan = All Years Databases = SCI-EXPANDED Lemmatization = On	1802 references
PubMed ( <a href="http://www.PubMed.org/">http://www.PubMed.org/</a> )	(Tissue distribution OR biodistribution OR dosimetry OR pharmacokinetics OR dermal OR oral OR inhalation OR uptake OR absorption OR route OR metabolism OR accumulation OR clearance OR renal OR hepatic OR excretion OR elimination) AND (nano* OR ultrafine*)	630 references



Data source: WOS, ISI Thomson Reuters: 1802 total source:  
web of knowledge

Query = TI = (nano\* OR nanotox\*) and TS = ((pharmacokinetic\*  
OR toxicokinetic\* OR disposition OR distribution OR ADME OR pbpk  
OR environment\*)) and TS = (toxic\*) Timespan = All Years.

Data bases = SCI-EXPANDED. Lemmatization = On 1802 records  
(1991–2011) 60 records (Before 2002)

FIGURE 1: The distribution by year of the 1802 publications documented in the Web of Knowledge (WoK—see Table 2). The exponential growth continued throughout the decade ending in 2010. The drop in 2011 is an artifact due to partial year reporting.

### 3. Results and Discussion

Bibliometric analysis was carried out on two corpora of the literature resulting from searching of PubMed and the Web of Knowledge (WoK) as described in Section 2.

**3.1. Growth of Nanoparticle ADME.** Figure 1 delineates the growth in the number of publication related to ADME, toxicity, and nanoparticles within the WoK. It can clearly be seen that a drastic increase in publication started near 2002. In the eleven years prior to 2002, only 60 articles were recorded in the WoK. Since, 1742 articles related to nanoparticle ADME have been documented. To better understand the structure of this growth, we examined the time

period before and after this critical point when research started to become mainstream.

We first sought to determine whether the growth evident from Figure 1 was driven in a small number of locations, or if the study of nanoparticle ADME had spread from isolated research centers broadly throughout the world. Figure 2 shows the distribution of publications by country of authorship for publication before and after 2002. While the study of ADME properties of nanoparticles may have originally been primarily segregated to industrialized countries (U.S., Canada, Western Europe, China, and Japan), it has since been picked up throughout the world. A large number of the world's nations have produced research focused on nanoparticle ADME. This global expansion of research highlights the importance of the topic and the general concern regarding nanoparticles.

The global spread of interest in nanoparticles could be caused by either an increased interest in the topics studied prior to the spread or an integration of nanoparticle research into more topics. To determine which one described the observed growth, we examined the subject areas for which ADME nanoscale research was being carried out (Figure 3). It is clear that the medical field drove the initial push of nanoparticle ADME research. Pharmaceutical scientists intent on controlling the release of medication pioneered the study of nanoparticle delivery systems. The topic of pharmacology/pharmacy contained over 50% of all publication prior to 2002. Upon investigating the journals in which this research is commonly published, the importance of the medical field on the inception of nano-ADME became more apparent (Figure 4). While publication is evenly spread amongst the represented journals prior to 2002, all of the journals are related to medical research. However, as this area has matured, environmental sciences and toxicology have shown marked growth. As seen in Figure 3, the number of articles related to these two fields has caught up to the number of publications related to medical applications. In addition, the number of specialty areas and topics has expanded. Both of these aspects of growth are also apparent when looking through the set of journals (Figure 4). Environmental Science & Technology has become the journal containing the most ADME nanoscale research evoking

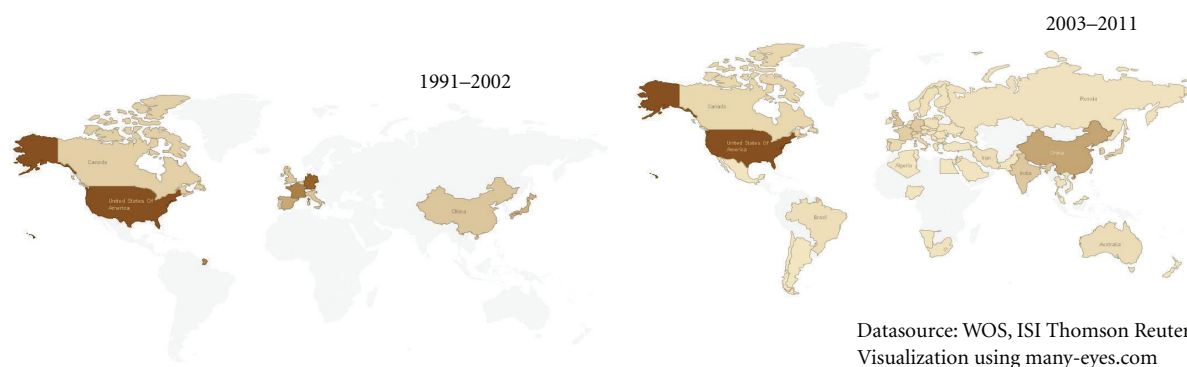


FIGURE 2: The distribution of publications by country of origin in the time before and after the boom of nanoresearch. The maps show record for the years prior to and after 2002. Prior to 2002 the majority of novel nano research was originally centralized in North America and certain pockets of Europe whereas China was a major source for manufacturing. More recently China has become a major player in research (not just manufacturing) and global efforts spanning South America, to portions of Asia and Africa, and Eastern Europe have also become evident alongside North America's effort. (see Table 2: total of 1802 record corpus from WoK analyzed by country of origin in WoK and exported to <http://www.ManyEyes.com/>).

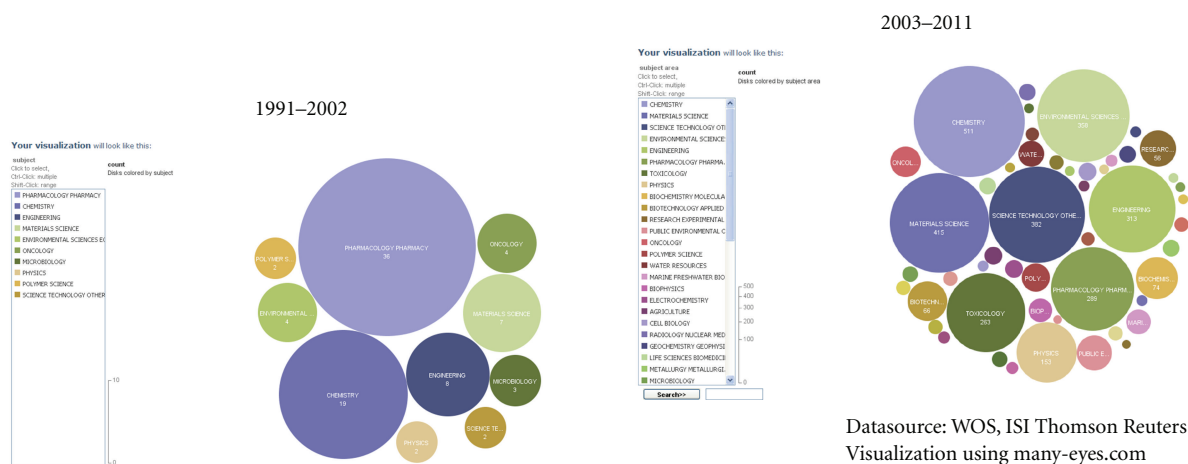


FIGURE 3: The distribution of publications by subject area in the time before and after the boom of nano research (i.e., ~2002) as classified by WoK subject heading citation analysis of 1802 records (see Table 2).

the former while the increase in specialty journals stresses the latter.

**3.2. Key Terms.** While it is clear that the study of nanoparticle ADME has grown, we considered it important to understand which physiological processes were being the most examined. By studying the frequency of terms contained within the collected nanoparticle ADME corpus of the literature, insights into the extent of the covered fields were obtained. We sought to uncover such information based on the corpus of the literature we had collected.

First we looked at the frequency of keywords associated with ADME in the literature base. Figure 5 displays these keyword frequencies and highlights important portions of the ADME process that are understudied. Uptake was the most studied part of nanoparticle ADME, particularly uptake via oral and inhalation routes. However, dermal uptake was less studied though this is a highly probable form of

environmental exposure. Additionally, the study of nanoparticle uptake has greatly outpaced research into the other parts of the ADME process: metabolism and elimination. This lack of focus on vital elements of the physiological processes responsible for actual dose at targeted tissues points to areas of the field that must be further developed.

Taking the abstracts for our set of articles, we then completed a two-word PhraseNet analysis. The resulting network of terms displayed in Figure 6 provides an excellent summary of concepts within the area of nanoparticle ADME. Key aspects of the research such as engineered properties, exposure types, size domains, key organs, and the underlying research domains are all evident. Such graphics provide a high-level view of the principles connected within the field. It is clear from Figure 6 that the study of the environmental impact of nanoparticles has driven a large part of the increased growth in nanoparticle ADME research, having become the key term centralized in the network.



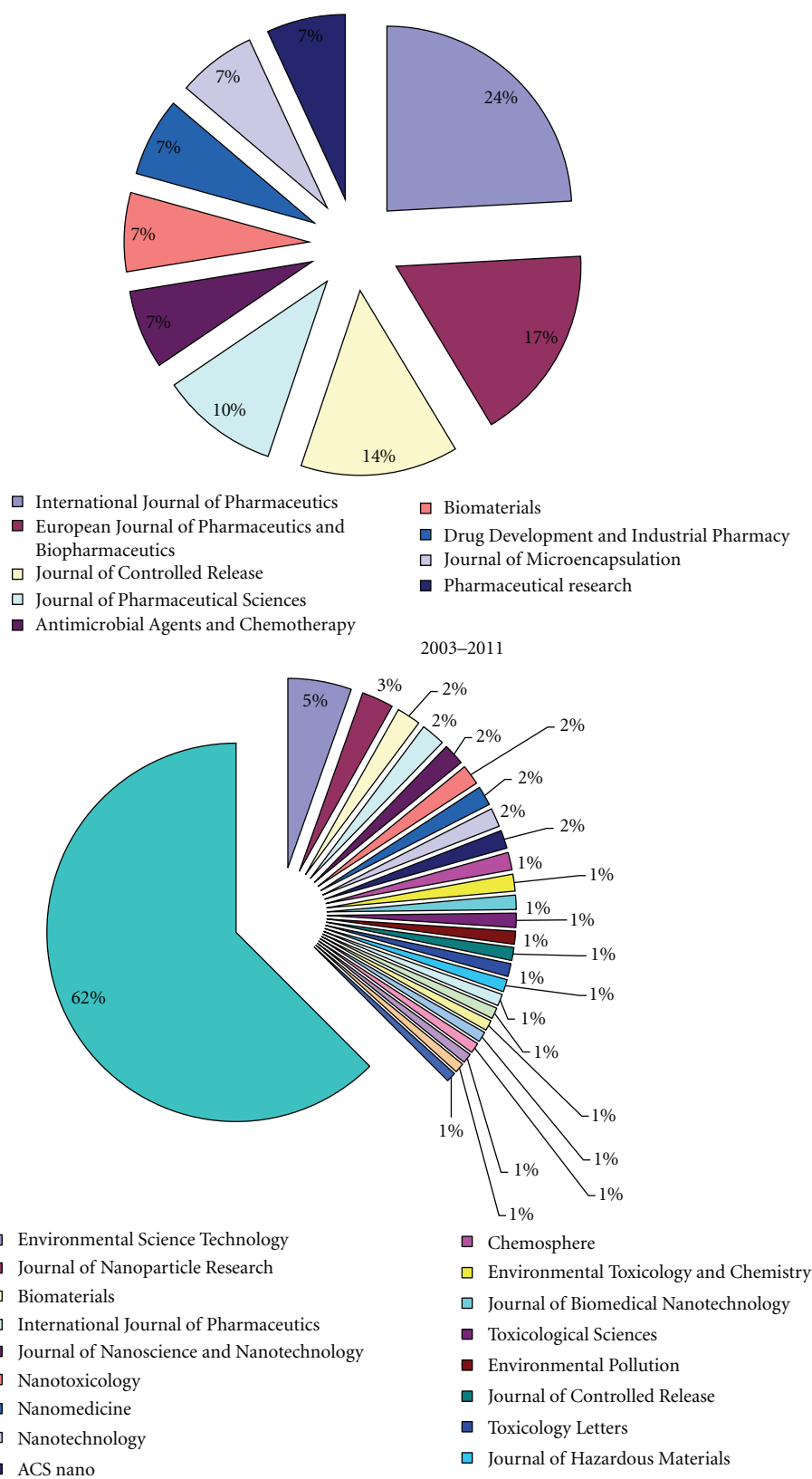


FIGURE 4: The distribution of publications by journal in the time before and after the boom of nano research as classified by WoK publication title analysis of 1802 records (see Table 2).

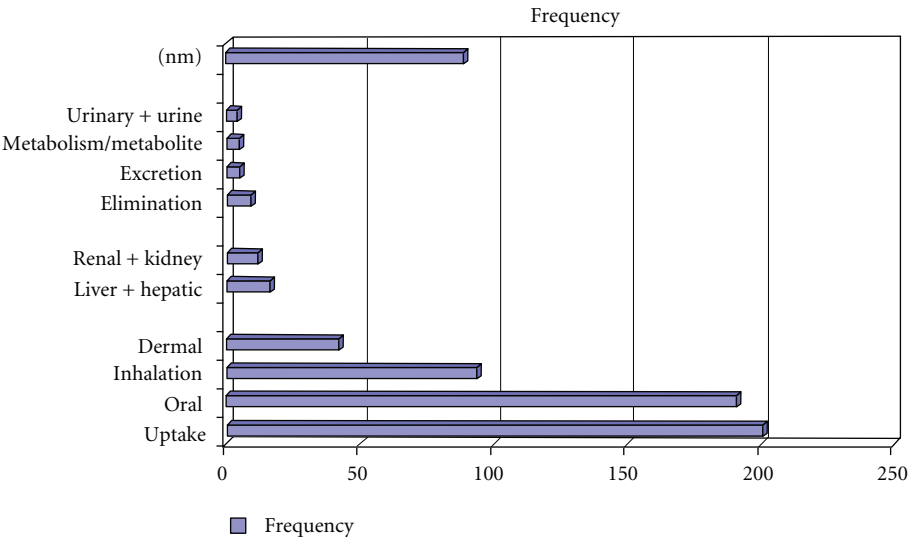


FIGURE 5: Frequency of keywords within the corpus of ADME nanoscale research, as classified by PubMed.org corpus from a custom keyword frequency analysis of 630 records (see—Table 2).

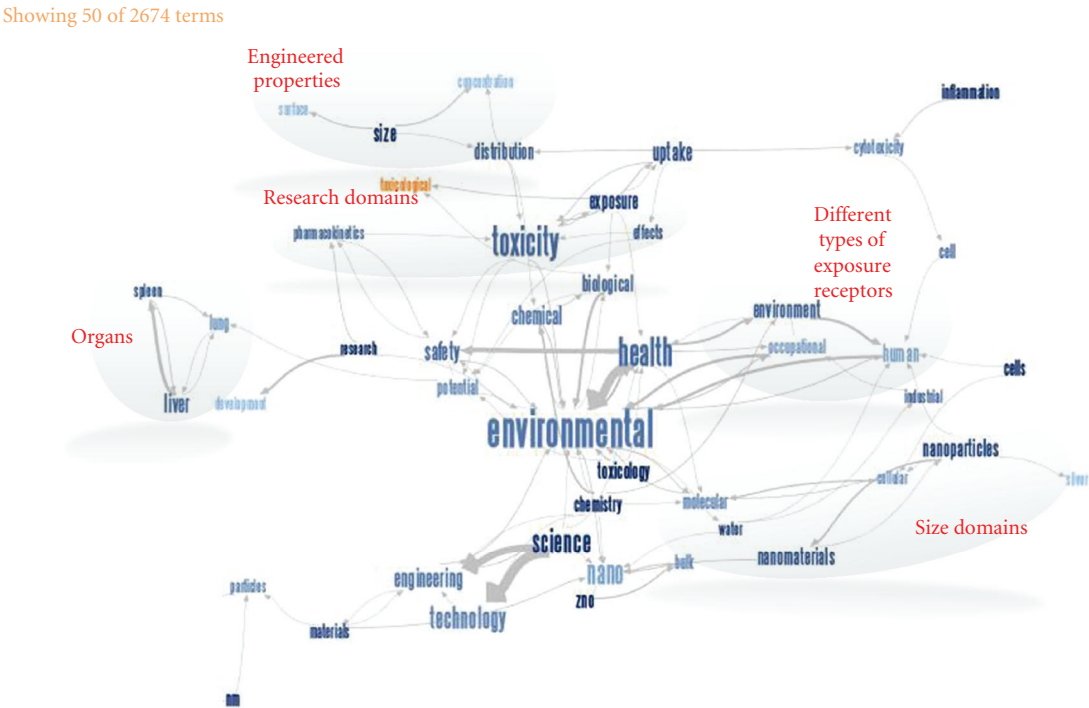


FIGURE 6: Phrase Net generated on the PubMed corpus of nanoparticle ADME publications in <http://www.ManyEyes.com/> from a custom keyword frequency analysis of 630 records (see—Table 2). Major themes have been manually circled and annotated.

3.3. *Publication Segregation.* Unfortunately, the large amount of nanoparticle ADME research does not necessarily mean that it is a cohesive area of research. In fact, the large increase in the number of journals accepting ADME research on nanoparticles (as seen in Figure 4) provides evidence to the contrary. As the field has grown, it has become harder to find and access all the publications that are relevant

to the topic. Figure 7 displays the citation analysis of the WoK publication list and indicates segregation has occurred within the corpus of research. While some distinct lines of research are starting to link to other lines, and there may be some pivotal research articles that have both impact factor in addition to memory between years (looking at zoom in of top 23 articles), there is overall a lack of crosstalk between

-z/histcite/

Datasource: WOS, ISI Thomson Reuters / visualization histogram from HistCite:  
[http://thomsonreuters.com/products\\_services/science/science\\_products/a-z/histcite/](http://thomsonreuters.com/products_services/science/science_products/a-z/histcite/)

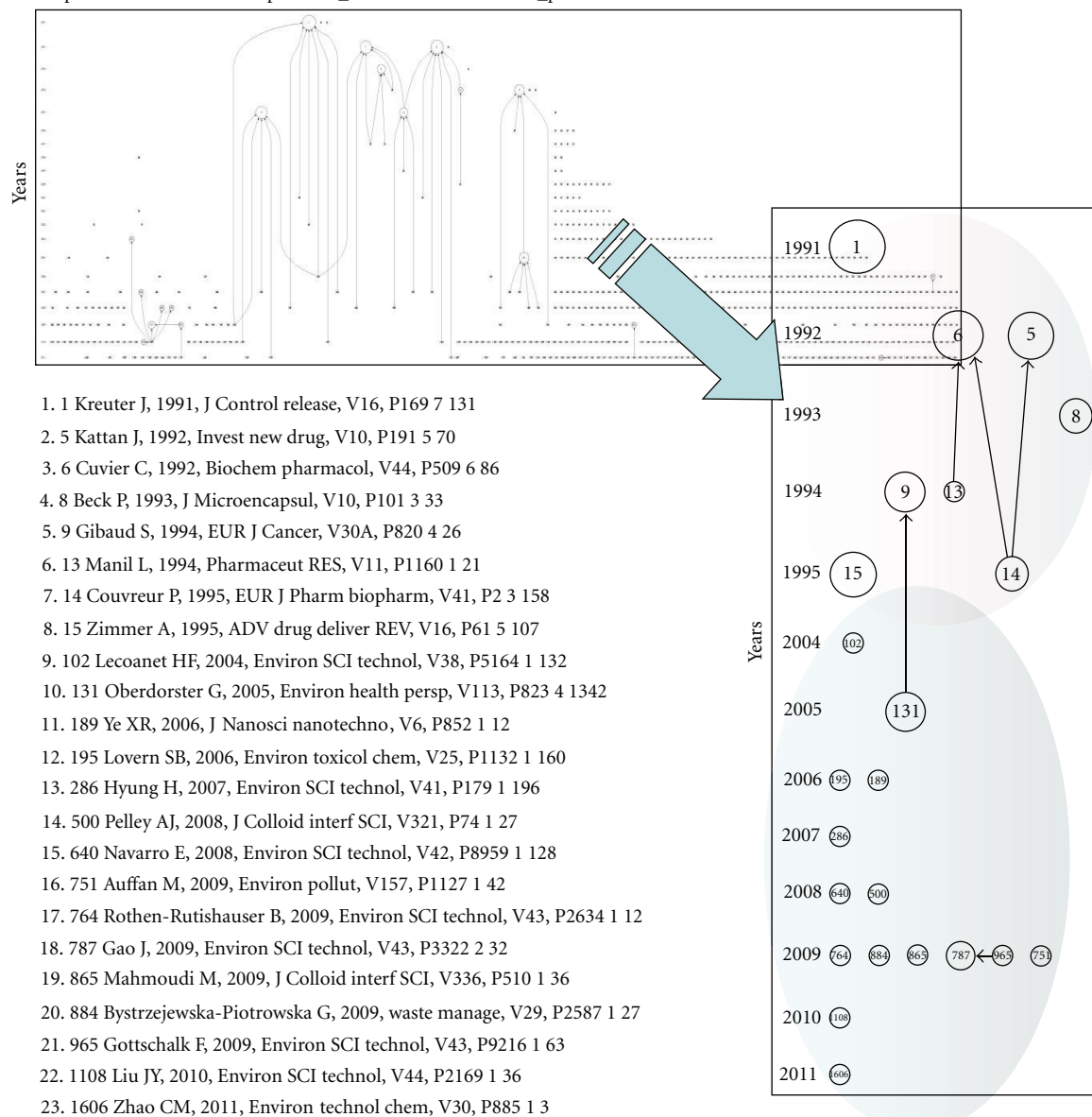


FIGURE 7: Histogram of WoK corpus of the nano-ADME literature from Table 2, generated using the HistCite package ([http://thomsonreuters.com/products\\_services/science/science\\_products/a-z/histcite/](http://thomsonreuters.com/products_services/science/science_products/a-z/histcite/)).

specialties and research efforts. We found it surprising that the majority of high-impact citations connected to none of the previous high-impact citations with the field. What is also apparent from the high-impact internal citation histogram is that the domains of nanobiomedicine (i.e., therapeutics) and nanotoxicology (adverse effects, and large contribution to environmental characterization) emerged over time. While nanobiomedicine dominated the high-impact citations prior to 2002, the high-impact citations after 2002 were primarily focused on environmental health and nanotoxicology efforts.

#### 4. Conclusions

Knowledge tools are effective in identifying trends in research related to nanomaterials [10]. This study described how the research landscape has changed rapidly for health and environmental research. Ten years ago, the medical community dominated ADME nanoscale research almost exclusively. Five years ago, the environmental community surpassed medical research in terms of volume of work and number of journals accepting papers in this area. With the growth of research focused on different aspects for nanoparticle ADME

and the number of specialty subject in the field, there is a clear need for effective communication amongst researchers. The development of a blended ontology agreed upon by all fields interested in nanoparticle ADME properties could ease this communication.

Based on the key term frequencies, there is a void in the literature that indicates some of the most important aspects of the ADME process for nanoparticles are understudied. We suggest that these areas be addressed more specifically in future research by environmental, health, and safety researchers. In order to reach a point where the pharmacokinetics of nanoparticles are truly understood, study of uptake properties is insufficient.

Finally, this study highlights the segregation of the current literature of what should be compatible academic and professional disciplines engaged in research on this topic. The lack of connectivity within the histogram of the nano-ADME literature seems to indicate that effective communication may not be occurring. It is important to discover whether this is a common aspect of histograms for other fields of research or a unique feature of nano-ADME research. Further study of the effects of ontology (or lack of consistent language) on research connectivity should be carried out in this field as well as others. While the problem appears to be lessening with key papers connecting the segregated fields, the results lend credence to the hypothesis that current differences in language may be impeding communication, and that blending terminology to avoid ambiguity could enhance collaborations among the health and environmental disciplines.

## Disclaimer

This paper was reviewed by EPA and approved for publication but does not necessarily reflect official agency policy. The appearance or absence of product, services, companies, organizations, home pages, or other websites in this paper does not imply any endorsement by the agency.

## References

- [1] W. H. de Jong and P. J. A. Borm, "Drug delivery and nanostructure: applications and hazards," *International Journal of Nanomedicine*, vol. 3, no. 2, pp. 133–149, 2008.
- [2] PEW Charitable Trust, Project on Emerging Nanotechnologies, 2011, <http://www.nanotechproject.org/inventories/consumer/>.
- [3] M. Auffan, J. Rose, J.-Y. Bottero, G. V. Lowry, J.-P. Jolivet, and M. R. Wiesner, "Towards a definition of inorganic nanoparticles from an environmental, health and safety perspective," *Nature Nanotechnology*, vol. 4, no. 10, pp. 634–641, 2009.
- [4] L. Yan, F. Zhao, S. Li, Z. Hu, and Y. Zhao, "Low-toxic and safe nanomaterials by surface-chemical design, carbon nanotubes, fullerenes, metallofullerenes, and graphenes," *Nanoscale*, vol. 3, no. 2, pp. 362–382, 2011.
- [5] U.S. Environmental Protection Agency, Report No. EPA 100/B-07/001, 2007, <http://www.epa.gov/osa/pdfs/nanotech/epa-nanotechnology-whitepaper-0207.pdf>.
- [6] IUPAC, *Compendium of Chemical Terminology*, The "Gold Book", Blackwell Science, 2nd edition, 1997, Online corrected version, "chirality", 2006, <http://en.wikipedia.org/wiki/Chirality>.
- [7] D. Fourches, D. Pu, C. Tassa et al., "Quantitative nanostructure-activity relationship modeling," *ACS Nano*, vol. 4, no. 10, pp. 5703–5712, 2010.
- [8] M. R. Goldsmith, C. B. George, G. Zuber et al., "The chiroptical signature of achiral metal clusters induced by dissymmetric adsorbates," *Physical Chemistry Chemical Physics*, vol. 8, no. 1, pp. 63–67, 2006.
- [9] G. M. Whitesides, "The "right" size in nanobiotechnology," *Nature Biotechnology*, vol. 21, no. 10, pp. 1161–1165, 2003.
- [10] D. de la Iglesia, S. Chlesa, J. Kern et al., "Nanoinformatics: new challenges for biomedical informatics at the nano level," *Studies in Health Technology and Informatics*, vol. 150, pp. 987–991, 2009.



## Review Article

# Sarcomere Imaging by Quantum Dots for the Study of Cardiac Muscle Physiology

Fuyu Kobirumaki-Shimozawa,<sup>1</sup> Kotaro Oyama,<sup>1,2</sup> Takahiro Serizawa,<sup>2</sup>  
Akari Mizuno,<sup>1,2</sup> Tatsuya Kagemoto,<sup>1,2</sup> Togo Shimozawa,<sup>3</sup> Shin'ichi Ishiwata,<sup>2</sup>  
Satoshi Kurihara,<sup>1</sup> and Norio Fukuda<sup>1</sup>

<sup>1</sup> Department of Cell Physiology, The Jikei University School of Medicine, 3-25-8 Nishi-Shinbashi, Minato-ku, Tokyo 105-8461, Japan

<sup>2</sup> Department of Physics, Waseda University, Tokyo 169-8555, Japan

<sup>3</sup> Department of Physics, Graduate School of Science, University of Tokyo, Tokyo 113-0033, Japan

Correspondence should be addressed to Norio Fukuda, noriof@jikei.ac.jp

Received 20 October 2011; Accepted 7 January 2012

Academic Editor: P. Bryant Chase

Copyright © 2012 Fuyu Kobirumaki-Shimozawa et al. This is an open access article distributed under the Creative Commons Attribution License, which permits unrestricted use, distribution, and reproduction in any medium, provided the original work is properly cited.

We here review the use of quantum dots (QDs) for the imaging of sarcomeric movements in cardiac muscle. QDs are fluorescence substances (CdSe) that absorb photons and reemit photons at a different wavelength (depending on the size of the particle); they are efficient in generating long-lasting, narrow symmetric emission profiles, and hence useful in various types of imaging studies. Recently, we developed a novel system in which the length of a particular, single sarcomere in cardiomyocytes can be measured at ~30 nm precision. Moreover, our system enables accurate measurement of sarcomere length in the isolated heart. We propose that QDs are the ideal tool for the study of sarcomere dynamics during excitation-contraction coupling in healthy and diseased cardiac muscle.

## 1. Mechanisms of Contraction and Relaxation of Cardiac Muscle

First, we briefly summarize the cellular mechanisms of the excitation-contraction (EC) coupling of cardiac muscle, based on the literature (i.e., [1–3] and references therein). Upon membrane depolarization,  $\text{Ca}^{2+}$  enters myocytes via sarcolemmal L-type  $\text{Ca}^{2+}$  channels, which induces the release of  $\text{Ca}^{2+}$  from the sarcoplasmic reticulum (SR) (i.e.,  $\text{Ca}^{2+}$ -induced  $\text{Ca}^{2+}$  release mechanism; CICR), resulting in an increase in  $[\text{Ca}^{2+}]_i$  and subsequently the binding of  $\text{Ca}^{2+}$  to troponin (Tn), resulting in the subsequent formation of cross-bridges (see Figure 1 for sarcomere structure).

Tn is a heterotrimer of distinct gene products: that is, TnC, TnI, and TnT (see [3, 4] and references therein).  $\text{Ca}^{2+}$  binds to the regulatory  $\text{Ca}^{2+}$ -binding site of TnC, resulting in the onset of conformational changes of the thin filament. During diastole, the C-terminal domain of TnI tightly binds to actin, and tropomyosin blocks the actomyosin interaction

(“off” state). However, when  $\text{Ca}^{2+}$  binds to the regulatory  $\text{Ca}^{2+}$ -binding site of TnC during systole, the C-terminal domain of TnI is dissociated from actin and binds to the N-terminal domain of TnC, due to the enhanced binding of TnC and TnI (“on” state). The transition from the “off” to “on” state is associated with a movement and conformational change of tropomyosin on the thin filament, facilitating the binding of myosin molecules to actin (see [3, 4] and references therein). Similar to  $\text{Ca}^{2+}$ , the strongly bound cross-bridges such as the rigor complex or the actomyosin-ADP complex can “turn on” the thin filament, as if  $\text{Ca}^{2+}$  were bound to TnC, further promoting the formation of cycling cross-bridges (e.g., [5–7]). Therefore, under physiologic conditions, both  $\text{Ca}^{2+}$  and strongly bound cross-bridges regulate the state of the thin filament in a coordinated fashion.

After the peak of contraction,  $[\text{Ca}^{2+}]_i$  is lowered via, mostly, four  $\text{Ca}^{2+}$ -transport systems: that is, (i) sequestration by the SR  $\text{Ca}^{2+}$ -ATPase pump, (ii) efflux via the sarcolemmal  $\text{Na}^+/\text{Ca}^{2+}$  exchanger, (iii) extrusion by the sarcolemmal

$\text{Ca}^{2+}$ -ATPase pump, and (iv) uptake into mitochondria via the  $\text{Ca}^{2+}$  uniporter [see [1, 2] and references therein].

Recent advances in molecular imaging technologies have enhanced our understanding of the EC coupling of cardiac muscle. In particular, the processes of the local changes of various ions at/near the T-tubules (such as the dynamics of  $\text{Ca}^{2+}$  sparks) in isolated myocytes have been elucidated (e.g., [1, 2]). In addition, a recent study greatly improved the quantification of  $\text{Ca}^{2+}$  sparks [8]. It should be stressed that compared to ions/currents, our knowledge is still limited regarding the sarcomere dynamics in localized, focal areas of cardiomyocytes. Indeed, although it is generally thought that all sarcomeres within a cardiomyocyte uniformly respond to a change in  $[\text{Ca}^{2+}]_i$  to produce mechanical force, this notion has yet to be verified. Therefore, careful experimentation employing advanced nanotechnologies is needed to fully reveal the mechanism by which EC coupling is regulated in localized areas at/near T-tubules in a cardiomyocyte, and the subsequent transmission throughout the myocyte.

## 2. Sarcomere Length Dependence of $\text{Ca}^{2+}$ Activation: Underling Mechanism for Frank-Starling's Law of the Heart

It is well established that active force production of cardiac muscle is more sarcomere length-(SL-) dependent than that of skeletal muscle (e.g., [3, 9–13]). Allen and Kurihara [14] applied the  $\text{Ca}^{2+}$ -sensitive photoprotein aequorin to cardiac muscle and simultaneously measured  $[\text{Ca}^{2+}]_i$  and twitch force at varying muscle lengths. Accordingly, they discovered that the increase in twitch force was not associated with a rise in  $[\text{Ca}^{2+}]_i$ , but with activation of myofilament proteins *per se*. Indeed, a number of later studies using various types of preparations have provided solid evidence that a change of only  $\sim 0.1 \mu\text{m}$  in SL causes a dramatic change in mechanical properties, especially under physiologic partial activation states where the average  $[\text{Ca}^{2+}]_i$  increases to  $\sim 10^{-6} \text{M}$  (e.g., [15, 16]).

What is the molecular basis for this pronounced SL dependence? It has been demonstrated that SL elongation causes a decrease in interfilament lattice spacing via the radial component of titin-based passive force in the sarcomere, promoting cross-bridge attachment [17–19]. More recently, we reported that the binding of myosin-ATP to actin upon reduction in the lattice spacing depends highly on the thin filament “on-off” state [7, 20]. It is therefore considered that interfilament lattice spacing and thin filament “on-off” switching are the two essential factors that regulate length-dependent activation.

## 3. Use of Quantum Dots (QDs) for the Detection of Sarcomere Length

Because of the large length dependence of active force, accurate measurement of SL is the key to unveiling the contracting functions of cardiac muscle at the molecular level. A number of studies have been conducted on cardiomyocytes, cardiac strips, and whole heart of various animal

species, but SL is usually averaged along the longitudinal axis of the myocyte (e.g., [21, 22] and references therein). Indeed, the averaging of SLs allows researchers to obtain stable and consistent values with minimal deviation, hence useful for quantification. However, it is likely that the SL value varies even within the same myocyte during cardiac beat, due to variations in the magnitude of the local rise in  $[\text{Ca}^{2+}]_i$  at/near the T-tubules, especially in diseased tissues (see [1, 2] and references therein). Therefore, the variance in SL may be transmitted over a long distance along the longitudinal axis, influencing the myocyte's mechanical properties (e.g., length-dependent activation). Thus, it is critical to establish a method by which one can visualize the motions of a single sarcomere at high spatial and temporal resolution in various regions of the myocyte.

In various fields within biological sciences, QDs are widely used to view the motions of molecules, because they are extremely efficient in generating long-lasting fluorescence, with their intrinsic brightness; in fact, they are many times more efficient than other classes of fluorophores (see e.g., [23, 24]). These characteristics of QDs are favorable for long-term imaging experiments in cells as well as *in vivo*. Indeed, Tada et al. [23] successfully conducted the tracking of the HER2 molecule in living mice. Later, Gonda et al. [24] dramatically enhanced the quality of the positioning of QDs and tracked the movement of cancer cells in anesthetized living mice at a precision of  $\sim 7 \text{ nm}$ .

By taking advantage of the nature of QDs, we recently developed a novel technique to measure the length of individual sarcomeres in isolated cardiomyocytes and in the whole heart [25] (see also Figure 1). In that study, we analyzed the movement of QDs (Qdot 655 Invitrogen, Carlsbad, CA, USA) conjugated with anti- $\alpha$ -actinin antibody attached to the Z-disks of sarcomeres in skinned rat ventricular myocytes during spontaneous sarcomeric oscillations (SPOC) that occur under partial activation states (i.e., ADP-SPOC and Ca-SPOC; see [26–30]), and in intact cardiomyocytes under electric field stimulation. It should be stressed that compared to a widely used organic dye (i.e., Alexa 488), QDs enable the measurement of the length of a single sarcomere at a resolution of  $\sim 30 \text{ nm}$  for a relatively long period (i.e., 1 min) [25]. Here, as shown in Figure 2, even when the myocyte was in motion (due to ADP-SPOC), we found that the QD fluorescence successfully provided clear striations along the myocyte compared to that obtained under the bright field (see also Supplementary Videos 1 and 2, see in Supplementary Material available online at doi:10.1155/2012/313814).

One interesting finding in our previous work [25] is that intact cardiomyocytes showed periodic outlines after treatment with a mixture of anti- $\alpha$ -actinin antibody-QDs and FuGENE HD (a lipid reagent; Roche Ltd., Basel, Switzerland), indicating the infiltration of the antibody-QDs into the myocytes and their subsequent attachment to the Z-disks. The myocytes treated in this way were shown to normally respond to electric field stimulations at various frequencies (1–5 Hz), indicating the usefulness of QDs for various physiological experiments with living myocytes. Our previous finding that the waveform properties upon

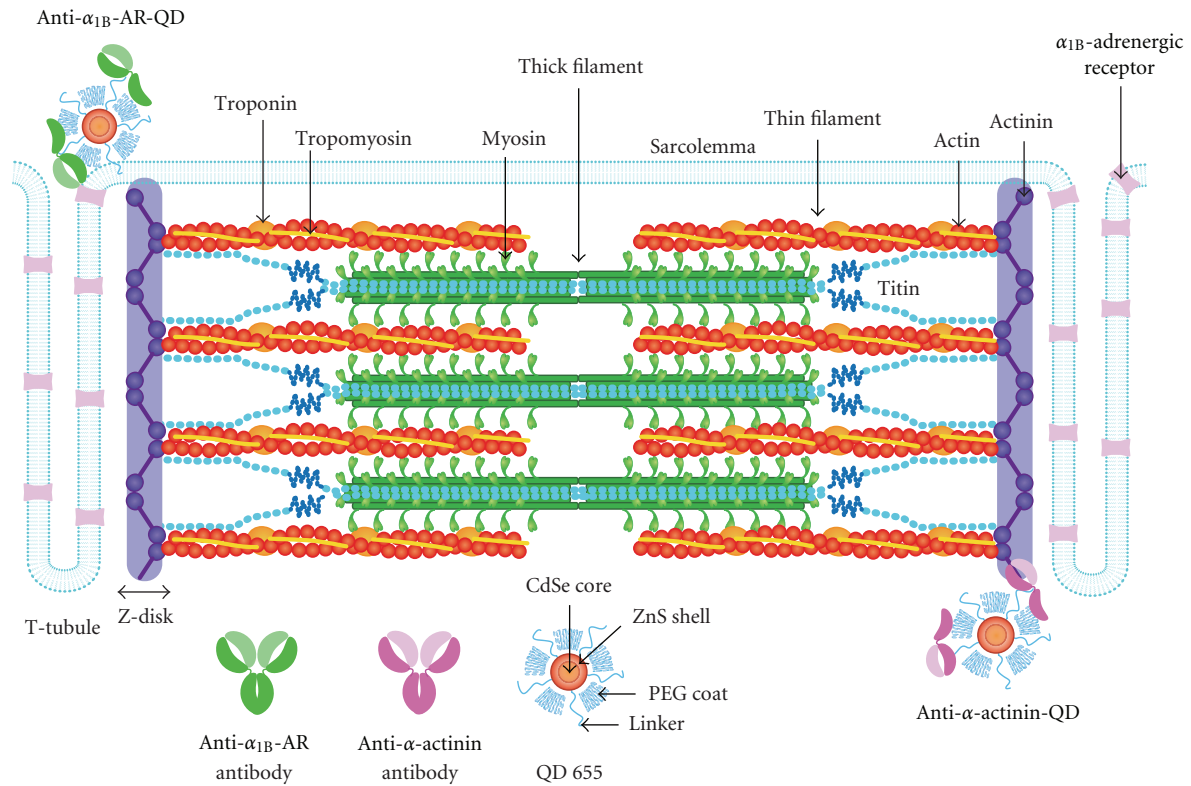


FIGURE 1: Schematic illustration indicating the structure of a cardiac sarcomere associated with T-tubules. As discussed in [33], T-tubules and Z-disks are considered to run in parallel in cardiac muscle, causing  $\text{Ca}^{2+}$  sparks at/near the Z-disks. Thick and thin filaments, and titin are shown in this illustration (for simplicity, only two titin molecules per half thick filament are shown) (cf. [37] for electron microscopic images of titin molecules in the sarcomere). Also, troponin and tropomyosin are bound to the thin filaments. As described in detail in earlier papers (e.g., [12, 13]), I-band titin is in a contracted state at the slack SL; straightening of the tandem Ig segment and, then, extension of the PEVK and N2B segments are thought to occur (resulting in passive force generation) in response to stretch. In the lower part of the figure, the antibodies we used in the present work and the structure of the QD (Qdot 655 Invitrogen, Carlsbad, CA, USA) are shown (number indicating the emission wavelength). The anti- $\alpha$ -actinin antibody-QDs bind to Z-disks, and anti- $\alpha_{1B}$ -adrenergic receptor (AR) antibody-QDs bind to the T-tubules.

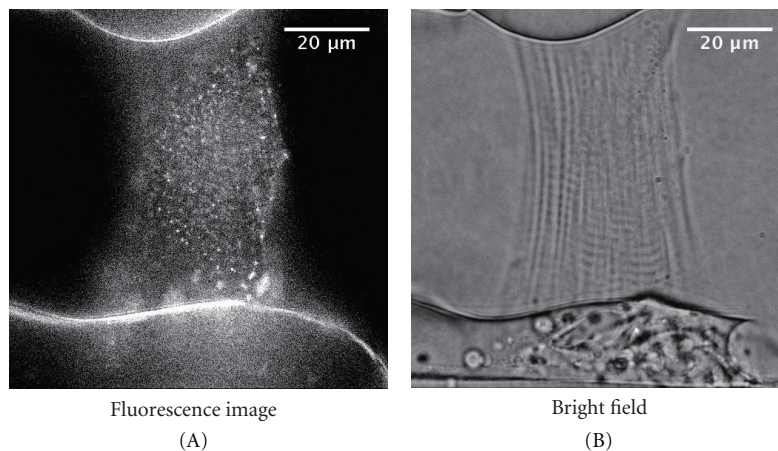


FIGURE 2: (A) Epi-illumination of a rat skinned myocyte treated with anti- $\alpha$ -actinin antibody-QDs excited by blue light during ADP-SPOC (see [25] for composition of the ADP-SPOC solution). Note the clear striations along the myocyte. (B) Same myocyte as in the (A) during ADP-SPOC, observed under the bright field. Observations were conducted under the same optics system as described in [25], and the temperature was maintained at 25°C. See Supplementary Videos 1 and 2.

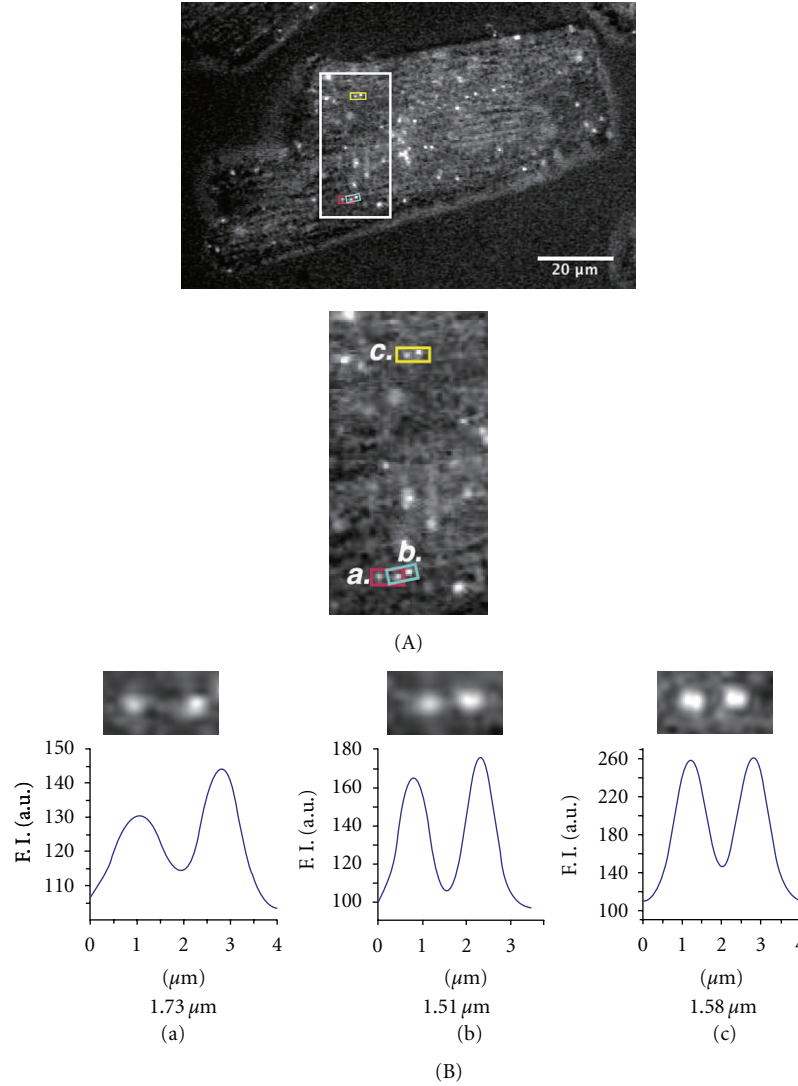


FIGURE 3: (A) Top, Epi-illumination image of an intact cardiomyocyte treated with anti- $\alpha_{1B}$ -adrenergic receptor antibody (sc-27136, Santa Cruz, CA; see [38]) QDs at 3 nM in oxygenated  $\text{Ca}^{2+}$ -free-HEPES-Tyrode's solution containing 20 mM 2,3-butane-dione monoxime at 25°C (see [25]). Note the periodic fluorescent profiles of QDs along the myocyte. Bottom, enlarged view of the area shown in the rectangular outline in the top of this figure. (a), (b), and (c) indicate the regions within the myocyte used for the length analyses in (B). (B) Analysis of the distance (indicated by the number below each graph) between the QD fluorescence signals in (a), (b), and (c) in (a). Analysis was conducted based on [25]. We found that the values differed for two sequential distances, that is, 1.73 and 1.51  $\mu\text{m}$ , respectively, in (a) and (b). The inhomogeneity of the length of the sarcomere in series may induce nonlinear phenomena such as SPOC upon activation (see [30]), because the  $\sim 0.2 \mu\text{m}$  difference in SL can affect the actomyosin interaction and titin-based restorative passive force (e.g., [10–13]). As previously shown [38],  $\alpha_{1B}$ -adrenergic receptors are predominantly localized at the T-tubules.

electric field stimulation became similar to those obtained during SPOC at high stimulation frequencies of 3–5 Hz (i.e., relatively slow shortening followed by quick re-lengthening) suggests that SPOC may facilitate the organization of sarcomeric waveform to efficiently produce mechanical force in living myocytes. Future studies should be directed to determine whether or not SPOC indeed occurs in the normal physiological setting.

Figure 3(A) shows the epi-fluorescent image of an intact cardiomyocyte treated with QDs conjugated with anti- $\alpha_{1B}$ -adrenergic receptor antibody (details given in the legend of Figure 3; see also Figure 1 for binding of the antibody-QD

complex to the T-tubule). We observed periodic fluorescent signals along the longitudinal axis of the myocyte, indicating the positions of the T-tubules. Figure 3(B) shows the results of the analyses of the distances between the peaks of the QD signals at different locations in the myocyte shown in Figure 3(A). We found that the distances between the T-tubules (even two sequential distances) differ within the myocyte to a magnitude greater than that found in skinned myocytes (i.e., as much as  $\sim 0.2 \mu\text{m}$ ; cf. [25]), suggesting relatively large variance of SL, as previously reported in an earlier study [31]. It has been reported that, albeit a probability lower than that during systole,  $\text{Ca}^{2+}$  sparks occur during



diastole in intact cardiomyocytes (e.g., [1, 2]). Consistent with this notion, we observed that  $\text{Ca}^{2+}$  sparks indeed randomly occurred under our experimental condition in various regions in an intact myocyte, followed by a marked  $\text{Ca}^{2+}$  wave, coupled presumably with autonomous depolarization of the sarcolemma (see Supplemental Video 3). These results may suggest that during diastole, differing magnitudes of  $\text{Ca}^{2+}$  sparks occurring at varying localized areas of the myocyte result in different magnitudes of contractions in sarcomeres within the cell, hence different lengths of the sarcomere.

It is worthwhile noting that FuGENE HD (cf. [25]) may cause irreversible damage to the sarcolemmal functions of cardiomyocytes, and this damage, albeit only a slight magnitude, may result in abnormal depolarization and/or repolarization. In contrast, we consider that the conjugation of QDs and the antibody specific to the extracellular domains of proteins present predominantly in the T-tubules, such as  $\alpha_{1B}$ -adrenergic receptors (shown in the present study), allows for visualization of mechanical performance of cardiomyocytes under physiologic conditions with, possibly, little or no damage of the sarcolemmal functions.

Here, a criticism may arise as to the verification of the observed distance between the QD fluorescent signals in intact cardiomyocytes (Figure 3(A)), because the signals indicate the positions of the T-tubules (not the Z-disks). Indeed, the T-tubules are reportedly disposed not simply over but around the Z-disks [32], and because of this, measuring the distance between two dots (fluorescence peaks) may cause some error in detecting SL in a localized area, especially during systole. However, considering the general consensus that the T-tubules and Z-disks are closely associated and run in parallel in mammalian ventricular cells (e.g., [21, 33]), it is reasonable to assume in the present study that the fluorescence signals obtained from QD-treated myocytes represent the locations of the Z-disks, and therefore, the distance between the two fluorescence peaks indicates the length of a single sarcomere within a particular region. Future studies, with, for example, a double optical path, are needed to clarify how the T-tubules and Z-disks are aligned in cardiomyocytes during diastole and systole.

#### 4. Sarcomere Length Measurement in the Whole Heart

Several groups have reported the results of SL measurement in the heart at the organ level, by using X-ray diffraction [34], postmortem histology [35], and two-photon imaging [21]. Time-resolved X-ray diffraction-based techniques appear to be suitable for measuring rapid changes in SL during contraction. However, in the whole heart, measured SL data provide a group average of several hundred cells and, therefore, are not suitable for determining SL values as a function of local movement of cardiomyocytes. Recently, Bub et al. [21] established a technique using two-photon microscopy to directly image striations of cardiomyocytes in the arrested isolated heart, stained with the fluorescent marker di-4-ANEPPS. While this system appears to be useful to accurately measure SL (or more precisely, the distance

between the T-tubules) alongside the cardiomyocyte, it is not applicable to the heart at work (especially to the heart of small animals with high heart rates), because of the slow camera frame rate ( $>1$  sec). In our previous study [25], we detected the fluorescence of QDs from myocytes at the surface of the LV of the whole heart of the rat, and found that the peak-to-peak fluorescence distance was  $\sim 2.00 \mu\text{m}$  (i.e., close to those obtained by using different methods; cf. [8, 34–36]) under the relaxed state. Because the experiment was conducted after perfusion of the heart with  $\text{Ca}^{2+}$  free-HEPES-Tyrod solution containing 80 mM 2,3-butanedione monoxime, we consider that the value reflects the SL during diastole. In this system, we observed epifluorescence of QDs with an EMCCD camera, allowing us to measure the length of a single sarcomere at 30 frames per second (fps). Therefore, in future studies, QDs may be a valuable tool to detect the length of a single sarcomere in a particular myocyte in the heart *in vivo*, after resolution of the problems associated with focus adjustment in the Z-direction during cardiac beat.

#### 5. Conclusion

In this article, we summarized the molecular mechanisms of the EC coupling of cardiac muscle, focusing on the contractile function. We highlighted the recent advances in the measurement of single sarcomere dynamics with QDs in skinned and intact myocytes, as well as in the whole heart. We also presented new data showing that QDs revealed differences in the length of sarcomeres within the same myocyte even during diastole, presumably due to the “on/off” of  $\text{Ca}^{2+}$ -sparks in localized regions. We therefore consider that QDs are a useful, powerful tool to quantitatively analyze the dynamics of cardiac muscle under various experimental settings.

#### Acknowledgments

The authors thank Naoko Tomizawa (Department of Cell Physiology, The Jikei University School of Medicine, Tokyo, Japan) for superb technical assistance. The work of the authors was supported in part by Grants-in-Aid for Scientific Research (N. Fukuda and S. Kurihara), Scientific Research on Innovative Areas (N. Fukuda) and for Challenging Exploratory Research (F. Kobirumaki-Shimozawa and N. Fukuda) from the Ministry of Education, Culture, Sports, Science and Technology of Japan and by grants from the Japan Science and Technology Agency (CREST) (N. Fukuda), the Vehicle Racing Commemorative Foundation (S. Kurihara), the Institute of Seizon and Life Sciences (S. Kurihara) and the CASIO Science Promotion Foundation (N. Fukuda). No conflicts of interest, financial or otherwise, are declared by the authors.

#### References

- [1] D. M. Bers, *Excitation-Contraction Coupling and Cardiac Contractile Force*, Kluwer-Academic, Dordrecht, The Netherlands, 2nd edition, 2001.

- [2] D. M. Bers, "Cardiac excitation-contraction coupling," *Nature*, vol. 415, no. 6868, pp. 198–205, 2002.
- [3] N. Fukuda, T. Terui, I. Ohtsuki, S. Ishiwata, and S. Kurihara, "Titin and troponin: central players in the Frank-Starling mechanism of the heart," *Current Cardiology Reviews*, vol. 5, no. 2, pp. 119–124, 2009.
- [4] R. J. Solaro and H. M. Rarick, "Troponin and tropomyosin: proteins that switch on and tune in the activity of cardiac myofilaments," *Circulation Research*, vol. 83, no. 5, pp. 471–480, 1998.
- [5] N. Fukuda, H. Fujita, T. Fujita, and S. Ishiwata, "Regulatory roles of MgADP and calcium in tension development of skinned cardiac muscle," *Journal of Muscle Research and Cell Motility*, vol. 19, no. 8, pp. 909–921, 1998.
- [6] N. Fukuda, H. Kajiwar, S. Ishiwata, and S. Kurihara, "Effects of MgADP on length dependence of tension generation in skinned rat cardiac muscle," *Circulation Research*, vol. 86, no. 1, pp. e1–e6, 2000.
- [7] T. Terui, Y. Shimamoto, M. Yamane et al., "Regulatory mechanism of length-dependent activation in skinned porcine ventricular muscle: role of thin filament cooperative activation in the Frank-Starling relation," *Journal of General Physiology*, vol. 136, no. 4, pp. 469–482, 2010.
- [8] P. Bankhead, C. Norman Scholfield, T. M. Curtis, and J. G. McGeown, "Detecting  $\text{Ca}^{2+}$  sparks on stationary and varying baselines," *American Journal of Physiology*, vol. 301, no. 3, pp. C717–C728, 2011.
- [9] A. M. Katz, "Ernest Henry Starling, his predecessors, and the 'Law of the Heart,'" *Circulation*, vol. 106, no. 23, pp. 2986–2992, 2002.
- [10] N. Fukuda and H. Granzier, "Role of the giant elastic protein titin in the Frank-Starling mechanism of the heart," *Current Vascular Pharmacology*, vol. 2, no. 2, pp. 135–139, 2004.
- [11] N. Fukuda and H. L. Granzier, "Titin/connectin-based modulation of the Frank-Starling mechanism of the heart," *Journal of Muscle Research and Cell Motility*, vol. 26, no. 6–8, pp. 319–323, 2005.
- [12] N. Fukuda, H. L. Granzier, S. Ishiwata, and S. Kurihara, "Physiological functions of the giant elastic protein titin in mammalian striated muscle," *Journal of Physiological Sciences*, vol. 58, no. 3, pp. 151–159, 2008.
- [13] N. Fukuda, T. Terui, S. Ishiwata, and S. Kurihara, "Titin-based regulations of diastolic and systolic functions of mammalian cardiac muscle," *Journal of Molecular and Cellular Cardiology*, vol. 48, no. 5, pp. 876–881, 2010.
- [14] D. G. Allen and S. Kurihara, "The effects of muscle length on intracellular calcium transients in mammalian cardiac muscle," *Journal of Physiology*, vol. 327, pp. 79–94, 1982.
- [15] D. G. Allen and J. C. Kentish, "The cellular basis of the length-tension relation in cardiac muscle," *Journal of Molecular and Cellular Cardiology*, vol. 17, no. 9, pp. 821–840, 1985.
- [16] N. Fukuda, D. Sasaki, S. Ishiwata, and S. Kurihara, "Length dependence of tension generation in rat skinned cardiac muscle: role of titin in the Frank-Starling mechanism of the heart," *Circulation*, vol. 104, no. 14, pp. 1639–1645, 2001.
- [17] O. Cazorla, Y. Wu, T. C. Irving, and H. Granzier, "Titin-based modulation of calcium sensitivity of active tension in mouse skinned cardiac myocytes," *Circulation Research*, vol. 88, no. 10, pp. 1028–1035, 2001.
- [18] N. Fukuda, Y. Wu, G. Farman, T. C. Irving, and H. Granzier, "Titin isoform variance and length dependence of activation in skinned bovine cardiac muscle," *Journal of Physiology*, vol. 553, part 1, pp. 147–154, 2003.
- [19] N. Fukuda, Y. Wu, G. Farman, T. C. Irving, and H. Granzier, "Titin-based modulation of active tension and interfilament lattice spacing in skinned rat cardiac muscle," *Pflügers Archiv European Journal of Physiology*, vol. 449, no. 5, pp. 449–457, 2005.
- [20] T. Terui, M. Sodnomtseren, D. Matsuba et al., "Troponin and titin coordinately regulate length-dependent activation in skinned porcine ventricular muscle," *Journal of General Physiology*, vol. 131, no. 3, pp. 275–283, 2008.
- [21] G. Bub, P. Camelliti, C. Bollensdorff et al., "Measurement and analysis of sarcomere length in rat cardiomyocytes in situ and in vitro," *American Journal of Physiology*, vol. 298, no. 5, pp. H1616–H1625, 2010.
- [22] N. M. P. King, M. Methawasin, J. Nedrud et al., "Mouse intact cardiac myocyte mechanics: cross-bridge and titin-based stress in unactivated cells," *Journal of General Physiology*, vol. 137, no. 1, pp. 81–91, 2011.
- [23] H. Tada, H. Higuchi, T. M. Wanatabe, and N. Ohuchi, "In vivo real-time tracking of single quantum dots conjugated with monoclonal anti-HER2 antibody in tumors of mice," *Cancer Research*, vol. 67, no. 3, pp. 1138–1144, 2007.
- [24] K. Gonda, T. M. Watanabe, N. Ohuchi, and H. Higuchi, "In vivo nano-imaging of membrane dynamics in metastatic tumor cells using quantum dots," *Journal of Biological Chemistry*, vol. 285, no. 4, pp. 2750–2757, 2010.
- [25] T. Serizawa, T. Terui, T. Kagemoto et al., "Real-time measurement of the length of a single sarcomere in rat ventricular myocytes: a novel analysis with quantum dots," *American Journal of Physiology*, vol. 301, no. 5, pp. C1116–C1127, 2011.
- [26] N. Fukuda, H. Fujita, T. Fujita, and S. Ishiwata, "Spontaneous tension oscillation in skinned bovine cardiac muscle," *Pflügers Archiv European Journal of Physiology*, vol. 433, no. 1–2, pp. 1–8, 1996.
- [27] N. Fukuda and S. Ishiwata, "Effects of pH on spontaneous tension oscillation in skinned bovine cardiac muscle," *Pflügers Archiv European Journal of Physiology*, vol. 438, no. 2, pp. 125–132, 1999.
- [28] D. Sasaki, H. Fujita, N. Fukuda, S. Kurihara, and S. Ishiwata, "Auto-oscillations of skinned myocardium correlating with heartbeat," *Journal of Muscle Research and Cell Motility*, vol. 26, no. 2–3, pp. 93–101, 2005.
- [29] D. Sasaki, N. Fukuda, and S. Ishiwata, "Myocardial sarcomeres spontaneously oscillate with the period of heartbeat under physiological conditions," *Biochemical and Biophysical Research Communications*, vol. 343, no. 4, pp. 1146–1152, 2006.
- [30] S. Ishiwata, Y. Shimamoto, and N. Fukuda, "Contractile system of muscle as an auto-oscillator," *Progress in Biophysics and Molecular Biology*, vol. 105, no. 3, pp. 187–198, 2011.
- [31] N. Sarai, Y. Kihara, T. Izumi, T. Mitsui, S. Matsuoka, and A. Noma, "Nonuniformity of sarcomere shortenings in the isolated rat ventricular myocyte," *Japanese Journal of Physiology*, vol. 52, no. 4, pp. 371–381, 2002.
- [32] C. Soeller and M. B. Cannell, "Two-photon microscopy: imaging in scattering samples and three-dimensionally resolved flash photolysis," *Microscopy Research and Technique*, vol. 47, no. 3, pp. 182–195, 1999.
- [33] R. M. Berne, M. N. Levy, B. M. Koeppen, and B. A. Stanton, *Physiology*, Mosby, St. Louis, Mo, USA, 4th edition, 1998.
- [34] N. Yagi, J. Shimizu, S. Mohri et al., "X-ray diffraction from a left ventricular wall of rat heart," *Biophysical Journal*, vol. 86, no. 4, pp. 2286–2294, 2004.



- [35] A. F. Grimm, H. L. Lin, and B. R. Grimm, "Left ventricular free wall and intraventricular pressure-sarcomere length distributions," *American Journal of Physiology*, vol. 239, no. 1, pp. H101–H107, 1980.
- [36] C. S. Chung and H. L. Granzier, "Contribution of titin and extracellular matrix to passive pressure and measurement of sarcomere length in the mouse left ventricle," *Journal of Molecular and Cellular Cardiology*, vol. 50, no. 4, pp. 731–739, 2011.
- [37] T. Funatsu, E. Kono, H. Higuchi et al., "Elastic filaments in situ in cardiac muscle: deep-etch replica analysis in combination with selective removal of actin and myosin filaments," *Journal of Cell Biology*, vol. 120, no. 3, pp. 711–724, 1993.
- [38] J. O-Uchi, H. Sasaki, S. Morimoto et al., "Interaction of  $\alpha 1$ -adrenoceptor subtypes with different G proteins induces opposite effects on cardiac L-type  $\text{Ca}^{2+}$  channel," *Circulation Research*, vol. 102, no. 11, pp. 1378–1388, 2008.

## Research Article

# Self-Organization of Motor-Propelled Cytoskeletal Filaments at Topographically Defined Borders

Alf Månsson,<sup>1</sup> Richard Bunk,<sup>2</sup> Mark Sundberg,<sup>1</sup> and Lars Montelius<sup>2</sup>

<sup>1</sup> School of Natural Sciences, Linnaeus University, 391 82 Kalmar, Sweden

<sup>2</sup> Division of Solid State Physics and The Nanometer Structure Consortium, Lund University, Box 118, S221 00 Lund, Sweden

Correspondence should be addressed to Alf Månsson, alf.mansson@lnu.se

Received 31 August 2011; Accepted 7 January 2012

Academic Editor: P. Bryant Chase

Copyright © 2012 Alf Månsson et al. This is an open access article distributed under the Creative Commons Attribution License, which permits unrestricted use, distribution, and reproduction in any medium, provided the original work is properly cited.

Self-organization phenomena are of critical importance in living organisms and of great interest to exploit in nanotechnology. Here we describe in vitro self-organization of molecular motor-propelled actin filaments, manifested as a tendency of the filaments to accumulate in high density close to topographically defined edges on nano- and microstructured surfaces. We hypothesized that this “edge-tracing” effect either (1) results from increased motor density along the guiding edges or (2) is a direct consequence of the asymmetric constraints on stochastic changes in filament sliding direction imposed by the edges. The latter hypothesis is well captured by a model explicitly defining the constraints of motility on structured surfaces in combination with Monte-Carlo simulations [cf. Nitta et al. (2006)] of filament sliding. In support of hypothesis 2 we found that the model reproduced the edge tracing effect without the need to assume increased motor density at the edges. We then used model simulations to elucidate mechanistic details. The results are discussed in relation to nanotechnological applications and future experiments to test model predictions.

## 1. Introduction

Self-organization of complex systems involves pattern or structure formation due to multiple local interactions of the participating elements when a system is left to itself. Whereas self-organization phenomena are of critical importance in biology, they are also of great interest to exploit for nanofabrication or, more dynamically, for the production of high local densities of certain molecules on a chip, for example, for biosensing. Molecular motors, predominantly myosins, and kinesins, with their respective cytoskeletal filaments, that is, actin filaments and microtubules, are instrumental for self-organization phenomena in living systems. They are thus the basis for organism motility (muscle contraction) as well as cell motility in general and transport of molecular cargoes within cells. Considerable efforts have been invested into exploiting this motion-generating machinery for nanotechnological applications [1–17]. Also self-organization phenomena of motor-propelled cytoskeletal filaments in vitro under different conditions have been considered in this context. Thus, in the presence of cross-linking molecules, stable

or meta-stable filament bundles of different shapes may form [18]. In the absence of cross-linkers, on the other hand, the filaments either move collectively in partly ordered, but dynamically changing swarms [19–21], or execute random diffusion like movement [19], depending on the conditions [22]. The diffusion-like behaviour can be partly controlled by chemical and topographical micro-, and/or nanopatterns and used as a versatile method to produce actin filament gradients [19] locked to the myosin-coated surface by removal of ATP. Actin filaments are readily functionalized with various biomolecules for example, extracellular matrix proteins [19], and may serve as templates for formation of gradients of other biomolecules, useful, for example, for tissue engineering and studies of cell adhesion. Alternatively, the filaments could be derivatized with gold [23] to produce complex electrical circuits.

In previous studies [19] of actomyosin-based self-organization on topographically and chemically nanopatterned surfaces we noted that the motor-propelled actin filaments tend to accumulate along edges of the motility supporting areas. We hypothesized [19] that this effect, that

we here denote the “edge-tracing effect,” is attributed to: (1) higher local motor density at the corner between a wall and the floor of the motor supporting area or (2) reduced probability for filaments to leave their current path along the wall-floor junction because the thermal fluctuations of the free leading end of the filament are limited to one (rather than two, as on an open surface area) direction in the surface plane. The asymmetric constraints imposed by the wall on stochastic changes in filament position according to the second hypothesis may also be extended to incorporate the idea that filaments which have just moved away from the edge have an increased likelihood of hitting the edge again (cf. reasoning in [24] for a molecule close to a cell surface). This possibility is considered in some detail here.

The motility of actin filaments on micro- and nanopatterned surfaces may be simulated by Monte-Carlo approaches [25, 26] where the winding filament paths on open areas are characterized by a persistence length (the length along a polymer/path over which the “memory” of a tangent angle of the polymer/path is maintained. For example, the higher flexural rigidity of the polymer the longer the persistence length.) equal to that of the actin filament whereas filaments when reaching borders are forced to follow these with 100% probability. The latter is a reasonable approximation using actin filaments and walls with overhanging roofs and combined chemical and topographical patterning [10, 27].

Here we first demonstrate the edge-tracing effect in experimental data using nanostructured surfaces with actin filament guiding tracks of the type described previously [10, 27]. We then perform Monte-Carlo simulations for similar surface track geometries as in the experiments showing excellent prediction of the edge-tracing effect. This corroborates the second hypothesis above because the simulations capture the asymmetric effects of the walls on stochastic changes in motion but do not include any effects of altered motor density. The simulation results also lead to additional testable predictions that open for further in depth insight into the edge-tracing mechanism. These predictions and approaches for testing them as well as the usefulness of the edge-tracing effect for nanotechnological applications are discussed. The experimental results have previously been published in a PhD thesis [28].

## 2. Methods

**2.1. Experiments.** The methods for protein preparations, in vitro motility assays and recording of in vitro motility assay data have been described in detail elsewhere [10, 29–31]. The in vitro motility assays were performed at 25°C, pH 7.4, 1 mM MgATP, and 40 mM ionic strength. The surfaces were preincubated with heavy meromyosin (200 µg/mL) for 2 min. The methods for nanostructuring have been described [10, 27, 31], including electron-beam lithography to produce bilayer resist channels (Figure 1) and surface derivatization of nanosized tracks and larger motility supporting areas with trimethylchlorosilane (TMCS).

**2.2. Model Simulations.** A Monte-Carlo simulation approach was developed on basis of previous work [25, 26] and im-

plemented in Matlab (Mathworks, Natick, MA). In the modelling, different geometries for a motility supporting area, delimited by walls like those surrounding the tracks in Figure 1, could be simulated from an ellipse and two second degree polynomials (Figure 2). The polynomials either caused the right part of the motility supporting area to be concave (dashed line) or convex (full line) inwards. For  $R_{\max} = R_{\min}$  (exclusively used here) and with very small  $L_1$ , the motility supporting area is approximately circular. The elliptical and polynomial parts were defined to make the border-defining function and the first derivative of this function continuous. The simulations were simplified by symmetry, allowing us to consider only the lower half of the zone in Figure 2.

In the simulations, the instantaneous angular changes in actin filament sliding direction on the open motility supporting area are assumed to be normally distributed with standard deviation

$$\Delta\varphi = \sqrt{\frac{v_f \cdot \Delta t}{L_P}}. \quad (1)$$

Here,  $v_f$  is the sliding velocity,  $\Delta t$  is the time interval (10 ms unless otherwise stated) between updates in sliding direction, and  $L_P$  is the actin filament persistence length [25, 26, 32] that has been found to be similar to the persistence length of HMM-propelled actin filament paths in the in vitro motility assay [32]. The angular changes in sliding direction are regularly drawn from a normal distribution using inbuilt Matlab functions. If filaments, as a result of these angular updates, enter coordinates outside the defined borders of the motility supporting zone, the filaments are guided along this border [25] (synonymously denoted “wall” or “edge”). The procedures that we employ to simulate guiding along curved borders are described in greater detail in Figure 3. The procedure when a filament first reaches the wall is straightforward (Figure 3(a)) and has been illustrated previously. In contrast, the subsequent procedure, when the filament is already in contact with the wall, is not immediately obvious. We here (Figure 3(b)) take the approach that filament fluctuations are first simulated (1; with standard deviation for angular change given by (1)) as if the wall was not present. If this results in a new position at 2 in Figure 3(b), that is, beyond the border of the motility supporting region, the filament is shifted to the wall at a new position (3 in Figure 3(b)) compatible with a sliding distance  $v_f \Delta t$  from the starting position (0). The edge-tracing with a filament in contact with the wall is interrupted if the thermal fluctuations bring the filament away from the wall, into the motility supporting area (Figure 3(c)).

## 3. Results and Discussions

**3.1. Edge-Tracing Effect—General Aspects.** Examples of the edge-tracing effect are shown in the experimental records in Figure 4. Here, actin filaments move along topographical borders (inset Figure 4(a)) separating TMCS areas with good motility quality from surrounding, resist-covered (PMMA), areas without motility. In Figures 4(a) and 4(b), results are

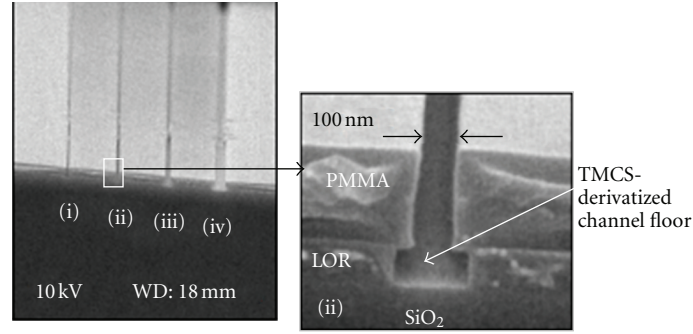


FIGURE 1: Scanning electron micrographs showing nanostructured surface produced by electron-beam lithography applied to bilayer resist layer on  $\text{SiO}_2$ , consisting of lift-off resist (LOR) and polymethylmethacrylate (PMMA). Following electron-beam exposure and development, the PMMA layer was made hydrophilic by oxygen-plasma ashing followed by trimethylchlorosilane (TMCS) derivatization of the exposed  $\text{SiO}_2$ . The nanoscale track illustrated here has similar walls as the motility supporting open areas illustrated below (e.g., Figure 4).

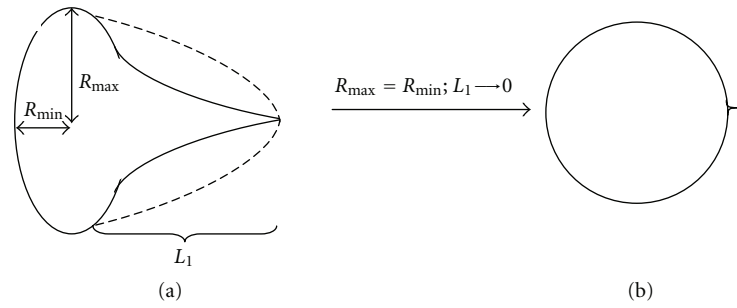


FIGURE 2: Geometry of motility supporting zone for simulations. (a) Generalized geometry with one part of the zone defined by an ellipse and another part defined by a second degree polynomial (e.g., filled or dashed line). Polynomials selected to be continuous with the ellipse and also with continuity of first derivative. (b) Special case with  $R_{\max} = R_{\min}$  and very small value of  $L_1$ . This special case was exclusively used here.

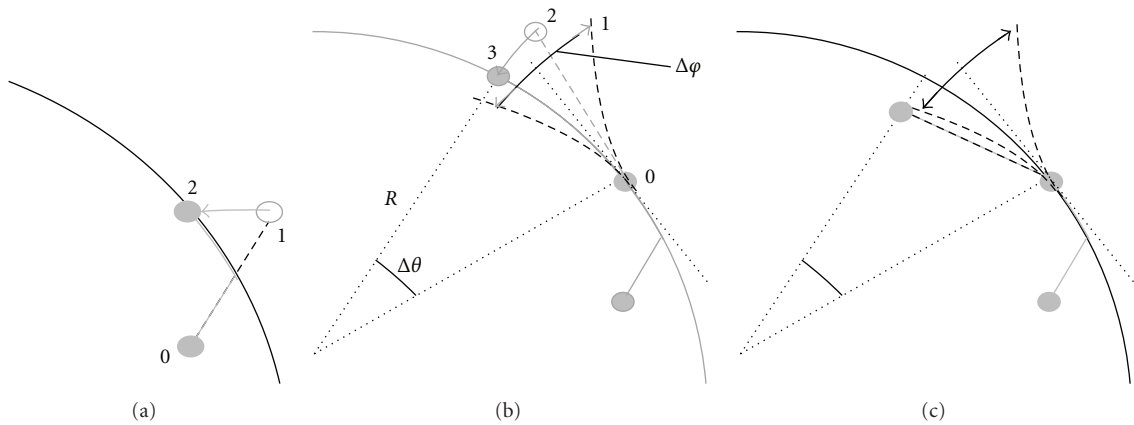


FIGURE 3: The principle of filament guiding at curved edges in the Monte-Carlo simulations. (a) Filament front (grey filled circle) reaches border from open motility supporting area. Without the border, the position 1 would be attained. In the guiding process, this is shifted to position 2 while ensuring that the total distance moved between positions 0 and 2 is equal to sliding velocity times the simulation time step ( $v_f \Delta t$ ). (b) Continued guiding along the wall. A new sliding direction is drawn from a Gaussian (with SD as in (1)) under the assumption that the wall is not present. Even if the new position will be outside the wall, the filament front is first moved a distance  $v_f \Delta t$  to that position (2). The filament is then shifted to position 3 on the border in a process that maintains the sliding distance,  $v_f \Delta t$ , between positions 0 and 3. (c) The process if the random update in sliding direction moves the filament away from the border. Note, that the ratio  $v_f \Delta t/R$  is unrealistically large in this example for enhanced clarity in description of the guiding process.

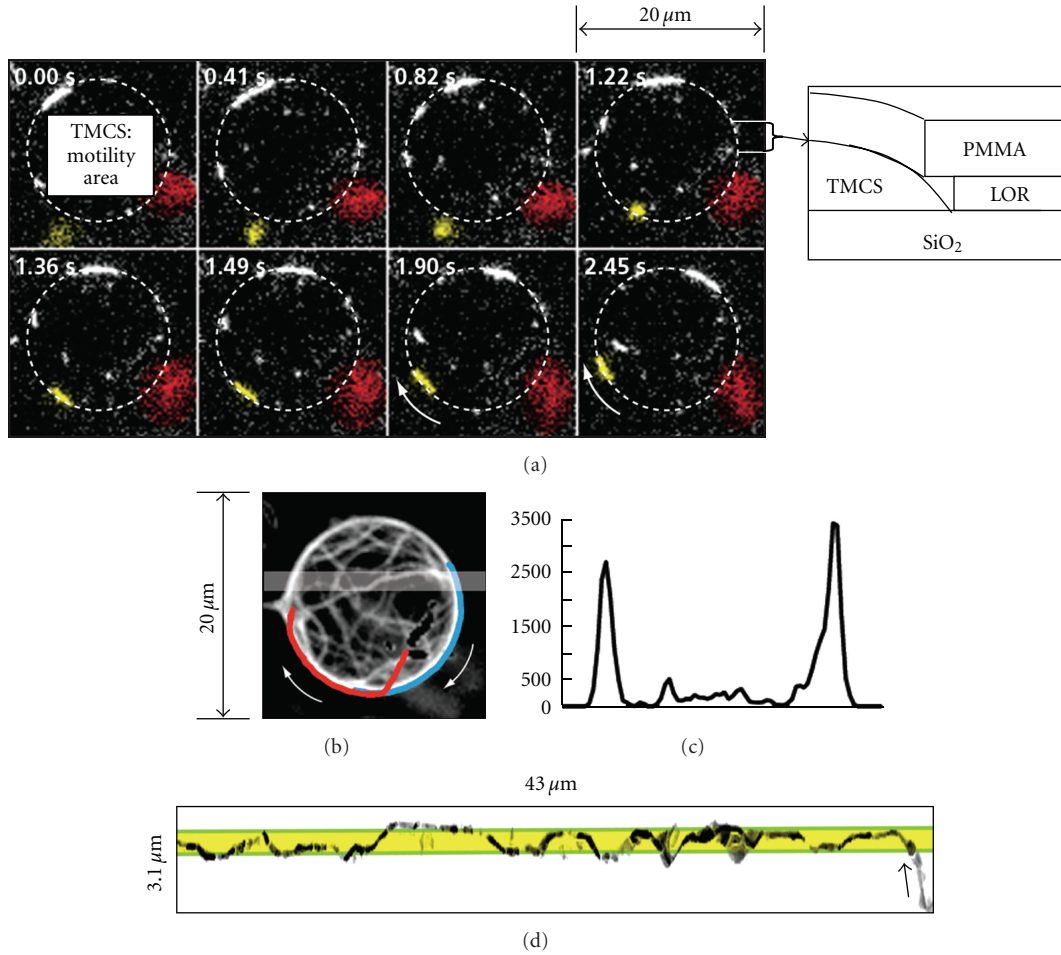


FIGURE 4: Experimental demonstration of the edge-tracing effect. (a) A time sequence of fluorescence micrographs showing actin filaments moving on a disk-shaped motility supporting TMCS surface surrounded by hydrophilic and negatively charged PMMA (see inset with schematic illustration of topography between full white lines in rightmost micrograph in first row). The lack of actin binding on PMMA indicated by red and yellow filaments floating in solution. Note that several of the HMM-propelled actin filaments on the disk-shaped TMCS-derivatized region move along the border of the motility supporting area. (b) Fluorescence micrograph integrated over 60 s to show sliding trajectories of 8 motile filaments (4 stationary filaments) sliding at velocity of about 3 μm/s. (c) Intensity profile indicating the density of actin filaments along the gray area in (b). (d) Time-integrated and color-enhanced fluorescence micrograph illustrating path of a filament (length 3.5 μm) entering a channel (yellow-green area) from an open zone at the arrow. The image is not to scale but magnified 2x vertically in order to more clearly illustrate the lateral position of the filament inside the channel. Green: approximate bottom channel borders (width 700 nm; LOR walls). Yellow: approximate top channel position (width 600 nm; with PMMA walls) for the type of channels illustrated in Figure 1. Figure 4(d) reproduced from [27] (DOI: 10.1088/0957-4484/16/6/014) with permission from Institute of Physics.

illustrated for a nearly circular disk-shaped motility supporting area, and in Figure 4(d) data are shown for filaments sliding along a 700 nm wide channel of the type illustrated in Figure 1. A simulation of the experimental situation in Figure 4(b) is illustrated in Figures 5(a) and 5(b) using similar conditions as in the experiment. That is, in Figure 5(a), about 10 filaments are assumed to be deposited randomly on the disk-shaped motility supporting surface followed by simulation of the filament paths for 60 s using similar velocity ( $\sim 3 \mu\text{m/s}$ ) as in the experiments. It is clear that the simulated behaviour is similar to that seen in the experiment in Figure 4(a) with preferential accumulation of filaments close to borders. This is also emphasized in Figure 5(b) where the radial

density distribution of the number of filaments is shown, corresponding to half the experimental intensity profile in Figure 4(c). We also simulated heavy meromyosin-propelled actin filament sliding along straight tracks similar to those in Figures 1 and 4(d). Typical results are illustrated for track widths between 0.2 and 1.2 μm in Figures 5(c)–5(e). It can be seen that, in accordance with the experimental result in Figure 4(d), the simulated paths exhibit an obvious edge-tracing effect. Moreover, after losing contact with an edge, the simulated filament paths, like the experimental one, either shifted rapidly back to the same wall or moved swiftly to the other wall (corresponding to reflection in the top border in the records in Figures 5(c)–5(e)).



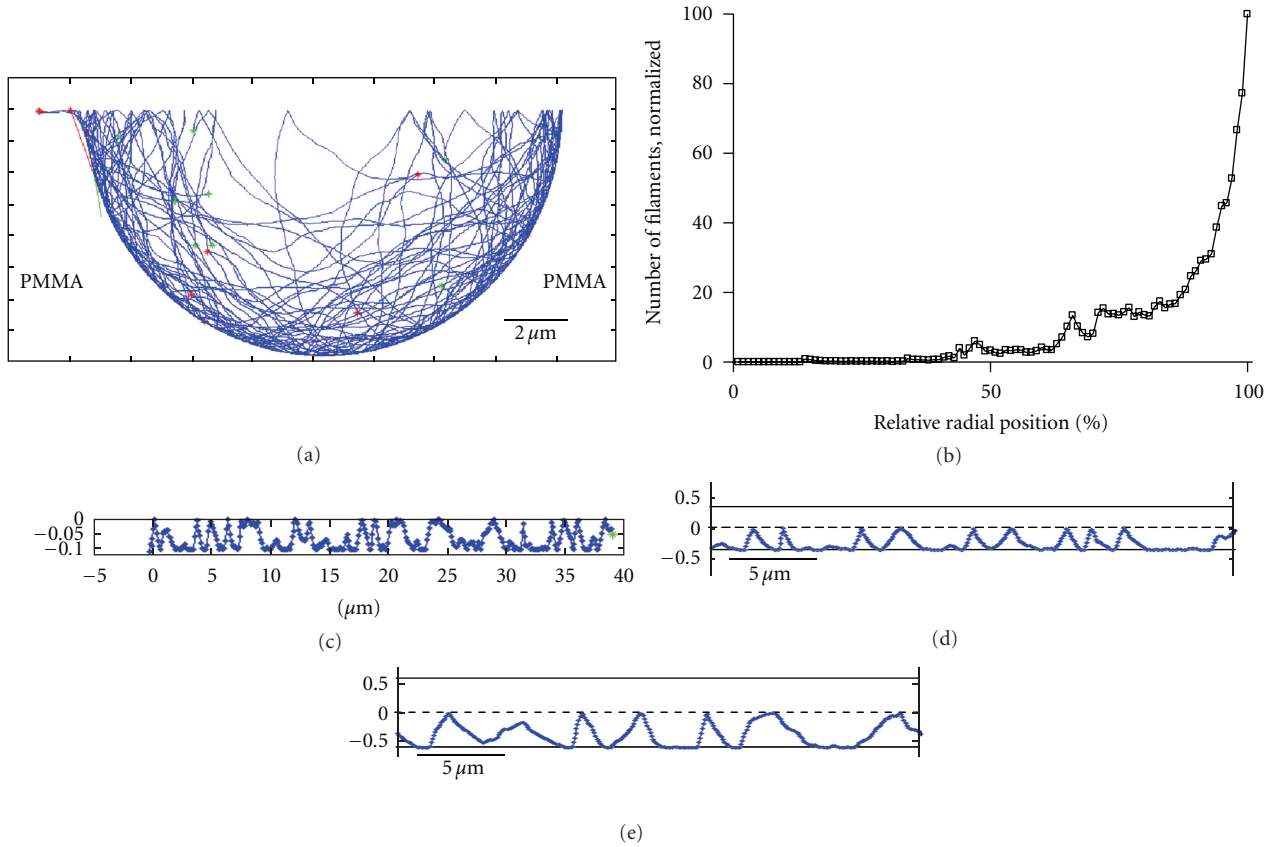


FIGURE 5: Monte-Carlo simulations of actin filament paths for the experimental situation in Figures 4(b) and 4(c) with 8 motile filaments (10 filaments in the simulations for practical reasons), a velocity of  $3\ \mu\text{m/s}$ , and a total integration time of 60 s. (a) Simulated filament paths (blue) with starting points (green) and end-points (red). The motility supporting area is indicated by weak red (circular part) and green (to the far left; polynomial part) lines. For symmetry reasons, the simulations were limited to a half-circular shape which simplified the algorithm. Thus, filament paths are reflected in the top border of the simulated area, corresponding to their motility with unchanged sliding direction past this border. (b) The radial distribution of filament positions accumulated during the entire simulation period. Here, 0 corresponds to the centre of the circular motility supporting zone, and 100% corresponds to the border with the LOR/PMMA-area. (c) Simulation of sliding along 200 nm wide track similar to that in Figure 1. Simulation limited to lower half of the track with reflection of filament paths in track midline (top of diagram). Thus, simulated filament paths at bottom of figure correspond either to motility at the lower or top edge of the track. (d) Simulation of sliding along 700 nm wide track (delimited by upper and lower full lines) as in Figure 4(d). Simulation only for lower half of track with reflection in midline (dashed line) as in Figure 5(c). (e) Simulation as in Figure 5(d) but track width increased to  $1.2\ \mu\text{m}$ .

**3.2. Edge-Tracing Radius of Motility Supporting Region versus Filament Persistence Length.** For further elucidation of the mechanisms underlying the edge-tracing effects we next turned to simulation of filament paths on motility supporting areas of different radii. The results for 50–100 simulated filaments for 3 different radii of the motility supporting area are illustrated in Figure 6(a). It is clear that the spatial variation of the number of filaments within a given motility supporting area is similar to that observed with considerably fewer filaments in Figure 5. However, it can also be seen more clearly in Figure 6(a) that the edge-tracing effect is superimposed on a linear increase in the number of filaments with radius. This linear increase is trivially expected for randomly distributed objects on a circular area due to increased circumference with increased radial distance. The edge-tracing effect (the filament number at edges in excess

of that expected from the linear increase with radius) in simulated data can be seen for example, for a radius ( $R$ )  $> 15\ \mu\text{m}$  for a motility supporting zone of  $20\ \mu\text{m}$  radius in Figure 6(a) (blue lines). The simulated edge-tracing effect, however, becomes more prominent with reduced radius of the motility supporting area (Figures 6(a)–6(c)) as well as with increased filament persistence length (Figure 6(c)); that is, the edge-tracing effect increased with a reduction of the  $R/L_P$  ratio (Figure 6(c)). In contrast, altered sliding velocity did not influence the edge-tracing effect in the simulations (Figure 6(d)). The edge-tracing effect was fully developed about 5 s after onset of the simulations for a  $20\ \mu\text{m}$  radius motility supporting zone, a velocity of  $2.5\ \mu\text{m/s}$  and a persistence length of  $10\ \mu\text{m}$ . In all other cases ( $R < 20\ \mu\text{m}$ ,  $v_f > 2.5\ \mu\text{m/s}$  and  $L_P \geq 10\ \mu\text{m}$ ), the effect was fully developed within 2.5 s.



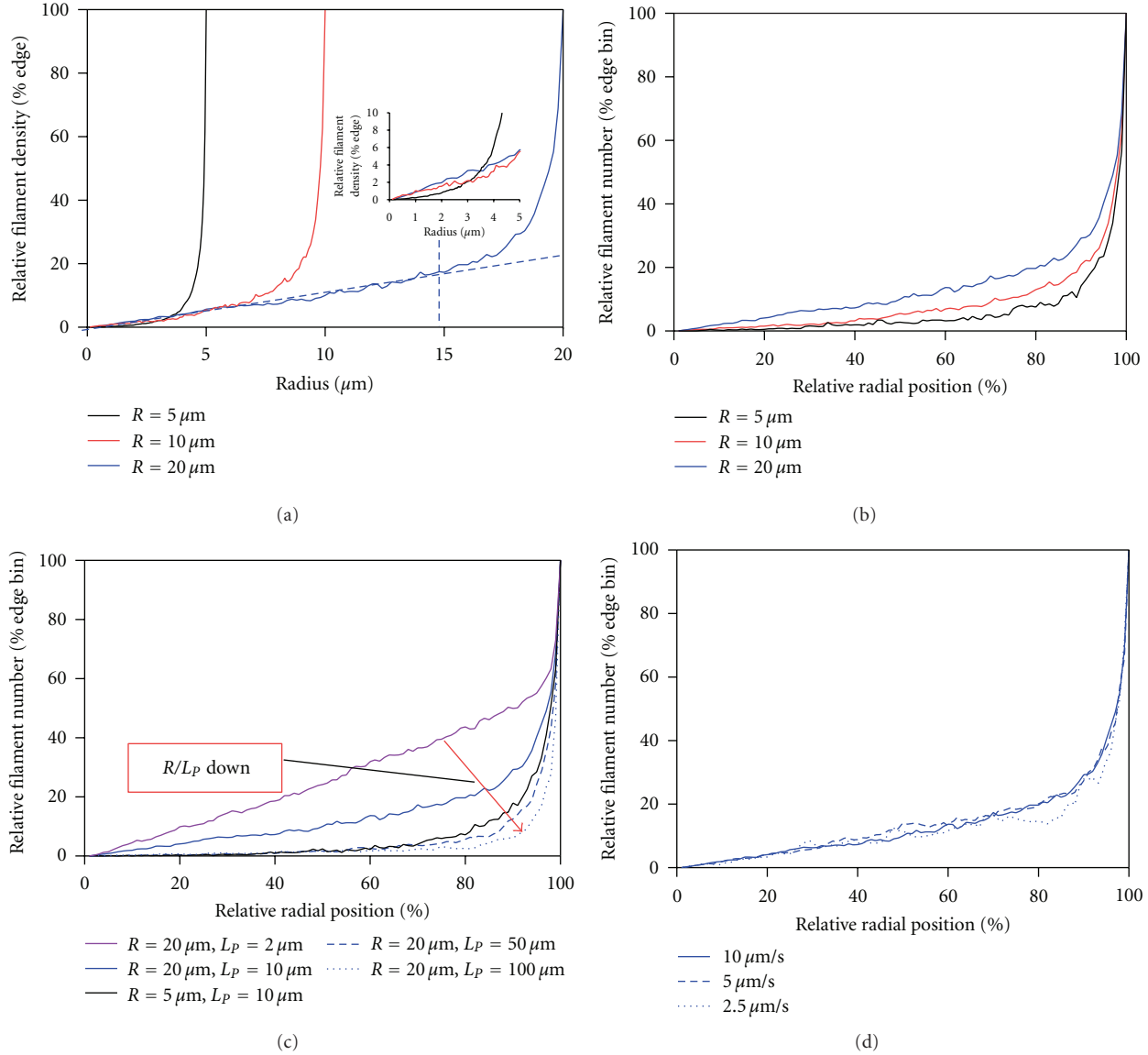


FIGURE 6: Radial filament distributions simulated for motor-propelled filaments. (a) The effect of radius ( $R$ ) of motility supporting region on the radial distribution of filaments.  $L_p = 10 \mu\text{m}$ ,  $V_f = 10 \mu\text{m/s}$ ,  $\Delta t = 0.01 \text{ s}$ . Note, a small linear increase in filament number with increased radius related to the increase of circumference. Edge-tracing effect corresponds to steep increase (in excess of the linear change) in number of filaments at periphery, for example, to the right of the dashed blue line for  $R = 20 \mu\text{m}$ . Inset: part of diagram at the origin shown in greater detail. (b) The data in A, replotted with the radial position normalized to the radius of the motility supporting region. (c) Radial filament distributions for different  $L_p - R$  combinations ( $v_f = 10 \mu\text{m/s}$  and  $\Delta t = 0.01 \text{ s}$ ). Note, increased edge-tracing with reduced  $R/L_p$  ratio. That is, under these conditions, the edge peak in filament number is shifted outwards and has increased amplitude relative to the expected linear increase for all radial distances. (d) Radial filament distributions for different sliding velocities ( $R = 20 \mu\text{m}$ ,  $L_p = 10 \mu\text{m}$  and  $\Delta t = 0.01 \text{ s}$ ). Distributions obtained during time periods over which no apparent time dependence of the distributions was noted. The unrealistically low value of  $L_p = 2 \mu\text{m}$  (compared to actin filaments and microtubules) was included in (c) to more clearly illustrate the effect of altered  $R/L_p$  ratio.

**3.3. Hypothesis 2—Detailed Mechanisms Underlying Edge-Tracing.** Before interpreting the simulation results in relation to experimental data it is important to consider what is actually happening in the simulations when a filament is guided at the edge. As described in Figure 3, the free leading end of the filament is assumed to execute thermal fluctuations governed by a Gaussian distribution with standard deviation as in (1). For a straight (corresponding to circular motility zone of infinite radius) rather than curved wall,

this would mean that in 50% of the trials (corresponding to capture by a new myosin head) the filament will move away from the wall. On this basis the filament would, on average, stay in contact with the wall for up to 100 nm before escaping. This may be inferred from the average value (1 failure before escape) for a corresponding geometric distribution and the average distance ( $\sim 40\text{--}100 \text{ nm}$ ; [32, 33]) between sequential captures of the actin filament tip on myosin heads. Furthermore, several events with edge tracing

for  $> 100$  nm would be expected. For instance, on the assumption of 100 nm distance between subsequent capture of the filament tip on myosin heads, the probability is  $1 - \sum_{i=1}^3 0.5^i = 12.5\%$  that filaments stay in contact with straight edges for  $>300$  nm before escaping. The occurrence of such events can be seen in the simulated data in Figures 5(c)–5(e) (corresponding to  $>4$  simulated points) and also appear to exist in the experimental data in Figure 4(d) (within the experimental uncertainty).

From Figure 3 it can be readily inferred that a concave wall towards the motility supporting area, as in Figures 4(a), 4(b), and 5(a), would reduce the probability of escape from the edge. Thus, for a filament that moves a distance  $v_f \Delta t$  along the edge, the edge tangent will rotate by an angle  $\Delta\theta$ , given by (cf. Figure 3(b))

$$\Delta\theta R = v_f \Delta t. \quad (2)$$

This rotation reduces the probability for the thermal oscillations of the actin filament tip to bring the tip to a position away from the wall. This can be interpreted as an elastic binding energy ( $\Delta U$ ) that tends to hold the free leading end of a filament in contact with edges with a concave curvature towards the motility supporting region. The energy can be expressed as

$$\Delta U = -\frac{1}{2R^2} v_f \Delta t L_p k_B T, \quad (3)$$

where  $k_B T$  is the Boltzmann factor. In contrast to concave edges (e.g., Figure 3) inwards convex edges (not further considered below) would have a tendency to “repel” the filament with a “repulsion energy,”  $\Delta U$ , with the same magnitude as in (3) but with a positive sign.

For both concave and convex edges,  $\Delta U$  is significant compared to thermal energy only if  $v_f \Delta t L_p \geq 2R^2$ . Particularly, the effect of elastic binding forces is negligible for all values of  $R$  studied here ( $R \geq 5 \mu\text{m}$ ), assuming realistic distances between successive encounters of actin filaments with myosin heads in the in vitro motility assay ( $\leq 100$  nm; see above) and an actin filament persistence length of  $\sim 10 \mu\text{m}$ ; [32]. The situation would be different for considerably increased values of  $L_p$ , reduced values of  $R$ , and/or increased distance ( $v_f \Delta t$ ) between successive motors, as if using stiff microtubules propelled by processive kinesin motors at low surface density.

It is important to note that edge tracing was observed in the Monte-Carlo simulations without the assumption of any other additional binding energy, for example, assuming higher myosin head densities to keep the filaments at edges. Under these conditions, the Monte-Carlo simulations, in combination with the asymmetric constraints imposed by borders (Figure 3), capture the essential elements of the second hypothesis put forward in Introduction. The faithful reproduction of the edge tracing in the simulations therefore supports this hypothesis.

Above, we have considered two mechanisms for the edge-tracing effect that may be viewed as two versions of hypothesis 2 because asymmetric constraints on changes in sliding direction at edges are central in both mechanisms. These

mechanisms are (i) the 50% probability of a filament to stay at a straight edge for each new capture by a myosin motor and (ii) the effect of an “elastic binding energy” at curved edges. However, despite the fact that we have shown the latter effect to be negligible under the conditions considered here the simulated filament paths remain close to the edges for considerably longer average distances than predicted by mechanism (i) ( $\leq 100$  nm). Therefore, there must be an additional mechanistically different version of hypothesis 2 (mechanism (iii)) that contributes to the edge-tracing effect. This is also suggested by the fact that the edge tracing effect was considerably enhanced by reduced  $R$  and increased  $L_p$  in the simulations despite negligible changes in  $\Delta U$  within the ranges of  $R$  and  $L_p$  studied. As a basis for mechanism (iii), we consider the fact that filaments which have once encountered the border will tend to be rectified in their sliding along that border. Further, the memory of this sliding direction is maintained for path lengths short compared to the persistence length *even if the filaments do not stay in direct contact with the edge*. More insight into the above mechanisms (particularly mechanism (iii)) are gained in Figure 7. Here, we simulate an ensemble of filament paths all with initial sliding direction along the tangent of a circle of  $20 \mu\text{m}$  radius. It can be seen (Figure 7) that the simulations predict that  $\sim 50\%$  of the filaments would be outside the circle after a few nm of sliding. This may be thought to correspond to mechanism (i) above. Thus, if there had been an edge along the drawn circle in Figure 7 and if the motility supporting region had been inside the circle (on top in Figure 7), these filaments would have remained sliding along that edge. Also most of those simulated filaments in Figure 7 that did not cross the circular line (towards the bottom of the figure) tend to move close to it as a result of their initial rectification along the tangent and a persistence length of  $10 \mu\text{m}$ . As a consequence, within about  $10 \mu\text{m}$  of sliding, 90% of all filaments, would again have reached and crossed the circular line (downwards in Figure 7). This means that, in the presence of an edge, the filaments would again be guided along this. It is straightforward to realize that this effect would increase when  $L_p$  increases relative to the radius of curvature of the zone with motility. Thus, filaments with larger  $L_p$  that have left the wall would “have a longer memory” of the sliding direction, thereby more rapidly hitting the wall again. It is illuminating to consider the extreme (but unrealistic) situation that the radius of the motility supporting zone would go to zero. Under these conditions the probability would go to 1 that filaments escaping from the edge immediately reach the edge again. The mentioned effects were seen in the simulations in Figure 6 as considerably increased edge-tracing effect, with larger fraction of the filaments closer to the edge, for reduced ratio of  $R/L_p$  (Figure 6(c)).

The edge-tracing effect was superimposed on the linear increase in filament number (cf. Figure 6(a)) expected with increased radius of the motility supporting region for diffusion like filament transport [19]. However, if  $R$  is small compared to  $L_p$ , the influence of ballistic transport is substantial for most filaments in the motility supporting region, consistent with our finding that the edge-tracing effect

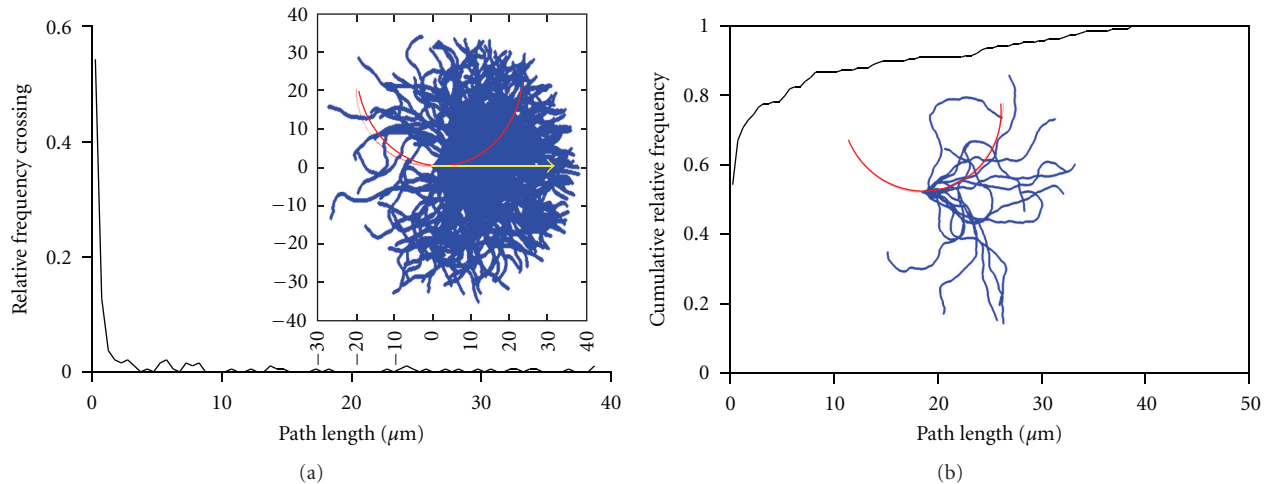


FIGURE 7: Monte-Carlo simulation of HMM-propelled actin filament sliding ( $L_P = 10 \mu\text{m}$ ) without guiding but with the same initial position and sliding direction for all filaments. (a) Distribution of sliding path lengths from onset of motility until the filament, for the first time, moves below red circle arc in inset. Inset: all 200 simulated filament paths starting on the red circular border at the starting point of the arrow. The direction of the latter represents the initial sliding direction. (b) Cumulative frequency distribution corresponding to frequency distribution in (a). Inset: a limited ensemble of 10 simulated filament paths clearly illustrating that also filaments that have moved toward the circle centre tend to rapidly reach and cross the circular border.

(see above) is fully developed within seconds. Clearly, in agreement with the discussions above, ballistic transport in a direction governed by the tangent along the edge, completely dominates transport for those filaments that have just left this edge.

It should be clear from the above discussion that the second hypothesis in the Introduction accounts well for the edge-tracing effect without the need to assume higher HMM densities close to edges. We have also shown that this second hypothesis, when considered in greater detail, may be subdivided into three different mechanisms ((i)–(iii) above).

The Monte-Carlo simulations predict that a large fraction of the “edge-tracing” filaments are not actually in contact with but rather very close to the edge. This is broadly consistent with our experimental results. However, it is important to note that these results were included here as a background to the simulations and not for critical testing of model predictions. For such testing, future dedicated experiments would be required where particular attention should be directed to the spatial resolution in the experimental records.

However, in spite of some experimental uncertainties, it is of interest to note that the experimental results for sliding along straight tracks (Figure 4(d)) and the simulations in Figures 5(c)–5(e) seem to be reasonably consistent with each other (within the spatial resolution) both with regard to the number of edge-tracing events and their duration. Future dedicated experiments to test the mechanisms above should include studies of guiding along straight borders (with mechanism (i) dominating) as well as studies of guiding along borders with varying curvature. The latter type of studies would particularly probe the importance of mechanism (iii) unless filaments of long persistence length (e.g., microtubules or actin filament bundles) are used in which case mechanism ii may also be important.

**3.4. Perspectives and Conclusions.** The present study has shown that the edge-tracing effect can be accounted for by asymmetric constraints on stochastic changes in filament sliding direction along edges (hypothesis 2 in the Introduction). Particularly at edges that are concave towards the motility supporting region, constraints seem to include an important component attributed to temporary rectification of filament sliding that tends to keep the filaments close to the edge for distances short compared to the filament persistence length. We have proposed experiments above to gain further insight into the three mechanisms encompassed within hypothesis 2 and to test for possible contribution of other factors. The increased insight into mechanisms behind the edge tracing effect may be useful for enhanced concentration of motor-transported cargoes at edges (cf. [13]). The results would also guide the production of gradients of actin filaments of certain shapes, thereby adding to the versatility of previous approaches [19]. One may also expect that edge-tracing could increase the versatility and spatial resolution of surface imaging methods based on molecular motor driven filament transport [34]. Finally, the results may be useful for faster and more efficient feeding of filaments into tracks of nanotransportation devices (see Supporting Information; [10, 27, 35]).

## Disclosure

Månsson is a cofounder, coowner, and CEO of the start-up company ActoSense Biotech AB (Kalmar, Sweden) aiming to develop diagnostic devices based on the aggregation of cytoskeletal elements, particularly actin filaments, in solution. Moreover, A. Månsson holds two Swedish patents in this field and application for one of these patents (about aggregation of actin filaments by analyte molecules) has also been filed in the US and Europe.

## Acknowledgments

This work was funded by the European commission (FP7) under the contract MONAD (NMP4-SL-2009-228971), The Swedish Research Council (Project no. 621-2010-5146), The Carl Trygger Foundation, The Swedish Foundation for Strategic Research, The Knowledge Foundation (KK-stiftelsen), The Faculty of Natural Sciences and Engineering at Linnaeus University, and The Nanometer Consortium at Lund University.

## References

- [1] H. Suzuki, A. Yamada, K. Oiwa, H. Nakayama, and S. Mashiko, "Control of actin moving trajectory by patterned poly(methylmethacrylate) tracks," *Biophysical Journal*, vol. 72, no. 5, pp. 1997–2001, 1997.
- [2] D. V. Nicolau, H. Suzuki, S. Mashiko, T. Taguchi, and S. Yoshikawa, "Actin motion on microlithographically functionalized myosin surfaces and tracks," *Biophysical Journal*, vol. 77, no. 2, pp. 1126–1134, 1999.
- [3] H. Hess, J. Clemmens, D. Qin, J. Howard, and V. Vogel, "Light-controlled molecular shuttles made from motor proteins carrying cargo on engineered surfaces," *Nano Letters*, vol. 1, no. 5, pp. 235–239, 2001.
- [4] Y. Hiratsuka, T. Tada, K. Oiwa, T. Kanayama, and T. Q. P. Uyeda, "Controlling the direction of kinesin-driven microtubule movements along microlithographic tracks," *Biophysical Journal*, vol. 81, no. 3, pp. 1555–1561, 2001.
- [5] R. Bunk, J. Klinth, J. Rosengren et al., "Towards a "nanotraffic" system powered by molecular motors," *Microelectronic Engineering*, vol. 67–68, pp. 899–904, 2003.
- [6] J. A. Jaber, P. B. Chase, and J. B. Schlenoff, "Actomyosin-driven motility on patterned polyelectrolyte mono- and multilayers," *Nano Letters*, vol. 3, no. 11, pp. 1505–1509, 2003.
- [7] H. Hess, G. D. Bachand, and V. Vogel, "Powering nanodevices with biomolecular motors," *Chemistry—A European Journal*, vol. 10, no. 9, pp. 2110–2116, 2004.
- [8] P. Manandhar, L. Huang, J. R. Grubich, J. W. Hutchinson, P. B. Chase, and S. Hong, "Highly selective directed assembly of functional actomyosin on Au surfaces," *Langmuir*, vol. 21, no. 8, pp. 3213–3216, 2005.
- [9] G. D. Bachand, S. B. Rivera, A. Carroll-Portillo, H. Hess, and M. Bachand, "Active capture and transport of virus particles using a biomolecular motor-driven, nanoscale antibody sandwich assay," *Small*, vol. 2, no. 3, pp. 381–385, 2006.
- [10] M. Sundberg, R. Bunk, N. Albet-Torres et al., "Actin filament guidance on a chip: toward high-throughput assays and lab-on-a-chip applications," *Langmuir*, vol. 22, no. 17, pp. 7286–7295, 2006.
- [11] M. G. L. Van Den Heuvel and C. Dekker, "Motor proteins at work for nanotechnology," *Science*, vol. 317, no. 5836, pp. 333–336, 2007.
- [12] A. Goel and V. Vogel, "Harnessing biological motors to engineer systems for nanoscale transport and assembly," *Nature Nanotechnology*, vol. 3, no. 8, pp. 465–475, 2008.
- [13] T. Fischer, A. Agarwal, and H. Hess, "A smart dust biosensor powered by kinesin motors," *Nature Nanotechnology*, vol. 4, no. 3, pp. 162–166, 2009.
- [14] L. Rios and G. D. Bachand, "Multiplex transport and detection of cytokines using kinesin-driven molecular shuttles," *Lab on a Chip*, vol. 9, no. 7, pp. 1005–1010, 2009.
- [15] A. Agarwal and H. Hess, "Biomolecular motors at the intersection of nanotechnology and polymer science," *Progress in Polymer Science*, vol. 35, no. 1–2, pp. 252–277, 2010.
- [16] T. Korten, A. Månsson, and S. Diez, "Towards the application of cytoskeletal motor proteins in molecular detection and diagnostic devices," *Current Opinion in Biotechnology*, vol. 21, no. 4, pp. 477–488, 2010.
- [17] H. Takatsuki, K. M. Rice, S. Asano et al., "Utilization of myosin and actin bundles for the transport of molecular cargo," *Small*, vol. 6, no. 3, pp. 452–457, 2010.
- [18] H. Hess, J. Clemmens, C. Brunner et al., "Molecular self-assembly of "nanowires" and "nanospools" using active transport," *Nano Letters*, vol. 5, no. 4, pp. 629–633, 2005.
- [19] P. G. Vikhorev, N. N. Vikhoreva, M. Sundberg et al., "Diffusion dynamics of motor-driven transport: gradient production and self-organization of surfaces," *Langmuir*, vol. 24, no. 23, pp. 13509–13517, 2008.
- [20] T. Butt, T. Mufti, A. Humayun et al., "Myosin motors drive long range alignment of actin filaments," *The Journal of Biological Chemistry*, vol. 285, no. 7, pp. 4964–4974, 2010.
- [21] V. Schaller, C. Weber, C. Semmrich, E. Frey, and A. R. Bausch, "Polar patterns of driven filaments," *Nature*, vol. 467, no. 7311, pp. 73–77, 2010.
- [22] P. Kraikivski, R. Lipowsky, and J. Kierfeld, "Enhanced ordering of interacting filaments by molecular motors," *Physical Review Letters*, vol. 96, no. 25, Article ID 258103, 4 pages, 2006.
- [23] F. Patolsky, Y. Weizmann, and I. Willner, "Actin-based metallic nanowires as bio-nanotransporters," *Nature Materials*, vol. 3, no. 10, pp. 692–695, 2004.
- [24] H. C. Berg and E. M. Purcell, "Physics of chemoreception," *Biophysical Journal*, vol. 20, no. 2, pp. 193–219, 1977.
- [25] T. Nitta, A. Tanahashi, M. Hirano, and H. Hess, "Simulating molecular shuttle movements: towards computer-aided design of nanoscale transport systems," *Lab on a Chip*, vol. 6, no. 7, pp. 881–885, 2006.
- [26] T. Nitta, A. Tanahashi, Y. Obara et al., "Comparing guiding track requirements for myosin-and kinesin-powered molecular shuttles," *Nano Letters*, vol. 8, no. 8, pp. 2305–2309, 2008.
- [27] R. Bunk, M. Sundberg, A. Månsson et al., "Guiding motor-propelled molecules with nanoscale precision through silanized bi-channel structures," *Nanotechnology*, vol. 16, no. 6, pp. 710–717, 2005.
- [28] R. Bunk, *Creation of a Nanometer-Scale Toolbox for Molecular Motor Transport-Circuits*, Lund University, 2005.
- [29] J. Klinth, A. Arner, and A. Månsson, "Cardiotonic bipyridine amrinone slows myosin-induced actin filament sliding at saturating [MgATP]," *Journal of Muscle Research and Cell Motility*, vol. 24, no. 1, pp. 15–32, 2003.
- [30] A. Månsson and S. Tågerud, "Multivariate statistics in analysis of data from the in vitro motility assay," *Analytical Biochemistry*, vol. 314, no. 2, pp. 281–293, 2003.
- [31] M. Sundberg, M. Balaz, R. Bunk et al., "Selective spatial localization of actomyosin motor function by chemical surface patterning," *Langmuir*, vol. 22, no. 17, pp. 7302–7312, 2006.
- [32] P. G. Vikhorev, N. N. Vikhoreva, and A. Månsson, "Bending flexibility of actin filaments during motor-induced sliding," *Biophysical Journal*, vol. 95, no. 12, pp. 5809–5819, 2008.
- [33] Y. Harada, K. Sakurada, T. Aoki, D. D. Thomas, and T. Yanagida, "Mechanochemical coupling in actomyosin energy transduction studied by in vitro movement assay," *Journal of Molecular Biology*, vol. 216, no. 1, pp. 49–68, 1990.

- [34] H. Hess, J. Clemmens, J. Howard, and V. Vogel, "Surface imaging by self-propelled nanoscale probes," *Nano Letters*, vol. 2, no. 2, pp. 113–116, 2002.
- [35] T. Kim, L. J. Cheng, M. T. Kao, E. F. Hasselbrink, L. Guo, and E. Meyhöfer, "Biomolecular motor-driven molecular sorter," *Lab on a Chip*, vol. 9, no. 9, pp. 1282–1285, 2009.



## Review Article

# Nanoparticulate Adjuvants and Delivery Systems for Allergen Immunotherapy

**Juliana De Souza Rebouças,<sup>1</sup> Irene Esparza,<sup>1</sup> Marta Ferrer,<sup>2</sup> María Luisa Sanz,<sup>2</sup>  
Juan Manuel Irache,<sup>1</sup> and Carlos Gamazo<sup>1</sup>**

<sup>1</sup>Adjuvant Unit, Department of Pharmacy and Pharmaceutical Technology, and Department of Microbiology, University of Navarra, 31008 Pamplona, Spain

<sup>2</sup>Department of Allergy and Clinical Immunology, Clínica Universidad de Navarra, 31008 Pamplona, Spain

Correspondence should be addressed to Carlos Gamazo, cgamazo@unav.es

Received 1 September 2011; Revised 19 October 2011; Accepted 25 October 2011

Academic Editor: Alf Månsson

Copyright © 2012 Juliana De Souza Rebouças et al. This is an open access article distributed under the Creative Commons Attribution License, which permits unrestricted use, distribution, and reproduction in any medium, provided the original work is properly cited.

In the last decades, significant progress in research and clinics has been made to offer possible innovative therapeutics for the management of allergic diseases. However, current allergen immunotherapy shows limitations concerning the long-term efficacy and safety due to local side effects and risk of anaphylaxis. Thus, effective and safe vaccines with reduced dose of allergen have been developed using adjuvants. Nevertheless, the use of adjuvants still has several disadvantages, which limits its use in human vaccines. In this context, several novel adjuvants for allergen immunotherapy are currently being investigated and developed. Currently, nanoparticles-based allergen-delivery systems have received much interest as potential adjuvants for allergen immunotherapy. It has been demonstrated that the incorporation of allergens into a delivery system plays an important role in the efficacy of allergy vaccines. Several nanoparticles-based delivery systems have been described, including biodegradable and nondegradable polymeric carriers. Therefore, this paper provides an overview of the current adjuvants used for allergen immunotherapy. Furthermore, nanoparticles-based allergen-delivery systems are focused as a novel and promising strategy for allergy vaccines.

## 1. Introduction

Over the past few years, a large increase in the prevalence of allergic diseases has been reported [1]. Epidemiological studies report that allergic sensitization is detected in more than 25% of the general population, particularly in industrialized countries [2]. Nowadays, *allergy* is defined as immediate reactions (also known as type I hypersensitivity) against foreign antigens, accompanied by a high IgE stimulus [3]. Various environmental proteins, namely, allergens, are recognized as foreign elements by the immune system of some individuals. Allergic diseases include rhinitis (hay fever), asthma, food allergy, allergic skin inflammation, ocular allergy, and anaphylaxis [4].

The etiology of allergic immune responses is complex, and several factors, including environmental and genetics, have been described as triggers of allergic diseases [5]. Recently, different gene polymorphisms were identified, and

they also affect the individual predisposition to develop allergy, known as atopy [6–9]. However, a genetic predisposition alone does not explain the increased prevalence of these diseases in the last decades. It has been proposed that this increase seems to be attributed to environmental factors acting on a genetic basis [7].

Since the first description of allergy in early 1900s, significant progress to research and clinics has been made in offer possible innovative therapeutics for the management of allergic diseases [10–13]. Remarkable advances in allergen immunotherapy include the use of purified allergens-based vaccines [14], blocking antibodies [15], the recombinant interleukins administration [16, 17], DNA vaccines [18], and gene therapy [19]. However, current approaches show limitations concerning the long-term efficacy and safety due to local side effects and risk of anaphylaxis. Effective and safe vaccines require the use of effective and safe adjuvants [20–23]. Therefore, this paper provides an overview of

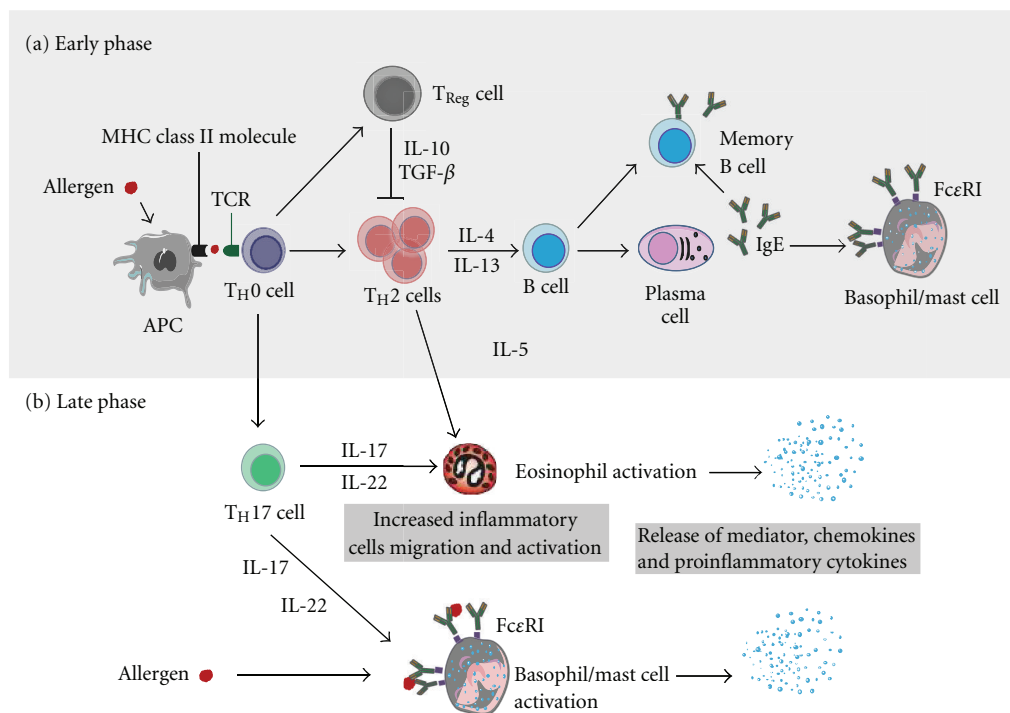


FIGURE 1: Mechanisms of allergic responses. Allergic response is constituted by two phases: an early phase (a) of initial sensitization and memory activation and a later phase response (b) after re-exposure to allergen, resulting in release of inflammatory mediators as a consequence of allergen cross-linking basophil/mast cell-bound specific IgE.

the currently adjuvants used for allergen immunotherapy. Furthermore, nanoparticles-based allergen-delivery systems are focused and discussed as a novel and promising strategy for allergy vaccines.

## 2. Immunological Aspects of Allergic Diseases

Allergic diseases are immunologic disorders characterized by an imbalance in the responses of activation of  $CD4^+$  T helper ( $T_H1$  and  $T_H2$ ) and T regulatory ( $T_{Reg}$ ) cells [24]. Among the many cells involved in allergic reaction,  $CD4^+$  T cells play a central role in the immune response against allergens. In atopic individuals, functional polarization of allergen-specific response of  $CD4^+$  T cells and cytokine profile is  $T_H2$ -polarized (Figure 1). In contrast, activated allergen-specific T cells from nonatopic subjects are  $T_H1$  polarized accompanied by secretion of  $IFN-\gamma$  and IL-2. Allergic inflammatory cytokines are secreted, particularly IL-4, IL-5, and/or IL-13. This latter is an important mediator of allergic inflammation. IL-13 promotes immunoglobulin class switching for IgE production and increases both recruitment and activation of inflammatory cells such as eosinophils, mast cells, and basophils [25, 26]. Recently, several studies suggest that  $T_H17$  and  $T_{Reg}$  also have a significant role in the development of allergic diseases [27, 28]. Current studies have demonstrated that these novel T cells, producing IL-17 and IL-10, regulate innate immunity by signal transduction, which mitigates their proinflammatory function (Figure 1) [29].

The mechanism of the allergic reaction is characterized by two phases: the initial sensitization phase, which is followed by the second phase that is characterized by immediate hypersensitivity symptoms. After an initial exposure (Figure 1(a)),  $T_H2$  pathway is initiated by the uptake of allergens by professional antigen-presenting cells (APCs) that present peptides on MHC class II molecules to naive  $CD4^+$  T cells, which activate a cell response. Thereafter, high amounts of specific IgE antibodies are produced and bind to high affinity IgE receptor (FcεRI) in membranes of circulating basophils and mast cells that reside in skin and mucous membranes. Upon re-exposure to the allergen (Figure 1(b)), an immediate hypersensitivity response is triggered as consequence of cross-linking of the allergen with two molecules of mast cell-bound IgE. This signal stimulates the release of histamine and other inflammatory mediators such as serine proteases, platelet activating factor, cytokines, leukotrienes and prostaglandins. These mediators increase vascular permeability and promote mucus production, which are responsible for the symptoms and signs of allergic diseases [25, 26].

## 3. Allergen-Specific Immunotherapy

Allergen-specific immunotherapy (SIT) involves the administration of increasing doses of allergen(s) in order to obtain a hyposensitization and long-term relief of symptoms occurring after natural allergen exposure. SIT

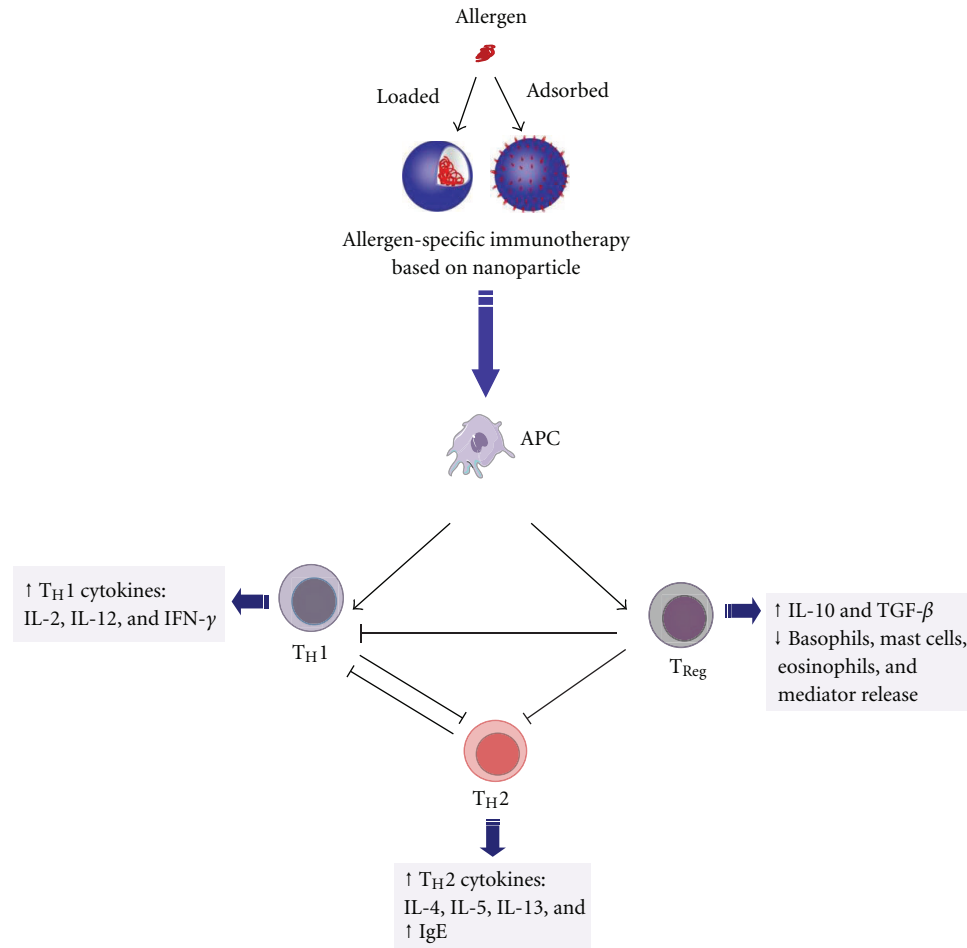


FIGURE 2: Immunomodulation of allergic diseases by using nanoparticle-based vaccines. Immunological changes after successful allergen specific-immunotherapy are indicated by whole arrows; truncated arrows indicate inhibitory effects. Redirection of allergic- $T_H2$  responses, in favour of T regulatory cell induction or/and  $T_H1$  activation, are depicted.

have been considered an efficient, safe, and long-term-benefit approach, which may be combined with appropriate allergen-avoidance strategies. However, discovery of allergen-specific immunotherapy raised a number of crucial questions regarding the route of administration, the dose response relationship, and the intervals between administrations [30].

Nowadays, several immunotherapeutic strategies have been achieved to modulate the immune system by different pathways [13]. Advances in the standardization of allergenic composition of vaccines, optimal dose of allergen and, above all, clinical studies that support their effectiveness are crucial not only to achieve more effective and safe vaccines, but also to provide greater dosing convenience [31].

**3.1. Mechanisms of Allergen-Specific Immunotherapy.** It has been established that an immune-tolerant state represents an essential step for a successful immunotherapy [32]. Several findings suggest that SIT acts through an immunomodulatory activity (Figure 2), changing the  $T_H1$ ,  $T_H2$ ,  $T_H17$ , and  $T_{Reg}$  cell differentiation [33–35]. Following SIT, an

increase in  $CD8^+$  cells and  $T_H1/T_H0$  ratio are observed. Also, a decrease in  $T_H2/T_H0$  ratio takes place. Additionally, a change in cytokine response with production of IL-4 and IFN- $\gamma$  (IL-4 to IFN- $\gamma$ ) is observed as result of downregulation of  $T_H2$  or increased  $T_H1$  response. In this context, the generation of allergen-specific  $T_{Reg}$  cells (producing IL-10 and TGF- $\beta$ ) suppressed proliferative and cytokine responses, initiating peripheral T-cell tolerance. In addition, the number of  $T_H2$  cells such as basophils and eosinophils is reduced at the allergen exposition sites (e.g., mucosa and skin), which reduces the IgE-mediated release of histamine by basophils [32–34].

Usually, SIT induces a transient increase in serum IgE, which decreases during the course of the treatment. Successful SIT is also associated with a high increase (10 to 100-fold) in IgG blocking antibodies such as IgG4 and IgG1. IgG4 acts by capturing the allergen before it crosslinks with the IgE that is bound on the surface IgE receptors of mast cells and basophils, inhibiting its activation. Still, IgG4 antibodies have anti-inflammatory activity through inhibition of the production of other IgG subtypes [35].

Recently, the counterregulatory role of IL-10 has been demonstrated. It is secreted by  $T_{Reg}$  cells during SIT, which modulates isotype formation and also change the response from an IgE to an IgG4-dominated phenotype. Other indirect function of  $T_{Reg}$  cells is the suppression of  $T_H17$  cells, accompanied by a decrease in IL-17 secretion [36].

**3.2. Routes of Administration.** Lately, several routes for allergen delivery have been assessed in immunotherapy. Since its discovery, the traditional SIT has been commonly given subcutaneously with high clinical efficacy [30]. However, subcutaneous immunotherapy (SCIT) is associated with a significant risk of severe adverse events [37, 38]. Thus, efforts have been done towards alternative routes (local and noninjection) for allergen delivery [39].

In the 1980s, the sublingual route appeared as a promising noninjection route [40]. Sublingual immunotherapy (SLIT) was regarded as an efficient and safe route. Usually, SLIT is recommended for patients with severe adverse reactions to conventional SCIT [41]. Similarly, local nasal immunotherapy (LNIT) proved to be effective and safe. However, the exact mechanisms of action and optimal dose of both SLIT and LNIT has not been established yet [39]. These noninjection routes were proposed by the World Health Organization (WHO) as viable alternatives to the subcutaneous route [42]. On the other hand, clinical efficacy of oral immunotherapy (OIT) was achieved with high doses of allergen. This has induced to a major research on the development of new mucosal adjuvants, discussed in the following section.

## 4. Adjuvants for Allergen Immunotherapy

The overall goal in allergen vaccine development is improving both clinical efficacy and safety. Nevertheless, the use of high amount of allergen on allergen immunotherapy is limited by a significant risk of allergic reactions [42]. Thus, effective and safe vaccines with reduced dose of allergen have been developed using adjuvants. Adjuvants (from Latin, *adjuvare*, aid) are defined as heterogeneous compounds that enhance the immune response against to coadministered antigens [43].

Ideally, adjuvants for allergy immunotherapy should stimulate a  $T_H1$  immune response without inducing autoimmunity and should not be mutagenic, carcinogenic, and teratogenic. Besides, optimal adjuvants need to be apyrogenic and stable in the vaccine formulation [44]. Despite the undeniable progress in this area, the use of adjuvants still has several disadvantages, which limits its use in human vaccines. Therefore, the benefits and risks related to the use of adjuvants for allergy immunotherapy need to be counterbalanced [45]. In this context, several novel adjuvants for allergen immunotherapy are currently being investigated and developed [43].

**4.1. Mechanisms of Action.** Traditionally, adjuvants exert their effects in different ways: the depot effect, the targeting to antigen-presenting cells, and the nonspecific modulation of

immune system [43]. The use of allergen extracts adsorbed to adjuvants protects the antigen from enzymatic degradation. On the other hand, depot formation entraps the antigen and provides its slow release. The persistence of the antigen increases the recruitment of APCs in the injection site, which triggers a prolonged inflammatory response. Then, the recruitment of competent cells activates innate and adaptive immune system.

Adjuvants can be divided into two groups according to their mechanisms of action as delivery systems and immunomodulatory adjuvants. However, some compounds can act by both mechanisms simultaneously [45–47].

**4.2. Traditional Adjuvants.** Hundreds of compounds and molecules have been extensively evaluated as adjuvants [45]. Aluminium salts and emulsions are traditionally used as general immunologic adjuvants. Recently, liposomes, immunostimulating complexes (ISCOMs), oligonucleotides, and microorganisms-derived adjuvants (i.e., MPL) have been introduced as novel adjuvants in allergy vaccines [44, 46–48].

**4.2.1. Aluminium Hydroxide.** Aluminium salts (alum) represents the most commonly used adjuvant in human vaccines. Francis and Durham showed that alum-precipitated diphtheria toxoid was more immunogenic than an aqueous toxoid [44]. Alum-adsorbed allergen extracts induce a strong  $T_H2$  response by a depot effect and also stimulates the activation of APCs, independent of Toll-like receptor (TLR) signalling, but dependent of NLR (NALP3) inflammasome [46]. Alum is the most common and safe adjuvant for injection immunotherapy in humans. However, some problems were reported after use of alum in allergic and prophylactic vaccines. These drawbacks include the enhanced sensitivity to alum and local granuloma formation at injection sites. Yet, tolerance induction has been observed after the use of aluminium. Thus, it seems to be rational to consider replacing alum compounds with other more inert molecules for the treatment of type I hypersensitivity [49].

**4.2.2. Emulsions.** Depot adjuvants based on Freund's adjuvants have been used in experimental studies and introduced in the clinic. Usually, the allergens are incorporated in a water-phase followed by the addition of oil and an emulsifying agent to form an emulsion. This allergen dosage forms have often a good immunogenic profile, with high efficacy, and prevented treatment-induced anaphylactic side effects. Nevertheless, frequent local reactions have limited the use of emulsions on long-term human prophylactic vaccines [46].

**4.2.3. Liposomes.** Liposomes are synthetic spheres based on a bilayer structure of phospholipids, which allow the encapsulation of hydrophilic antigens [50]. Liposomes act as both delivery carrier and immunomodulators. However, their low stability and manufacturing problems limited the use of these systems as adjuvants in human vaccines [46, 48].

**4.2.4. Monophosphoryl Lipid A.** Currently, novel adjuvants derived from Gram-negative bacterial cell components have been investigated. Monophosphoryl lipid A (MPL; Corixa, USA), a purified lipopolysaccharide extracted from *Salmonella minnesota*, has been used as adjuvant in allergy vaccines [44]. MPL increases the activation of dendritic cells and T cells, inducing a shift in cytokine production with a potent  $T_H1$  response [45]. In addition, MPL has been shown to enhance both mucosal and systemic immunity after intranasal administration. Clinically, SIT with MPL has shown good efficacy and attenuated toxicity [44, 51].

**4.2.5. ISCOMs.** Immune stimulating complexes (ISCOMs) are spherical complexes of about 40 nm, with a strong negative charge, composed of saponin, cholesterol and phospholipids. The micelles consist of three layers, hydrophilic-hydrophobic-hydrophilic. ISCOMs-incorporated antigens can trigger humoral, mucosal, and cellular immune responses [48, 52].

**4.2.6. Oligonucleotides.** Synthetic oligonucleotides containing immunostimulatory CpG (ISS) motifs present a strong induction of  $T_H1$  response. Conjugation of ISS with allergen showed enhancement in its immunogenicity and also reduced its allergenicity [53]. Moreover, it caused an increase in the activation of both dendritic and T cells, which induced a shift in cytokine production to a  $T_H1$  profile [54].

**4.2.7. Particulate Delivery Systems.** Particulate delivery systems belong to the category of adjuvants that facilitate the antigen uptake by APCs or by increasing the influx of professional APCs into the injection site. Among the different types of particulated delivery systems, polymer nanoparticles are a group of delivery systems with interesting abilities as adjuvants for both conventional and mucosal vaccination, since they can enhance the delivery of the loaded antigen to the gut lymphoid cells due to their ability to be captured and internalized by cells of the GALT. We will discuss in more detail the use of polymeric nanoparticles as adjuvants in the following section.

## 5. Nanoparticles-Based Allergen-Delivery Systems

Currently, nanoparticles-based allergen-delivery systems have received much interest as potential adjuvants for allergen immunotherapy [55]. It has been demonstrated that incorporation of allergens into a delivery system plays an important role in the efficacy of allergy vaccines. In the last years, several nanoparticles-based delivery systems have been described, including biodegradable and nonbiodegradable polymeric carriers [44, 45].

**5.1. Biodegradable Polymeric Nanoparticles.** Polymeric nanoparticles are colloidal carriers that vary in size from 10 to 1000 nm [56]. They can be divided into two categories: nanocapsules and nanospheres. Nanocapsules are vesicular systems in which the drug is confined to a cavity surrounded

by a polymer membrane, whereas nanospheres are polymeric matrix in which the drug is physically and uniformly dispersed. Obtaining one or another type of nanoparticle depends on the preparation method used [57].

Over the last thirty years, different types of polymers and copolymers have been used to design nanoparticles. Among them, biodegradable polymers are the most used as great promise the field of drug-delivery systems. These types of nanoparticles provide controlled/sustained release properties, subcellular size, and biocompatibility with tissues and cells [58], and they are well established carrier systems with high potential for the delivery of bioactive macromolecules, including peptides, proteins, and nucleic acid vaccines [59]. Encapsulation in the polymers allows maintaining the integrity and activity of these biomolecules, protecting them from exposure to extreme pH conditions, bile and pancreatic secretions, and augments the immunopotentiating effect of the antigens [60].

It is well known that properties of nanoparticles such as size, surface charge, hydrophobicity/hydrophilicity, and steric effects of particle coating can determine its compatibility with the immune system [61–63].

Furthermore, nanoparticles can also be designed to provoke an immune response, by either direct immunostimulation of antigen presenting cells or delivering antigens to specific cellular compartments [64].

For the obtention of the desired therapeutic response, size particle control is important since microparticles are rapidly cleared by reticuloendothelial system, while nanoparticles have prolonged circulation time and are efficient drug, enzyme, and protein carriers by any route of administration [65, 66].

Furthermore, in order to achieve the desired therapeutic response with these biodegradable polymeric devices, it is also important, to select the right polymer to be used as an encapsulating agent, since its nature significantly influences the size and the release profile of the nanoparticles [67]. These biodegradable polymers can be either natural (chitosan, alginate, carrageenan, albumin, gelatin, collagen, among others) or synthetic [poly(lactic acids), PLA), poly(lactide-co-glycolic acids), PLGA), poly(methyl methacrylate), PMMA), poly( $\epsilon$ -caprolactone), PCL), poly(alkyl-cyanoacrylates), PACA), and copolymers]. The former generally provide a relatively quick drug release, while the latter enable extended drug release over periods from days to several weeks [67, 68]. However, the use of synthetic polymer can be limited due to the need of organic solvents and harsh formulation conditions [58, 68]. The most commonly and extensively used polymeric nanoparticles for vaccine purposes are described in this section.

**5.1.1. Polyesters.** Polyesters are thermoplastic polymers with hydrolytically labile aliphatic ester linkages in their structure. Although all polyesters are theoretically degradable, only aliphatic ones with short aliphatic chains between ester bonds can degrade in the time required for most of the biomedical application [69]. These polymers are the most used biodegradable polymers as drug-delivery systems and



have attracted considerable attention as drug carriers due to their biocompatibility and biodegradability.

(1) *Poly(lactides)*. For vaccination purposes, polyesters such as PLA and PLGA (of variable MW and composition) have been the most popular materials for the preparation of polymer nanoparticles [70]. Due to its well-documented biocompatibility, safety, and biodegradability, these polymers are FDA approved for several clinical applications in humans [59].

PLGA is a polyester composed by one or more of three different hydroxy acid monomers, D-lactic, L-lactic, and/or glycolic acids [71]. These copolymers undergo hydrolysis of its ester groups in the presence of water, and the degradation time depends on the LA:GA monomer ratio (50:50 up to 100:0), molecular mass, end functional group (free or esterified carboxylic acid), and the shape and structure of the matrix [69]. These parameters also determine the encapsulation efficiency and release rate of drugs and antigens from this material [72]. For instance, it has been demonstrated that nanoparticles prepared from a 75:25 PLGA copolymer (a slow degradation rate polymer) presented slower release rate of antigen than those prepared from a 50:50 PLGA copolymer (a fast degradation rate polymer) [73].

The application of these polymeric particles to antigen delivery has been widely investigated from the early 90s [59]. Several authors have reported that due to its ability to efficiently target professional antigen presenting cells (APCs), the effects of PLGA entrapped antigen on the cellular and humoral immune response have several times been shown to be superior to application of soluble, free antigen [74–77].

Thus, both nano- and microparticles of PLGA can be used to increase and modulate immune responses against encapsulates antigens and to facilitate appropriate processing and presenting antigens to T cells [78–80]. Therefore, in recent years, these polymers have been studied for allergen-delivery use, finding that the PLGA nanoparticles are of great interest for therapy of allergies [81–83]. As an example, PLGA nanoparticles loaded with Bet v1 (the major allergen of birch pollen) reduce the predominance of the  $T_H2$  response, increasing the Bet v1 IgG2a levels, concomitant with an increase in IFN- $\gamma$  and IL-10 levels [82, 83].

Other less commonly used polylactide particles include poly(DL-lactide glycolide) or PLG microparticles that are also able to induce CD8<sup>+</sup> T cell responses [84]. These particles have been used as a vehicle for Ole e 1, the main olive pollen allergen, in the designing of allergen-specific vaccine [85].

Despite its obvious interest as nanoparticulate adjuvants and delivery systems for immunotherapy, the use of these polymers as peptide or protein delivery may negatively affect the stability of the loaded compound due to the bulk degradation mechanism of the polymer and the acidic degradation obtained products [59, 69, 86–89]. Another limitation of these nanoparticles is their insufficient stability and penetration capacity upon mucosal administration [59].

Thus, recent research has been focused on the search for additional strategies to improve the efficiency of these

nanoparticles by addressing its limitations. Overall, most of these strategies involve the modification of the surface of the particles by using a suitable stabilizer. The substance most commonly used for this purpose is poly(ethylene glycol) (PEG) [59], which is a hydrophilic, non-ionic, and biocompatible polymer that can be added to the particles by different routes, including covalent bonding and mixing during nanoparticle preparation or surface adsorption [90]. For instance, it was demonstrated that PLA-PEG nanoparticles, with a high PEG coating density and small size, are significantly better transporters across the nasal mucosa than noncoated PLA and even than PLA-PEG nanoparticles with a lower coating density [91].

Different studies have been performed using these nanoparticles for vaccine purposes. For example, it has been demonstrated that recombinant hepatitis B surface antigen encapsulated within PEGylated PLGA nanoparticles allows generating very fast immune responses compared to the non encapsulated antigen counterpart [92]. Other authors achieved an enhancement of the transport of the PEG-PLA nanoparticles encapsulated tetanus toxin across the intestinal barrier [93, 94].

(2) *Poly( $\epsilon$ -Caprolactone)*. Poly( $\epsilon$ -caprolactone) (PCL) is a biocompatible, bioerodable, biodegradable and semicrystalline polyester that can be used for the formulation of nanoparticles [68]. Due to the semicrystallinity and hydrophobicity, the *in vivo* degradation of PCL is much slower than PLGA, making it more appropriate for long-term delivery systems, extending over a period of more than one year [58, 95]. Furthermore, PCL particles, unlike polylactides, do not generate an acidic environment that could negatively affect the antigenicity of the encapsulated antigens or allergens [96].

However, most of the PCL studies found in the field of immunotherapy have been performed using PCL microparticles/microspheres [95]. Studies that use this polymer as nanoparticles for allergen immunotherapy have not been found and it has been little used as nanoparticulate adjuvant system for vaccine development. For example, PCL nanospheres together with mucoadhesive polymers (alginate or chitosan) were used as a potential carrier for *Streptococcus equi* surface proteins. Serum IgG antibody levels of animals vaccinated with *S. equi* antigens encapsulated or adsorbed onto PCL particles were significantly higher than those caused by free antigens or even free antigens adjuvanted with cholera toxin B subunit [97]. Thus, although no examples of the use of PCL nanoparticles for allergen immunotherapy were found, the good results obtained by different authors by using these PCL-nanoparticles in the field of vaccination suggest these systems as potential adjuvants in allergen immunotherapy.

5.1.2. *Poly(Anhydrides)*. In contrast to polylactide nanoparticles, the degradation products of polyanhydrides are non-cytotoxic and less acidic than those of polyesters, which can improve the stability of encapsulated antigen [88]. The copolymers between methyl vinyl ether and maleic



anhydride (PVMA) (commercialized as Gantrez AN from ISP, Corp.) are a good example of these polyanhydrides. Due to the presence of reactive anhydride groups which do not need time-consuming chemical activation, this copolymer allows to easily prepare nanoparticles under mild conditions, using a solvent displacement method [98]. Moreover, a recent research concluded that the use of Gantrez AN 119 nanoparticles prepared by using reduced amount of organic solvent (acetone) facilitates the encapsulation of the antigen and offers a mild irritation at mucosal epithelia when orally unstabilised nanoparticles are used [99].

One of the most important properties of the Gantrez nanoparticles is their ability to develop strong bioadhesive interactions with components of the gut mucosa [100]. In addition, their surface can be easily modified by simple incubation with different excipients or ligands in order to modify their *in vivo* distribution [101, 102], and even to increase its affinity for the intestinal mucosa [100]. This makes Gantrez nanoparticles good candidates for oral immunotherapy treatments, which have many evident advantages (patient compliance, safest route, least expensive route etc). In fact, some studies have demonstrated the efficacy of these particles by this route. For example, Gómez and coworkers [103] found enhancements in both  $T_H1$  and  $T_H2$  markers (IgG2a and IgG1, resp.) after oral administration Gantrez AN nanoparticles loaded with ovalbumin as allergen model. Moreover, these carriers were able to protect a model of sensitized mice to ovalbumin from anaphylactic shock. Thus, these PVMA nanoparticles have been widely used as carriers for controlled delivery of antigens such as *Lolium perenne* (allergenic proteins of rye-grass pollen) (N), [88, 103–106].

Another advantage of this copolymer is that it can easily react with amino groups, which makes easy to load or link different types of immunostimulants, like proteins or even *lipopolysaccharides*.

Also, the loading of antigens into these bioadhesive nanoparticles has demonstrated to enhance the immune responses in terms of a potent  $T_H1$  adjuvant capacity [103, 105, 107]. This strong response may be due to the effect produced by the nanoparticles that promote close interactions between antigen and antigen-presenting cells, and also act as agonists of various Toll-like receptors (TLRs), mainly TLR2 and TLR 4 [86, 108].

Other polyanhydrides based on hydrophobic moieties or on oligomeric ethylene glycol-containing anhydrides have been shown promise as novel vaccine carriers with immunomodulatory capabilities [88].

**5.1.3. Poly(*Gamma*-Glutamic Acid).** Poly( $\gamma$ -glutamic acid) ( $\gamma$ -PGA) is a high molecular weight polypeptide composed of  $\gamma$ -linked glutamic acid units and  $\alpha$ -carboxylate side chains produced by certain strains of *Bacillus* [109]. Due to the amphiphilic nature of the hydrophobically modified  $\gamma$ -PGA copolymer, it is possible to form nanoparticles with a simple methodology [110]. In recent years, a research group has developed biodegradable nanoparticles using  $\gamma$ -PGA with L-phenylalanine ethyl ester and evaluated the feasibility of protein entrapment on/into this carriers as well

as their biological potential. As a result of these rechearches, ovalbumin (OVA), as a model protein, was successfully encapsulated in these nanoparticles, which also did not induce any cytotoxicity against HL-60 cells [109].

Subsequent studies also showed that these particles are activators of human monocyte-derived dendritic cells and strongly stimulate the production of chemokines and inflammatory cytokines as well as upregulation of costimulatory molecules and immunomodulatory mediators involved in efficient T cell priming. Furthermore, *in vitro* studies with monocyte-derived dendritic cells and grass pollen allergen *Phleum pratense* loaded  $\gamma$ -PGA nanoparticles showed an increase allergen-specific IL-10 production and proliferation of autologous  $CD4^+$  memory T cells [110].

Additionally, studies show that these biodegradable nanoparticles induce *in vitro* innate immune cell activation, produce antigen-specific immune responses *in vivo* through the TLR 4 and MyD88-dependent signaling pathway, and can influence innate and adaptive immune responses by first-line host sensor [111].

In conclusion, these systems seem to be a new and good adjuvants and antigen carriers for allergen-specific immunotherapy.

**5.1.4. Poly(Vinylpyrrolidone).** Although fewer employees than polymers described before, there are some studies that suggest the interest of using poly(vinylpyrrolidone) (PVP) for the obtention of promising allergen-delivery nanocarriers. For example, Madan and coworkers [112] showed a successful entrapment of antigens of *Aspergillus fumigatus* (pathogenic fungi responsible of several allergic diseases) and found a sustained IgG antibody levels for approximately 12 weeks in comparison to IgG levels for 7 days with free antigen after immunization of male BALB/c mice. Moreover, IgE levels of allergens loaded PVP nanoparticles were lower than observed in free allergens studies.

**5.1.5. Polysaccharides.** The most investigated polysaccharide for mucosal vaccine delivery is chitosan, poly(D-glucosamine). This polymer is prepared by the partial N-deacetylation of chitin, a natural polymer, the second most abundant natural polysaccharide in nature, which is derived from the cuticles of insect species or crustaceans such as crabs and shrimp [113].

Chitosan is soluble in weekly acid solutions, resulting in the formation of a cationic polymer with high charge density, and can therefore form polyelectrolyte complexes with a large variety of anionic polymers [69]. Besides, due to the presence of highly reactive amino groups along its structure, chitosan is susceptible to chemical or biological functionalization [114]. Also, the preparation of chitosan nanoparticles based on the basis this polymer can be easily done without the use of organic solvents, which is interesting to maintain the immunogenicity of the antigens [115].

Chitosan possesses other advantageous properties such as low production costs, biocompatibility, biodegradability, and nontoxicity that, along with its ability to enhance the penetration of macromolecules across the intestinal and

nasal barriers, make it a suitable candidate for the design of mucosal vaccine formulations [68, 69, 116–119]. Thus, slowed mucociliary transport as well as a transient increase in paracellular absorption should lead to an improved immunological response [115].

Several studies have reported the use of chitosan-based nanocarriers for gene delivery [120–122]. CS-based nanocomplexes have been developed for the targeted delivery of plasmid DNA (pDNA) and also as carriers for RNA [122, 123].

Chitosan nanoparticles incorporating soluble antigens as diphtheria and tetanus toxoids and plasmid DNA induced high and long-lasting IgG immune responses, demonstrating the effectiveness of these devices for intranasal vaccination [93, 124]. This significant systemic and mucosal immune response enhancement after nasally administered chitosan nanoparticles has been demonstrated also for influenza, pertussis, and diphtheria vaccines [115, 124]. However, until now, the mechanism by which the antigen is delivered to the nasal mucosa and the role of the physicochemical characteristics of the particles in this processes have not been well determined, and there is some contradictory theories [124].

For oral vaccination studies, Roy and coworkers have demonstrated the effectiveness of orally delivered chitosan-DNA nanoparticles in inducing protective immunity in the peanut allergy mouse model [125]. More specifically, chitosan nanoparticles loaded with the gene for Ara h2 (main peanut allergen) allow to obtain a significant reduction in the levels of serum IgE, plasma histamine, and vascular leakage and the induction of specific mucosal IgA antibodies.

Other studies show a significant amelioration of ovalbumin-induced food allergy symptoms when the TGF- $\beta$  expressing DNA vector is orally administered after its encapsulation in chitosan nanoparticles, compared to the previously reported protein-based strategies [126].

However, in spite of all the described advantageous properties of chitosan, this polymer has a major limitation: its low solubility at physiological pH and therefore loses of its ability to enhance drug permeability and absorption [127, 128].

To improve this drawback, several derivatives of chitosan have been studied, such as trimethyl chitosan (TMC), that shows high solubility, bioadhesive properties, and ability to enhance permeability over a wide pH range [129, 130]. In fact, a recent study shows that trimethylated chitosan nanoparticles obtained by using a new mild method induced stronger humoral and mucosal immune responses compared to generate by chitosan conventional nanoparticles [131].

Other interesting alternative is the use of chitosan together with other biodegradable polyelectrolyte polymers with opposite charge to obtain combined nanoparticles suitable for mucosal vaccinations. A typical example of this second polymer can be sodium alginate, another biodegradable and biocompatible polysaccharide. For instance, it has been demonstrated that alginate-chitosan-coated nanoparticles are an effective system for subcutaneous and oral vaccination with the recombinant hepatitis B surface antigen [132–134]. Another study shows that these nanoparticles can prevent a

burst release of loaded ovalbumin and improve its stability in simulated intestinal fluid at 37°C [132].

**5.2. Nondegradable Polymeric Nanoparticles.** Nondegradable nanoparticles of different materials such as latex, gold, silica, or polystyrene are being evaluated as antigen carriers for induction of immunity [70, 77, 135]. It is considered that by using these particles, the antigen can be presented to the immune system for extended periods of time, and thus improve the immunogenicity, probably due to the persistence of the nanoparticles in the tissues [70, 77].

On the other hand, these polymers have several technological advantages [64]. For example, polystyrene nanoparticles can be made with several functional groups on their surface to achieve effective conjugation with a variety of antigens. Furthermore, when the antigen is covalently coupled to the particle, it induces higher cellular and humoral responses than in the cases where the antigen is absorbed [136].

For latex particles, some examples in the literature have demonstrated that this polymer was presented 1000–10,000-fold more efficiently by MHC-Class I molecules than soluble antigens [137] or antigens presented via MHC-Class II molecules [138]. Gold nanoparticles also appear to enhance the effect of DNA vaccination by improving delivery onto cellular interiors [139]. However, these results are obtained using electroporation, which may not be applicable in humans due to cell mortality. In the absence of this technique, so by passive diffusion, the immunological effects were not so interesting [140]. Other recent studies show that the use of gold nanoparticles along with alum can enhance the immune response against PfMSP-119 and PvMSP-119 [141].

However, in general terms, it was shown that nondegradable particles were much less effective at cross-presenting antigens than degradable ones [142, 143]. Also, to use this type of nanoparticles for vaccination purposes is necessary to consider aspects of toxicity and particles aggregation in the tissues, which requires follow-up studies of *in vivo* clearance and the determination of possible adverse effects resulting from its use [77].

## 6. Conclusion

In summary, the use of nanotechnology platforms, although widespread in recent years for vaccination purposes [98, 106], is emerging in the field of allergen immunotherapy [103–105]. Given the promising results obtained so far, polymeric nanoparticles can be of interest to develop new therapeutic strategies able to improve both clinical efficacy and safety of allergen vaccines.

On the other hand, our knowledge of the nanoparticle interaction with the immune system has been increased in recent years, but it still remains insufficient. Thus, further studies related to the immunomodulatory effects of the polymeric nanoparticles are required to improve our understanding, and therefore our capability, to design better specific and effective allergen vaccines.

## Funding

This research was financially supported by Health Department of “Gobierno de Navarra” (Grant no. 28/2007), “Instituto de Salud Carlos III” (Grant no. PS09/01083), and “Fundación Ramón Areces”. J. D. S. Rebouças was also financially supported by “Asociación de Amigos”, University of Navarra, Spain. M. Ferrer and M. L. Sanz and M.B. are supported by grant RD07/0064 from the Spanish Research Network on Adverse Reactions to Allergens and Drugs (RIRAAF: Red de Investigación de Reacciones Adversas a Alérgenos y Fármacos) of the Carlos III Health Institute.

## References

- [1] D. J. Martino and S. L. Prescott, “Silent mysteries: epigenetic paradigms could hold the key to conquering the epidemic of allergy and immune disease,” *Allergy*, vol. 65, no. 1, pp. 7–15, 2010.
- [2] S. H. Sicherer and H. A. Sampson, “Peanut allergy: emerging concepts and approaches for an apparent epidemic,” *Journal of Allergy and Clinical Immunology*, vol. 120, no. 3, pp. 491–503, 2007.
- [3] P. G. H. Gell and R. R. A. Coombs, *Clinical Aspects of Immunology*, Blackwell, Oxford, UK, 1st edition, 1963.
- [4] J. O. Warner, M. A. Kaliner, C. D. Crisci et al., “Allergy practice worldwide: a report by the World Allergy Organization Specialty and Training Council,” *International Archives of Allergy and Immunology*, vol. 139, no. 2, pp. 166–174, 2006.
- [5] A. P. Grammatikos, “The genetic and environmental basis of atopic diseases,” *Annals of Medicine*, vol. 40, no. 7, pp. 482–495, 2008.
- [6] D. Vercelli, “Discovering susceptibility genes for asthma and allergy,” *Nature Reviews Immunology*, vol. 8, no. 3, pp. 169–182, 2008.
- [7] C. Ober, S. A. Leavitt, A. Tsalenko et al., “Variation in the interleukin 4-receptor  $\alpha$  gene confers susceptibility to asthma and atopy in ethnically diverse populations,” *American Journal of Human Genetics*, vol. 66, no. 2, pp. 517–526, 2000.
- [8] G. M. Hunninghake, M. E. Soto-Quirós, L. Avila et al., “Polymorphisms in IL13, total IgE, eosinophilia, and asthma exacerbations in childhood,” *Journal of Allergy and Clinical Immunology*, vol. 120, no. 1, pp. 84–90, 2007.
- [9] X. Liu, T. H. Beaty, P. Deindl et al., “Associations between specific serum IgE response and 6 variants within the genes IL4, IL13, and IL4RA in German children: the German Multicenter Atopy Study,” *Journal of Allergy and Clinical Immunology*, vol. 113, no. 3, pp. 489–495, 2004.
- [10] L. O’Mahony, M. Akdis, R. Cramer, and C. A. Akdis, “Novel immunotherapeutic approaches for allergy and asthma,” *Autoimmunity*, vol. 43, no. 7, pp. 493–503, 2010.
- [11] N. Novak, “New insights into the mechanism and management of allergic diseases: atopic dermatitis,” *Allergy*, vol. 64, no. 2, pp. 265–275, 2009.
- [12] V. Niederberger and R. Valenta, “Molecular approaches for new vaccines against allergy,” *Expert Review of Vaccines*, vol. 5, no. 1, pp. 103–110, 2006.
- [13] J. M. Rolland, L. M. Gardner, and R. E. O’Hehir, “Allergen-related approaches to immunotherapy,” *Pharmacology and Therapeutics*, vol. 121, no. 3, pp. 273–284, 2009.
- [14] G. Pauli and H. J. Malling, “The current state of recombinant allergens for immunotherapy,” *Current Opinion in Allergy and Clinical Immunology*, vol. 10, no. 6, pp. 575–581, 2010.
- [15] R. T. Strait, S. C. Morris, and F. D. Finkelman, “IgG-blocking antibodies inhibit IgE-mediated anaphylaxis in vivo through both antigen interception and Fc $\gamma$ RIIb cross-linking,” *The Journal of Clinical Investigation*, vol. 116, no. 3, pp. 833–841, 2006.
- [16] Y. Ma, K. T. Hayglass, A. B. Becker et al., “Novel cytokine peptide-based vaccines: an interleukin-4 vaccine suppresses airway allergic responses in mice,” *Allergy*, vol. 62, no. 6, pp. 675–682, 2007.
- [17] Y. Ma, K. T. HayGlass, A. B. Becker et al., “Novel recombinant interleukin-13 peptide-based vaccine reduces airway allergic inflammatory responses in mice,” *American Journal of Respiratory and Critical Care Medicine*, vol. 176, no. 5, pp. 439–445, 2007.
- [18] P. Pulsawat, S. Piboonpocanun, S. Sirivichayakul et al., “Production and immunogenicity of hypoallergenic codon-optimized DNA vaccine encoding mature Der p 1 allergen,” *Journal of Investigational Allergology and Clinical Immunology*, vol. 20, no. 7, pp. 582–590, 2010.
- [19] G. K. Gupta and D. K. Agrawal, “CpG oligodeoxynucleotides as TLR9 agonists: therapeutic application in allergy and asthma,” *BioDrugs*, vol. 24, no. 4, pp. 225–235, 2010.
- [20] D. I. Bernstein, T. Epstein, K. Murphy-Berendts, and G. M. Liss, “Surveillance of systemic reactions to subcutaneous immunotherapy injections: year 1 outcomes of the ACAAI and AAAAI Collaborative Study,” *Annals of Allergy, Asthma and Immunology*, vol. 104, no. 6, pp. 530–535, 2010.
- [21] S. Broos, K. Lundberg, T. Akagi et al., “Immunomodulatory nanoparticles as adjuvants and allergen-delivery system to human dendritic cells: implications for specific immunotherapy,” *Vaccine*, vol. 28, no. 31, pp. 5075–5085, 2010.
- [22] R. Klippstein and D. Pozo, “Nanotechnology-based manipulation of dendritic cells for enhanced immunotherapy strategies,” *Nanomedicine*, vol. 6, no. 4, pp. 523–529, 2010.
- [23] I. Schöll, G. Boltz-Nitulescu, and E. Jensen-Jarolim, “Review of novel particulate antigen delivery systems with special focus on treatment of type I allergy,” *Journal of Controlled Release*, vol. 104, no. 1, pp. 1–27, 2005.
- [24] S. Romagnani, “Immunologic influences on allergy and the TH1/TH2 balance,” *Journal of Allergy and Clinical Immunology*, vol. 113, no. 3, pp. 395–400, 2004.
- [25] D. S. Robinson, “Th-2 cytokines in allergic disease,” *British Medical Bulletin*, vol. 56, no. 4, pp. 956–968, 2000.
- [26] M. I. Araujo, R. A. Campos, L. S. Cardoso, S. C. Oliveira, and E. M. Carvalho, “Immunomodulation of the allergic inflammatory response: new developments,” *Inflammation and Allergy—Drug Targets*, vol. 9, no. 2, pp. 73–82, 2010.
- [27] Y. Zhao, J. Yang, and Y.-D. Gao, “Altered expressions of helper T cell (Th)1, Th2, and Th17 cytokines in CD8+ and  $\gamma\delta$  T cells in patients with allergic asthma,” *Journal of Asthma*, vol. 48, no. 5, pp. 429–436, 2011.
- [28] O. Palomares, G. Yaman, A. K. Azkur, T. Akkoc, M. Akdis, and C. A. Akdis, “Role of Treg in immune regulation of allergic diseases,” *European Journal of Immunology*, vol. 40, no. 5, pp. 1232–1240, 2010.
- [29] K. Oboki, T. Ohno, H. Saito, and S. Nakae, “Th17 and allergy,” *Allergology International*, vol. 57, no. 2, pp. 121–134, 2008.
- [30] A. J. Frew, “Allergen immunotherapy,” *Journal of Allergy and Clinical Immunology*, vol. 125, no. 2, pp. S306–S313, 2010.
- [31] R. Valenta and D. Kraft, “From allergen structure to new forms of allergen-specific immunotherapy,” *Current Opinion in Immunology*, vol. 14, no. 6, pp. 718–727, 2002.



- [32] S. J. Till, J. N. Francis, K. Nouri-Aria, and S. R. Durham, "Mechanisms of immunotherapy," *Journal of Allergy and Clinical Immunology*, vol. 113, no. 6, pp. 1025–1034, 2004.
- [33] M. Larché, C. A. Akdis, and R. Valenta, "Immunological mechanisms of allergen-specific immunotherapy," *Nature Reviews Immunology*, vol. 6, no. 10, pp. 761–771, 2006.
- [34] G. Ciprandi, G. L. Marseglia, and M. A. Tosca, "Allergen-specific immunotherapy: an update on immunological mechanisms of action," *Monaldi Archives for Chest Disease*, vol. 65, no. 1, pp. 34–37, 2006.
- [35] C. A. Akdis and M. Akdis, "Mechanisms and treatment of allergic disease in the big picture of regulatory T cells," *Journal of Allergy and Clinical Immunology*, vol. 123, no. 4, pp. 735–746, 2009.
- [36] M. Akdis and C. A. Akdis, "Therapeutic manipulation of immune tolerance in allergic disease," *Nature Reviews Drug Discovery*, vol. 8, no. 8, pp. 645–660, 2009.
- [37] D. I. Bernstein, T. Epstein, K. Murphy-Berendts, and G. M. Liss, "Surveillance of systemic reactions to subcutaneous immunotherapy injections: year 1 outcomes of the ACAAI and AAAAI Collaborative Study," *Annals of Allergy, Asthma and Immunology*, vol. 104, no. 6, pp. 530–535, 2010.
- [38] S. R. Roy, J. R. Sigmon, J. Olivier, J. E. Moffitt, D. A. Brown, and G. D. Marshall, "Increased frequency of large local reactions among systemic reactors during subcutaneous allergen immunotherapy," *Annals of Allergy, Asthma and Immunology*, vol. 99, no. 1, pp. 82–86, 2007.
- [39] G. W. Canonica and G. Passalacqua, "Noninjection routes for immunotherapy," *Journal of Allergy and Clinical Immunology*, vol. 111, no. 3, pp. 437–448, 2003.
- [40] C. Ozdemir, "An immunological overview of allergen specific immunotherapy—subcutaneous and sublingual routes," *Therapeutic Advances in Respiratory Disease*, vol. 3, no. 5, pp. 253–262, 2009.
- [41] G. W. Canonica, J. Bousquet, T. Casale et al., "Sub-lingual immunotherapy: world allergy organization position paper 2009," *Allergy*, vol. 64, no. 91, pp. 1–59, 2009.
- [42] J. Bousquet, R. Lockey, H. J. Malling et al., "Allergen immunotherapy: therapeutic vaccines for allergic diseases—a WHO position paper," *Journal of Allergy and Clinical Immunology*, vol. 102, no. 4, pp. 558–562, 1998.
- [43] W. Wang and M. Singh, "Selection of adjuvants for enhanced vaccine potency," *World Journal of Vaccines*, vol. 1, pp. 33–78, 2011.
- [44] J. N. Francis and S. R. Durham, "Adjuvants for allergen immunotherapy: experimental results and clinical perspectives," *Current Opinion in Allergy and Clinical Immunology*, vol. 4, no. 6, pp. 543–548, 2004.
- [45] A. W. Wheeler and S. R. Woroniecki, "Immunological adjuvants in allergy vaccines: past, present and future," *Allergology International*, vol. 50, no. 4, pp. 295–301, 2001.
- [46] J. C. Aguilar and E. G. Rodríguez, "Vaccine adjuvants revisited," *Vaccine*, vol. 25, no. 19, pp. 3752–3762, 2007.
- [47] Y. Perrie, A. R. Mohammed, D. J. Kirby, S. E. McNeil, and V. W. Bramwell, "Vaccine adjuvant systems: enhancing the efficacy of sub-unit protein antigens," *International Journal of Pharmaceutics*, vol. 364, no. 2, pp. 272–280, 2008.
- [48] A. des Rieux, V. Fievez, M. Garinot, Y. J. Schneider, and V. Préat, "Nanoparticles as potential oral delivery systems of proteins and vaccines: a mechanistic approach," *Journal of Controlled Release*, vol. 116, no. 1, pp. 1–27, 2006.
- [49] R. K. Gupta, "Aluminum compounds as vaccine adjuvants," *Advanced Drug Delivery Reviews*, vol. 32, no. 3, pp. 155–172, 1998.
- [50] A. C. Allison and G. Gregoriadis, "Liposomes as immunological adjuvants," *Nature*, vol. 252, no. 5480, article 252, 1974.
- [51] G. De Becker, V. Moulin, B. Pajak et al., "The adjuvant monophosphoryl lipid A increases the function of antigen-presenting cells," *International Immunology*, vol. 12, no. 6, pp. 807–815, 2000.
- [52] I. Schöll, G. Boltz-Nitulescu, and E. Jensen-Jarolim, "Review of novel particulate antigen delivery systems with special focus on treatment of type I allergy," *Journal of Controlled Release*, vol. 104, no. 1, pp. 1–27, 2005.
- [53] H. Tighe, K. Takabayashi, D. Schwartz et al., "Conjugation of immunostimulatory DNA to the short ragweed allergen Amb a 1 enhances its immunogenicity and reduces its allergenicity," *Journal of Allergy and Clinical Immunology*, vol. 106, no. 1, pp. 124–134, 2000.
- [54] M. K. Tulic, P. O. Fiset, P. Christodoulopoulos et al., "Amb a 1-immunostimulatory oligodeoxynucleotide conjugate immunotherapy decreases the nasal inflammatory response," *Journal of Allergy and Clinical Immunology*, vol. 113, no. 2, pp. 235–241, 2004.
- [55] S. Broos, K. Lundberg, T. Akagi et al., "Immunomodulatory nanoparticles as adjuvants and allergen-delivery system to human dendritic cells: implications for specific immunotherapy," *Vaccine*, vol. 28, no. 31, pp. 5075–5085, 2010.
- [56] J. Kreuter, "Nanoparticles," in *Encyclopaedia of Pharmaceutical Technology*, J. Swarbrick and J. C. Boylan, Eds., vol. 10, pp. 165–190, Marcel Dekker, New York, NY, USA, 1994.
- [57] P. Couvreur, G. Barratt, E. Fattal, P. Legrand, and C. Vauthier, "Nanocapsule technology: a review," *Critical Reviews in Therapeutic Drug Carrier Systems*, vol. 19, no. 2, pp. 99–134, 2002.
- [58] A. Kumari, S. K. Yadav, and S. C. Yadav, "Biodegradable polymeric nanoparticles based drug delivery systems," *Colloids and Surfaces B*, vol. 75, no. 1, pp. 1–18, 2010.
- [59] N. Csaba, M. Garcia-Fuentes, and M. J. Alonso, "Nanoparticles for nasal vaccination," *Advanced Drug Delivery Reviews*, vol. 61, no. 2, pp. 140–157, 2009.
- [60] T. Madan, N. Munshi, T. K. De, A. Maitra, P. Usha Sarma, and S. S. Aggarwal, "Biodegradable nanoparticles as a sustained release system for the antigens/allergens of *Aspergillus fumigatus*: preparation and characterisation," *International Journal of Pharmaceutics*, vol. 159, no. 2, pp. 135–147, 1997.
- [61] P. Aggarwal, J. B. Hall, C. B. McLeland, M. A. Dobrovolskaia, and S. E. McNeil, "Nanoparticle interaction with plasma proteins as it relates to particle biodistribution, biocompatibility and therapeutic efficacy," *Advanced Drug Delivery Reviews*, vol. 61, no. 6, pp. 428–437, 2009.
- [62] M. A. Dobrovolskaia, P. Aggarwal, J. B. Hall, and S. E. McNeil, "Preclinical studies to understand nanoparticle interaction with the immune system and its potential effects on nanoparticle biodistribution," *Molecular Pharmaceutics*, vol. 5, no. 4, pp. 487–495, 2008.
- [63] M. A. Dobrovolskaia and S. E. McNeil, "Immunological properties of engineered nanomaterials," *Nature Nanotechnology*, vol. 2, no. 8, pp. 469–478, 2007.
- [64] M. Kalkanidis, G. A. Pietersz, S. D. Xiang et al., "Methods for nano-particle based vaccine formulation and evaluation of their immunogenicity," *Methods*, vol. 40, no. 1, pp. 20–29, 2006.
- [65] J. C. Gautier, J. L. Grangier, A. Barbier et al., "Biodegradable nanoparticles for subcutaneous administration of growth hormone releasing factor (hGRF)," *Journal of Controlled Release*, vol. 20, no. 1, pp. 67–77, 1992.

- [66] P. Couvreur et al., "Biodegradable polymeric nanoparticles as drug carrier for antitumor agents," in *Polymeric Nanoparticles and Microspheres*, P. Guiot and P. Couvreur, Eds., pp. 27–93, CRC Press, Boca Raton, Fla, USA, 1986.
- [67] V. W. Bramwell and Y. Perrie, "Particulate delivery systems for vaccines: what can we expect?" *Journal of Pharmacy and Pharmacology*, vol. 58, no. 6, pp. 717–728, 2006.
- [68] J. M. Irache, I. Esparza, C. Gamazo, M. Agüeros, and S. Espuelas, "Nanomedicine: novel approaches in human and veterinary therapeutics," *Veterinary Parasitology*, vol. 180, no. 1–2, pp. 47–71, 2011.
- [69] K. S. Soppimath, T. M. Aminabhavi, A. R. Kulkarni, and W. E. Rudzinski, "Biodegradable polymeric nanoparticles as drug delivery devices," *Journal of Controlled Release*, vol. 70, no. 1–2, pp. 1–20, 2001.
- [70] L. J. Peek, C. R. Middaugh, and C. Berkland, "Nanotechnology in vaccine delivery," *Advanced Drug Delivery Reviews*, vol. 60, no. 8, pp. 915–928, 2008.
- [71] R. C. Mundargi, V. R. Babu, V. Rangaswamy, P. Patel, and T. M. Aminabhavi, "Nano/micro technologies for delivering macromolecular therapeutics using poly(D,L-lactide-co-glycolide) and its derivatives," *Journal of Controlled Release*, vol. 125, no. 3, pp. 193–209, 2008.
- [72] H. Tamber, P. Johansen, H. P. Merkle, and B. Gander, "Formulation aspects of biodegradable polymeric microspheres for antigen delivery," *Advanced Drug Delivery Reviews*, vol. 57, no. 3, pp. 357–376, 2005.
- [73] A. G. A. Coombes, E. C. Lavelle, P. G. Jenkins, and S. S. Davis, "Single dose, polymeric, microparticle-based vaccines: the influence of formulation conditions on the magnitude and duration of the immune response to a protein antigen," *Vaccine*, vol. 14, no. 15, pp. 1429–1438, 1996.
- [74] I. D. Spiers, J. E. Eyles, L. W. J. Baillie, E. D. Williamson, and H. O. Alpar, "Biodegradable microparticles with different release profiles: effect on the immune response after a single administration via intranasal and intramuscular routes," *Journal of Pharmacy and Pharmacology*, vol. 52, no. 10, pp. 1195–1201, 2000.
- [75] M. Igartua, R. M. Hernández, A. Esquisabel, A. R. Gascón, M. B. Calvo, and J. L. Pedraz, "Enhanced immune response after subcutaneous and oral immunization with biodegradable PLGA microspheres," *Journal of Controlled Release*, vol. 56, no. 1–3, pp. 63–73, 1998.
- [76] J. H. Eldrige, J. K. Staas, J. A. Meulbroek, J. R. McGhee, T. R. Tice, and R. M. Gilley, "Biodegradable microspheres as a vaccine delivery system," *Molecular Immunology*, vol. 28, no. 3, pp. 287–294, 1991.
- [77] B. Combadière and B. Mahé, "Particle-based vaccines for transcutaneous vaccination," *Comparative Immunology, Microbiology and Infectious Diseases*, vol. 31, no. 2–3, pp. 293–315, 2008.
- [78] H. Sun, K. G. J. Pollock, and J. M. Brewer, "Analysis of the role of vaccine adjuvants in modulating dendritic cell activation and antigen presentation in vitro," *Vaccine*, vol. 21, no. 9–10, pp. 849–855, 2003.
- [79] C. Clawson, C. T. Huang, D. Futalan et al., "Delivery of a peptide via poly(D,L-lactide-co-glycolic) acid nanoparticles enhances its dendritic cell-stimulatory capacity," *Nanomedicine*, vol. 6, no. 5, pp. 651–661, 2010.
- [80] C. S. W. Chong, M. Cao, W. W. Wong et al., "Enhancement of T helper type 1 immune responses against hepatitis B virus core antigen by PLGA nanoparticle vaccine delivery," *Journal of Controlled Release*, vol. 102, no. 1, pp. 85–99, 2005.
- [81] I. Schöll, G. Boltz-Nitulescu, and E. Jensen-Jarolim, "Review of novel particulate antigen delivery systems with special focus on treatment of type I allergy," *Journal of Controlled Release*, vol. 104, no. 1, pp. 1–27, 2005.
- [82] I. Schöll, T. Kopp, B. Bohle, and E. Jensen-Jarolim, "Biodegradable PLGA particles for improved systemic and mucosal treatment of Type I allergy," *Immunology and Allergy Clinics of North America*, vol. 26, no. 2, pp. 349–364, 2006.
- [83] I. Schöll, A. Weissenböck, E. Förster-Waldl et al., "Allergen-loaded biodegradable poly(D,L-lactide-co-glycolic) acid nanoparticles down-regulate an ongoing Th2 response in the BALB/c mouse model," *Clinical and Experimental Allergy*, vol. 34, no. 2, pp. 315–321, 2004.
- [84] C. D. Partidos, P. Vohra, D. H. Jones, G. Farrar, and M. W. Steward, "Induction of cytotoxic T-cell responses following oral immunization with synthetic peptides encapsulated in PLG microparticles," *Journal of Controlled Release*, vol. 62, no. 3, pp. 325–332, 1999.
- [85] E. Batanero, P. Barral, M. Villalba, and R. Rodríguez, "Biodegradable poly (DL-lactide glycolide) microparticles as a vehicle for allergen-specific vaccines: a study performed with Ole e 1, the main allergen of olive pollen," *Journal of Immunological Methods*, vol. 259, no. 1–2, pp. 87–94, 2002.
- [86] A. I. Camacho, R. Da Costa Martins, I. Tamayo et al., "Poly(methyl vinyl ether-co-maleic anhydride) nanoparticles as innate immune system activators," *Vaccine*, vol. 29, no. 41, pp. 7130–7135, 2011.
- [87] P. Johansen, Y. Men, H. P. Merkle, and B. Gander, "Revisiting PLA/PLGA microspheres: an analysis of their potential in parenteral vaccination," *European Journal of Pharmaceutics and Biopharmaceutics*, vol. 50, no. 1, pp. 129–146, 2000.
- [88] S. K. Mallapragada and B. Narasimhan, "Immunomodulatory biomaterials," *International Journal of Pharmaceutics*, vol. 364, no. 2, pp. 265–271, 2008.
- [89] M. Murillo, C. Gamazo, J. M. Irache, and M. M. Goñi, "Polyester microparticles as a vaccine delivery system for brucellosis: influence of the polymer on release, phagocytosis and toxicity," *Journal of Drug Targeting*, vol. 10, no. 3, pp. 211–219, 2002.
- [90] M. L. Hans and A. M. Lowman, "Biodegradable nanoparticles for drug delivery and targeting," *Current Opinion in Solid State and Materials Science*, vol. 6, no. 4, pp. 319–327, 2002.
- [91] A. Vila, H. Gill, O. McCallion, and M. J. Alonso, "Transport of PLA-PEG particles across the nasal mucosa: effect of particle size and PEG coating density," *Journal of Controlled Release*, vol. 98, no. 2, pp. 231–244, 2004.
- [92] D. J. Bharali, V. Pradhan, G. Elkin et al., "Novel nanoparticles for the delivery of recombinant hepatitis B vaccine," *Nanomedicine*, vol. 4, no. 4, pp. 311–317, 2008.
- [93] A. Vila, A. Sánchez, M. Tobío, P. Calvo, and M. J. Alonso, "Design of biodegradable particles for protein delivery," *Journal of Controlled Release*, vol. 78, no. 1–3, pp. 15–24, 2002.
- [94] A. Vila, A. Sánchez, C. Évora, I. Soriano, O. McCallion, and M. J. Alonso, "PLA-PEG particles as nasal protein carriers: the influence of the particle size," *International Journal of Pharmaceutics*, vol. 292, no. 1–2, pp. 43–52, 2005.
- [95] V. R. Sinha, K. Bansal, R. Kaushik, R. Kumria, and A. Trehan, "Poly-ε-caprolactone microspheres and nanospheres: an overview," *International Journal of Pharmaceutics*, vol. 278, no. 1, pp. 1–23, 2004.
- [96] S. R. Jameela, N. Suma, A. Misra, R. Raghuvanshi, S. Ganga, and A. Jayakrishnan, "Poly(ε-caprolactone) microspheres as



- a vaccine carrier," *Current Science*, vol. 70, no. 7, pp. 669–671, 1996.
- [97] H. F. Florindo, S. Pandit, L. Lacerda, L. M. D. Gonçalves, H. O. Alpar, and A. J. Almeida, "The enhancement of the immune response against *S. equi* antigens through the intranasal administration of poly- $\epsilon$ -caprolactone-based nanoparticles," *Biomaterials*, vol. 30, no. 5, pp. 879–891, 2009.
- [98] P. Arbós, M. A. Arangoa, M. A. Campanero, and J. M. Irache, "Quantification of the bioadhesive properties of protein-coated PVM/MA nanoparticles," *International Journal of Pharmaceutics*, vol. 242, no. 1-2, pp. 129–136, 2002.
- [99] K. Vandamme, V. Melkebeek, E. Cox et al., "Influence of reaction medium during synthesis of Gantrez® AN 119 nanoparticles for oral vaccination," *European Journal of Pharmaceutics and Biopharmaceutics*, vol. 74, no. 2, pp. 202–208, 2010.
- [100] P. Arbós, M. A. Campanero, M. A. Arangoa, M. J. Renedo, and J. M. Irache, "Influence of the surface characteristics of PVM/MA nanoparticles on their bioadhesive properties," *Journal of Controlled Release*, vol. 89, no. 1, pp. 19–30, 2003.
- [101] H. H. Salman, C. Gamazo, M. A. Campanero, and J. M. Irache, "Salmonella-like bioadhesive nanoparticles," *Journal of Controlled Release*, vol. 106, no. 1-2, pp. 1–13, 2005.
- [102] K. Yoncheva, S. Gómez, M. A. Campanero, C. Gamazo, and J. M. Irache, "Bioadhesive properties of pegylated nanoparticles," *Expert Opinion on Drug Delivery*, vol. 2, no. 2, pp. 205–218, 2005.
- [103] S. Gómez, C. Gamazo, B. S. Roman, M. Ferrer, M. L. Sanz, and J. M. Irache, "Gantrez® AN nanoparticles as an adjuvant for oral immunotherapy with allergens," *Vaccine*, vol. 25, no. 29, pp. 5263–5271, 2007.
- [104] S. Gómez, C. Gamazo, B. San Roman et al., "A novel nanoparticulate adjuvant for immunotherapy with *Lolium perenne*," *Journal of Immunological Methods*, vol. 348, no. 1-2, pp. 1–8, 2009.
- [105] S. Gómez, C. Gamazo, B. S. Roman, C. Vauthier, M. Ferrer, and J. M. Irache, "Development of a novel vaccine delivery system based on gantrez nanoparticles," *Journal of Nanoscience and Nanotechnology*, vol. 6, no. 9-10, pp. 3283–3289, 2006.
- [106] J. M. Irache, H. H. Salman, S. Gomez, S. Espuelas, and C. Gamazo, "Poly(anhydride) nanoparticles as adjuvants for mucosal vaccination," *Frontiers in Bioscience*, vol. 2, pp. 876–890, 2010.
- [107] J. Ochoa, J. M. Irache, I. Tamayo, A. Walz, V. G. DelVecchio, and C. Gamazo, "Protective immunity of biodegradable nanoparticle-based vaccine against an experimental challenge with *Salmonella* Enteritidis in mice," *Vaccine*, vol. 25, no. 22, pp. 4410–4419, 2007.
- [108] I. Tamayo, J. M. Irache, C. Mansilla, J. Ochoa-Repáraz, J. J. Lasarte, and C. Gamazo, "Poly(anhydride) nanoparticles act as active Th1 adjuvants through toll-like receptor exploitation," *Clinical and Vaccine Immunology*, vol. 17, no. 9, pp. 1356–1362, 2010.
- [109] T. Akagi, T. Kaneko, T. Kida, and M. Akashi, "Preparation and characterization of biodegradable nanoparticles based on poly( $\gamma$ -glutamic acid) with L-phenylalanine as a protein carrier," *Journal of Controlled Release*, vol. 108, no. 2-3, pp. 226–236, 2005.
- [110] S. Broos, K. Lundberg, T. Akagi et al., "Immunomodulatory nanoparticles as adjuvants and allergen-delivery system to human dendritic cells: implications for specific immunotherapy," *Vaccine*, vol. 28, no. 31, pp. 5075–5085, 2010.
- [111] T. Uto, T. Akagi, K. Yoshinaga, M. Toyama, M. Akashi, and M. Baba, "The induction of innate and adaptive immunity by biodegradable poly( $\gamma$ -glutamic acid) nanoparticles via a TLR4 and MyD88 signaling pathway," *Biomaterials*, vol. 32, no. 22, pp. 5206–5212, 2011.
- [112] B. S. Zolnik, Á. González-Fernández, N. Sadrieh, and M. A. Dobrovolskaia, "Minireview: nanoparticles and the immune system," *Endocrinology*, vol. 151, no. 2, pp. 458–465, 2010.
- [113] D. H. Lee and I. J. Kang, "Drug delivery system using biodegradable nanoparticles carrier," *Kona*, vol. 24, pp. 159–166, 2006.
- [114] R. Jayakumar, N. Nwe, S. Tokura, and H. Tamura, "Sulfated chitin and chitosan as novel biomaterials," *International Journal of Biological Macromolecules*, vol. 40, no. 3, pp. 175–181, 2007.
- [115] L. Illum, I. Jabbal-Gill, M. Hinchcliffe, A. N. Fisher, and S. S. Davis, "Chitosan as a novel nasal delivery system for vaccines," *Advanced Drug Delivery Reviews*, vol. 51, no. 1–3, pp. 81–96, 2001.
- [116] K. Bowman and K. W. Leong, "Chitosan nanoparticles for oral drug and gene delivery," *International Journal of Nanomedicine*, vol. 1, no. 2, pp. 117–128, 2006.
- [117] A. Masotti and G. Ortaggi, "Chitosan micro- and nanospheres: fabrication and applications for drug and DNA delivery," *Mini-Reviews in Medicinal Chemistry*, vol. 9, no. 4, pp. 463–469, 2009.
- [118] K. Nagpal, S. K. Singh, and D. N. Mishra, "Chitosan nanoparticles: a promising system in novel drug delivery," *Chemical and Pharmaceutical Bulletin*, vol. 58, no. 11, pp. 1423–1430, 2010.
- [119] I. M. Van der Lubben, J. C. Verhoef, G. Borchard, and H. E. Junginger, "Chitosan for mucosal vaccination," *Advanced Drug Delivery Reviews*, vol. 52, no. 2, pp. 139–144, 2001.
- [120] G. Borchard, "Chitosans for gene delivery," *Advanced Drug Delivery Reviews*, vol. 52, no. 2, pp. 145–150, 2001.
- [121] H. L. Jiang, Y. K. Kim, R. Arote et al., "Chitosan-graft-polyethylenimine as a gene carrier," *Journal of Controlled Release*, vol. 117, no. 2, pp. 273–280, 2007.
- [122] W. E. Rudzinski and T. M. Aminabhavi, "Chitosan as a carrier for targeted delivery of small interfering RNA," *International Journal of Pharmaceutics*, vol. 399, no. 1-2, pp. 1–11, 2010.
- [123] A. V. Il'ina and V. P. Varlamov, "Chitosan-based polyelectrolyte complexes: a review," *Applied Biochemistry and Microbiology*, vol. 41, no. 1, pp. 5–11, 2005.
- [124] A. Vila, A. Sánchez, K. Janes et al., "Low molecular weight chitosan nanoparticles as new carriers for nasal vaccine delivery in mice," *European Journal of Pharmaceutics and Biopharmaceutics*, vol. 57, no. 1, pp. 123–131, 2004.
- [125] K. Roy, H. Q. Mao, S. K. Huang, and K. W. Leong, "Oral gene delivery with chitosan-DNA nanoparticles generates immunologic protection in a murine model of peanut allergy," *Nature Medicine*, vol. 5, no. 4, pp. 387–391, 1999.
- [126] F. Li, L. Wang, X. M. Jin, C. H. Yan, S. Jiang, and X. M. Shen, "The immunologic effect of TGF- $\beta$ 1 chitosan nanoparticle plasmids on ovalbumin-induced allergic BALB/c mice," *Immunobiology*, vol. 214, no. 2, pp. 87–99, 2009.
- [127] S. Zhu, F. Qian, Y. Zhang, C. Tang, and C. Yin, "Synthesis and characterization of PEG modified N-trimethylaminoethylmethacrylate chitosan nanoparticles," *European Polymer Journal*, vol. 43, no. 6, pp. 2244–2253, 2007.

- [128] S. A. Agnihotri, N. N. Mallikarjuna, and T. M. Aminabhavi, "Recent advances on chitosan-based micro- and nanoparticles in drug delivery," *Journal of Controlled Release*, vol. 100, no. 1, pp. 5–28, 2004.
- [129] A. Domard, M. Rinaudo, and C. Terrassin, "New method for the quaternization of chitosan," *International Journal of Biological Macromolecules*, vol. 8, no. 2, pp. 105–107, 1986.
- [130] A. F. Kotze, M. M. Thanou, H. L. Luessen, A. B. G. De Boer, J. C. Verhoef, and H. E. Junginger, "Effect of the degree of quaternization of N-trimethyl chitosan chloride on the permeability of intestinal epithelial cells (Caco-2)," *European Journal of Pharmaceutics and Biopharmaceutics*, vol. 47, no. 3, pp. 269–274, 1999.
- [131] S. Mangal, D. Pawar, N. K. Garg et al., "Pharmaceutical and immunological evaluation of mucoadhesive nanoparticles based delivery system(s) administered intranasally," *Vaccine*, vol. 29, no. 31, pp. 4953–4962, 2011.
- [132] O. Borges, G. Borchard, J. C. Verhoef, A. De Sousa, and H. E. Junginger, "Preparation of coated nanoparticles for a new mucosal vaccine delivery system," *International Journal of Pharmaceutics*, vol. 299, no. 1–2, pp. 155–166, 2005.
- [133] O. Borges, M. Silva, A. de Sousa, G. Borchard, H. E. Junginger, and A. Cordeiro-da-Silva, "Alginate coated chitosan nanoparticles are an effective subcutaneous adjuvant for hepatitis B surface antigen," *International Immunopharmacology*, vol. 8, no. 13–14, pp. 1773–1780, 2008.
- [134] O. Borges, J. Tavares, A. de Sousa, G. Borchard, H. E. Junginger, and A. Cordeiro-da-Silva, "Evaluation of the immune response following a short oral vaccination schedule with hepatitis B antigen encapsulated into alginate-coated chitosan nanoparticles," *European Journal of Pharmaceutical Sciences*, vol. 32, no. 4–5, pp. 278–290, 2007.
- [135] J. Ho, F. M. N. Al-Deen, A. Al-Abboodi et al., "N,N'-Carbonyldiimidazole-mediated functionalization of superparamagnetic nanoparticles as vaccine carrier," *Colloids and Surfaces B*, vol. 83, no. 1, pp. 83–90, 2011.
- [136] T. Fifi, A. Gamvrellis, B. Crimeen-Irwin et al., "Size-dependent immunogenicity: therapeutic and protective properties of nano-vaccines against tumors," *Journal of Immunology*, vol. 173, no. 5, pp. 3148–3154, 2004.
- [137] R. Song and C. V. Harding, "Roles of proteasomes, transporter for antigen presentation (TAP), and  $\beta$ 2-microglobulin in the processing of bacterial or particulate antigens via an alternate class I MHC processing pathway," *Journal of Immunology*, vol. 156, no. 11, pp. 4182–4190, 1996.
- [138] L. Vidard, M. Kovacs-Bankowski, S. K. Kraeft, L. B. Chen, B. Benacerraf, and K. L. Rock, "Analysis of MHC class II presentation of particulate antigens by B lymphocytes," *Journal of Immunology*, vol. 156, no. 8, pp. 2809–2818, 1996.
- [139] L. Zhang, G. Widera, S. Blecher, D. A. Zaharoff, B. Mossop, and D. Rabussay, "Accelerated immune response to DNA vaccines," *DNA and Cell Biology*, vol. 22, no. 12, pp. 815–822, 2003.
- [140] D. M. Mahvi, F. S. Shi, N. S. Yang et al., "Immunization by particle-mediated transfer of the granulocyte-macrophage colony-stimulating factor gene into autologous tumor cells in melanoma or sarcoma patients: report of a phase I/II study," *Human Gene Therapy*, vol. 13, no. 14, pp. 1711–1721, 2002.
- [141] S. Parween, P. K. Gupta, and V. S. Chauhan, "Induction of humoral immune response against PfMSP-119 and PvMSP-119 using gold nanoparticles along with alum," *Vaccine*, vol. 29, no. 13, pp. 2451–2460, 2011.
- [142] Y. J. Kwon, S. M. Standley, S. L. Goh, and J. M. J. Fréchet, "Enhanced antigen presentation and immunostimulation of dendritic cells using acid-degradable cationic nanoparticles," *Journal of Controlled Release*, vol. 105, no. 3, pp. 199–212, 2005.
- [143] Y. J. Kwon, E. James, N. Shastri, and J. M. J. Fréchet, "In vivo targeting of dendritic cells for activation of cellular immunity using vaccine carriers based on pH-responsive microparticles," *Proceedings of the National Academy of Sciences of the United States of America*, vol. 102, no. 51, pp. 18264–18268, 2005.

## Research Article

# Interaction between Pheromone and Its Receptor of the Fission Yeast *Schizosaccharomyces pombe* Examined by a Force Spectroscopy Study

Shintaro Sasuga,<sup>1</sup> Ryohei Abe,<sup>1</sup> Osamu Nikaido,<sup>1</sup> Shoichi Kiyosaki,<sup>1</sup> Hiroshi Sekiguchi,<sup>2</sup> Atsushi Ikai,<sup>3</sup> and Toshiya Osada<sup>1</sup>

<sup>1</sup> Department of Life Science, Graduate School of Bioscience and Biotechnology, Tokyo Institute of Technology, B-2 4259 Nagatsuta-cho, Midori-ku, Kanagawa, Yokohama 226-8501, Japan

<sup>2</sup> Department of Advanced Materials Science, Graduate School of Frontier Sciences, The University of Tokyo, #609 Kiban Bldg, 5-1-5 Kashiwanoha, Kashiwa City, Chiba 277-8561, Japan

<sup>3</sup> Innovation Laboratory, Tokyo Institute of Technology, 4259 Nagatsuta-cho, Midori-ku, Kanagawa, Yokohama 226-8501, Japan

Correspondence should be addressed to Toshiya Osada, [tosada@bio.titech.ac.jp](mailto:tosada@bio.titech.ac.jp)

Received 29 August 2011; Revised 22 November 2011; Accepted 26 November 2011

Academic Editor: Peng Xiong

Copyright © 2012 Shintaro Sasuga et al. This is an open access article distributed under the Creative Commons Attribution License, which permits unrestricted use, distribution, and reproduction in any medium, provided the original work is properly cited.

Interaction between P-factor, a peptide pheromone composed of 23 amino acid residues, and its pheromone receptor, Mam2, on the cell surface of the fission yeast *Schizosaccharomyces pombe* was examined by an atomic force microscope (AFM). An AFM tip was modified with P-factor derivatives to perform force curve measurements. The specific interaction force between P-factor and Mam2 was calculated to be around 120 pN at a probe speed of 1.74  $\mu\text{m/s}$ . When the AFM tip was modified with truncated P-factor derivative lacking C-terminal Leu, the specific interaction between the tip and the cell surface was not observed. These results were also confirmed with an assay system using a green fluorescent protein (GFP) reporter gene to monitor the activation level of signal transduction following the interaction of Mam2 with P-factor.

## 1. Introduction

The fission yeast *Schizosaccharomyces pombe* (*S. pombe*) has become a popular tool for analyzing heterologous GPCR due to the tractability of genetic and biochemical manipulation [1–4]. Most yeast systems for the studying of GPCR signaling use reporter constructs to provide readouts for transcription from signal-dependent promoters and are used for clinical and pharmaceutical studies, for example, a drug screening, due to similarities between the yeast mating response pathway and human GPCR signal transduction pathways [5]. The fission yeast has two haploid mating-cell types: P cells and M cells. Under nutrition depletion, the cells cease to divide with the cAMP cascade and conjugate with cells of the opposite mating type to form diploid zygotes. The conjugation between the two mating types is controlled by diffusible peptide pheromones, P-factor and M-factor.

Pheromones are defined as chemical substances that mediate communication between individuals of the same species. The perception of pheromones results in individual changes of physiological conditions and/or behaviors. Mating type-specific pheromones are secreted from cells and are sensed by cells of the opposite mating type [6, 7]. For example, P-factor released from P cells binds to its receptor, Mam2 on M cells, and stimulates M cells for mating. The two types of the fission yeast pheromone receptors belong to G protein-coupled receptors (GPCRs), the largest family of transmembrane receptors. The receptors with seven transmembrane domains are coupled with a heterotrimeric G protein complex and are responsible for transmitting extracellular signals to intracellular responses by stimuli of pheromones. The receptors undergo a conformational change from an inactive form to an active form upon pheromone binding. The active receptors induce  $G\alpha$  subunit Gpa1 to facilitate GDP to GTP

exchange and the dissociation of  $G\alpha$  from the G protein complex [8]. The  $G\alpha$  subunit with GTP then interacts with downstream effectors to engage signaling cascades including the MAP kinase pathway.

Since the invention of the atomic force microscope (AFM) by Binnig et al., it has become a powerful tool to study biological samples not only for imaging at the molecular level but also for measuring their mechanical properties [9–15]. As an AFM tip makes direct contact with the sample, the physical properties as well as the topography of the surface can be examined. For example, interaction force between single molecules can be measured under physiological conditions [16–21]. For these measurements, the AFM tip modified with specific ligands is used to scan over cell surface with its receptors. The tip makes contact with the cell surface allowing binding between ligand and receptor. The tip retraction then induces stretching of the complex molecules followed by forced dissociation of the complex. This technique has already permitted us to quantify unbinding forces of numerous ligand-receptor pairs, either on an artificial surface or on the surface of living cells.

In this study, we investigated the interaction between P-factor and Mam2 by both AFM and the reporter assay. Our study showed that P-factor had specific interaction with Mam2 and was able to induce the signal transduction pathway. The removal of Leu at C terminal of P-factor by carboxypeptidase Sxa2 was reported to result in an inactivation of P-factor function [22]. Our study showed that P-factor lacking C-terminal Leu had no ability to bind Mam2 or induce the signal transduction pathway.

## 2. Materials and Methods

**2.1. Peptides.** Peptides used in this study are listed in Table 1. The customized peptides were obtained from Operon Co. Ltd., (Tokyo, Japan). Each peptide was prepared as a stock solution of 1 mM in Milli-Q water and stored at  $-80^{\circ}\text{C}$ .

**2.2. An AFM Tip Preparation.** Coupling of peptides to AFM  $\text{Si}_3\text{N}_4$  tips (OMCL-TR400PSA, Olympus, Tokyo, Japan; nominal value 0.02 N/m) was done using a heterobifunctional polyethylene glycol (PEG) linker as shown in Figure 1(a) [23, 24]. The AFM tips were cleaned in a UV ozone cleaner (UV/Ozone ProCleaner, Bioforce Nano sciences Inc., IA, USA) under ultraviolet light and exposed for 2 h to APTES (3-aminopropyl triethoxysilane) vapors in a 2-liter desiccator filled with argon and containing 30  $\mu\text{L}$  of APTES and 10  $\mu\text{L}$  of N,N-diisopropylethylamine (Sigma-Aldrich, Tokyo, Japan). The tips were then kept for up to 3 days in an argon-filled atmosphere until use. Amino-group bearing tips were incubated for 60 min with 1 mg/mL of N-hydroxy-succinimide ester-PEG-maleimide (NHS-PEG-MAL, 3400 Da, Nektar Therapeutics, Huntsville, AL) in PBS (phosphate-buffered saline). They were then washed several times with PBS to remove unanchored linker molecules. The final binding step was achieved by a reaction between the linker maleimide end and cysteine residues of peptides. The tips were incubated with each peptide (final concentration of

TABLE 1: List of peptides used in this study.

P-factor	TYADFLRAYQSWNTFVNPDRPNL
C-P-factor	CTYADFLRAYQSWNTFVNPDRPNL
C-P-factor $\Delta\text{Leu}$	CTYADFLRAYQSWNTFVNPDRPN

1  $\mu\text{M}$ ) in PBS for 30 min and then were abundantly washed with PBS to remove unbound peptides.

**2.3. AFM Measurement.** Force measurements were carried out at room temperature with an NVB-100 AFM (Olympus, Inc., Tokyo, Japan) which was set on an inverted optical microscope (IX70, Olympus, Inc., Tokyo, Japan) [25–27]. The modified AFM tips were placed on the nitrogen starved cell surface, and force curve measurements were executed on different positions with a scan speed of around 1.74  $\mu\text{m/s}$  and using a relative trigger of 20–40 nm on the cantilever deflection (Figure 1(b)). The force curves from about 1024 positions ( $32 \times 32$ ) were recorded in each experimental condition to make a histogram of the rupture force in force curves. In the inhibition experiments, the force measurements were performed in an experimental buffer with free P-factor (final concentration of 1  $\mu\text{M}$ ). To calibrate the response of the cantilever deflection signal as a function of piezoelectrics, standard force curve measurements were carried out on a bottom of the dish, and the spring constant of the cantilever was calibrated by the thermal vibration method [28].

**2.4. Strains and Media.** Two *S. pombe* strains used in this study ( $\text{h}^- \text{sxa2} > \text{GFP pMAM3G/pAL7}$  and  $\text{h}^- \text{mam2::ura4}^+ \text{sxa2} > \text{GFP pMAM3G/pAL7}$ ) were derived from ARC010 ( $\text{h}^- \text{leu1-32 ura4-D18}$ ). The *S. pombe* cells were grown in YES (0.5% yeast extract, 3% glucose and SP Supplements), YES 10 (0.5% yeast extract, 3% glucose and SP Supplements, 10  $\mu\text{g/mL}$  G418 sulfate), EMM (Edinburgh Minimal Medium, Sunrise Science Product), or YCB (Yeast Carbon Base, Becton, Dickinson and Company, Franklin Lakes, NJ, USA). Transformants were plated onto MMA (Minimal Medium Agar, Sunrise Science Product) or MMA supplemented with 1.25% leucine (120  $\mu\text{L/plate}$ ). To select for the *ura4*<sup>−</sup> cells, transformants were plated onto the YES plates containing 0.1% 5-fluoroorotic acid (YES-FOA). *Escherichia coli* strain DH5 $\alpha$  was used for the subcloning of the plasmid preparation. Oligonucleotide synthesis was performed by Operon Co., Ltd.

**2.5. GFP Reporter Strain.** The *sxa2* genes were replaced with green fluorescent protein (GFP) by standard homologous recombination method. Briefly, the plasmid was constructed as follows. Three DNA fragments were separately amplified, which were then fused together. The first fragment, the target gene (including upstream, open reading frame, and downstream sequences), was amplified from an *S. pombe* genomic DNA using primers X1, 2 (*sxa2*) introducing NotI restriction site. The *sxa2* fragment was ligated into the multicloning site of pTA2 vector (TOYOBO Co., Ltd., Osaka, Japan).



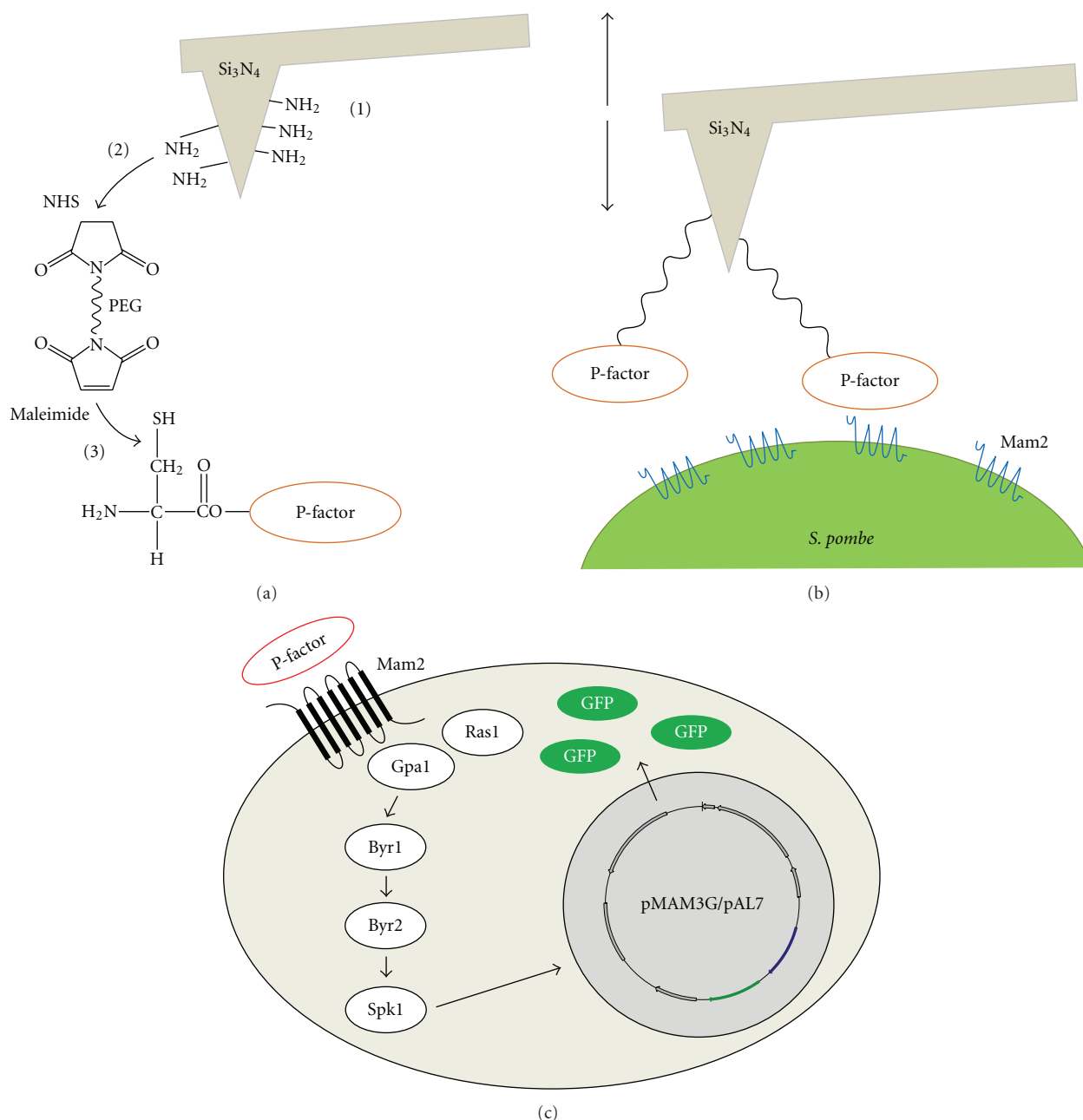


FIGURE 1: Schematic overview of experiments. (a) AFM tip modification with peptides. Si<sub>3</sub>N<sub>4</sub> AFM tips are aminosilanized by exposure to APTES vapors. A heterobifunctional PEG linker is anchored to amino-group bearing tips through its NHS end. Peptide is attached to the PEG linker free end via a maleimide-cysteine bond. (b) Force spectroscopy method. Peptide-modified AFM tips approached the cell surface on a 200 nm z-scan size at a speed of 1.74  $\mu\text{m/s}$  and were retracted at the same speed. (c) The reporter assay. Pheromone binding to its receptors on the cell surface activates the intracellular signaling pathway that leads to the expression of GFP. The released Gpa1 (Galpha) with GTP from a heterotrimeric G protein activates the MAP kinase cascade of Byr2 (MAP3K), Byr1 (MAP2K), and Spk1 (MAPK). Activation of Byr2 also requires Ras1.

Inverse PCR was performed using primers X3, 4 (*sxa2*). The second fragment: GFP-coding sequence was amplified from a Monster Green Fluorescent Protein pHMGFP Vector (Promega, Madison, WI, USA) using primers G1, 2. The third fragment: *ura4* gene and 200 bp downstream of the target gene were amplified from an *S. pombe* genomic DNA using primers U1, 2 and X1, 2 (*sxa2*) introducing XbaI

restriction site. After the fragments were digested by XbaI, they were ligated and performed PCR using primers X5, U2 (*sxa2*). Then three fragments were simultaneously ligated with In-Fusion Advantage PCR Cloning Kit (Clontech, Palo Alto, CA, USA), resulting in replacing GFP vector. The resulting plasmid sequences were confirmed by sequence analysis. The resulting plasmid was treated with NotI, and



TABLE 2: List of primers used in this study.

X1	GCGGCCGC AGCTGTGTTTGTTCGAATG
X2	GCGGCCGC GGAAGTTAGGCTTGTGTGC
X3	TCAATATCACAAGCT AAGTTTAATATCGGAAAATTTAA
X4	CTTGATCACGCCCAT TGAAGAGAGACAATGA
X5	CGCCAGGCCGGCTAA AAGTTTAATATCGGAAAATTTAA
X6	AAATCTAGA ATTTCTTATTTGGGAACGA
G1	ATGGGCGTGATCAAGCCCGAC
G2	TTAGCCGGCCTGGCGGGG
U1	AAATCTAGA TCTATCTTCTTAATCGCATGGAAG
U2	AGCTTGTGATATTGACGAACTTT
M31	AAAGAATTCTTTTAGAAAGTGTCTATTGTACC
M32	AAAGGTCTCTCATGACGAATTATGGGAAGATCAAG
G3	AAAGGCTCTACATGGGCGTGATCAAGCCC
G4	AAATCTAGATTAGCCGGCCTGGCGGGGTAGT
V1	AAAGAATTCGAGCTCGGTACCC
V2	AAAGAATTCGAACTAATGACCCCGTAATTGA
MU1	AAAGGTCTCTGGCCGCATCGGGATTGCATTGAGAGTT
MU2	AAA GGTCTCAAATGTCAGAGGGAGCAAGAACA
MD1	AAA GGTCTCACTTACGCCTGAATGTATCTTTTTTG
MD2	AAAGGTCTCAGGCCGCTCAAAGCCATAACTGTGCATTTATA
UR1	AAACACCTGCTTGTTCATTTCTATCTTCTTAATCGCATGGAAG
UR2	AAACACCTGCTTGTTAAGAGCTTGTGATATTGACGAACTTT

subsequently used to transform *S. pombe* strain using a lithium acetate method. Transformed cells were plated onto MMA plates supplemented with leucine. The plates were incubated at 32°C, and, after 2-3 days, positive colonies were selected. To check for correct integration, PCR was performed on a genomic DNA. Then correctly transformed cells were plated onto YES-FOA plates to remove the *ura4* marker. After 2 days, positive colonies were selected and checked by PCR. Thereafter, the resultant transformants were performed on additional gene replacement. Next, we introduced an additional reporter to make the cells more susceptible to P-factor. The second reporter system expressed GFP under the control of *mam3* gene, which was expressed depending on pheromone P-factor. The plasmid was constructed as follows. Three fragments named *mam3P*, and GFP and pTL2M5-P were amplified by PCR using KOD-plus-Neo. The fragment *mam3P* including *mam3* upstream region from -1,047 to -1 was amplified from an *S. pombe* genomic DNA using M31 and M32 primers, each introducing EcoRI and BsaI restriction site. The fragment GFP was GFP-coding sequence from pHMGFP Vector using G3 and G4 primers introducing BsaI and XbaI restriction site. The fragment pTL2M5-P containing no hCMV promoter region was amplified from pTL2M5 (Asahi Glass Co., Ltd., Japan) using V1 and V2 primers introducing EcoRI and XbaI restriction site. Then, three fragments were treated with proper restriction enzymes and simultaneously ligated with Ligation-Convenience Kit (Nippon Gene, Japan). The plasmid was named pMAM3G. The sequence of pMAM3G was confirmed by sequence analysis. The pMAM3G was

transformed into *sxa2::GFP* strain with pAL7 vector following the above method. Colonies were selected by YES10 medium containing 10 µg/mL of G418 three times. All DNA fragments used for the plasmid construction were amplified by PCR using the KOD-plus-Neo (TOYOBO) in accordance with the supplier's instructions. All primers used here are listed in Table 2.

**2.6. Construction of Mam2Δ Strain.** The *mam2* open reading frame was replaced with 1.8 kb *ura4<sup>+</sup>* fragment by standard homologous recombination method. Plasmid was constructed as follows. Three fragments named *mam2up*, and *mam2dw* and 1.8 kb *ura4<sup>+</sup>* were amplified by PCR from the *S. pombe* genomic DNA. The fragment *mam2up* including *mam2* upstream position -1,067 to -1 relative to *mam2* ATG was amplified using MU1 and MU2 primers introducing BsaI restriction site. The fragment *mam2dw* including *mam2* downstream position +1,048 to +2,055 relative to *mam2* ATG was amplified using MD1 and MD2 primers introducing BsaI restriction site. The fragment 1.8 kb *ura4<sup>+</sup>* position -643 to +1,230 relative to *mam2* ATG was amplified using UR1 and UR2 primers introducing AarI restriction site. Three fragments were digested with BsaI or AarI. Then, we prepared the fragment containing pUC ori. and Km<sup>R</sup> gene of pSL6Z digested with NotI. Four fragments were ligated simultaneously with Ligation-Convenience Kit. The sequence of the plasmid was confirmed by sequence analysis. The plasmid was treated with NotI and subsequently used to transform *S. pombe* strain using the lithium acetate method.

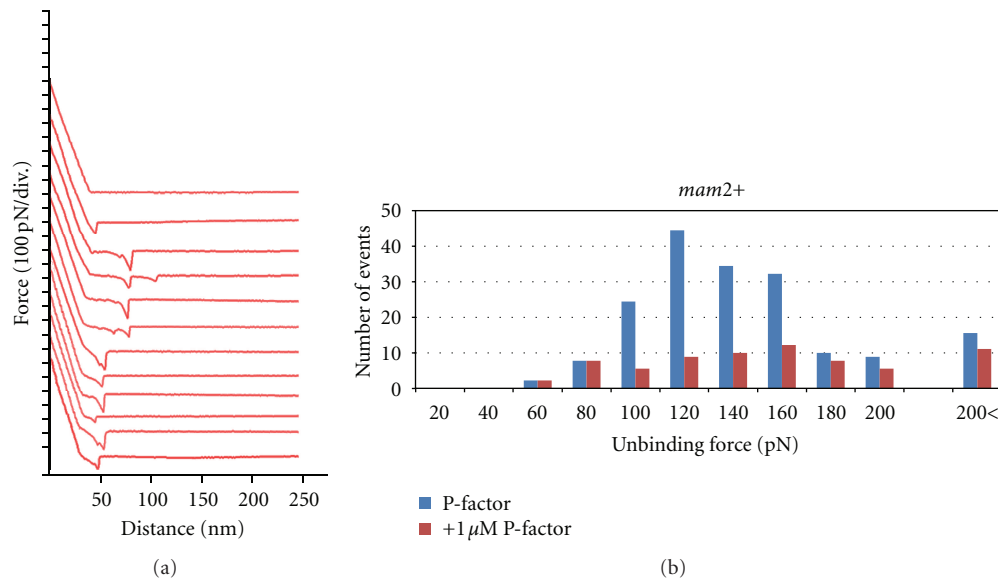


FIGURE 2: (a) Typical retraction force curves between P-factor and the cells. Vertical axis indicates cantilever deflections as a function of the cantilever-sample retraction distance. The first curve from the top shows no interaction, and the other curves display specific unbinding events between peptide and the cell. The vertical force jump of events allows access to the specific unbinding force. (b) Force histogram of unbinding events (blue columns) obtained after analysis of 1024 force curves. The mean unbinding force is 120 pN, for a mean loading rate of 1.74  $\mu\text{m/s}$ . In the presence of free 1  $\mu\text{M}$  P-factor, the number of unbinding events decreased (red columns).

Transformants were plated onto MMA plates supplemented with leucine. The plates were incubated at 32°C, and, after 3 days, positive colonies were selected. To check for correct integration, PCR was performed on the genomic DNA of transformants.

**2.7. GFP Assay for Mam2 Signaling.** Reporter strains were grown in YES10 media at 32°C for 24–36 h and were inoculated into 5 mL of the fresh YES10 media. Then the cells were grown at 30°C for 18 h and harvested. After having been washed twice with sterile water, cells were transferred to YCB media at OD<sub>600</sub> of 1.0 for nitrogen starvation. The cells were incubated at 30°C for 2 h and used for AFM study and Mam2 signaling assay. For the signaling assay (Figure 1(c)), 1 mL aliquots of cells were transferred to 24-well microplate containing 1  $\mu\text{L}$  of peptide solution (final concentration of 1  $\mu\text{M}$ ). After incubation at 30°C for 20 h, the cells were washed three times with PBS and resuspended in the same volume of PBS. Fluorescence intensity of GFP was measured by a fluorescence spectrophotometer (Hitachi F-3010, Japan). The cells expressing GFP were excited at 491 nm, and fluorescence emission was detected at 515 nm.

### 3. Results and Discussion

A force-volume mode of AFM was carried out to examine specific interactions between pheromone and pheromone receptor. Using the AFM tip cross-linked with P-factor derivatives via a heterobifunctional PEG linker, 1024 AFM force curves were then obtained over different spots

on *mam2+* strain cells expressing pheromone receptors. Although most of retraction curves (around 90%) showed no interaction (Figure 2(a), upper curve), some retraction curves presented a downward deflection abruptly ending with a force jump (Figure 2(a), others). Since the PEG linker used to attach the peptide to the AFM tip has a total length of 30 nm, only events occurring after 30 nm extension were considered valid interaction events and were included into further analyses. The distribution of unbinding force is shown in Figure 2(b). To verify the specificity of the unbinding force, force curves were also obtained in the presence of 1  $\mu\text{M}$ -free P-factor where specific interaction was expected to be inhibited. Ranging from 100 to 160 pN, 122 interaction peaks (11.9%) were detected without free P-factor while 33 unbinding events (3.2%) were detected with free P-factor. The number of events clearly decreased and the unbinding probability fell to 3.2 from 11.9%. Next, we carried out force curve measurements to examine interaction force between the AFM tip modified with P-factor and *mam2Δ* strain cells expressing no pheromone receptors, and between the AFM tip modified with P-factor $\Delta\text{Leu}$  and *mam2+* strain cells. When *mam2Δ* strain cells were used for force curve measurements with P-factor-modified tips, the unbinding probabilities were not affected with or without free P-factor, showing 2.7% without free P-factor and 2.9% with free P-factor (Figure 3(a)). When the AFM tip was modified with truncated P-factor derivative lacking C-terminal Leu, which was reported to have no P-factor function, the specific interaction was not observed, and the unbinding probabilities were almost the same with (3.5%) or without (3.1%) free P-factor (Figure 3(b)). From these three kinds of force curve measurements, the unbinding forces

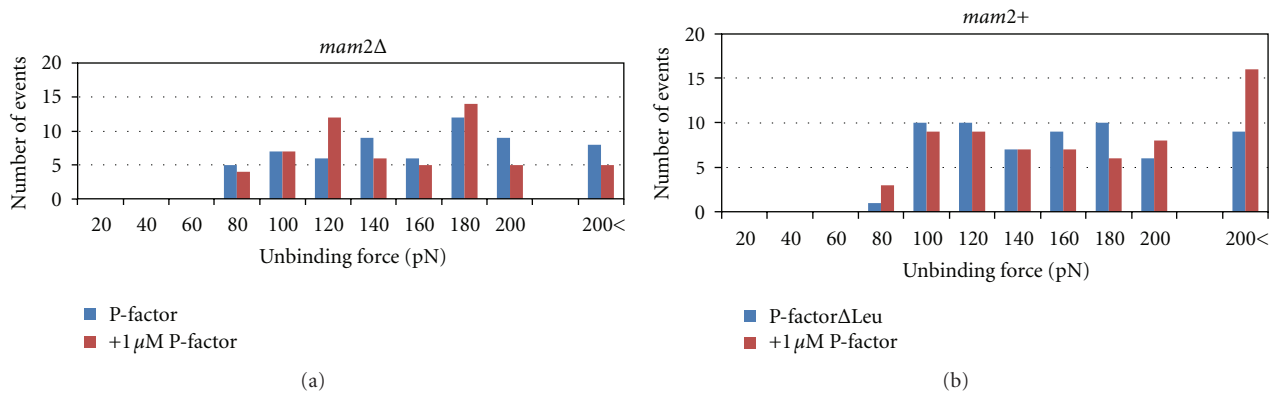


FIGURE 3: Force histogram of unbinding events with (red columns) or without (blue columns) free 1  $\mu$ M P-factor. (a) Unbinding events between AFM tip modified with P-factor and *mam2Δ* strain cells. (b) Unbinding events between AFM tip modified with P-factor $\Delta$ Leu and *mam2+* strain cells.

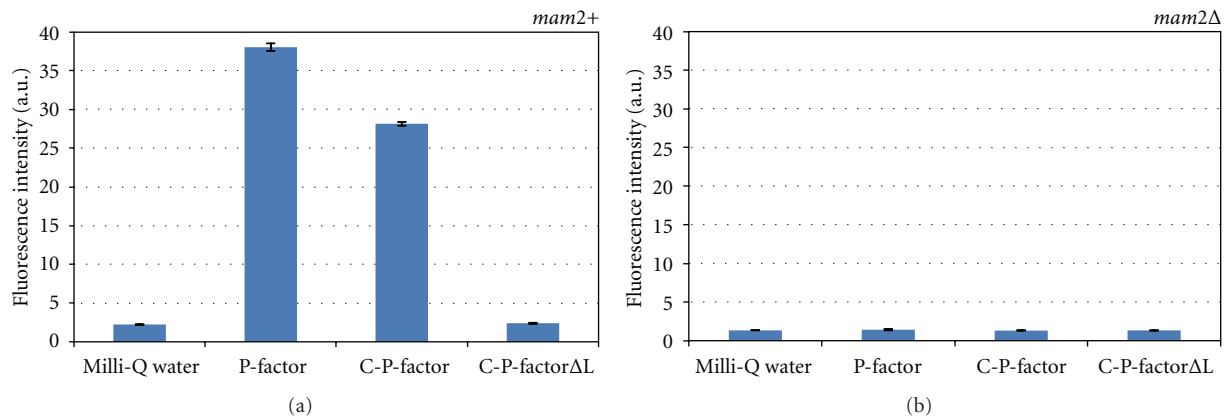


FIGURE 4: GFP production of *mam2+* strain cell (a) and *mam2Δ* strain cell (b). Under nutrition depletion, each cell was treated with Milli-Q water (control), 1  $\mu$ M of P-factor, C-P-factor, or P-factor $\Delta$ Leu. Values are means with SD of triplicate samples.

observed in the first force curve measurement were supposed to be caused by the specific interaction between P-factor and its receptor.

To examine the interaction of Mam2 with P-factor derivatives with a method other than AFM, we carried out Mam2-signaling assay. Binding of P-factor to Mam2 on the cell surface activates the intracellular signaling pathway that leads to the expression of the genes necessary to bring about cell fusion. Replacing the response genes with a reporter construct, such as GFP, provides a simple readout for signaling. The interaction of Mam2 and P-factor was investigated in an *S. pombe* strain containing *sxa2* > GFP pMAM3G/pAL7 reporter constructs. The expression of GFP in response to P-factor is monitored with a fluorescence spectrophotometer (Figure 4). When 1  $\mu$ M P-factor was added to the *mam2+* strain cells, fluorescence intensity of the cells at 515 nm increased, which indicated that GFP was produced in the response of the cells to P-factor (Figure 4(a)). The addition of cysteine at N-terminal of P-factor slightly affect its ability to induce the signal transduction pathway. Since the *mam2+* strain cells showed no response against 1  $\mu$ M C-P-factor $\Delta$ Leu, this peptide was not able to induce the

signal transduction pathway. The *mam2Δ* strain cells (*sxa2* > GFP pMAM3G/pAL7,  $\Delta$ mam2) showed no response with the addition of any peptides including P-factor (Figure 4(b)). Without Mam2, P-factor was not able to induce the signal transduction pathway. The reporter assay confirmed the result of AFM study. The specific interaction was only observed by AFM study under the condition in which the reporter assay showed the positive result.

## 4. Conclusions

We examined here the interaction between P-factor and Mam2 by both AFM and the reporter assay. The unbinding force was calculated to be around 120 pN at probe speed of 1.74  $\mu$ m/s. The reporter assay using a fluorescent reporter gene showed results similar to AFM studies. P-factor derivative having no specific interaction to Mam2 by AFM did not activate Mam2-specific signaling pathway. This yeast-based method combined AFM, and the reporter assay will be available for the signaling study of heterologous GPCRs and screening of their ligands.

## Acknowledgments

The authors thank Drs Giga-Hama Y and Tohda H for the *S. pombe* strain. This work was supported by a Grant-in-Aid for creative scientific research (no. 19GS0418) from the Japan Society for the Promotion of Science (JSPS) to A. Ikai.

## References

- [1] J. Kurjan, "The pheromone response pathway in *Saccharomyces cerevisiae*," *Annual Review of Genetics*, vol. 27, pp. 147–179, 1993.
- [2] J. Davey, "Fusion of a fission yeast," *Yeast*, vol. 14, no. 16, pp. 1529–1566, 1998.
- [3] S. J. Dowell and A. J. Brown, "Yeast assays for G-protein-coupled receptors," *Receptors and Channels*, vol. 552, no. 5-6, pp. 343–352, 2002.
- [4] G. Ladds, A. Goddard, and J. Davey, "Functional analysis of heterologous GPCR signalling pathways in yeast," *Trends in Biotechnology*, vol. 23, no. 7, pp. 367–373, 2005.
- [5] L. Silverman, R. Campbell, and J. R. Broach, "New assay technologies for high-throughput screening," *Current Opinion in Chemical Biology*, vol. 2, no. 3, pp. 397–403, 1998.
- [6] Y. Fukui, Y. Kaziro, and M. Yamamoto, "Mating pheromone-like diffusible factor released by *Schizosaccharomyces pombe*," *EMBO Journal*, vol. 5, no. 8, pp. 1991–1993, 1986.
- [7] U. Leupold, "Sex appeal in fission yeast," *Current Genetics*, vol. 12, no. 7, pp. 543–545, 1987.
- [8] M. Whiteway, L. Hougan, D. Dignard et al., "The STE4 and STE18 genes of yeast encode potential  $\beta$  and  $\gamma$  subunits of the mating factor receptor-coupled G protein," *Cell*, vol. 56, no. 3, pp. 467–477, 1989.
- [9] M. Radmacher, M. Fritz, J. P. Cleveland, D. A. Walters, and P. K. Hansma, "Imaging adhesion forces and elasticity of lysozyme adsorbed on mica with the atomic force microscope," *Langmuir*, vol. 10, no. 10, pp. 3809–3814, 1994.
- [10] K. Mitsui, M. Hara, and A. Ikai, "Mechanical unfolding of  $\alpha$ 2-macroglobulin molecules with atomic force microscope," *FEBS Letters*, vol. 385, no. 1-2, pp. 29–33, 1996.
- [11] M. Rief, M. Gautel, F. Oesterhelt, J. M. Fernandez, and H. E. Gaub, "Reversible unfolding of individual titin immunoglobulin domains by AFM," *Science*, vol. 276, no. 5315, pp. 1109–1112, 1997.
- [12] A. Kis, S. Kasas, B. Babić et al., "Nanomechanics of microtubules," *Physical Review Letters*, vol. 89, no. 24, Article ID 248101, 4 pages, 2002.
- [13] R. Afrin, M. T. Alam, and A. Ikai, "Pretransition and progressive softening of bovine carbonic anhydrase II as probed by single molecule atomic force microscopy," *Protein Science*, vol. 14, no. 6, pp. 1447–1457, 2005.
- [14] J. P. Michel, I. L. Ivanovska, M. M. Gibbons et al., "Nanoindentation studies of full and empty viral capsids and the effects of capsid protein mutations on elasticity and strength," *Proceedings of the National Academy of Sciences of the United States of America*, vol. 103, no. 16, pp. 6184–6189, 2006.
- [15] G. Lee, K. Abdi, Y. Jiang, P. Michaely, V. Bennett, and P. E. Marszalek, "Nanospring behaviour of ankyrin repeats," *Nature*, vol. 440, no. 7081, pp. 246–249, 2006.
- [16] E. L. Florin, V. T. Moy, and H. E. Gaub, "Adhesion forces between individual ligand-receptor pairs," *Science*, vol. 264, no. 5157, pp. 415–417, 1994.
- [17] V. T. Moy, E. L. Florin, and H. E. Gaub, "Intermolecular forces and energies between ligands and receptors," *Science*, vol. 266, no. 5183, pp. 257–259, 1994.
- [18] P. Hinterdorfer, W. Baumgartner, H. J. Gruber, K. Schilcher, and H. Schindler, "Detection and localization of individual antibody-antigen recognition events by atomic force microscopy," *Proceedings of the National Academy of Sciences of the United States of America*, vol. 93, no. 8, pp. 3477–3481, 1996.
- [19] M. Gad, A. Itoh, and A. Ikai, "Mapping cell wall polysaccharides of living microbial cells using atomic force microscopy," *Cell Biology International*, vol. 21, no. 11, pp. 697–706, 1997.
- [20] R. Merkel, P. Nassoy, A. Leung, K. Ritchie, and E. Evans, "Energy landscapes of receptor-ligand bonds explored with dynamic force spectroscopy," *Nature*, vol. 397, no. 6714, pp. 50–53, 1999.
- [21] H. Sekiguchi, H. Arakawa, H. Taguchi, T. Ito, R. Kokawa, and A. Ikai, "Specific interaction between GroEL and denatured protein measured by compression-free force spectroscopy," *Biophysical Journal*, vol. 85, no. 1, pp. 484–490, 2003.
- [22] G. Ladds, E. M. Rasmussen, T. Young, O. Nielsen, and J. Davey, "The *sxa2*-dependent inactivation of the P-factor mating pheromone in the fission yeast *Schizosaccharomyces pombe*," *Molecular Microbiology*, vol. 20, no. 1, pp. 35–42, 1996.
- [23] C. Lesoil, T. Nonaka, H. Sekiguchi et al., "Molecular shape and binding force of Mycoplasma mobile's leg protein Gli349 revealed by an AFM study," *Biochemical and Biophysical Research Communications*, vol. 391, no. 3, pp. 1312–1317, 2010.
- [24] A. Yersin, T. Osada, and A. Ikai, "Exploring transferrin-receptor interactions at the single-molecule level," *Biophysical Journal*, vol. 94, no. 1, pp. 230–240, 2008.
- [25] H. Kim, F. Asgari, M. Kato-Negishi et al., "Distribution of olfactory marker protein on a tissue section of vomeronasal organ measured by AFM," *Colloids and Surfaces B: Biointerfaces*, vol. 61, no. 2, pp. 311–314, 2008.
- [26] H. Kim, H. Uehara, R. Afrin et al., "Application of the atomic force microscopy to the study of expressed molecules in or on a single living cell," in *Applied Scanning Probe Methods IX: Characterization*, B. Bhushan and H. Fuchs, Eds., NanoScience and Technology, pp. 149–175, Springer, Berlin, Germany, 2008.
- [27] H. Kim, H. Arakawa, N. Hatae et al., "Quantification of the number of EP3 receptors on a living CHO cell surface by the AFM," *Ultramicroscopy*, vol. 106, no. 8-9, pp. 652–662, 2006.
- [28] J. L. Hutter and J. Bechhoefer, "Calibration of atomic-force microscope tips," *Review of Scientific Instruments*, vol. 64, no. 7, pp. 1868–1873, 1993.

## Research Article

# Micromechanical Thermal Assays of $\text{Ca}^{2+}$ -Regulated Thin-Filament Function and Modulation by Hypertrophic Cardiomyopathy Mutants of Human Cardiac Troponin

Nicolas M. Brunet,<sup>1,2,3</sup> Goran Mihajlović,<sup>4,5</sup> Khaled Aledealat,<sup>4,6</sup> Fang Wang,<sup>1,7</sup> Peng Xiong,<sup>4,8</sup> Stephan von Molnár,<sup>4,8</sup> and P. Bryant Chase<sup>1,8</sup>

<sup>1</sup> Department of Biological Science, The Florida State University, P.O. Box 3064295, Tallahassee, FL 32306, USA

<sup>2</sup> Institute of Molecular Biophysics, The Florida State University, Tallahassee, FL 32306, USA

<sup>3</sup> Donders Institute for Brain, Cognition and Behavior, Centre for Cognitive Neuroimaging, Radboud University Nijmegen, 6500 HB Nijmegen, The Netherlands

<sup>4</sup> Department of Physics, The Florida State University, Tallahassee, FL 32306, USA

<sup>5</sup> San Jose Research Center, Hitachi Global Storage Technologies, San Jose, CA 95135, USA

<sup>6</sup> Department of Physics, Jordan University of Science and Technology, Irbid 22110, Jordan

<sup>7</sup> Department of Neurobiology, College of Basic Medical Science, Southern Medical University, Guangzhou 510515, China

<sup>8</sup> Integrative NanoScience Institute (INSI), The Florida State University, Tallahassee, FL 32306, USA

Correspondence should be addressed to P. Bryant Chase, chase@bio.fsu.edu

Received 2 August 2011; Accepted 2 November 2011

Academic Editor: Seunghun Hong

Copyright © 2012 Nicolas M. Brunet et al. This is an open access article distributed under the Creative Commons Attribution License, which permits unrestricted use, distribution, and reproduction in any medium, provided the original work is properly cited.

Microfabricated thermoelectric controllers can be employed to investigate mechanisms underlying myosin-driven sliding of  $\text{Ca}^{2+}$ -regulated actin and disease-associated mutations in myofilament proteins. Specifically, we examined actin filament sliding—with or without human cardiac troponin (Tn) and  $\alpha$ -tropomyosin (Tm)—propelled by rabbit skeletal heavy meromyosin, when temperature was varied continuously over a wide range ( $\sim 20$ – $63^\circ\text{C}$ ). At the upper end of this temperature range, reversible dysregulation of thin filaments occurred at pCa 9 and 5; actomyosin function was unaffected. Tn-Tm enhanced sliding speed at pCa 5 and increased a transition temperature ( $T_i$ ) between a high activation energy ( $E_a$ ) but low temperature regime and a low  $E_a$  but high temperature regime. This was modulated by factors that alter cross-bridge number and kinetics. Three familial hypertrophic cardiomyopathy (FHC) mutations, cTnI R145G, cTnI K206Q, and cTnT R278C, cause dysregulation at temperatures  $\sim 5$ – $8^\circ\text{C}$  lower; the latter two increased speed at pCa 5 at all temperatures.

## 1. Introduction

Biomolecular motors have clear promise for transport applications in micro- and nanofabricated devices although control of motion remains a major challenge [1–4]. Toward that end, we constructed a microfabricated thermoelectric controller for rapid and reversible actuation using myosin, the biomolecular motor of muscle, and its partner filament, actin [5, 6]. Thermal control of kinesin-microtubule motility using thermally responsive polymers has also been demonstrated as a possible temperature-dependent control mechanism for biomolecular motors [7]. We present here novel applications of our thermoelectric control system to

investigate changes in actin-myosin motility when  $\text{Ca}^{2+}$ -regulated thin (actin) filaments are used, and when thin-filament  $\text{Ca}^{2+}$ -regulatory protein mutations are introduced that underlie an inherited cardiovascular disease, familial hypertrophic cardiomyopathy (FHC) [8–10]. Results provide insights into mechanisms of altered function when thin filaments are reconstituted with human cardiac  $\text{Ca}^{2+}$ -regulatory proteins troponin (Tn) and tropomyosin (Tm), and further modulated by FHC-related mutations in cardiac Tn.

In the heart—and in vertebrate striated muscles in general—contraction is physiologically controlled by binding of cytoplasmic  $\text{Ca}^{2+}$  to thin filaments. Thin filaments are comprised of three major proteins: actin, Tm, and Tn that



is itself a complex of three polypeptides [11].  $\text{Ca}^{2+}$  activates thin filaments by binding to Tn, leading to structural changes that ultimately expose myosin-binding sites on actin subunits [11]. Our previous work on the thermoelectric controller utilized only myosin and unregulated F-actin, that is,  $\text{Ca}^{2+}$ -independent motility achieved using actin filaments without Tn or Tm [5, 6]. This study was initiated because  $\text{Ca}^{2+}$ -regulated thin filaments could have several advantages over unregulated F-actin in a thermoelectric nanoactuator. First,  $\text{Ca}^{2+}$  would provide a secondary control mechanism that is separate from temperature. An additional benefit is that the  $\text{Ca}^{2+}$ -regulatory proteins Tn and Tm at saturating  $\text{Ca}^{2+}$  can enhance function of the actomyosin system [12–20]. These effects of Tn and Tm on actomyosin function, however, appear to vary markedly over the limited temperature ranges studied previously [16, 18, 21] and thus could introduce nonlinearities to a thermoelectric nano-actuator.

Temperature has obvious physiological relevance as a determinant of mammalian striated muscle contraction. It affects several fundamental aspects of muscle structure and function [22–24] although temperature effects on muscle function appear to be greater at low temperatures used in many experiments than at physiological temperature; examples are isometric tetanic tension [25–27] and maximum mechanical power output [28]. Temperature also modulates the control of striated muscle contraction by  $\text{Ca}^{2+}$  regulatory proteins Tn and Tm, although there are both qualitative and quantitative discrepancies on this point in the striated muscle literature [22, 26, 29, 30]. Interestingly, mild hypothermia has been reported to be a positive inotropic effector in living cardiac muscle due to interplay between temperature and cardiac thin filament  $\text{Ca}^{2+}$  regulation [31]. Our thermoelectric controller allows us to address these issues and more in a single experiment through rapid exploration of broad temperature regimes surrounding physiological temperature.

Some mutations in Tn and Tm alter thin-filament function in ways that might make the mutant proteins useful in biomolecular motor-based transport applications. In particular, mutations associated with familial hypertrophic cardiomyopathy (FHC)—one of a growing number of diseases caused by mutations in the genes for sarcomere proteins including thin-filament  $\text{Ca}^{2+}$ -regulatory proteins [8–10]—may be especially useful in bionanomechanical systems even though those mutations are devastating for patients [32–41]. The molecular basis by which these mutations alter thin-filament function and bring about cardiovascular disease is unknown [8, 10, 42]. Our thermoelectric controller could provide important insight into mechanisms by which these mutations in myofilament proteins alter contractile function, and directly or indirectly signal changes in gene expression that underlie the progression to pathological cardiac hypertrophy in FHC.

## 2. Materials and Methods

**2.1. Protein Preparations: Myosin, Heavy Meromyosin, Actin, Troponin, and Tropomyosin.** Florida State University's Institutional Animal Care and Use Committee approved all

procedures and protocols involving vertebrate animals. Adult New Zealand White rabbits were housed in Florida State University's Laboratory Animal Resources facility and were handled in accordance with the current National Institutes of Health/National Research Council Guide for the Care and Use of Laboratory Animals. Briefly, rabbits were injected IM with 3 mg Acepromazine + 10 mg/kg Xylazine + 50 mg/kg Ketamine. Following verification of appropriate surgical depth of anesthesia, the rabbits were exsanguinated via laceration of the carotid artery. The euthanized animals were skinned, eviscerated, and chilled on ice. Back and leg muscles were removed for acetone powder, or back muscles only for myosin preparation [12, 13, 43]. Myosin and the soluble chymotryptic digest fragment heavy meromyosin (HMM) were prepared from fast skeletal muscle as described [12, 13, 43, 44]. HMM was made from myosin stored <5 weeks in glycerol (1:1) at  $-20^{\circ}\text{C}$ ; HMM was used within 3 days after preparation. Rabbit muscle actin was purified from muscle acetone powder as described [12, 13, 43, 45]. F-actin was labeled with rhodamine phalloidin (RhPh; Molecular Probes) for fluorescence microscopy (Figure 1(a)). F-actin ( $33\text{ }\mu\text{g/mL}$ ) and RhPh ( $1\text{ }\mu\text{M}$ ) were incubated in actin buffer (AB) with 1 mM DTT at  $4^{\circ}\text{C}$  overnight; fluorescently labeled F-actin was stable at  $4^{\circ}\text{C}$  for at least 2 weeks.

Recombinant human  $\alpha$ -Tm was expressed in *E. coli* as a homodimeric fusion protein with maltose binding protein (MBP);  $\alpha$ -Tm was purified following removal of the MBP affinity tag via thrombin cleavage [13, 33]. After removal of the MBP tag, recombinant  $\alpha$ -Tm has two extra amino acids (GS-) at the N-terminus; GS- is a conservative alternative to the AS-dipeptide in bacterially expressed Tm that substitutes functionally for acetylation of Tm's N-terminus [46, 47]. Purified Tn from human cardiac muscle (cTn) was obtained from Research Diagnostics (Flanders, NJ), or coexpressed recombinantly (rHcTn) in *E. coli* as a fusion protein with glutathione S-transferase (GST); the ternary rHcTn complex was purified following removal of the GST affinity tag via cleavage with TEV protease [13]. FHC mutations of rHcTn were introduced via site-directed mutagenesis to the bacterial coexpression plasmid; changes were verified by DNA sequencing. Proteins were assessed by coomassie-stained Tricine-SDS PAGE [48] and quantitative analysis with a Kodak EDAS 290 digital imaging system.

**2.2. In Vitro Motility Assays.** The speed of RhPh F-actin over HMM-coated surfaces was measured to assess the kinetics of actomyosin interactions and, for reconstituted thin filaments, their regulation by  $\text{Ca}^{2+}$ . All aspects of the motility experiments with unregulated F-actin, such as flow cell assembly, solution preparation, assay procedures, and data collection were conducted as described [5, 13, 43, 49]. [HMM] applied to flow cells was  $250\text{ }\mu\text{g mL}^{-1}$  in the majority of assays to achieve high density of HMM ( $\rho$ ) on the nitrocellulose-coated motility surface; to reduce  $\rho$  in a limited set of experiments,  $75\text{ }\mu\text{g mL}^{-1}$  HMM was applied to the flow cell.

The standard motility buffer (MB) contained 10 mM ethylene glycol-bis(2-aminoethylether)-N,N,N',N'-tetraacetic

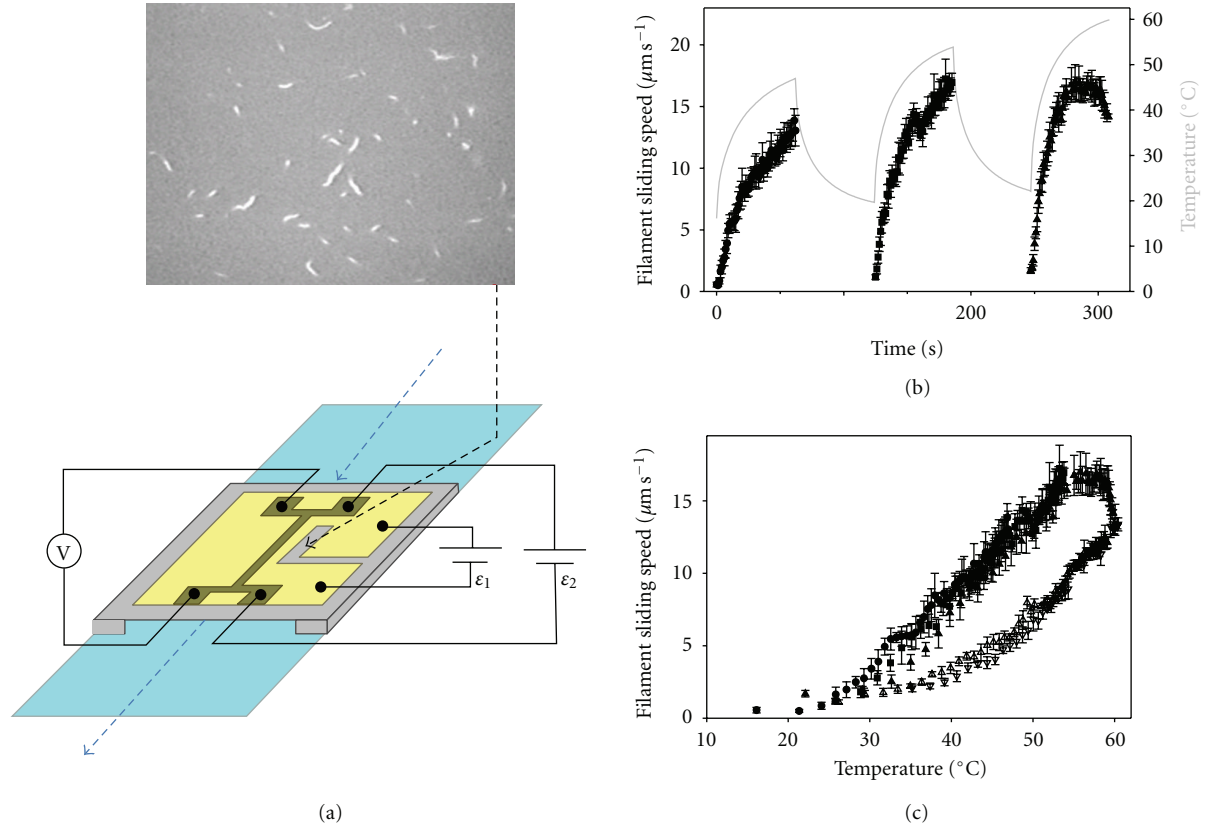


FIGURE 1: Temperature dependence of HMM-driven sliding of RhPh-labeled actin filaments determined using a microfabricated thermoelectric heater. (a) Modified flow cells were constructed as described [5]. Flow cells consisted of a microscope slide (light blue) and a modified cover slip (gray and gold), separated by two, thin spacers and held together by nonfluorescent vacuum grease. Solutions (Section 2.2) are pipetted through the flow cell as indicated by the blue, dashed arrows. To warm the flow cell, current is injected via circuit  $\varepsilon_1$  into a microfabricated thermoelectric heater (gold) on the coverslip's outer surface; flow cells are cooled by circulating chilled water through a copper coil wrapped around the microscope objective. Temperature is monitored via a linear, resistive thermometer (dark gold structure) that was microfabricated on the inner face of the coverslip (i.e., on the same side where actomyosin motility occurred, and opposite to the side with the thermoelectric heater); temperature is obtained from a calibrated voltage readout (V) with bias current set by circuit  $\varepsilon_2$ . Motion of fluorescently labeled filaments on the inner side of the coverslip (top micrograph) is observed and recorded through a window (black, dashed arrow) located immediately adjacent to the thermometer. (b) Time course of temperature (gray line; right ordinate) and sliding speed (solid symbols; left ordinate) for regulated thin filaments (F-actin plus native cTn and  $\alpha$ -Tm) at pCa 5 during the heating phase of three cycles of heating and cooling (Section 2). Points represent mean  $\pm$  S.D. of the sliding speed for 3–8 filaments during 1 s. Note that the upper limit of the temperature-dependent increase in sliding speed occurs at  $\sim 54^\circ\text{C}$  ( $t > 4.5$  min). (c) The data from (b) were replotted to eliminate time: cycle 1 (●), cycle 2 (■), and cycle 3 (▲). An additional dataset for unregulated F-actin sliding is shown: cycle 1 (△) and cycle 2 (▽). Note that the sliding speed of regulated thin filaments at the highest temperature is almost the same as for unregulated F-actin.

acid (EGTA), 20 mM 3-(N-Morpholino)propanesulfonic acid (MOPS),  $[\text{K}^+] = 50$  mM,  $[\text{Na}^+] = 15$  mM, pMg 3 (pMg =  $-\log_{10}[\text{Mg}^{2+}]$ , where  $[\text{Mg}^{2+}]$  is in molar units), and appropriate amounts of Tris<sup>+</sup>, and acetate (anion) to obtain an ionic strength of 0.085 M at pH 7. Concentrations of  $\text{Ca}^{2+}$ ,  $\text{Mg}^{2+}$ ,  $\text{Na}^+$ ,  $\text{K}^+$  were determined taking into account known metal ion binding constants and their enthalpies [32, 50]; solution composition was chosen to minimize enthalpic changes in pH in flow cells when temperature was varied. Glucose (3 mg/mL), 0.1 mg/mL glucose oxidase, 0.018 mg/mL catalase (Boehringer-Mannheim), and 40 mM dithiothreitol (DTT) were added immediately prior to an assay to minimize photooxidation and photobleaching [49]. Experiments were conducted at saturating  $[\text{Ca}^{2+}]$  (pCa 5, where pCa =  $-\log_{10}[\text{Ca}^{2+}]$ , with  $[\text{Ca}^{2+}]$  in molar units) or,

where indicated, at low  $[\text{Ca}^{2+}]$  (pCa 9); note that  $[\text{Ca}^{2+}]$  does not affect sliding speed of unregulated F-actin [12, 14]. Methylcellulose (final concentration 0.3%), dialyzed against sodium azide (0.02%), was added to MB to prevent actin filament diffusion away from the assay surface [12, 49, 51]. Solutions for assays with reconstituted thin filaments were the same as for unregulated F-actin, except for the last two solutions: the buffer applied to the flow cell before MB contained 75 nM each of  $\alpha$ -Tm and either native cTn or recombinant hcTn and was incubated for three minutes before infusing MB containing the same concentrations of Tn and Tm [12, 13, 32, 50]. The minimum concentrations of native or WT Tn and Tm added to MB to obtain well-regulated filaments at  $30^\circ\text{C}$  were determined by titrations and applying the following criteria: filament sliding was

TABLE 1: Metabolite concentrations in standard and modified motility buffers.

Metabolites	Standard <sup>1</sup>	Modified solutions for motility assays <sup>2</sup>		
	Motility buffer	Control	High Pi	Low ATP
[ATP]	2 mM	2 mM	2 mM	0.2 mM
Sucrose phosphorylase	—	5.3 $\mu\text{g/mL}$	—	5.3 $\mu\text{g/mL}$
Sucrose	—	10 mM	10 mM	10 mM
[Pi]	$\sim 10 \mu\text{M}$	$\sim 1 \mu\text{M}$	4 mM	$\sim 1 \mu\text{M}$
Creatine kinase (CK)	—	0.1 mg/mL	0.1 mg/mL	0.1 mg/mL
Creatine (Cr)	—	30 $\mu\text{M}$	30 $\mu\text{M}$	12 $\mu\text{M}$
Creatine phosphate (CP)	—	1 mM	1 mM	1 mM
[ADP]	$\sim 10 \mu\text{M}$	0.42–0.57 $\mu\text{M}$	0.42–0.57 $\mu\text{M}$	$\sim 0.02 \mu\text{M}$

Values for [ATP], [Pi], and [ADP] represent final concentrations in motility buffers. [Pi] in columns 3 and 5 were estimated using  $K_{\text{eq}} = 0.06$  for the reaction  $\text{sucrose} + \text{Pi} \rightarrow \alpha\text{-D-glucose-1-phosphate} + \text{D-fructose}$  [52, 54]. [ADP] estimates are based on the equilibrium constant ( $K_{\text{eq}}$ ) for the reaction  $\text{ATP} + \text{Cr} \leftrightarrow \text{ADP} + \text{CP}$ , and are given in columns 3–4 with lowest and highest value corresponding to the lowest (27°C) and highest (42°C) temperatures employed, respectively. The estimate of [ADP] in column 2 was based on Chase and Kushmerick [53].

<sup>1</sup>Motility buffer (MB) employed in the majority of experiments (data in Figures 1–4) did not include sucrose phosphorylase and creatine kinase.

<sup>2</sup>Modified motility buffers were used for experiments shown in Figure 5.

inhibited at pCa 9, while motility was fast and uniform at pCa 5 and standard temperature of 30°C [12, 13, 32, 50]. In a limited set of motility experiments, standard MB was modified to vary metabolite concentrations (Table 1) as follows: either 5.3  $\mu\text{g mL}^{-1}$  sucrose phosphorylase and 10 mM sucrose were added to reduce inorganic phosphate (Pi) [52] or acetate was partially replaced by Pi to achieve the high Pi condition (sucrose phosphorylase was not added); contaminating ADP was reduced to  $<1 \mu\text{M}$  by addition of creatine phosphate (CP) and creatine phosphokinase (CK) [53].

Motility data were collected while varying temperature by employing modified flow cells containing microfabricated Au heater and thermometer elements (Figure 1(a)), where the thermometer is located immediately adjacent to the viewing region [5]. In experiments using the thermoelectric heater, cooling was achieved by circulating chilled water through a copper coil wrapped around the microscope objective; in a limited set of experiments, assays at constant temperature were achieved by circulating temperature-controlled water through the coil surrounding the objective [13, 43]. Motility speed was analyzed using MetaMorph software (Universal Imaging) as described [5]. Stacks of frames (one stack for each second of temperature transient data, or 10–12 stacks for each constant temperature experiment from one flow cell) were created from digitized movies.

**2.3. Statistical Analyses.** Averages and error estimates were calculated with Microsoft Excel 2000. Averages are given as unweighted mean  $\pm$  SD. Linear regression analyses were performed using Microsoft Excel 2000 or SigmaPlot (Windows versions 8.0 and 11.2; SPSS Inc., Chicago, IL); nonlinear regression analyses were performed using SigmaPlot.

A transition temperature ( $T_t$ ) was estimated from Arrhenius transformed speed versus temperature data that exhibited a change in slope with temperature. To obtain  $T_t$ , the data were divided into two parts (high- and low-temperature regimes) that were separated by two adjacent points on the Arrhenius plot's temperature axis; several such

divisions of each dataset were processed using the following algorithm. Linear regressions were obtained for each regime, and the intersection point determined for those regressions. In general, the intersection point does not fall between the two data points that separate the high and low temperature regimes. The small number of intersection points that did fall between the high- and low-temperature regimes were considered to be candidates for  $T_t$ ; in the few instances when there was more than one candidate point, the median value was chosen for  $T_t$ .

### 3. Results

**3.1. Temperature Dependence of Unregulated F-Actin and Regulated Thin-Filament Sliding.** To examine sliding of  $\text{Ca}^{2+}$ -regulated thin filaments over a broad range of temperatures, we employed a thermoelectric controller (Figure 1(a)) that enables both rapid and continuous variation of a flow cell's temperature [5]. Figure 1(b) shows sliding speed (solid symbols) as a function of time for thin filaments reconstituted with native cTn· $\alpha$ -Tm at pCa 5 during three heating phases of cyclic heating and cooling ( $\sim 20$ – $60^\circ\text{C}$ ). Note that the peak temperature (gray line) increased with each cycle. Speed increased with temperature during the heating phase of each cycle over most of the range examined. As temperature increased during the third cycle, however, sliding speed of regulated actin reached a maximum at  $\sim 54^\circ\text{C}$ , and then speed declined above  $\sim 58^\circ\text{C}$  (Figure 1(b)). This anomalous decline in speed for regulated thin filaments is particularly evident in Figure 1(c), solid symbols where data from all three heating cycles of Figure 1(b) were combined to show the temperature dependence of sliding speed. Superposition of the data from three cycles suggests that brief exposure to elevated temperature over at least the first two cycles was fully reversible.

Comparison of regulated versus unregulated F-actin sliding speed at high temperature suggests that the anomalous decline for regulated thin-filament speed is more likely due to an effect of temperature on Tn·Tm rather than on

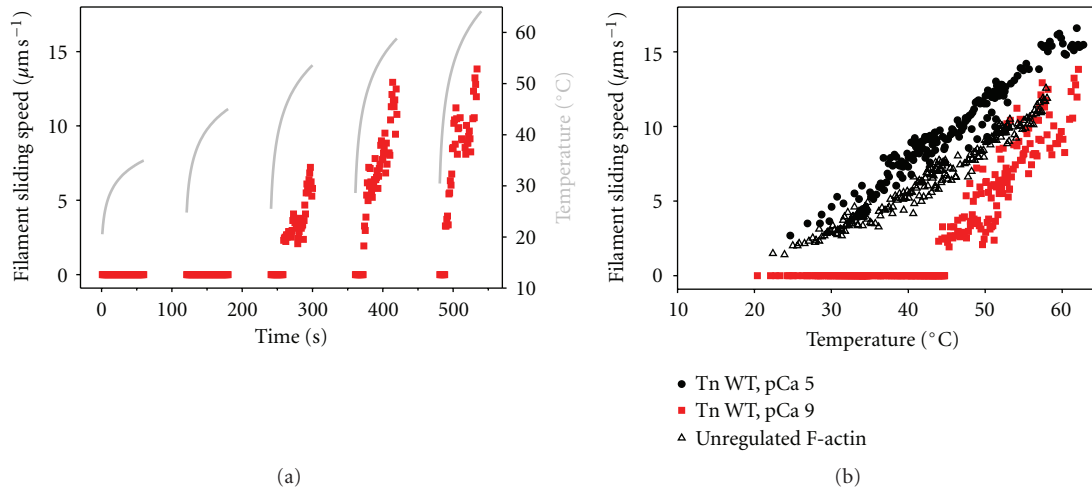


FIGURE 2: Thin filaments remain motile but lose  $\text{Ca}^{2+}$ -regulation at high temperature. (a) Time course of temperature (gray line; right ordinate) and sliding speed (solid squares, red fill; left ordinate) for regulated thin filaments (F-actin plus rhcTn and  $\alpha$ -Tm) at pCa 9 during the heating phase of five cycles of heating and cooling. Points represent the mean sliding speed for 3–5 filaments during 1 s. At pCa 9, nonzero sliding speeds in heating cycles 3–5 indicate loss of  $\text{Ca}^{2+}$ -regulation (dysregulation); note that temperature-dependent loss of  $\text{Ca}^{2+}$ -regulation is fully reversible following cooling (beginning of cycles 4–5). (b) Data from (a) (pCa 9; solid squares, red fill) were replotted to eliminate time. Additional data for regulated thin filaments (F-actin plus rhcTn and  $\alpha$ -Tm) at pCa 5 (●) and unregulated F-actin ( $\Delta$ ) from the same series of experiments are also shown for comparison.

actin or HMM. Regulated filament speed at pCa 5 (solid symbols) was at least as fast as that for unregulated F-actin (open symbols) at each temperature over the range examined ( $\sim 20$ – $60^{\circ}\text{C}$ ) (Figure 1(c)), consistent with previous reports over more limited temperature ranges [12, 13, 16, 20]. The speed of unregulated F-actin, however, increased continuously over the entire temperature range—even at the highest temperatures examined, where regulated thin-filament speed declined. To test the hypothesis that Tn·Tm is responsible for the anomalous decline in speed (Figure 1), we examined the effect of temperature on regulated thin-filament motility at pCa 9, that is, in the absence of activating  $\text{Ca}^{2+}$ . Figure 2(a) shows sliding speed (red symbols) as a function of time for thin filaments reconstituted with rHcTn· $\alpha$ -Tm at pCa 9 during five heating phases of cyclic heating and cooling. Note that the peak temperature (gray line) increased with each cycle, as in Figure 1(b). Data from all five heating cycles of Figure 2(a) were combined to show the temperature dependence of sliding speed in Figure 2(b). As expected in the absence of  $\text{Ca}^{2+}$ , regulated thin filaments exhibited little or no motion (note red symbols at speed  $\sim 0$ ) over a broad range of temperatures ( $\sim 20$ – $43^{\circ}\text{C}$ ). Above  $\sim 43^{\circ}\text{C}$ , filament sliding was observed indicating loss of  $\text{Ca}^{2+}$  regulation (red symbols; Figure 2) although the average speed was generally less than or similar to that of unregulated F-actin (open symbols; Figure 2(b)). As for native cTn (Figure 1(c), solid symbols), rHcTn WT regulated thin filaments at pCa 5 (Figure 2(b), solid symbols) were faster than unregulated F-actin (Figure 2(b), open symbols); an anomalous decline in speed with WT rHcTn (Figure 2(b), solid black circles) occurred at slightly a higher temperature (by  $\sim 4$ – $5^{\circ}\text{C}$ ) than for native cTn (Figure 1(c), solid symbols), suggesting increased stability of the recombinantly expressed protein or its interactions with

F-actin- $\alpha$ -Tm. The apparent loss of  $\text{Ca}^{2+}$ -regulation, indicated in Figure 2 by thin filament sliding (nonzero speeds) at pCa 9 for temperatures above  $\sim 43^{\circ}\text{C}$ , is completely reversible because thin-filaments stopped moving after temperature was lowered during the cooling phase of each cycle at pCa 9 (Figure 2(a)).

Arrhenius analysis of the data in Figure 1(c) reveals that the activation energy ( $E_a$ ) for regulated thin-filament speed at pCa 5 exhibited two distinct values, with a change in the slope at  $T_t \sim 38^{\circ}\text{C}$  (Figure 3, solid symbols and black solid lines). For regulated thin filaments (Figure 3, solid symbols and black solid lines),  $E_a$  at temperatures below physiological ( $100.4 \text{ kJ/mol}$ ) was  $>2$ -fold greater than  $E_a$  for the higher-temperature regime ( $41.8 \text{ kJ/mol}$ ), while the latter value was closer to that of unregulated F-actin ( $61.9 \text{ kJ/mol}$ ) (Figure 3, open symbols and black dashed line). Temperature has a dramatic, nonlinear effect on the viscosity of water [55], and the speed of filament sliding varies inversely with solvent viscosity [43, 56]; we therefore asked whether temperature-dependent changes in solvent viscosity could explain the nonlinear Arrhenius relation (Figure 3). The data in Figure 3 were processed to remove the temperature dependence of solvent viscosity by first normalizing viscosity with respect to that of water at  $37^{\circ}\text{C}$  (i.e., body temperature), and second assuming that speed varies inversely with solvent viscosity [43, 56]. After removing the effects of viscosity, slopes of the Arrhenius plots were reduced (Figure 3, blue lines).  $E_a$  for unregulated F-actin decreased from  $61.9 \text{ kJ mol}^{-1}$  to  $47.0 \text{ kJ mol}^{-1}$  (Figure 3, blue dashed line). For regulated thin filaments,  $E_a$  decreased from  $100.4$  to  $83.9 \text{ kJ mol}^{-1}$  for  $T < 38^{\circ}\text{C}$ , and from  $41.8$  to  $26.6 \text{ kJ mol}^{-1}$  for  $T > 38^{\circ}\text{C}$  (Figure 3, black versus blue solid lines). The latter value of  $E_a$  is suggestive of a diffusion-limited process, in accord with the previously observed inverse relationship between



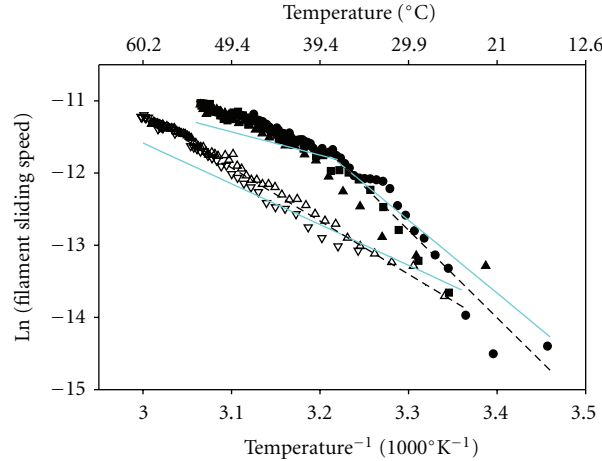


FIGURE 3: Correction for temperature-dependent effects of solvent viscosity (solid, cyan lines) on filament sliding speed of regulated thin filaments (solid symbols) and unregulated F-actin (open symbols). Data from Figure 1(c) were replotted in Arrhenius form (symbols as in Figure 1), with data omitted for regulated thin filaments above  $\sim 54^\circ\text{C}$  and filament sliding speeds expressed in  $\mu\text{m s}^{-1}$ . Dashed lines (black) are linear least squares regressions on the data before correction for temperature-dependent changes in solvent viscosity. Note the change in slope at  $\sim 38^\circ\text{C}$  ( $T_t$ ) for regulated thin filaments. Effects of temperature-dependent changes in solvent viscosity (normalized to that at body temperature,  $37^\circ\text{C}$ ) were removed by assuming that speed varies inversely with viscosity, as demonstrated experimentally [43]; the net result of this correction in all instances is a decrease in apparent  $E_a$ .

speed and viscosity [43, 56]. Despite the reduction of slopes for regulated thin-filaments, the ratio of  $E_a$ 's between the two temperature regimes increased from 2.4 to 3.1. Below  $38^\circ\text{C}$ , the ratio of  $E_a$ 's for regulated thin-filament sliding speed with respect to that of unregulated F-actin increased from 1.6 to 1.8. It is clear from this analysis that it is important to consider temperature-dependent changes in solvent viscosity when evaluating actin filament sliding speed. Nonlinearities in the Arrhenius plot (Figure 3), however, cannot be explained by temperature-dependent changes in solvent viscosity.

**3.2. Influence of FHC Mutations in Troponin on the Temperature Dependence of Thin-Filament Sliding.** Because the temperature dependence of maximum filament sliding speed is influenced by the presence and function of  $\text{Tn}\cdot\text{Tm}$  (Figures 1–3), and FHC-related mutations in troponin profoundly influence the  $\text{Ca}^{2+}$  dependence of myofilament function [8–10, 57], we utilized the thermoelectric controller to investigate temperature effects on thin filaments reconstituted with  $\text{rHcTn}\cdot\alpha\text{-Tm}$  when one of three FHC-related mutations— $\text{TnI R145G}$ ,  $\text{TnI K206Q}$ , or  $\text{TnT R278C}$ —was incorporated into the troponin complex (Section 2). At  $\text{pCa } 5$ , filament sliding speed for two mutants ( $\text{TnI K206Q}$  and  $\text{TnT R278C}$ ) was faster than WT over the range of temperatures examined, consistent with previously reported data for  $\text{TnI K206Q}$  using recombinant rat cardiac  $\text{Tn}$  [32]. In contrast, speed with  $\text{TnI R145G}$  was similar to WT (Figure 4).

The micromechanical thermal assays with thin filaments containing FHC mutations in  $\text{rHcTn}$  suggest that either the mutant troponins are intrinsically less thermally stable, or the regulatory interaction of mutant troponin with F-actin- $\alpha\text{-Tm}$  is less stable, or both (Figure 4(a)). All three of the FHC mutants exhibited anomalous declines in speed

at lower temperatures than WT  $\text{rHcTn}$ , with the  $\text{cTnT R278C}$  and  $\text{cTnI R145G}$  mutations resulting in  $\sim 4\text{--}5^\circ\text{C}$  decreases, and the  $\text{cTnI K206Q}$  mutation leading to a larger,  $\sim 8\text{--}9^\circ\text{C}$  decrease in the temperature at which the anomalous decline in speed occurred as temperature continued to rise (Figure 4(a)).

Arrhenius analysis suggests that there was little effect of the FHC mutations on  $T_t$  for thin filaments reconstituted with WT or mutant  $\text{rHcTn}$ , with values of  $38\text{--}41^\circ\text{C}$  where they could be unambiguously determined (Figure 4(b)). This was similar to the value of  $T_t = \sim 38^\circ\text{C}$  obtained with native  $\text{cTn}$  (Figure 3). The slopes of the high- and low-temperature regimes were more similar for the two fastest mutants ( $\text{cTnT R278C}$  and  $\text{cTnI K206Q}$ ) compared with WT or the  $\text{cTnI R145G}$  mutant (Figure 4(b)); in fact, it was not possible to unambiguously identify a value of  $T_t$  from data with  $\text{TnI K206Q}$  by the algorithm used (Section 2). When the data for unregulated F-actin from Figure 2(b) (open symbols) were plotted in Arrhenius form (Figure 4(b), gray dashed lines), a value of  $T_t \sim 33^\circ\text{C}$  was obtained in contrast to the dataset in Figures 1 and 3, where  $T_t$  for unregulated F-actin could not be determined because there were not sufficient points below  $T_t$  to define a low-temperature regime.

**3.3. Influence of Factors that Affect Cross-Bridge Number and Kinetics on Temperature Dependence of Unregulated F-Actin and Regulated Thin-Filament Sliding Speed.** To address whether changes in the number of cross-bridges and distribution of cross-bridge states could be responsible for differences in sliding speed and  $E_a$  between unregulated F-actin and regulated thin filaments at saturating  $\text{Ca}^{2+}$ , we studied the effects of altered HMM density, and metabolite concentrations which are known to affect the fraction of



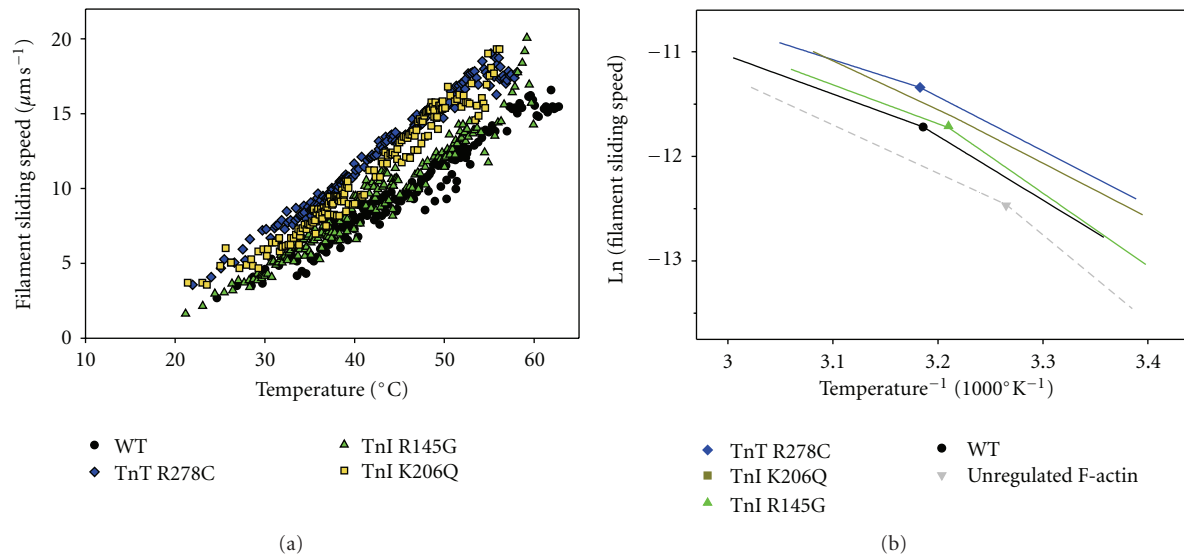


FIGURE 4: Influence of FHC-linked mutations in human cardiac troponin on temperature dependence of thin-filament sliding at pCa 5. Thin filaments were reconstituted with  $\alpha$ -Tm and either rhcTn WT (circles, black), rhcTn TnI,R145G (triangles, green), rhcTn TnI,K206Q (squares, yellow), or rhcTn TnT, R278C (diamonds, blue). Data were obtained during the heating phases of multiple heating/cooling cycles, as in Figure 1; note that WT data were replotted from Figure 2(b). (a) Points represent the mean sliding speed for 3–8 filaments during 1 s. Note that speeds with TnI mutant K206Q [32] and TnT mutant R278C were generally elevated over WT. (b) Arrhenius analysis of data from (a). Symbols and colors as in (a); unregulated F-actin from the same series of experiments (Figure 2(b)) was also included in (b) (inverted triangle and dashed lines; light gray). Each dataset was fit by two linear regressions after omitting data above  $\sim 60^\circ\text{C}$  (WT),  $\sim 54^\circ\text{C}$  (cTnI R145G),  $\sim 51.5^\circ\text{C}$  (cTnI K206Q), or  $\sim 55^\circ\text{C}$  (cTnT R278C). Regression lines are shown without correction for temperature-dependent changes in solvent viscosity; points correspond to  $T_i$ , the intersection of each pair of lines. Filament sliding speeds are expressed in  $\mu\text{m s}^{-1}$ .

weakly versus strongly bound cross-bridges. Solutions were modified in the following ways, and compared with a control condition that was itself modified in comparison with assays reported in Figures 1–4 (Section 2): decreased [ATP] from 2 mM (Control) to 200  $\mu\text{M}$ , increased [Pi] from  $\sim 1 \mu\text{M}$  (Control) to 4 mM, or reduced HMM density ( $\rho$ ) from 0.25 mg/mL (Control) to 0.075 mg/mL (Figure 5). In these experiments only, motility assays were performed at steady-state temperatures of 27, 32, 37, or  $42^\circ\text{C}$  so that we could calculate metabolite concentrations in the presence of CP/CK to buffer ATP/ADP and reduce ADP (Section 2), conditions that did not apply to the nonsteady state temperature assays reported in Figures 1–4.

Sliding speed increased with temperature for each condition tested for both regulated thin filaments at pCa 5 and unregulated F-actin (Figure 5) as expected for the temperature range examined. Sliding speed with respect to the Control condition was reduced significantly for the low ATP condition at the two highest temperatures for unregulated F-actin (Figure 5(a)) and at the three highest temperature points for regulated thin filaments (Figure 5(b)). Sliding speed at high Pi (Figure 5) was higher than in Control conditions at the two lower temperatures for both regulated thin filaments and unregulated F-actin. Decreasing  $\rho$  had little effect on unregulated F-actin sliding speed (Figure 5(a)) but decreased regulated thin-filament speed significantly at the three lowest temperatures (27, 32, and  $37^\circ\text{C}$ , Figure 5(b)). Addition of Tn·Tm was typically associated with increased speed, but not at low ATP, which

is in good agreement with the results of Homsher et al. [16]. At reduced  $\rho$ , the enhancing effect of Tn·Tm was greater at higher temperatures. The fraction of motile filaments at reduced  $\rho$  increased over the three lowest temperatures (27, 32, and  $37^\circ\text{C}$ ) for unregulated F-actin (inset, Figure 5(a)), but over the entire temperature range for regulated thin filaments (inset Figure 5(b)).

#### 4. Discussion

In this study, we utilized microfabricated thermoelectric devices to rapidly and reversibly investigate the influence of temperature on myosin-driven sliding of  $\text{Ca}^{2+}$ -regulated, muscle thin filaments over a wide temperature range ( $\sim 20$ – $60^\circ\text{C}$ ). To investigate molecular mechanisms of normal cardiac function and pathophysiology, thin filaments were reconstituted with human cardiac Tn and Tm, or with FHC-related mutants of human cardiac Tn. The major results of this study are as follows.

- At pCa 5, sliding speed of regulated thin filaments increased reversibly with increasing temperature ( $\sim 20$ – $54^\circ\text{C}$ ) as expected and was faster than unregulated F-actin over that range.
- Reversible dysregulation—loss of  $\text{Ca}^{2+}$ -regulation—occurred at both pCa 5 and pCa 9 at the upper end of the temperature range examined; this suggests thermal unfolding of the cardiac regulatory proteins and/or their dissociation from actin.

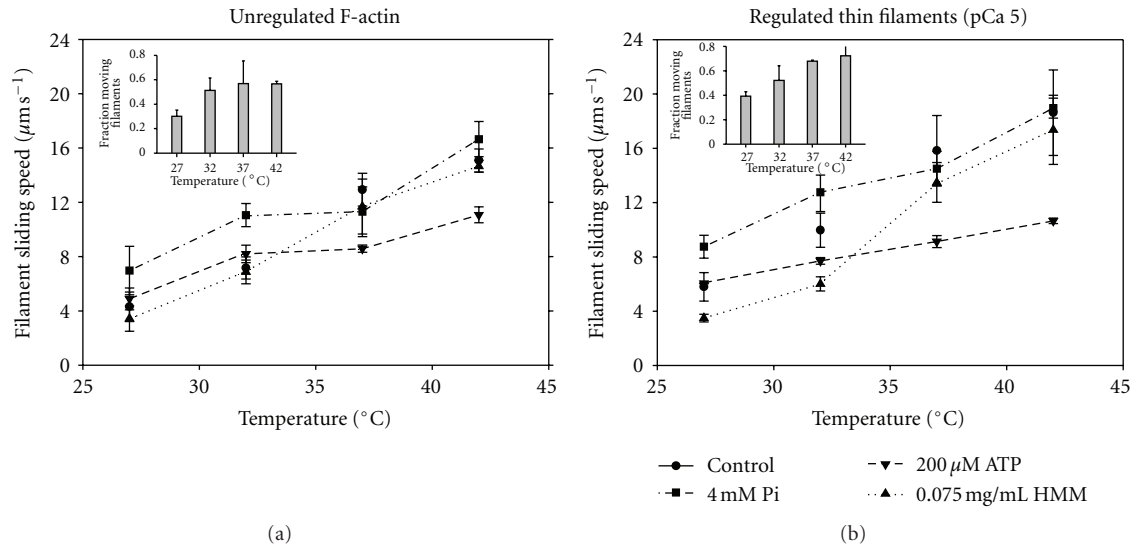


FIGURE 5: Influence of motility conditions on temperature dependence of filament sliding speeds for (a) unregulated F-actin and (b) regulated thin filaments (F-actin plus native cTn and  $\alpha$ -Tm) at pCa 5. Points are the mean of means  $\pm$  S.D. from 45–75 filaments in each of  $\geq 3$  individual flow cells and are plotted against steady-state temperature (27–42  $^{\circ}\text{C}$ ) for four conditions. For this series of experiments only, control conditions (circles, solid lines) were  $[\text{Pi}] = \sim 1 \mu\text{M}$  (achieved by removal of contaminating Pi; Section 2);  $[\text{ATP}] = 2 \text{ mM}$  (buffered by CP and CK; Section 2), and high  $\rho$  achieved by infusing 0.25 mg/mL [HMM] into the flow cell. Conditions were modified to test low ATP (200  $\mu\text{M}$  ATP; inverted triangles, short dashed lines); high Pi (4 mM Pi; squares, long dash dotted lines); or low  $\rho$  (0.075 mg/mL HMM; triangles, dash dotted line). Lines were drawn to connect the points. Insets: temperature dependence of fraction of filaments moving under low  $\rho$  condition plotted for (a) unregulated F-actin and (b) regulated thin filaments at pCa 5. Note that the fraction of regulated thin filaments, but not unregulated F-actin, increases continuously over this temperature range.

- (c) Arrhenius analysis indicates two temperature regimes with different  $E_a$ ; the transition temperature between those regimes was higher for regulated thin filaments than unregulated F-actin, and this is explained by a simple model.
- (d) Factors that alter cross-bridge number and kinetics— $[\text{ATP}]$ ,  $[\text{Pi}]$ , and  $\rho_{\text{HMM}}$ —alter the temperature dependence of sliding speed of both regulated thin filaments and unregulated F-actin in qualitatively similar ways that provide insight into rate limiting factors.
- (e) Three FHC mutants in cTn (cTnI R145G, cTnI K206Q, and cTnT R278C) destabilize regulatory protein structure and/or interactions with F-actin-Tm and may also alter the kinetics of thin filament sliding at pCa 5.

**4.1. Functional Assays for Thermal Stability of Regulated Thin Filaments and  $\text{Ca}^{2+}$ -Regulatory Proteins.** A custom thermoelectric controller [5] that was used in this study (Figure 1(a)), and miniaturized versions thereof [6], provide a novel approach to evaluate contractile protein function over a wide range of temperatures and multiple temperature cycles. The multiple datasets collected this way with native and WT regulatory proteins (Figures 1–3) complement and expand the range of information that can be obtained using conventional motility assays [16, 58, 59] and traditional approaches to studying protein structure in solution [60–63]. Our device provides a simpler readout of temperature

than relying on intensity of the fluorescent label [64]. Speed of unregulated F-actin increased monotonically over the temperature range used (Figures 1–2, open symbols), indicating that HMM and actin are not affected detrimentally at temperatures below 60  $^{\circ}\text{C}$ ; this is consistent with previous functional measurements [5, 64] and structural assays showing that the structure of Ph-stabilized F-actin in solution is thermally stable up to 78  $^{\circ}\text{C}$  [62], while unfolding of subfragment 1 (S1) was reported for temperatures greater than 58  $^{\circ}\text{C}$  in the presence of analogs of ATP or ADP  $\cdot$  Pi [63].

Dysregulation of thin filaments at elevated temperatures was observed at both pCa 5 (Figures 1–2) and pCa 9 (Figure 2), suggesting that altered function was likely due to dissociation of Tn  $\cdot$  Tm from actin or denaturation of Tn and/or Tm. At pCa 5, the anomalous decline in sliding speed for regulated thin filaments above  $\sim 54^{\circ}\text{C}$  suggests a loss of regulation (dysregulation) because as temperature increased, speed decreased toward that of unregulated F-actin (Figure 1(c)). At pCa 9, filament sliding was observed at temperatures above  $\sim 43^{\circ}\text{C}$ ; speed increased with temperature and was generally lower than, but approached that of unregulated F-actin (Figure 2), indicating that cTn stabilizes actin  $\cdot$  Tm at pCa 5. Taken together, these results from microthermal heater assays provide functional correlates that are consistent with previous solution studies showing half-maximal dissociation of Tm from Ph-stabilized F-actin  $\cdot$  Tm complex (no Tn) at 46–48  $^{\circ}\text{C}$ , and unfolding of Tm alone in solution that was resolved into two separate calorimetric domains with maxima of 42 and 51  $^{\circ}\text{C}$  [61, 62]. More generally, our results demonstrate that microthermal

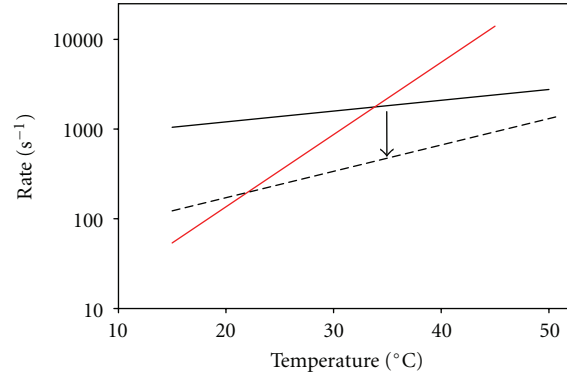


FIGURE 6: Temperature dependence of two apparent rate constants that may limit actin filament sliding speed at pCa 5. Data in Figure 3 ( $T < \sim 54^\circ\text{C}$ ) for sliding speed of regulated thin filaments were fitted to (2). The inverse of each of the exponential rate terms in the denominator of (2) is plotted: for WT regulated thin filaments, one rate exhibits only slight temperature sensitivity (solid black line) while the other is markedly temperature sensitive (red line). The rate-limiting step for filament sliding is the smaller of the two rates, and  $T_t$  is the intersection of the two lines. The less temperature sensitive rate is also shown for unregulated F-actin (dashed black line; data from Figure 3). Note that by assuming the temperature-sensitive rate (red line) is similar for both instances, decreasing the less temperature sensitive rate (black arrow, as observed experimentally with unregulated F-actin) decreases  $T_t$ .

heater assays can provide unique, molecular level insights into muscle thin-filament function, particularly when the maximum temperature is limited such that the effects of temperature on  $\text{Ca}^{2+}$  regulation are fully reversible (Figure 2(a)).

**4.2. Temperature Dependence of  $\text{Ca}^{2+}$ -Regulated Thin-Filament Sliding at pCa 5.** Comparison of temperature-dependence of regulated thin-filament sliding at pCa 5 with that of unregulated F-actin provides insights into the roles of cardiac troponin and tropomyosin. This is important in light of the observation that not only do Tn-Tm modulate the thin filament side of actomyosin interactions but cTn can also directly accelerate myosin ATPase activity even in the absence of actin and Tm [20]. This direct effect of cTn on myosin kinetics is presumed to at least partially underlie Tn-Tm's enhancement of maximum unloaded sliding speed under a wide variety of conditions (e.g., Figures 1(c), 2(b), 3, 4(b), and 5), although it is also possible that there are differences in the myosin binding interface due to Tm-S1 interactions [65] or regulatory protein-induced structural changes in actin itself [15].

While it is clear that Tn-Tm modulate filament sliding speed primarily by affecting the number of cross-bridges at submaximal  $\text{Ca}^{2+}$  activation [12, 14, 50], the most straightforward mechanism by which Tn-Tm could directly enhance actomyosin kinetics at saturating  $\text{Ca}^{2+}$  is through a reduction in the time that cross-bridges spend in the strongly bound state ( $t_s$ ) under the unloaded conditions of a motility assay, as observed experimentally [33]. The maximum sliding speed ( $s_m$ ) for regulated thin filaments at saturating  $\text{Ca}^{2+}$  or for unregulated F-actin is simply related to myosin step size ( $d_x$ ) and  $t_s$  as proposed by Uyeda et al. [51]:

$$s_m = \frac{d_x}{t_s}. \quad (1)$$

To accommodate the observed, biphasic Arrhenius plots (Figures 3 and 4(b)), we assume that  $d_x = 0.0055 \mu\text{m}$  [66] for all conditions examined and rewrite (1) to express  $t_s$  as the sum of two exponential terms:

$$s_m = \frac{0.0055}{(ae^{-bT} + ce^{-dT})}, \quad (2)$$

which, when fit to the data for regulated thin filaments in Figure 3, yields  $s_m = 0.0055 / (0.301e^{-0.1855T} + 0.00145e^{-0.0277T})$  with  $R^2 = 0.97$ . Separating the two terms and plotting them as rates, we can see that one varies little with temperature (black solid line; Figure 6) and while the other is highly temperature sensitive (red solid line; Figure 6). Assuming that the more highly temperature-dependent term is similar for both regulated thin filaments and unregulated F-actin, regression estimates were obtained for unregulated F-actin sliding in Figure 3,  $c = 0.0225$  and  $d = 0.0676$  ( $R^2 = 0.97$ ), and the corresponding rate prediction was plotted in Figure 6 (black dashed line).

If the intersections of the red line with the two black lines in Figure 6 are related to discontinuities in the Arrhenius plots (Figures 3 and 4(b)) and thus values of  $T_t$ , then the simple analysis of (1), (2) is in accord with observations that the transition from high to low  $E_a$  will occur at higher temperature for regulated thin filaments (red and solid black lines) than for unregulated F-actin (red and dashed black lines). In this model, the rate limitation for filament sliding at a given temperature would be the lower of the two rates from the red line and one black line: at low temperatures, the steeper, red value is limiting, while the shallower, black value is limited at elevated temperatures (Figure 6). The temperature dependence of unloaded filament sliding speed has been reported to vary as a function of temperature in some but not all conditions [16, 58, 59]. For unregulated F-actin, Arrhenius plots have been previously reported to be linear within  $20$ – $60^\circ\text{C}$  [5] and  $7$ – $25^\circ\text{C}$  [16], but nonlinear within  $3$ – $42^\circ\text{C}$  with a transition temperature ( $T_t$ ) of  $15.4^\circ\text{C}$  [59],

and 10–35°C with a  $T_t \sim 25^\circ\text{C}$  [58, 67].  $T_t$  depends not only on the experimental conditions but also on whether  $\text{Ca}^{2+}$ -regulatory proteins are present. The Arrhenius plot of fish myofibrillar ATPase at saturating  $\text{Ca}^{2+}$  exhibited a discontinuity [68], while this was not the case for *in vitro* motility sliding speed and actin-activated MgATPase activity with fish myosin and unregulated F-actin [69]. For regulated thin filaments, Homsher et al. [16] reported a break in the Arrhenius plot around 12.5°C that was not observed for unregulated F-actin within the 7–25°C temperature range. In this study using micromechanical thermal assays, discontinuities in Arrhenius plots for regulated thin filaments (Figures 3 and 4(b)) occurred at a higher temperature than when  $T_t$  could be identified for unregulated F-actin (Figure 4(b)). While there is no universal agreement in the limited data available on absolute values for  $T_t$  for filament sliding, there does appear to be general agreement that Tn·Tm modulates the temperature dependence of unloaded filament sliding. Our data suggest that this modulation of  $T_t$  by human cardiac Tn·Tm occurs around physiological temperature.

The existence of discontinuities in Arrhenius plots suggests that different factors are rate-limiting to filament sliding above and below  $T_t$ . What factors could contribute to this difference? Prior experiments with regulated thin filaments at subsaturating levels of  $\text{Ca}^{2+}$  suggested that the number of cross-bridges is limiting to sliding speed at 30°C [12, 50]. The data in Figure 5 indicate that sliding speed is markedly sensitive to a reduction in the density ( $\rho$ ) of HMM on the flow cell surface at 27 and 32°C for both unregulated F-actin and especially regulated thin filaments at maximal  $\text{Ca}^{2+}$  activation. At higher temperatures (37 and 42°C), however, there was little or no effect of the same reduction in  $\rho$  on sliding speed for either unregulated F-actin or regulated thin filaments (Figure 5). In addition, the fraction of moving filaments at low  $\rho$  increased with temperature for regulated thin filaments at pCa 5 over the entire temperature range (Figure 5(b), inset), while for unregulated F-actin, the fraction started at a lower value and plateaued (Figure 5(a), inset). Taken together, these observations suggest an increase in strong cross-bridges with temperature for both unregulated F-actin and regulated thin filaments, consistent with previous reports using *in vitro* assays and permeabilized muscle fibers [70–72]. Thus, it appears that Tn·Tm can modulate at least one rate-limiting factor, and also  $T_t$ , around physiological temperature: once a temperature ( $T_t$ ) is attained at which the availability of cross-bridges is great enough to guarantee continuous filament sliding, further increase of speed with temperature will only depend on less temperature-sensitive kinetic rates that are associated with transitions between strongly bound cross-bridge states, and will therefore be characterized by low  $E_a$  (Figure 6, cross-over from red to black lines).

In addition to the number of cross-bridges, filament sliding speed can be altered by variations in the substrate and products of the ATPase reaction through modulation of actomyosin kinetics. According to the model implicit in (1), changes in metabolite concentration would primarily influence  $t_s$ , and therefore  $s_m$ , and also the number of

attached cross-bridges. For example, Tn·Tm could affect the kinetics of ATP-induced cross-bridge dissociation that has been suggested to limit filament sliding speed, at least in fast skeletal muscle at low temperature [16, 73]. When [ATP] was reduced to 200  $\mu\text{M}$ —a substrate concentration that is similar to the apparent  $K_d$  for sarcomere shortening velocity and filament sliding speed [16, 53, 74, 75]—inhibition of speed was greater for regulated thin filaments at pCa 5 than unregulated F-actin (Figure 5), as reported by Homsher et al. [16]. Inhibition of  $s_m$  at low ATP levels is explained by slower ATP-induced detachment of cross-bridges at the end of attached phase the cycle, which increases  $t_s$  (1); the fraction of strongly attached cross-bridges would also increase, although the dominant factor in determining  $s_m$  in this instance is slower cross-bridge cycling. The relatively greater inhibition of regulated thin-filament sliding was accentuated at higher, more physiological temperatures (Figure 5). The net result was a generally shallow slope of speed versus temperature for both regulated thin filaments and unregulated F-actin (Figure 5) that corresponds to a regime of relatively low  $E_a$ . The expectation would then be that reduced [ATP] should shift  $T_t$  to a lower temperature (Figure 6) although it was not resolved in this experiment, likely because of the lower limit of temperature examined.

There are some interesting parallels with reduced [ATP] effects, along with significant differences, when the concentration of product Pi was increased from micromolar levels to 4 mM (Table 1), that is, the highest concentration that we could achieve without necessitating an increase in ionic strength. Temperature has previously been shown to modulate the effect of Pi on isometric force in muscle fibers, although there is disagreement about whether Pi is either more [29, 76] or less [77] inhibitory of isometric force as temperature increases. While Pi inhibits isometric force, elevated Pi increases sliding speed for both regulated thin filaments at pCa 5 and unregulated F-actin, although the effect predominates at lower temperatures and is more pronounced for regulated thin-filaments (Figure 5). Maximum velocity of sarcomere shortening [52, 70, 78, 79] and unloaded sliding of unregulated F-actin [80] have previously been reported to increase with elevated Pi. This is generally understood to be the result of reversal of cross-bridge attachment, which decreases  $t_s$  as demonstrated at the single molecule level by Baker et al. [81], thus reducing the number of strongly attached cross-bridges and increasing  $s_m$  (1). The relatively greater enhancement of sliding speed at lower temperatures results in a generally shallow slope of speed versus temperature for both regulated thin filaments and unregulated F-actin (Figure 5) that corresponds to a regime of relatively low  $E_a$ ; in contrast to the result with low ATP, the expectation is that elevated Pi should shift  $T_t$  to a higher temperature (Figure 6). Taken together, the data in Figure 5 illustrate that the relative importance of factors which influence cross-bridge cycling kinetics and/or filament sliding speed varies with temperature around the physiological range, and which are rate-limiting also varies as implicated in Figure 6. This suggests that energetic state may impact cardiac function when core body temperature varies,



such as in mild hypothermia or with exercise, in ways that may seem counterintuitive [31].

**4.3. Implications for Understanding Cardiovascular Diseases.** Figure 4 illustrates that the microthermal heater can be used to study effects of disease-related mutations in human cardiac  $\text{Ca}^{2+}$  regulatory proteins on function of individual thin filaments. This clearly goes beyond, and will ultimately help explain, prior work that examined physical properties of the mutant proteins in bulk solution, and the  $\text{Ca}^{2+}$ -dependence of function. cTn mutations may influence not just  $s_m$  (TnI K206Q and TnT R278C), but also the temperature dependence of  $E_a$  (TnI K206Q and TnT R278C) and possibly  $T_t$  (TnI K206Q). The mutations may also influence the temperature at which thin-filament structure is affected to the extent that dysregulation occurs and  $\text{Ca}^{2+}$  dependent function is altered, whether the disease-related change in function is most relevant in the myofilaments, or perhaps in the nucleus [82]. For all three Tn mutants examined (TnI R145G, TnI K206Q, and TnT R278C) mutations destabilized thin-filament structure and function at lower temperatures than WT; this effect was particularly noticeable for an FHC mutant of human cardiac Tm (E180G) that causes extreme shifts in  $\text{Ca}^{2+}$  sensitivity [33, 40]. Thus, we anticipate that the thermoelectric heater will be generally useful for characterization of clinically relevant mutants of thin filament protein structural stability through assessment of function at the level of individual thin filaments.

**4.4. Conclusion.** Results demonstrate the utility of our thermoelectric controller for investigating molecular mechanisms underlying biomolecular motor function, and cardiovascular diseases related to altered biomechanics of cardiac myofilament proteins. This assay provides a novel view of structure-function relationships for cardiac thin filaments.

## Acknowledgments

The authors gratefully acknowledge L. A. McFadden for purifying myosin and actin; V. F. Miller for expression and M. Seavy for HPLC purification of tropomyosin; R. Dhanarajan from the Biological Science Molecular Cloning Facility for assistance with mutagenesis; Dr. S. Miller from the Biological Science DNA Sequencing Facility for assistance with DNA sequencing; L. A. Compton for assistance with gel analysis; K. Riddle from the Biological Science Imaging Resource for assistance with MetaMorph; Dr. J. R. Grubich for assistance with preliminary experiments; J. Bhuvasekhar and W. Chase for assistance with data analysis; Dr. B. Schoffstall for critical comments. This work was supported by NIH/NHLBI HL63974 (PBC), American Heart Association FL/PR Affiliate 0315097B (NMB), and NSF NIRT Grant ECS-0210332 (PX).

## References

- [1] H. Hess, "Toward devices powered by biomolecular motors," *Science*, vol. 312, no. 5775, pp. 860–861, 2006.
- [2] H. Hess and V. Vogel, "Molecular shuttles based on motor proteins: active transport in synthetic environments," *Journal of Biotechnology*, vol. 82, no. 1, pp. 67–85, 2001.
- [3] M. Sundberg, R. Bunk, N. Albet-Torres et al., "Actin filament guidance on a chip: toward high-throughput assays and lab-on-a-chip applications," *Langmuir*, vol. 22, no. 17, pp. 7286–7295, 2006.
- [4] J. A. Jaber, P. B. Chase, and J. B. Schlenoff, "Actomyosin-driven motility on patterned polyelectrolyte mono- and multilayers," *Nano Letters*, vol. 3, no. 11, pp. 1505–1509, 2003.
- [5] G. Mihajlović, N. M. Brunet, J. Trbović, P. Xiong, S. Von Molnár, and P. B. Chase, "All-electrical switching and control mechanism for actomyosin-powered nanoactuators," *Applied Physics Letters*, vol. 85, no. 6, pp. 1060–1062, 2004.
- [6] T. J. Grove, K. A. Puckett, N. M. Brunet et al., "Packaging actomyosin-based biomolecular motor-driven devices for nanoactuator applications," *IEEE Transactions on Advanced Packaging*, vol. 28, no. 4, pp. 556–563, 2005.
- [7] L. Ionov, M. Stamm, and S. Diez, "Reversible switching of microtubule motility using thermoresponsive polymer surfaces," *Nano Letters*, vol. 6, no. 9, pp. 1982–1987, 2006.
- [8] M. S. Parmacek and R. J. Solaro, "Biology of the troponin complex in cardiac myocytes," *Progress in Cardiovascular Diseases*, vol. 47, no. 3, pp. 159–176, 2004.
- [9] J. C. Tardiff, "Thin filament mutations: developing an integrative approach to a complex disorder," *Circulation Research*, vol. 108, no. 6, pp. 765–782, 2011.
- [10] F. Ahmad, J. G. Seidman, and C. E. Seidman, "The genetic basis for cardiac remodeling," *Annual Review of Genomics and Human Genetics*, vol. 6, pp. 185–216, 2005.
- [11] A. M. Gordon, E. Homsher, and M. Regnier, "Regulation of contraction in striated muscle," *Physiological Reviews*, vol. 80, no. 2, pp. 853–924, 2000.
- [12] A. M. Gordon, M. A. LaMadrid, Y. Chen, Z. Luo, and P. B. Chase, "Calcium regulation of skeletal muscle thin filament motility *in vitro*," *Biophysical Journal*, vol. 72, no. 3, pp. 1295–1307, 1997.
- [13] B. Schoffstall, N. M. Brunet, S. Williams et al., " $\text{Ca}^{2+}$  sensitivity of regulated cardiac thin filament sliding does not depend on myosin isoform," *Journal of Physiology*, vol. 577, no. 3, pp. 935–944, 2006.
- [14] E. Homsher, B. Kim, A. Bobkova, and L. S. Tobacman, "Calcium regulation of thin filament movement in an *in vitro* motility assay," *Biophysical Journal*, vol. 70, no. 4, pp. 1881–1892, 1996.
- [15] E. Homsher, D. M. Lee, C. Morris, D. Pavlov, and L. S. Tobacman, "Regulation of force and unloaded sliding speed in single thin filaments: effects of regulatory proteins and calcium," *Journal of Physiology*, vol. 524, no. 1, pp. 233–243, 2000.
- [16] E. Homsher, M. Nili, I. Y. Chen, and L. S. Tobacman, "Regulatory proteins alter nucleotide binding to acto-myosin of sliding filaments in motility assays," *Biophysical Journal*, vol. 85, no. 2, pp. 1046–1052, 2003.
- [17] J. A. Gorga, D. E. Fishbaugher, and P. VanBuren, "Activation of the calcium-regulated thin filament by myosin strong binding," *Biophysical Journal*, vol. 85, no. 4, pp. 2484–2491, 2003.
- [18] E. W. Clemmens and M. Regnier, "Skeletal regulatory proteins enhance thin filament sliding speed and force by skeletal HMM," *Journal of Muscle Research and Cell Motility*, vol. 25, no. 7, pp. 515–525, 2004.
- [19] H. Fujita, D. Sasaki, S. Ishiwata, and M. Kawai, "Elementary steps of the cross-bridge cycle in bovine myocardium with and



- without regulatory proteins," *Biophysical Journal*, vol. 82, no. 2, pp. 915–928, 2002.
- [20] B. Schoffstall, V. A. Labarbera, N. M. Brunet et al., "Interaction between troponin and myosin enhances contractile activity of myosin in cardiac muscle," *DNA and Cell Biology*, vol. 30, no. 9, pp. 653–659, 2011.
  - [21] H. Fujita and M. Kawai, "Temperature effect on isometric tension is mediated by regulatory proteins tropomyosin and troponin in bovine myocardium," *Journal of Physiology*, vol. 539, no. 1, pp. 267–276, 2002.
  - [22] P. P. de Tombe and G. J. M. Stienen, "Impact of temperature on cross-bridge cycling kinetics in rat myocardium," *Journal of Physiology*, vol. 584, no. 2, pp. 591–600, 2007.
  - [23] P. M. L. Janssen, L. B. Stull, and E. Marbán, "Myofilament properties comprise the rate-limiting step for cardiac relaxation at body temperature in the rat," *American Journal of Physiology*, vol. 282, no. 2, pp. H499–H507, 2002.
  - [24] D. A. Martyn, B. B. Adhikari, M. Regnier, J. Gu, S. Xu, and L. C. Yu, "Response of equatorial X-ray reflections and stiffness to altered sarcomere length and myofilament lattice spacing in relaxed skinned cardiac muscle," *Biophysical Journal*, vol. 86, no. 2, pp. 1002–1011, 2004.
  - [25] M. E. Coupland and K. W. Ranatunga, "Force generation induced by rapid temperature jumps in intact mammalian (rat) skeletal muscle fibres," *Journal of Physiology*, vol. 548, no. 2, pp. 439–449, 2003.
  - [26] D. G. Stephenson and D. A. Williams, "Temperature-dependent calcium sensitivity changes in skinned muscle fibres of rat and toad," *Journal of Physiology*, vol. 360, pp. 1–12, 1985.
  - [27] K. W. Ranatunga and S. R. Wylie, "Temperature-dependent transitions in isometric contractions of rat muscle," *Journal of Physiology*, vol. 339, pp. 87–95, 1983.
  - [28] K. W. Ranatunga, "Temperature dependence of mechanical power output in mammalian (rat) skeletal muscle," *Experimental Physiology*, vol. 83, no. 3, pp. 371–376, 1998.
  - [29] E. P. Debold, J. Romatowski, and R. H. Fitts, "The depressive effect of Pi on the force-pCa relationship in skinned single muscle fibers is temperature dependent," *American Journal of Physiology*, vol. 290, no. 4, pp. C1041–C1050, 2006.
  - [30] B. R. MacIntosh, "Role of calcium sensitivity modulation in skeletal muscle performance," *News in Physiological Sciences*, vol. 18, no. 6, pp. 222–225, 2003.
  - [31] J. Weisser, J. Martin, E. Bisping et al., "Influence of mild hypothermia on myocardial contractility and circulatory function," *Basic Research in Cardiology*, vol. 96, no. 2, pp. 198–205, 2001.
  - [32] J. Köhler, Y. Chen, B. Brenner et al., "Familial hypertrophic cardiomyopathy mutations in troponin I (K183Δ, G203S, K206Q) enhance filament sliding," *Physiological Genomics*, vol. 14, pp. 117–128, 2003.
  - [33] F. Wang, N. M. Brunet, J. R. Grubich et al., "Facilitated cross-bridge interactions with thin filaments by familial hypertrophic cardiomyopathy mutations in  $\alpha$ -tropomyosin," *Journal of Biomedicine and Biotechnology*, vol. 2011, Article ID 435271, 12 pages, 2011.
  - [34] B. Gafurov, S. Fredricksen, A. Cai, B. Brenner, P. B. Chase, and J. M. Chalovich, "The  $\Delta$ 14 mutation of human cardiac troponin T enhances ATPase activity and alters the cooperative binding of S1-ADP to regulated actin," *Biochemistry*, vol. 43, no. 48, pp. 15276–15285, 2004.
  - [35] F. Takahashi-Yanaga, S. Morimoto, K. Harada et al., "Functional consequences of the mutations in human cardiac troponin I gene found in familial hypertrophic cardiomyopathy," *Journal of Molecular and Cellular Cardiology*, vol. 33, no. 12, pp. 2095–2107, 2001.
  - [36] R. Lang, A. V. Gomes, J. Zhao, P. R. Housmans, T. Miller, and J. D. Potter, "Functional analysis of a troponin I (R145G) mutation associated with familial hypertrophic cardiomyopathy," *Journal of Biological Chemistry*, vol. 277, no. 14, pp. 11670–11678, 2002.
  - [37] D. Szczesna, R. Zhang, J. Zhao, M. Jones, G. Guzman, and J. D. Potter, "Altered regulation of cardiac muscle contraction by troponin T mutations that cause familial hypertrophic cardiomyopathy," *Journal of Biological Chemistry*, vol. 275, no. 1, pp. 624–630, 2000.
  - [38] F. Yanaga, S. Morimoto, and I. Ohtsuki, "Ca<sup>2+</sup> sensitization and potentiation of the maximum level of myofibrillar ATPase activity caused by mutations of troponin T found in familial hypertrophic cardiomyopathy," *Journal of Biological Chemistry*, vol. 274, no. 13, pp. 8806–8812, 1999.
  - [39] K. Elliott, H. Watkins, and C. S. Redwood, "Altered regulatory properties of human cardiac troponin I mutants that cause hypertrophic cardiomyopathy," *Journal of Biological Chemistry*, vol. 275, no. 29, pp. 22069–22074, 2000.
  - [40] F. Bai, A. Weis, A. K. Takeda, P. B. Chase, and M. Kawai, "Enhanced active cross-bridges during diastole: molecular pathogenesis of tropomyosin's HCM mutations," *Biophysical Journal*, vol. 100, no. 4, pp. 1014–1023, 2011.
  - [41] M. C. Mathur, P. B. Chase, and J. M. Chalovich, "Several cardiomyopathy causing mutations on tropomyosin either destabilize the active state of actomyosin or alter the binding properties of tropomyosin," *Biochemical and Biophysical Research Communications*, vol. 406, no. 1, pp. 74–78, 2011.
  - [42] A. Kataoka, C. Hemmer, and P. B. Chase, "Computational simulation of hypertrophic cardiomyopathy mutations in Troponin I: influence of increased myofilament calcium sensitivity on isometric force, ATPase and [Ca<sup>2+</sup>]<sub>i</sub>," *Journal of Biomechanics*, vol. 40, no. 9, pp. 2044–2052, 2007.
  - [43] P. B. Chase, Y. Chen, K. L. Kulin, and T. L. Daniel, "Viscosity and solute dependence of F-actin translocation by rabbit skeletal heavy meromyosin," *American Journal of Physiology*, vol. 278, no. 6, pp. C1088–C1098, 2000.
  - [44] S. S. Margossian and S. Lowey, "Preparation of myosin and its subfragments from rabbit skeletal muscle," *Methods in Enzymology*, vol. 85, no. C, pp. 55–71, 1982.
  - [45] J. D. Pardee and J. Aspudich, "Purification of muscle actin," *Methods in Enzymology*, vol. 85, no. C, pp. 164–181, 1982.
  - [46] R. W. Heald and S. E. Hitchcock-DeGregori, "The structure of the amino terminus of tropomyosin is critical for binding to actin in the absence and presence of troponin," *Journal of Biological Chemistry*, vol. 263, no. 11, pp. 5254–5259, 1988.
  - [47] P. B. Monteiro, R. C. Lataro, J. A. Ferro, and F. D. C. Reinach, "Functional  $\alpha$ -tropomyosin produced in *Escherichia coli*. A dipeptide extension can substitute the amino-terminal acetyl group," *Journal of Biological Chemistry*, vol. 269, no. 14, pp. 10461–10466, 1994.
  - [48] H. Schagger and G. Von Jagow, "Tricine-sodium dodecyl sulfate-polyacrylamide gel electrophoresis for the separation of proteins in the range from 1 to 100 kDa," *Analytical Biochemistry*, vol. 166, no. 2, pp. 368–379, 1987.
  - [49] S. J. Kron, Y. Y. Toyoshima, T. Q. P. Uyeda, and J. A. Spudich, "Assays for actin sliding movement over myosin-coated surfaces," *Methods in Enzymology*, vol. 196, pp. 399–416, 1991.

- [50] B. Liang, Y. Chen, C. K. Wang et al., "Ca<sup>2+</sup> regulation of rabbit skeletal muscle thin filament sliding: role of cross-bridge number," *Biophysical Journal*, vol. 85, no. 3, pp. 1775–1786, 2003.
- [51] T. Q. P. Uyeda, S. J. Kron, and J. A. Spudich, "Myosin step size estimation from slow sliding movement of actin over low densities of heavy meromyosin," *Journal of Molecular Biology*, vol. 214, no. 3, pp. 699–710, 1990.
- [52] E. Pate and R. Cooke, "Addition of phosphate to active muscle fibers probes actomyosin states within the powerstroke," *Pflügers Archiv*, vol. 414, no. 1, pp. 73–81, 1989.
- [53] P. B. Chase and M. J. Kushmerick, "Effect of physiological ADP concentrations on contraction of single skinned fibers from rabbit fast and slow muscles," *American Journal of Physiology*, vol. 268, no. 2, pp. C480–C489, 1995.
- [54] R. Silverstein, J. Voet, D. Reed, and R. H. Abeles, "Purification and mechanism of action of sucrose phosphorylase," *Journal of Biological Chemistry*, vol. 242, no. 6, pp. 1338–1346, 1967.
- [55] R. C. Weast, *CRC Handbook of Chemistry and Physics*, CRC Press, Boca Raton, Fla, 1982, 63rd edition, 1982.
- [56] P. B. Chase, T. M. Denking, and M. J. Kushmerick, "Effect of viscosity on mechanics of single, skinned fibers from rabbit psoas muscle," *Biophysical Journal*, vol. 74, no. 3, pp. 1428–1438, 1998.
- [57] A. V. Gomes and J. D. Potter, "Molecular and cellular aspects of troponin cardiomyopathies," *Annals of the New York Academy of Sciences*, vol. 1015, pp. 214–224, 2004.
- [58] R. Rossi, M. Maffei, R. Bottinelli, and M. Canepari, "Temperature dependence of speed of actin filaments propelled by slow and fast skeletal myosin isoforms," *Journal of Applied Physiology*, vol. 99, no. 6, pp. 2239–2245, 2005.
- [59] M. Anson, "Temperature dependence and arrhenius activation energy of F-actin velocity generated *in vitro* by skeletal myosin," *Journal of Molecular Biology*, vol. 224, no. 4, pp. 1029–1038, 1992.
- [60] N. Golitsina, Y. An, N. J. Greenfield et al., "Effects of two familial hypertrophic cardiomyopathy-causing mutations on  $\alpha$ -tropomyosin structure and function," *Biochemistry*, vol. 38, no. 12, p. 3850, 1999.
- [61] E. V. Kremneva, O. P. Nikolaeva, N. B. Gusev, and D. I. Levitsky, "Effects of troponin on thermal unfolding of actin-bound tropomyosin," *Biochemistry*, vol. 68, no. 7, pp. 802–809, 2003.
- [62] E. Kremneva, S. Boussouf, O. Nikolaeva, R. Maytum, M. A. Geeves, and D. I. Levitsky, "Effects of two familial hypertrophic cardiomyopathy mutations in  $\alpha$ -tropomyosin, Asp175Asn and Glut180Gly, on the thermal unfolding of actin-bound tropomyosin," *Biophysical Journal*, vol. 87, no. 6, pp. 3922–3933, 2004.
- [63] J. W. Shriver and U. Kamath, "Differential scanning calorimetry of the unfolding of myosin subfragment 1, subfragment 2, and heavy meromyosin," *Biochemistry*, vol. 29, no. 10, pp. 2556–2564, 1990.
- [64] H. Kato, T. Nishizaka, T. Iga, K. Kinoshita, and S. Ishiwata, "Imaging of thermal activation of actomyosin motors," *Proceedings of the National Academy of Sciences of the United States of America*, vol. 96, no. 17, pp. 9602–9606, 1999.
- [65] P. Vibert, R. Craig, and W. Lehman, "Steric-model for activation of muscle thin filaments," *Journal of Molecular Biology*, vol. 266, no. 1, pp. 8–14, 1997.
- [66] C. Veigel, M. L. Bartoo, D. C. S. White, J. C. Sparrow, and J. E. Molloy, "The stiffness of rabbit skeletal actomyosin cross-bridges determined with an optical tweezers transducer," *Biophysical Journal*, vol. 75, no. 3, pp. 1424–1438, 1998.
- [67] P. Höök and L. Larsson, "Actomyosin interactions in a novel single muscle fiber *in vitro* motility assay," *Journal of Muscle Research and Cell Motility*, vol. 21, no. 4, pp. 357–365, 2000.
- [68] T. S. Moerland and B. D. Sidell, "Contractile responses to temperature in the locomotory musculature of striped bass *Morone saxatilis*," *Journal of Experimental Zoology*, vol. 240, no. 1, pp. 25–33, 1986.
- [69] T. J. Grove, L. A. Mcfadden, P. B. Chase, and T. S. Moerland, "Effects of temperature, ionic strength and pH on the function of skeletal muscle myosin from a eurythermal fish, *Fundulus heteroclitus*," *Journal of Muscle Research and Cell Motility*, vol. 26, no. 4–5, pp. 191–197, 2005.
- [70] M. Kawai, K. Kawaguchi, M. Saito, and S. Ishiwata, "Temperature change does not affect force between single actin filaments and HMM from rabbit muscles," *Biophysical Journal*, vol. 78, no. 6, pp. 3112–3119, 2000.
- [71] C. Karatzaferi, M. K. Chinn, and R. Cooke, "The force exerted by a muscle cross-bridge depends directly on the strength of the actomyosin bond," *Biophysical Journal*, vol. 87, no. 4, pp. 2532–2544, 2004.
- [72] Y. Zhao and M. Kawai, "Kinetic and thermodynamic studies of the cross-bridge cycle in rabbit psoas muscle fibers," *Biophysical Journal*, vol. 67, no. 4, pp. 1655–1668, 1994.
- [73] M. Nyitrai, R. Rossi, N. Adamek, M. A. Pellegrino, R. Bottinelli, and M. A. Geeves, "What limits the velocity of fast-skeletal muscle contraction in mammals?" *Journal of Molecular Biology*, vol. 355, no. 3, pp. 432–442, 2006.
- [74] R. Cooke and W. Bialek, "Contraction of glycerinated muscle fibers as a function of the ATP concentration," *Biophysical Journal*, vol. 28, no. 2, pp. 241–258, 1979.
- [75] E. Pate, M. Lin, K. Franks-Skiba, and R. Cooke, "Contraction of glycerinated rabbit slow-twitch muscle fibers as a function of MgATP concentration," *American Journal of Physiology*, vol. 262, no. 4, pp. C1039–C1046, 1992.
- [76] E. P. Debold, H. Dave, and R. H. Fitts, "Fiber type and temperature dependence of inorganic phosphate: implications for fatigue," *American Journal of Physiology*, vol. 287, no. 3, pp. C673–C681, 2004.
- [77] M. E. Coupland, E. Puchert, and K. W. Ranatunga, "Temperature dependence of active tension in mammalian (rabbit psoas) muscle fibres: effect of inorganic phosphate," *Journal of Physiology*, vol. 536, no. 3, pp. 879–891, 2001.
- [78] P. B. Chase and M. J. Kushmerick, "Effects of pH on contraction of rabbit fast and slow skeletal muscle fibers," *Biophysical Journal*, vol. 53, no. 6, pp. 935–946, 1988.
- [79] C. Karatzaferi, K. Franks-Skiba, and R. Cooke, "Inhibition of shortening velocity of skinned skeletal muscle fibers in conditions that mimic fatigue," *American Journal of Physiology*, vol. 294, no. 3, pp. R948–R955, 2008.
- [80] E. Homsher, F. Wang, and J. R. Sellers, "Factors affecting movement of F-actin filaments propelled by skeletal muscle heavy meromyosin," *American Journal of Physiology*, vol. 262, no. 3, pp. C714–C723, 1992.
- [81] J. E. Baker, C. Brosseau, P. B. Joel, and D. M. Warshaw, "The biochemical kinetics underlying actin movement generated by one and many skeletal muscle myosin molecules," *Biophysical Journal*, vol. 82, no. 4, pp. 2134–2147, 2002.
- [82] F. Z. Asumda and P. B. Chase, "Nuclear cardiac troponin and tropomyosin are expressed early in cardiac differentiation of rat mesenchymal stem cells," *Differentiation*, vol. 83, no. 2, pp. 106–115.

## Research Article

# Detection of Target ssDNA Using a Microfabricated Hall Magnetometer with Correlated Optical Readout

Steven M. Hira,<sup>1</sup> Khaled Aledealat,<sup>2</sup> Kan-Sheng Chen,<sup>2</sup> Mark Field,<sup>3</sup> Gerard J. Sullivan,<sup>3</sup> P. Bryant Chase,<sup>4,5</sup> Peng Xiong,<sup>2,5</sup> Stephan von Molnár,<sup>2,5</sup> and Geoffrey F. Strouse<sup>1,5</sup>

<sup>1</sup> Department of Chemistry and Biochemistry, The Florida State University, Tallahassee, FL 32306-4390, USA

<sup>2</sup> Physics Department, The Florida State University, Tallahassee, FL 32306-4350, USA

<sup>3</sup> Teledyne Scientific Company LLC, Thousand Oaks, CA 90360, USA

<sup>4</sup> Department of Biological Science, The Florida State University, Tallahassee, FL 32306, USA

<sup>5</sup> Integrative NanoScience Institute, The Florida State University, Tallahassee, FL 32306, USA

Correspondence should be addressed to Geoffrey F. Strouse, strouse@chem.fsu.edu

Received 8 July 2011; Accepted 20 August 2011

Academic Editor: Alf Månsson

Copyright © 2012 Steven M. Hira et al. This is an open access article distributed under the Creative Commons Attribution License, which permits unrestricted use, distribution, and reproduction in any medium, provided the original work is properly cited.

Sensing biological agents at the genomic level, while enhancing the response time for biodetection over commonly used, optics-based techniques such as nucleic acid microarrays or enzyme-linked immunosorbent assays (ELISAs), is an important criterion for new biosensors. Here, we describe the successful detection of a 35-base, single-strand nucleic acid target by Hall-based magnetic transduction as a mimic for pathogenic DNA target detection. The detection platform has low background, large signal amplification following target binding and can discriminate a single, 350 nm superparamagnetic bead labeled with DNA. Detection of the target sequence was demonstrated at 364 pM (<2 target DNA strands per bead) target DNA in the presence of 36  $\mu$ M nontarget (noncomplementary) DNA (<10 ppm target DNA) using optical microscopy detection on a GaAs Hall mimic. The use of Hall magnetometers as magnetic transduction biosensors holds promise for multiplexing applications that can greatly improve point-of-care (POC) diagnostics and subsequent medical care.

## 1. Introduction

The ability to detect and discriminate specific nucleic acid sequences within a biological mixture has implications for genome sequencing and single-nucleotide polymorphism (SNP) detection, biowarfare target detection, and the development of an efficient point-of-care (POC) device for pathogen identification [1–6]. Through the integration of biology with nanotechnology, a detection platform utilizing magnetic transduction can capitalize on the high biological specificity of DNA base pairing, the scalability of nanotechnology, the selectivity of self-assembled monolayer technology, and the sensitivity of magnetic transduction [7, 8]. Coupling the extreme sensitivity of Hall-based magnetic detection, which operates over a wide magnetic field and temperature range, with the versatility and specificity of DNA base pairing can allow the realization of a new biological detection strategy that will improve POC diagnostics and subsequent medical treatment.

In this paper the detection of a 35-base pair DNA target sequence is demonstrated at the single-bead level on a Hall magnetometer biosensor. The biosensor is able to identify a single-bead bound to target DNA (35 bases) and is amenable to the discrimination of DNA at the 364 pM concentration in a background of 36  $\mu$ M noncomplementary DNA (<10 ppm). The detection strategy utilizes three-strand DNA annealing to colocalize a superparamagnetic (SPM) bead labeled probe strand, a label-free target strand, and a receptor strand at the surface of the Hall device. Localization of the SPM bead on the surface of the Hall cross' active area through annealing of all three DNA strands induces a voltage change in the Hall junction due to a change in the local magnetic field. This study demonstrates the effective use of an optical/magnetic bead detection platform to measure DNA at the picomolar (pM) level in the presence of  $\mu$ M extraneous DNA. At the concentrations of DNA used in the mimic, the device platform can be optimized for clinical



translation. Development of single-nucleotide mismatch and real-world pathogen samples are underway, but are beyond the scope of the current study.

Many biosensors [9–24] still suffer from limitations in stability, portability, sensitivity, and selectivity. Traditional ELISA based sensor platforms are sensitive at the pM level and require 1–2 days for detection of a protein target. GMR sensors, which are recent additions to the biosensor field, can detect at the pM or femtomolar (fM) levels if magnetically assisted [25]. Optics-based sensors, whether colorimetric or using FRET assays, allow detection at the attomolar (aM) to nanomolar (nM) level. A novel approach utilized in some optics-based biosensors is the use of three-strand DNA annealing to produce an optical response that is directly proportional to the annealing event. The use of three-strand ssDNA annealing strategies has been investigated for biological target detection for the last 15 years and has been shown to increase overall sensitivity. Mirkin et al. first used the controlled assembly and aggregation of DNA labeled Au nanoparticles in solution as a colorimetric sensor [26]. Years later Taton et al. [14] utilized the tethering of DNA-coated Au nanoparticles to DNA-coated surfaces using an unlabeled target sequence for Ag-amplified colorimetric detection with single-nucleotide mismatch sensitivity. The technology has evolved further and been shown to detect  $\sim 6 \times 10^6$  copies of genomic DNA using Ag-amplified scanometric detection on a commercial platform [27, 28]. In addition to the assembly of Au nanoparticles, the assembly of Ag nanoparticles onto smooth metal films using three-strand DNA assembly has been demonstrated for surface-enhanced Raman spectroscopic detection of DNA sequences [29]. Optical methods focused on fluorescence blotting assays have reached aM sensitivities [23], while methods employing energy transfer detection of the three-strand assembly allow nM pathogen DNA detection [20]. Despite these applications of multisequence DNA assembly in the literature, the use of three-strand assemblies for magnetic detection has only been suggested and remains underutilized [30].

Sensing technologies based on magnetic transduction, whether Hall magnetometry or giant magnetoresistive (GMR), circumvent many of the limitations of classical sensor designs since they exhibit low sensitivity to the surrounding biological matrix of samples, can be mass produced, and, if configured properly, can offer dynamic detection in a microfabricated scalable platform [31, 32]. Magnetic transduction-based sensing technologies cover a wide range of methods including GMR sensors through the use of spin valves [25, 33–37] or bead array counters (BARCs) [38, 39] and Hall-based sensors [40–45]. Already, examples of GMR devices have demonstrated detection of matrix-insensitive protein assays at the fM level using a magnetic transduction-based device [37] and aM level by adding additional magnetic beads to amplify the signal [46]. The use of Hall magnetometry for DNA biosensing could represent the next generation for magnetic transduction-based devices, since a Hall junction is a 4-point probe device (current, voltage), scalable down to the nanoscale, can be mass produced using standard lithographic and fabrication methods, displays a linear response through a wide range of magnetic fields [47]

with minimal influence of temperature [48] (which varies to optimize DNA annealing), and can operate at high frequency allowing for phase-sensitive detection of the transient fields associated with SPM nanoscale beads. Hall biosensors may thus offer a useful alternative to exclusively fluorescence-based microarray technologies.

## 2. Materials and Methods

**2.1. Substrate Fabrication and Passivation.** The  $1 \mu\text{m}^2$  Hall junction is fabricated into the surface of an epitaxially grown heterostructure consisting of a GaAs substrate containing an InAs quantum well core, and  $\text{SiO}_2$  (60 nm) was sputtered onto the device followed by a layer of Ti (5 nm) and deposition of  $3 \mu\text{m}$  gold pads (20 nm thick) directly over the protected Hall junction. Registry of the gold pad was accomplished by photolithography using alignment markers in the photomask. Mimic microarrays ( $3 \mu\text{m}$  diameter circles and  $2 \mu\text{m} \times 4 \mu\text{m}$  rectangular gold patterns) were fabricated onto the (100) face of a single-crystal GaAs wafer. The substrates were cleaned prior to use for 1 min at low power in oxygen plasma (Harrick Plasma PDC-001). The substrates were rinsed with absolute ethanol for 1 min and dried under a constant stream of nitrogen gas, and the  $\text{SiO}_2$  surface was passivated by 2-[methoxy(polyethyleneoxy)propyl]-trimethoxysilane (Gelest) [49].

**2.2. DNA Immobilization and Hybridization.** Synthetic DNA oligonucleotides were commercially synthesized (Midland Certified Reagent Company). The two-strand DNA system consisted of a 5' disulfide modified complementary receptor sequence 5'-RSSR/-GAC TAC TCT ATC GGC AGC TAA GAT TGT CAC AGT CG-3', a 5' disulfide modified noncomplementary receptor sequence 5'-RSSR/-CGA CTG TGA CAA TCT TAG CTG CCG ATA GAG TAG TC-3', and a 5' modified biotinylated probe sequence with an internal fluorescein dT 5'-BIOTIN/-CGA C-/iFLUORDT/-G TGA CAA TCT TAG CTG CCG ATA GAG TAG TC-3'. The three-strand DNA system consisted of a probe sequence 5'-TCA TTC ACA CAC -/iFLUORDT/-CG/3BIOTIN/-3' labeled with an internal fluorescein dT and biotin, receptor sequence 5'-/RSSR/GTC TTG TCT CCT GTC AGC TA-3' with a disulfide modifier, a 35-base unmodified target sequence 5'-CGA GTG TGT GAA TGA TAG CTG ACA GGA GAC AAG AC-3', and a 35-base unmodified nontarget control sequence 5'-GTC TAA GAG TGT CCT GGC TAT GAT CCG TGA GTA TG-3'. The lyophilized DNA was buffer-exchanged using an NAP-V size exclusion column (GE Healthcare) equilibrated with 20 mM sodium phosphate buffer, 50 mM NaCl pH 7.0.

The receptor DNA (disulfide not previously reduced) was incubated on top of the device in the form of a  $50 \mu\text{L}$  droplet at a DNA concentration of  $9 \mu\text{M}$  for 6 hrs in an enclosed incubation chamber. The incubation chamber also contains a supersaturated NaCl solution to maintain constant humidity within the enclosed chamber. The device was immersed in 5 mL of  $18.2 \text{ M}\Omega\text{-cm}$  nanopure  $\text{H}_2\text{O}$  (Barnstead) containing 0.1% Tween-20 (v/v), twice in 5 mL of  $18.2 \text{ M}\Omega\text{-cm}$  nanopure  $\text{H}_2\text{O}$  to rinse and remove unbound

DNA, and dried under a constant stream of nitrogen gas. The reporter DNA was bioconjugated to the SPM nanobead (350 nm mean size, Bangs Laboratories) through a biotin-streptavidin linkage at 30°C for 1 hr. The DNA-nanobead conjugate was purified away from free DNA using magnetic separation and washing the sample 5 times with 20 mM sodium phosphate buffer, 300 mM NaCl, pH 7.0. The three-strand DNA strategy included a preconjugation step of the target DNA to the probe DNA-SPM conjugate at 80°C and was allowed to slowly cool to room temperature over 1 hr. Unbound nucleic acid was removed by magnetic separation. The hybridization assay was carried out by incubating a 25  $\mu$ L droplet of target biotinylated DNA (7  $\mu$ M) bound to streptavidin-coated SPM beads for 2 hrs in an enclosed incubation chamber containing a super saturated NaCl solution. The device was washed once in 5 mL of 20 mM sodium phosphate buffer with 300 mM NaCl at pH 7.0 containing 0.1% Tween-20 (v/v), twice in 5 mL of 20 mM sodium phosphate buffer with 300 mM NaCl at pH 7.0, stored in 20 mM phosphate buffer with 300 mM NaCl at pH 7.0, and protected from ambient light.

**2.3. Microscopy.** Fluorescence microscopy was carried out on an inverted Nikon TE2000-E2 Eclipse microscope (Nikon Instruments Inc.) equipped with a Nikon CFI Plan Apochromat 40x objective (NA 0.95, 0.14 mm WD). Wide-field imaging of the substrates utilized an EXFO E-Cite illumination source and a FITC filter (Chroma, ex: 480/30, DCLP: 505, em: 535/40). Images were acquired on a Photometrics Coolsnap HQ<sub>2</sub> CCD camera. Bright-field overlays utilized differential interference contrast (DIC) to observe the differences in the index of refraction of the samples. The data were analyzed using Nikon NIS Elements software. Scanning electron microscopy (SEM) was carried out on a FEI Nova 400 Nano SEM and utilizing a through-the-lens (TLD) detector. The SEM images were acquired using a 32-scan average.

**2.4. Hall Measurement.** The detection of preimmobilized SPM beads was achieved by employing an ac phase-sensitive technique as previously reported [45]. The Hall device was biased with a dc current  $I = 50 \mu$ A, and the beads were magnetized with an ac magnetic field; lock-in detection of the ac Hall voltage occurred at the magnetic field frequency. The application of an additional dc magnetic field reduced the SPM bead susceptibility and thus the ac magnetic field generated by the beads. This produced a drop in the ac Hall voltage signal indicating the presence of the beads.

### 3. Results and Discussion

**3.1. Design.** A schematic of the Hall magnetometer-based biosensor and detection strategy used for detection of a single-stranded DNA (ssDNA) target sequence by three-strand annealing over the surface of a 1  $\mu$ m<sup>2</sup> Hall junction is shown in Figure 1. The biosensor platform is assembled in parallel steps to limit the processing time for target

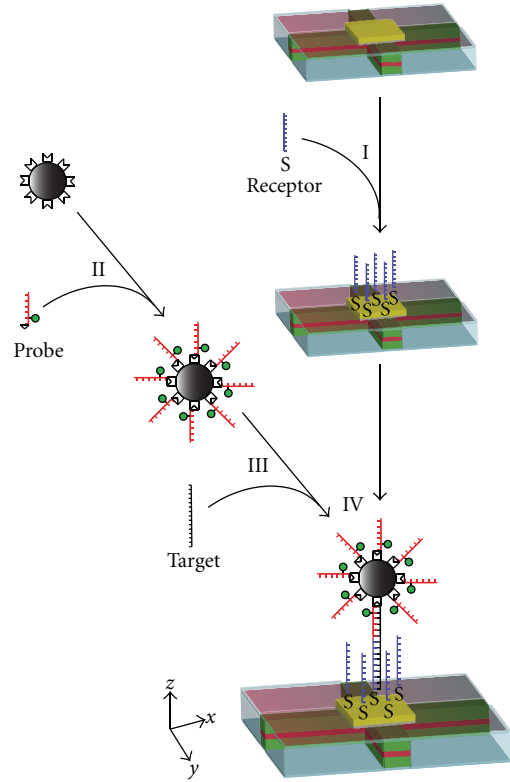


FIGURE 1: Generalized schematic for the detection of label-free target DNA using Hall magnetometry. The label-free target DNA (black) is detected by immobilization at the Hall device via complementary base pairing with receptor DNA (blue) preassembled on the Hall device surface to additional complementary probe DNA (red) with an internal fluorescent marker pre-conjugated to the surface of a magnetic nanobead resulting in a detectable Hall signal. Nanobead is not drawn to scale.

detection. This parallels work by others to detect three-strand annealing using different sensor modalities, SERS [29] and colorimetry-(gold plasmon shift) based technologies, by simultaneously annealing the target, sensor, and probe sequences [14, 26–28]. Our platform is composed of six 1  $\mu$ m<sup>2</sup> Hall junctions (Figure 2(a)) etched into an epitaxially grown, vertically integrated InAs quantum well heterostructure isolated from the surrounding environment by a 60 nm overlayer of silicon dioxide, as previously described [42, 44]. The six available Hall junctions are divided into a set of three bioactive sensors (i, ii, and iii) and three nonactive controls (ic, iic, and iiic). The bioactive sensors are generated via patterning 3  $\mu$ m gold bonding pads evaporated onto the SiO<sub>2</sub> layer only over the bioactive junctions (i, ii, iii). The bonding pads provide a site for self-assembly of the receptor single-strand DNA onto the surface of the Hall junction sensor without modifying the properties of the InAs quantum well heterostructures. The nonactive controls do not have the gold bonding pad. To minimize biofouling of the device by the biological constituents in the sample via nonspecific interactions, the exposed SiO<sub>2</sub> surface is selectively modified by a polyethylene-glycol-conjugated silane moiety [49]. The bioactive junctions are modified by self-assembly of the



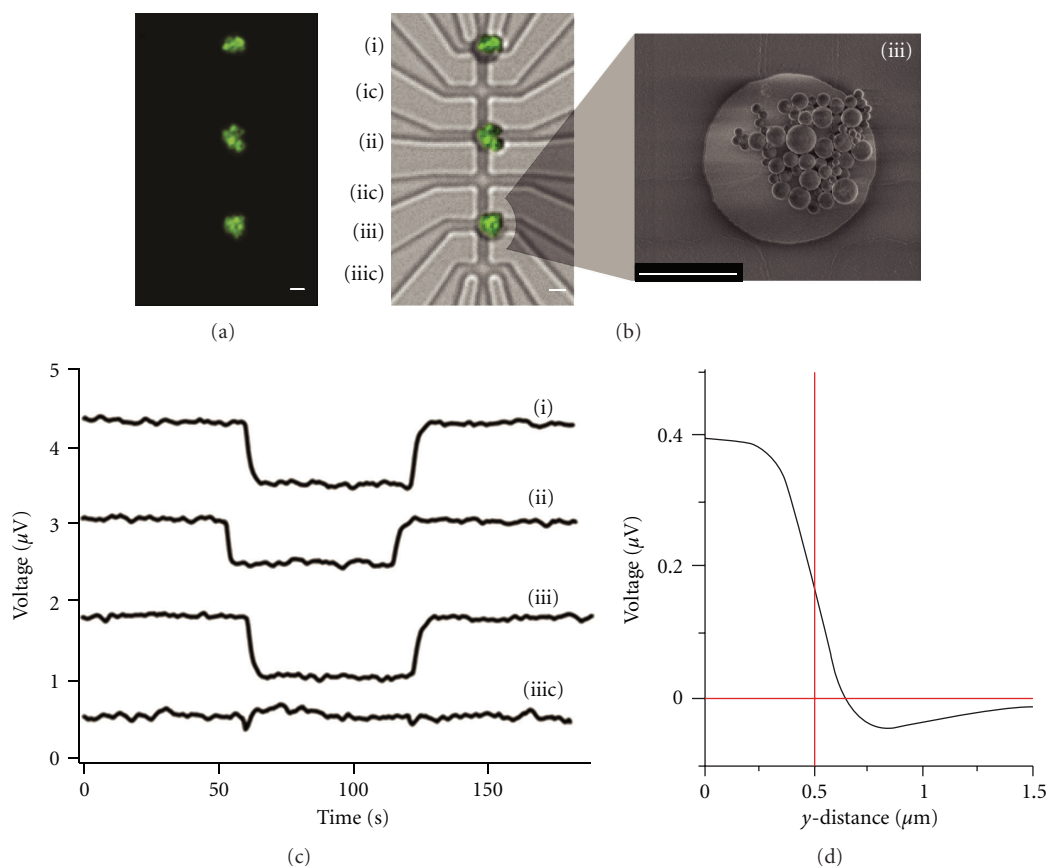


FIGURE 2: (a) Optical microscopy characterization (wide-field fluorescence and DIC overlay) of three-strand DNA assembly is shown by the presence of green fluorescence indicating the presence of probe DNA. (b) SEM was used to evaluate the location and to quantify the number of nanobeads contributing to the Hall response for (iii), where the grey box designates the location of the underlying Hall junction. (c) Hall responses for three active junctions (i, ii, iii) and a single control junction (iiic) are plotted as Hall voltage offset versus time; the presence of nanobeads over the active Hall junctions results in a drop in Hall voltage when a dc magnetic field is applied. (d) The theoretical device signal stemming from a single 344 nm SPM bead is shown to the right as a function of position over the Hall junction further illustrating the local sensitivity of Hall magnetometry. Scale bars =  $2 \mu m$  in (a) and (b).

receptor ssDNA (blue in Figure 1) onto the gold pads by exposure of a solution of the receptor to the Hall junction platform (Figure 1(I)) and subsequent washing to remove unbound DNA. The fluorescein-labeled probe ssDNA sequence (red in Figure 1) is preappended to the SPM bead platform via streptavidin-biotin conjugation (Figure 1-(II)).

Prior to the detection of the target DNA sequence (black in Figure 1), the probe strand and the target strand were prehybridized (Figure 1-(III)). The detection of the target DNA was then accomplished by annealing the SPM bead-probe-target complex with the receptor sequence (blue) preassembled at the surface of the Hall device platform at room temperature (Figure 1-(IV)). The assembly of the three-strand sequence requires 3 hrs, which is equivalent to standard FRET, plasmonic, GMR and SERS-based detection scenarios, but far faster than optical chip techniques that can require 16–24 hrs to achieve hybridization. Although the simultaneous addition of all three ssDNA components is experimentally feasible, stepwise assembly allowed the added benefit that the observed signal is not artificially enhanced by nonspecific, non-DNA bound SPM beads. All unbound

nucleic acid species and nucleic acid-labeled SPM beads are removed by magnetic separation prior to final three-strand DNA assembly and washed prior to Hall detection. The strategy allows a specific binding event at the electrically isolated gold pad to induce a direct voltage response in the device without altering the device properties directly, as would be observed in SPR-based devices. The sequential, parallel assembly strategy (Figure 1(I)–(IV)) allows convenient concentration amplification for the target ssDNA from extraneous DNA fragments.

**3.2. Detection.** In Figure 2 the detection of the 35-base target on the dual optical/Hall device sensor is shown for a  $25 \mu L$  droplet containing  $7 \mu M$  DNA. The specificity of the assembly of the three-strand DNA complex onto the gold pad (grey circle) over the Hall junction is clearly observed in the wide-field fluorescence overlaid with differential interference contrast (DIC) micrograph (Figure 2(a)). The observed green photoluminescence in Figure 2(a) arises from the fluorescein label on the probe strand and requires the three-strand annealing process to occur in order for the

probe to be optically detectable. The lack of nonspecific binding of the probe to regions outside of the gold pad region confirms the specificity of the three-strand assembly protocol. The specificity of the assembly on the gold pads is further confirmed by comparing the optical micrograph (Figure 2(a)) and a scanning electron micrograph of the same region (Figure 2(b); see Figure S1 in Supplementary Material available online at doi:10.1155/2012/492730). Scanning electron microscopy (SEM) imaging of junction (iii) indicates that  $\sim 73$  beads are present on the  $3\ \mu\text{m}$  (diameter) gold pad. Inspection of the DIC image of junction (iii) (Figure 2(a)) reveals the registry between the underlying Hall junction in the SEM image (Figure 2(b), grey box), and the gold pad on the surface of the Hall magnetometer results in only  $\sim 12$  na-nobeads being positioned directly or partially over the active area of the Hall junction.

For detection of DNA annealing, the presence of the SPM bead is measured as a change in voltage by the use of both ac and dc magnetic fields. The use of both ac and dc fields allows for a binding event signal to be cleanly isolated by using lock-in detection. In the absence of the external dc field, no signal is detectable in the Hall junction. The ac magnetic field of 3.76 mT at 93 Hz is used to induce magnetization of the SPM nanobeads. The 70.6 mT dc magnetic field (NdFeB) is applied perpendicular to the Hall junction to shift the magnetization of the nanobeads to lower susceptibility as given by the expression  $\Delta V_H \propto \Delta M$ , where  $\Delta M$  is the change in the ac magnetization before and after the dc field was applied. The Hall sensor was operated in constant current mode with an applied dc current of 50  $\mu\text{A}$ .

The voltage responses to binding of the target sequence with the preappended probe and 350 nm magnetic beads to receptor strands on the three active junctions (i, ii, iii), plus one control junction without any beads (iiic) are shown in Figure 2(c). The voltage response for all junctions and controls are shown in Figure S1. The voltage across the control junction (iiic) is  $0 \pm 0.03\ \mu\text{V}$ . The successful assembly of ssDNA over the active Hall junctions results in a sharp drop in the measured Hall voltage for all three active sensor elements when a dc field was applied. The Hall voltage measurements are  $0.79\ \mu\text{V}$  (signal/noise (S/N) 40),  $0.55\ \mu\text{V}$  (S/N 28), and  $0.78\ \mu\text{V}$  (S/N 39), for (i, ii, iii), respectively. In Figure 2, the observed step function is generated by the application and removal of the external dc magnetic field in the presence of the small ac field to allow lock-in detection. The S/N was determined by averaging the change in signal when the dc field was applied and dividing it by the average standard deviation from zero measured in the absence of the applied dc field. The standard deviation in measured signals for the active junctions is  $0 \pm 0.02\ \mu\text{V}$  as shown in Figure S1.

To analyze the voltage change per binding event, the number of beads per Hall junction must be assessed. In Figure 2(a) and Figure S1, the SEM micrographs indicate the presence of 41 beads on junction (i), 68 beads on junction (ii), and 73 beads on junction (iii). In Figure 2(c), the voltage response for the three pads is similar regardless of the number of beads bound at the center of the Hall junction (Figure 2(c)). The largest expected voltage change in the Hall magnetometer will occur for beads directly

over the Hall junction, falling rapidly for beads positioned  $>0.5\ \mu\text{m}$  from the device center (Figure 2(d)). Directly over the Hall junction (shaded region Figure 2(b)), junction (i) has 8 beads, junction (ii) has 11 beads, and junction (iii) has 12 beads. Calculation of the predicted voltage response as a function of the distance of the bead from the center of the Hall junction is shown in Figure 2(d). For a single 350 nm magnetic bead approximately 272 nm from the Hall device, a voltage response of  $0.4\ \mu\text{V}$  per bead is expected. The experimental value of  $\sim 0.6\text{--}0.8\ \mu\text{V}$  measured in Figure 2(c) following DNA annealing of the target and probe indicates that more than one bead but not all of the bound beads contribute to the measured Hall voltage. For junction (iii), the result suggests the measured voltage is likely dominated by the 12 beads directly over the Hall junction (only beads contained within the grey box in Figure 2(b)). Due to the large size dispersion and subsequent large magnetic content variability in the commercially obtained SPM beads utilized in this study, the calculation of the number of beads contributing to the measured signal cannot be obtained if more than one bead lies directly over the underlying Hall junction. Based on the theoretical voltage (Figure 2(d)) and the observed voltage in response to DNA annealing (Figure 2(c)), a single bead should be detectable.

**3.3. Single-Bead Detection.** Although magnetic transduction devices are remarkably sensitive with detection of a single bead ( $<500\ \text{nm}$ ) reported for an antibody-antigen sandwich-assay-based assembly of a magnetic bead on a micron-sized Hall device [44], and the multiple-bead detection by GMR devices [36], the report of three-strand DNA target detection at the single-magnetic-bead level by a Hall device has not been reported to date. Single-bead detection was observed for a 35-base pair DNA annealing event onto a Hall device, as shown in Figure 3. The Hall voltage response (Figure 3(b)) and corresponding SEM image (Figure 3(c)) for the two-strand annealing event (Figure 3(a)) indicate a voltage of  $0.34 \pm 0.03\ \mu\text{V}$  ( $0 \pm 0.04\ \mu\text{V}$  for control junction) for the two observed beads near the Hall junction. The two-dimensional (2D) theoretical Hall response has recently been modeled with respect to SPM bead position over the Hall junction [50]. The theoretical response for a single bead over the Hall junction in Figure 3 is shown in Figure 3(d), where red indicates a SPM particle positioned at the center of the device, while blue is a SPM outside the detectable range of the Hall junction. The measured voltage in Figure 3 is consistent with the theoretical value for a single bead, and therefore it is believed that the measured Hall voltage reflects only one of the two beads, since only one of the beads lies within the red zone for the theoretical plot (arrow in Figure 3(c)). Improvement of the signal-to-noise ratio can be achieved by operating the Hall device at higher frequencies; however, it is important to note that the sensitivity of the device can clearly distinguish a single-bead binding event from the noise floor by an order of magnitude at the frequency utilized in this study.

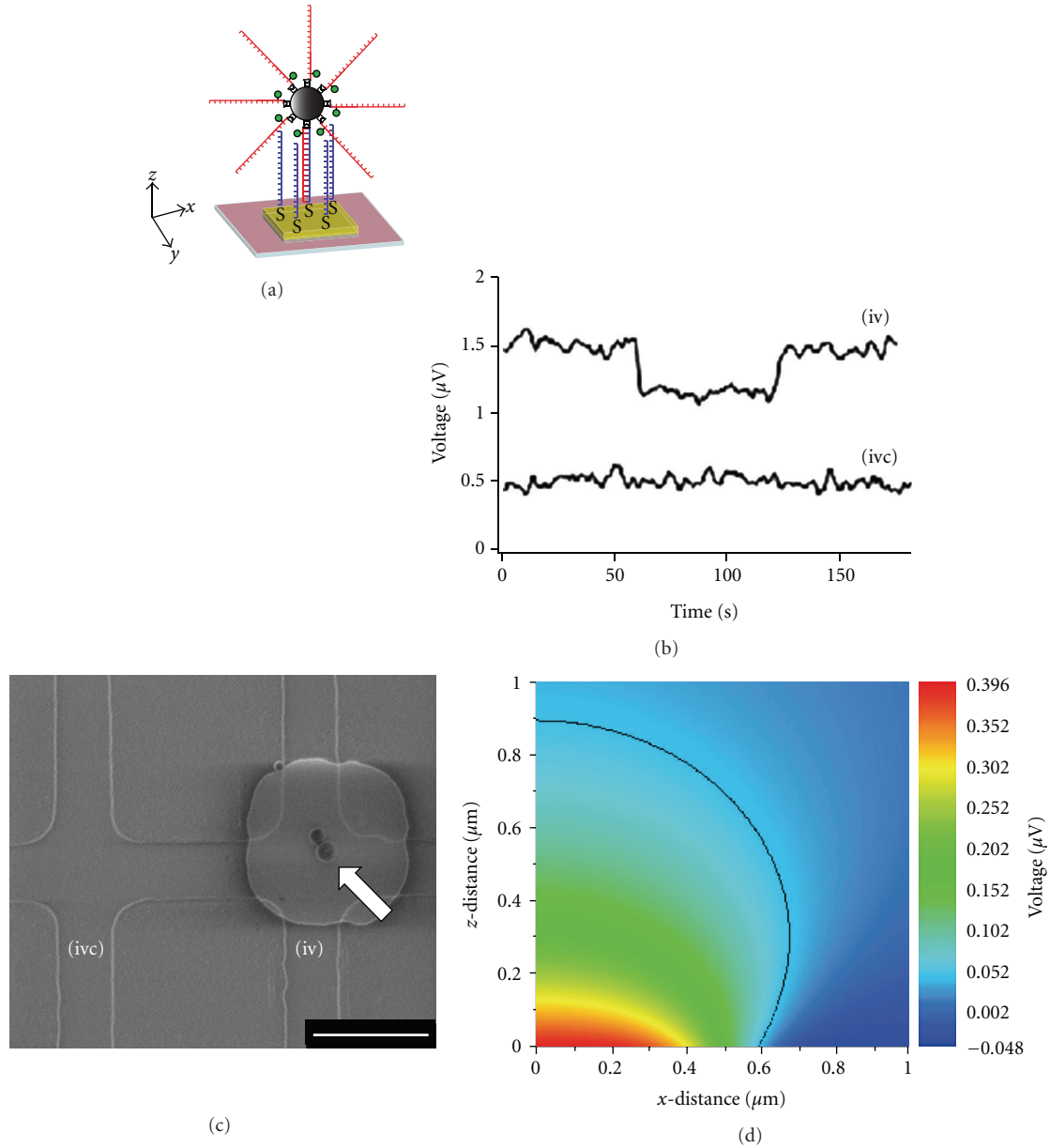


FIGURE 3: Sequence-specific two-strand DNA assembly and subsequent Hall detection of a single 344 nm nanobead. (a) Pictorial representation of two-strand DNA assembly, where the probe DNA (red) is complementary to the receptor DNA (blue). (b) Hall response data for the active (iv) and control Hall junction (ivc) plotted as Hall voltage versus time, where the drop in Hall voltage corresponds to the presence of a magnetic nanobead. (c) SEM was used to confirm that only one nanobead contributed significantly to the signal measured in (iv); scale bar = 2  $\mu\text{m}$ . (d) The theoretical Hall device cross-sectional response for a single 344 nm SPM bead as a function of position from the center of the junction, where red indicates strongest change in voltage, aqua indicates weakest voltage change, and blue indicates a negative voltage readout. The noise floor for the device is outlined in black for reference.

**3.4. Selectivity and Detection Limits.** The limit of detection for DNA in a real sample will reflect the length and sequence of target DNA (both of which influence annealing temperature), and the concentration of DNA, and the concentration of DNA present in a milieu of nontarget DNA. Since sensitivity will be influenced by bead size and the area of the transduction platform, the concentration limit of detection for target DNA was assessed using optical microscopy

analysis of the binding of the target DNA onto  $2 \times 4 \mu\text{m}$  gold patterns that serve as mimics of the GaAs Hall devices.

The thermodynamic stability of the three-strand DNA approach has been used for several sensor approaches, including optical, SERS, and colorimetric platforms. In the current study the stability of the three strands was experimentally verified using a gel shift assay (Figure S3). In Figures 4(a) and 4(b), binding of the 35-base pair three-strand DNA

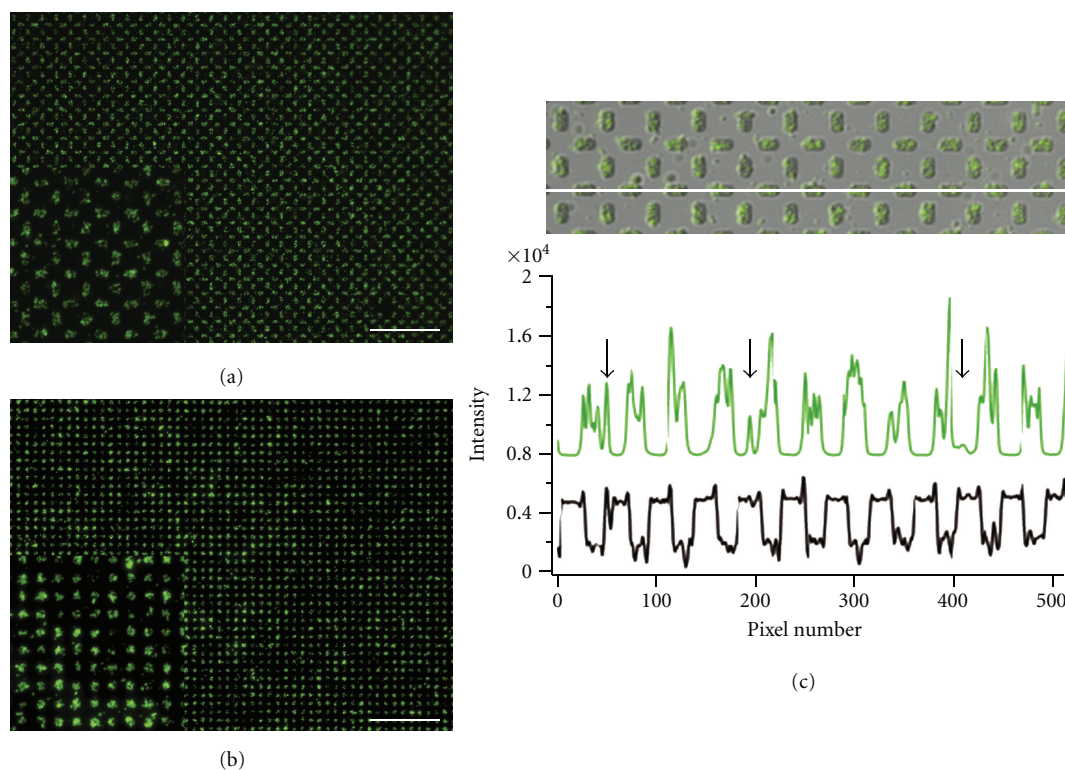


FIGURE 4: Three-strand DNA assembly on a mimic array (patterned on a GaAs substrate) for (a) complementary target only and (c) 10 ppm target in nontarget DNA. The inlays in the lower left of (a) and (c) are an enlarged portion of (a) and (c), respectively. Scale bars =  $50\ \mu\text{m}$ . (b) A line scan of the wide-field fluorescence microscopy image in (a) showing fluorescein-labeled probe DNA (green) and DIC (black) intensity correlates fluorescence intensity with nanobeads located primarily over gold pads, where the black arrows signify the presence of a small number of nonspecifically bound nanobeads.

assembly onto a mimic was assessed by the fluorescently labeled probe sequence conjugated to the 350 nm magnetic beads. Inspection of a line scan for the fluorescence intensity from the probe sequence shows good correlation with the Hall mimic patterns (Figure 4(b)). The signal fluctuations do not indicate single-bead response as the fluorescein intensity depends on the particle size, number of DNA probe strands, labeling efficiency, and focal plane of the microscopy image. Little intensity is observed over the control PEGylated regions surrounding gold pads (identified with black arrows). The discrimination level is  $>10,000$  counts above background for selective target DNA binding at the gold pads in buffered solution (Figure 4(a) and Figure S2).

An important measure of device performance is the ability to discriminate target ssDNA in the presence of extraneous (noncomplementary) sequences in solution, particularly at low levels of target DNA. The ability to discriminate target DNA in the presence of nontarget sequences was analyzed by optical microscopy on  $3\ \mu\text{m}$  patterned GaAs Hall device mimics in a buffered solution. Since the sensitivity of the device was demonstrated to achieve a limit of detection that is consistent with a single bead ( $0.34\ \mu\text{V}$  versus  $0 \pm 0.04\ \mu\text{V}$  noise floor), the choice of an optical mimic to only probe fidelity over a Hall junction allows analysis of the limit of detection for the three-strand annealing process. Fluorescently tagged nanobeads were selectively annealed at gold

pads at a concentration of 364 pM target DNA in a solution containing  $36\ \mu\text{M}$  nontarget DNA, which corresponds to less than two complementary target DNA sequences per 350 nm nanobead (Figure 4(c)). The measurements equate to detection at the 10 ppm level target. For comparison, a mimic array in which the receptor strand was noncomplementary to the target strand clearly demonstrated that nonspecific DNA binding is not observed (Figure S2). Although we have not yet tested cellular extracts of nucleic acids, the sensitivity and selectivity of the device—detection of a single SPM bead at a Hall junction, corresponding to 1-2 target DNA molecules—clearly demonstrate for the first time that this technology holds substantial promise for biomoleculesensing.

## 4. Conclusion

The device strategy utilizing three-strand DNA assembly on a Hall magnetometer provides a detection platform with high specificity, low limit of detection (single SPM bead, and small numbers of target DNA molecules), and very high fidelity. Sensitivity of the Hall biosensor is attributable to the properties of the Hall junction and is dependent on the size of the Hall junction, the frequency of the ac field oscillation, the moment of the SPM bead, and the distance of the SPM bead from the Hall junction. In the nanotechnology device,



the use of a SPM nanobead does not hinder the specificity of Watson-Crick base pairing for the target nucleic acid as evidenced by sequence-specific DNA hybridization (Figure 2 and Figure S2). At the detection frequency employed in this study, the 3D plot in Figure 3(d) indicates the possibility of detecting an SPM bead at distances approaching  $0.9\ \mu\text{m}$  off the surface of the device when the SPM bead is located directly over the center of the Hall junction, which may allow much longer sequences of DNA to be detected. Higher frequency measurements will decrease the noise level and therefore increase the sensitivity of the device to the magnetic bead position.

We have demonstrated the successful use of Hall magnetometry to detect a 35-base target DNA at the single-magnetic-bead level that could be applied for POC diagnostics. Reduction of the dimension of the gold pad and improved registry, as well as bead homogeneity could be used to further improve upon the overall device performance. Extrapolation of the device to a microarray of selectively labeled Hall sensors could represent a transformative biosensor platform. The parallel Hall device strategy could allow multiple DNA sequences to be simultaneously detected in a biological matrix since each magnetic bead and probe strand can be bar-coded by dye photoluminescence [23] and SPM bead size since the response will be proportional to the SPM moment. Alternatively, the receptor DNA on the Hall junction can be selectively dip-penned for multisequence analysis [51]. By eliminating concerns associated with sample amplification [3] such an array would allow screening for nucleic acid targets of biomedical interest such as pathogens or disease-related mutations [52–56].

## Acknowledgments

Support was provided by NIH grant GM079592. The authors thank Kimberly A. Riddle and Thomas J. Fellers in the Florida State University's Biological Science Imaging Resource (BSIR) for extensive SEM characterization and Eric J. Lochner in the Center of Materials Research and Technology (MARTECH) at FSU for material characterization.

## References

- [1] D. V. Lim, J. M. Simpson, E. A. Kearns, and M. F. Kramer, "Current and developing technologies for monitoring agents of bioterrorism and biowarfare," *Clinical Microbiology Reviews*, vol. 18, no. 4, pp. 583–607, 2005.
- [2] D. Ivnitski, D. J. O'Neil, A. Gattuso, R. Schlicht, M. Calidonna, and R. Fisher, "Nucleic acid approaches for detection and identification of biological warfare and infectious disease agents," *BioTechniques*, vol. 35, no. 4, pp. 862–869, 2003.
- [3] J. Ince and A. McNally, "Development of rapid, automated diagnostics for infectious disease: advances and challenges," *Expert Review of Medical Devices*, vol. 6, no. 6, pp. 641–651, 2009.
- [4] D. A. Giljohann and C. A. Mirkin, "Drivers of biodiagnostic development," *Nature*, vol. 462, no. 7272, pp. 461–464, 2009.
- [5] O. Lazcka, F. J. D. Campo, and F. X. Muñoz, "Pathogen detection: a perspective of traditional methods and biosensors," *Biosensors & Bioelectronics*, vol. 22, no. 7, pp. 1205–1217, 2007.
- [6] J. Wang, "Electrochemical biosensors: towards point-of-care cancer diagnostics," *Biosensors & Bioelectronics*, vol. 21, no. 10, pp. 1887–1892, 2006.
- [7] T. M. Herne and M. J. Tarlov, "Characterization of DNA probes immobilized on gold surfaces," *Journal of the American Chemical Society*, vol. 119, no. 38, pp. 8916–8920, 1997.
- [8] T. Wink, S. J. Van Zuilen, A. Bult, and W. P. Van Bennekom, "Self-assembled monolayers for biosensors," *Analyst*, vol. 122, no. 4, pp. R43–R50, 1997.
- [9] G. Festag, A. Steinbrück, A. Wolff, A. Csaki, R. Möller, and W. Fritzsche, "Optimization of gold nanoparticle-based DNA detection for microarrays," *Journal of Fluorescence*, vol. 15, no. 2, pp. 161–170, 2005.
- [10] X. D. Song, J. Shi, and B. Swanson, "Flow cytometry-based biosensor for detection of multivalent proteins," *Analytical Biochemistry*, vol. 284, no. 1, pp. 35–41, 2000.
- [11] L. Shi, L. H. Reid, W. D. Jones et al., "The MicroArray Quality Control (MAQC) project shows inter- and intraplatform reproducibility of gene expression measurements," *Nature Biotechnology*, vol. 24, no. 9, pp. 1151–1161, 2006.
- [12] Y. W. C. Cao, R. Jin, and C. A. Mirkin, "Nanoparticles with Raman spectroscopic fingerprints for DNA and RNA detection," *Science*, vol. 297, no. 5586, pp. 1536–1540, 2002.
- [13] C. T. Campbell and G. Kim, "SPR microscopy and its applications to high-throughput analyses of biomolecular binding events and their kinetics," *Biomaterials*, vol. 28, no. 15, pp. 2380–2392, 2007.
- [14] T. A. Taton, C. A. Mirkin, and R. L. Letsinger, "Scanometric DNA array detection with nanoparticle probes," *Science*, vol. 289, no. 5485, pp. 1757–1760, 2000.
- [15] B. Dubertret, M. Calame, and A. J. Libchaber, "Single-mismatch detection using gold-quenched fluorescent oligonucleotides," *Nature Biotechnology*, vol. 19, no. 4, pp. 365–370, 2001.
- [16] W. R. Algar, M. Massey, and U. J. Krull, "The application of quantum dots, gold nanoparticles and molecular switches to optical nucleic-acid diagnostics," *TrAC Trends in Analytical Chemistry*, vol. 28, no. 3, pp. 292–306, 2009.
- [17] S. Husale, H. H. J. Persson, and O. Sahin, "DNA nanomechanics allows direct digital detection of complementary DNA and microRNA targets," *Nature*, vol. 462, no. 7276, pp. 1075–1078, 2009.
- [18] N. G. Clack, K. Salaita, and J. T. Groves, "Electrostatic readout of DNA microarrays with charged microspheres," *Nature Biotechnology*, vol. 26, no. 7, pp. 825–830, 2008.
- [19] D. S. Johnson, W. Li, D. B. Gordon et al., "Systematic evaluation of variability in ChIP-chip experiments using predefined DNA targets," *Genome Research*, vol. 18, no. 3, pp. 393–403, 2008.
- [20] W. R. Algar and U. J. Krull, "Toward a multiplexed solid-phase nucleic acid hybridization assay using quantum dots as donors in fluorescence resonance energy transfer," *Analytical Chemistry*, vol. 81, no. 10, pp. 4113–4120, 2009.
- [21] B. S. Gaylord, A. J. Heeger, and G. C. Bazan, "DNA detection using water-soluble conjugated polymers and peptide nucleic acid probes," *Proceedings of the National Academy of Sciences of the United States of America*, vol. 99, no. 17, pp. 10954–10957, 2002.
- [22] J. Zhang, B. P. Ting, N. R. Jana, Z. Gao, and J. Y. Ying, "Ultrasensitive electrochemical DNA biosensors based on the detection of a highly characteristic solid-state process," *Small*, vol. 5, no. 12, pp. 1414–1417, 2009.



- [23] Y. Li, Y. T. H. Cu, and D. Luo, "Multiplexed detection of pathogen DNA with DNA-based fluorescence nanobarcodes," *Nature Biotechnology*, vol. 23, no. 7, pp. 885–889, 2005.
- [24] W. J. Qin, O. S. Yim, P. S. Lai, and L. Y. L. Yung, "Dimeric gold nanoparticle assembly for detection and discrimination of single nucleotide mutation in Duchenne muscular dystrophy," *Biosensors & Bioelectronics*, vol. 25, no. 9, pp. 2021–2025, 2010.
- [25] V. C. Martins, F. A. Cardoso, J. Germano et al., "Femtomolar limit of detection with a magnetoresistive biochip," *Biosensors & Bioelectronics*, vol. 24, no. 8, pp. 2690–2695, 2009.
- [26] C. A. Mirkin, R. L. Letsinger, R. C. Mucic, and J. J. Storhoff, "A DNA-based method for rationally assembling nanoparticles into macroscopic materials," *Nature*, vol. 382, no. 6592, pp. 607–609, 1996.
- [27] J. J. Storhoff, S. S. Marla, P. Bao et al., "Gold nanoparticle-based detection of genomic DNA targets on microarrays using a novel optical detection system," *Biosensors & Bioelectronics*, vol. 19, no. 8, pp. 875–883, 2004.
- [28] J. J. Storhoff, A. D. Lucas, V. Garimella, Y. P. Bao, and U. R. Müller, "Homogeneous detection of unamplified genomic DNA sequences based on colorimetric scatter of gold nanoparticle probes," *Nature Biotechnology*, vol. 22, no. 7, pp. 883–887, 2004.
- [29] G. Braun, S. J. Lee, M. Dante, T. Q. Nguyen, M. Moskovits, and N. Reich, "Surface-enhanced raman spectroscopy for DNA detection by nanoparticle assembly onto smooth metal films," *Journal of the American Chemical Society*, vol. 129, no. 20, pp. 6378–6379, 2007.
- [30] S. P. Mulvaney, C. L. Cole, M. D. Kniller et al., "Rapid, femtomolar bioassays in complex matrices combining microfluidics and magnetoelectronics," *Biosensors & Bioelectronics*, vol. 23, no. 2, pp. 191–200, 2007.
- [31] D. L. Arruda, W. C. Wilson, C. Nguyen et al., "Microelectrical sensors as emerging platforms for protein biomarker detection in point-of-care diagnostics," *Expert Review of Molecular Diagnostics*, vol. 9, no. 7, pp. 749–755, 2009.
- [32] J. Schotter, P. B. Kamp, A. Becker, A. Pühler, G. Reiss, and H. Brückl, "Comparison of a prototype magnetoresistive biosensor to standard fluorescent DNA detection," *Biosensors & Bioelectronics*, vol. 19, no. 10, pp. 1149–1156, 2004.
- [33] J. Germano, V. C. Martins, F. A. Cardoso et al., "A portable and autonomous magnetic detection platform for biosensing," *Sensors*, vol. 9, no. 6, pp. 4119–4137, 2009.
- [34] D. L. Graham, H. A. Ferreira, N. Feliciano, P. P. Freitas, L. A. Clarke, and M. D. Amaral, "Magnetic field-assisted DNA hybridisation and simultaneous detection using micron-sized spin-valve sensors and magnetic nanoparticles," *Sensors and Actuators B*, vol. 107, no. 2, pp. 936–944, 2005.
- [35] H. A. Ferreira, D. L. Graham, N. Feliciano, L. A. Clarke, M. D. Amaral, and P. P. Freitas, "Detection of cystic fibrosis related DNA targets using AC field focusing of magnetic labels and spin-valve sensors," *IEEE Transactions on Magnetics*, vol. 41, no. 10, pp. 4140–4142, 2005.
- [36] D. A. Hall, R. S. Gaster, T. Lin et al., "GMR biosensor arrays: a system perspective," *Biosensors & Bioelectronics*, vol. 25, no. 9, pp. 2051–2057, 2010.
- [37] S. J. Osterfeld, H. Yu, R. S. Gaster et al., "Multiplex protein assays based on real-time magnetic nanotag sensing," *Proceedings of the National Academy of Sciences of the United States of America*, vol. 105, no. 52, pp. 20637–20640, 2008.
- [38] D. R. Baselt, G. U. Lee, M. Natesan, S. W. Metzger, P. E. Sheehan, and R. J. Colton, "A biosensor based on magnetoresistance technology," *Biosensors & Bioelectronics*, vol. 13, no. 7–8, pp. 731–739, 1998.
- [39] R. L. Edelstein, C. R. Tamanaha, P. E. Sheehan et al., "The BARC biosensor applied to the detection of biological warfare agents," *Biosensors & Bioelectronics*, vol. 14, no. 10–11, pp. 805–813, 2000.
- [40] Y. Li, P. Xiong, S. Von Molnár, S. Wirth, Y. Ohno, and H. Ohno, "Hall magnetometry on a single iron nanoparticle," *Applied Physics Letters*, vol. 80, no. 24, pp. 4644–4646, 2002.
- [41] A. Sandhu, Y. Kumagai, A. Lapicki, S. Sakamoto, M. Abe, and H. Handa, "High efficiency Hall effect micro-biosensor platform for detection of magnetically labeled biomolecules," *Biosensors & Bioelectronics*, vol. 22, no. 9–10, pp. 2115–2120, 2007.
- [42] G. Mihajlović, P. Xiong, S. von Molnár et al., "Detection of single magnetic bead for biological applications using an InAs quantum-well micro-Hall sensor," *Applied Physics Letters*, vol. 87, no. 11, Article ID 112502, 3 pages, 2005.
- [43] G. Mihajlović, P. Xiong, S. von Molnár, M. Field, and G. J. Sullivan, "InAs quantum well Hall devices for room-temperature detection of single magnetic biomolecular labels," *Journal of Applied Physics*, vol. 102, no. 3, Article ID 034506, 9 pages, 2007.
- [44] P. Manandhar, K. S. Chen, K. Aledealat et al., "The detection of specific biomolecular interactions with micro-Hall magnetic sensors," *Nanotechnology*, vol. 20, no. 35, Article ID 355501, 2009.
- [45] P. A. Besse, G. Boero, M. Demierre, V. Pott, and R. Popovic, "Detection of a single magnetic microbead using a miniaturized silicon Hall sensor," *Applied Physics Letters*, vol. 80, no. 22, Article ID 4199, 3 pages, 2002.
- [46] R. S. Gaster, D. A. Hall, C. H. Nielsen et al., "Matrix-insensitive protein assays push the limits of biosensors in medicine," *Nature Medicine*, vol. 15, no. 11, pp. 1327–1332, 2009.
- [47] G. Mihajlovic and S. von Molnar, in *Nanoscale Magnetic Materials and Applications*, J. P. Liu, E. Fullerton, O. Gutflisch, and D. J. Sellmyer, Eds., pp. 685–710, Springer, New York, NY, USA, 2009.
- [48] M. Behet, J. Bekaert, J. De Boeck, and G. Borghs, "InAs/Al<sub>0.2</sub>Ga<sub>0.8</sub>Sb quantum well Hall effect sensors," *Sensors and Actuators A*, vol. 81, no. 1–3, pp. 13–17, 2000.
- [49] B. Kannan, R. P. Kulkarni, and A. Majumdar, "DNA-based programmed assembly of gold nanoparticles on lithographic patterns with extraordinary specificity," *Nano Letters*, vol. 4, no. 8, pp. 1521–1524, 2004.
- [50] K. Aledealat, G. Mihajlović, K. Chen et al., "Dynamic micro-hall detection of superparamagnetic beads in a microfluidic channel," *Journal of Magnetism and Magnetic Materials*, vol. 322, no. 24, pp. L69–L72, 2010.
- [51] L. M. Demers, D. S. Ginger, S. J. Park, Z. Li, S. W. Chung, and C. A. Mirkin, "Direct patterning of modified oligonucleotides on metals and insulators by dip-pen nanolithography," *Science*, vol. 296, no. 5574, pp. 1836–1838, 2002.
- [52] J. Köhler, Y. Chen, B. Brenner et al., "Familial hypertrophic cardiomyopathy mutations in troponin I (K183Δ, G203S, K206Q) enhance filament sliding," *Physiological Genomics*, vol. 14, pp. 117–128, 2003.
- [53] M. S. Parmacek and R. J. Solaro, "Biology of the troponin complex in cardiac myocytes," *Progress in Cardiovascular Diseases*, vol. 47, no. 3, pp. 159–176, 2004.
- [54] B. Gafurov, S. Fredricksen, A. Cai, B. Brenner, P. B. Chase, and J. M. Chalovich, "The Δ14 mutation of human cardiac troponin T enhances ATPase activity and alters the cooperative binding of S1-ADP to regulated actin," *Biochemistry*, vol. 43, no. 48, pp. 15276–15285, 2004.

- [55] F. Bai, A. Weis, A. K. Takeda, P. B. Chase, and M. Kawai, "Enhanced active cross-bridges during diastole: molecular pathogenesis of tropomyosin's HCM mutations," *Biophysical Journal*, vol. 100, no. 4, pp. 1014–1023, 2011.
- [56] M. C. Mathur, P. B. Chase, and J. M. Chalovich, "Several cardiomyopathy causing mutations on tropomyosin either destabilize the active state of actomyosin or alter the binding properties of tropomyosin," *Biochemical and Biophysical Research Communications*, vol. 406, no. 1, pp. 74–78, 2011.

## Research Article

# Electric-Field-Directed Self-Assembly of Active Enzyme-Nanoparticle Structures

Alexander P. Hsiao<sup>1</sup> and Michael J. Heller<sup>1,2</sup>

<sup>1</sup>Department of Bioengineering, University of California San Diego, La Jolla, CA 92093-0412, USA

<sup>2</sup>Department of NanoEngineering, University of California San Diego, La Jolla, CA 92093-0412, USA

Correspondence should be addressed to Michael J. Heller, mheller@ucsd.edu

Received 2 September 2011; Accepted 13 October 2011

Academic Editor: Seunghun Hong

Copyright © 2012 A. P. Hsiao and M. J. Heller. This is an open access article distributed under the Creative Commons Attribution License, which permits unrestricted use, distribution, and reproduction in any medium, provided the original work is properly cited.

A method is presented for the electric-field-directed self-assembly of higher-order structures composed of alternating layers of biotin nanoparticles and streptavidin-/avidin-conjugated enzymes carried out on a microelectrode array device. Enzymes included in the study were glucose oxidase (GOx), horseradish peroxidase (HRP), and alkaline phosphatase (AP); all of which could be used to form a light-emitting microscale glucose sensor. Directed assembly included fabricating multilayer structures with 200 nm or 40 nm GOx-avidin-biotin nanoparticles, with AP-streptavidin-biotin nanoparticles, and with HRP-streptavidin-biotin nanoparticles. Multilayered structures were also fabricated with alternate layering of HRP-streptavidin-biotin nanoparticles and GOx-avidin-biotin nanoparticles. Results showed that enzymatic activity was retained after the assembly process, indicating that substrates could still diffuse into the structures and that the electric-field-based fabrication process itself did not cause any significant loss of enzyme activity. These methods provide a solution to overcome the cumbersome passive layer-by-layer assembly methods to efficiently fabricate higher-order active biological and chemical hybrid structures that can be useful for creating novel biosensors and drug delivery nanostructures, as well as for diagnostic applications.

## 1. Introduction

With recent advances in the assembly of nanoparticles (NPs) into higher-order structures and components, the ability to incorporate biologically active molecules has become more important [1, 2]. Considerable research efforts are now directed towards the fabrication and integration of biologically active molecules into NP structures that could be used in drug delivery, biological and chemical sensors, and diagnostics. In most cases, these higher-order structures are fabricated with passive layer-by-layer (LBL) techniques to self-assemble the molecules into organized structures through specific interactions including covalent binding, gold-thiol interactions, electrostatic interactions, and protein-ligand binding [3–11]. However, passive processes are concentration dependent and these methods require complex processes and long incubation times in high concentration solutions of molecules. Moreover, in order to direct the assembly onto specific sites, blocking

agents or physical patterning such as lithography is necessary [12]. To circumvent these issues, active processes have been developed, including DC electrophoretic deposition and magnetic-field-assisted deposition [13–18]. Also, work has been carried out on the use of AC dielectrophoretic techniques to manipulate NPs [19–21]. The application of electric fields allows for rapid, site-directed concentration of macromolecules, polymers, and NPs to enhance the self-assembly process. Such methods have been employed to produce colloidal aggregates as well as pattern NPs atop electrode surfaces [17, 22–29]. In addition, nonspecific binding and high background, which play a crucial role in the incorporation and detection of biological molecules, can be reduced with electrode patterns which direct the molecules toward the active site where deposition is preferred and away from nonactive regions. More recently, the method of electrophoretic deposition has been applied to biological components. This powerful tool has enabled devices to be made which utilize the electric fields to enhance DNA

hybridization, to form protein layers for biosensors, and to pattern cells [30–36]. Recently we have shown the ability to construct higher-order NP structures by electric-field-directed self-assembly through the specific interactions of complementary DNA sequences as well as through protein-molecule interactions (Figures 1(a) and 1(b)) [14, 37, 38]. We now present the ability to integrate active enzymes into these NP structures by directed electrophoretic means (Figure 1(c)), thus providing a new bottom-up fabrication method for patterning and constructing structures from NPs in a rapid and combinatorial fashion atop a microarray.

## 2. Materials and Methods

**2.1. CMOS Microarray Setup.** An ACV 400 CMOS electronic microarray (Nanogen, Inc.), shown in Figure 2, which consists of 400 individually controllable  $55\text{ }\mu\text{m}$ -diameter platinum electrodes was used for all layer assembly experiments. The microarray chip is overcoated by the manufacturer with a streptavidin-embedded polyacrylamide hydrogel which serves as a permeation layer. The device was computer controlled using ACV400 software. The software allowed each electrode to be configured to independently source 0 to 5 V or 0 to  $1\text{ }\mu\text{A}$  per electrode, with each electrode on the array capable of being independently biased.

**2.2. Chip Preparation.** To prepare the chip surface as depicted in the cross-section in Figure 2, the microarray chip was first washed by pipetting  $20\text{ }\mu\text{L}$  deionized water ( $\text{dH}_2\text{O}$ , Millipore,  $18\text{ M}\Omega$ ) onto and off the chip a total of 10 times. Subsequently,  $20\text{ }\mu\text{L}$  of a  $2\text{ }\mu\text{M}$  biotin-dextran (Sigma) solution in  $\text{dH}_2\text{O}$  was pipetted onto the chip and allowed to incubate for 30 minutes at room temperature. The chip was then washed again with  $\text{dH}_2\text{O}$ , followed by incubation with  $20\text{ }\mu\text{L}$  of a  $1\text{ mg/mL}$  solution of streptavidin (Sigma) in  $\text{dH}_2\text{O}$  for 30 minutes at room temperature. Finally, the chip was washed with  $100\text{ mM}$  L-histidine buffer and kept moist prior to use.

**2.3. Preparation of NPs and Enzymes.** Yellow-green fluorescent biotin-coated NPs,  $200\text{ nm}$  and  $40\text{ nm}$  in diameter (Molecular Probes, ex505, em515), were diluted to  $0.01\%$  ( $38\text{ pM}$  for  $200\text{ nm}$  NPs and  $4.7\text{ nM}$  for  $40\text{ nm}$  NPs) in  $100\text{ mM}$  L-histidine buffer. This suspension was vortexed and sonicated in a water bath for 15 minutes just prior to use to break up any aggregates. Additionally, glucose oxidase-avidin (GOx-avidin, Rockland) was diluted to  $30\text{ nM}$ , streptavidin-alkaline phosphatase (streptavidin-AP, Sigma) was diluted to  $40\text{ nM}$ , and streptavidin-peroxidase (streptavidin-HRP, Sigma) was diluted to  $95\text{ nM}$  in  $100\text{ mM}$  L-histidine buffer just prior to use.

**2.4. DC Electric-Field-Directed Assembly of Streptavidin/Avidin Enzymes and Biotin NPs.** NP and enzyme addressing conditions are derived from previous work [14]. In brief,  $20\text{ }\mu\text{L}$  of the  $200\text{ nm}$  biotin NP solution or enzyme solution was pipetted onto the chip. The selected electrodes were biased positive and activated with a constant DC current

of  $0.25\text{ }\mu\text{A}$  for 15 seconds to concentrate and assemble the particles or enzymes atop the activated electrodes. The solution was then removed and the chip washed with  $20\text{ }\mu\text{L}$  of L-histidine buffer a total of three times. Assembly of the layer structures was achieved by alternating the addressing of biotin NPs with streptavidin/avidin enzymes. Every structure was capped with a final layer of biotin NPs. Different layer structures include layers of biotin NPs and GOx-avidin, layers of biotin NPs and streptavidin-AP, layers of biotin NPs and streptavidin-HRP, and layers of biotin NPs with alternate GOx-avidin and streptavidin-HRP to produce bienzyme structures. Identical conditions were employed to assemble layers of  $40\text{ nm}$  biotin NPs with streptavidin-AP.

**2.5. Monitoring of Layer Assembly by Fluorescence and ImageJ Calculations.** Monitoring of layer growth was done by real-time imaging on an epifluorescent Leica microscope, with a Hamamatsu Orca-ER CCD using a custom LabVIEW interface. Images were acquired throughout the layering process and processed in ImageJ. For analysis, each image had its background subtracted with a rolling ball radius of 50. The image was then inverted and threshold fixed using the IsoData threshold. Manual adjustments were made to include as many electrodes as possible. A corresponding mask was generated to ensure each measured electrode area was identical. Raw integrated density values for each electrode were then acquired by mapping the data in the original image to the generated mask image.

**2.6. Verification of Enzyme Activity via X-Ray Film.** The verification of enzyme activity was performed on chips composed of alternate layers of  $200\text{ nm}$  biotin NPs with either GOx-avidin or streptavidin-AP as the enzyme layers. All 400 electrodes on the array were activated to maximize the total number of fabrication sites for the layer structures. For the structures assembled with GOx-avidin, a reaction solution consisting of  $227\text{ mM}$  glucose (Sigma),  $8.4\text{ mM}$  luminol (Fluka), and  $0.1\text{ mg/mL}$  peroxidase (Sigma) in  $0.035\text{ M}$  Tris-HCl ( $\text{pH } 8.4$ ) was prepared. The chips were washed with  $100\text{ mM}$  L-histidine buffer and then with  $0.1\text{ M}$  Tris-HCl ( $\text{pH } 8.0$ ). Subsequently,  $15\text{ }\mu\text{L}$  of the reaction solution was pipetted onto the chip surface. For chips with layer structures assembled using streptavidin-AP, the chips were washed with  $100\text{ mM}$  L-histidine buffer and then  $15\text{ }\mu\text{L}$  of CDP-star chemiluminescent reagent (Sigma) was dispensed onto the chips.

The chips were then wrapped in plastic wrap to prevent solution loss and placed into a cassette with X-ray film (Denville Scientific) for overnight exposure. The film was developed in a Hope MicroMax developer, scanned, and analyzed using ImageJ. The relative intensity from each chip was normalized to a chip that did not undergo layer assembly which was cleaned, prepared with the appropriate reaction solution, and exposed overnight as well.

**2.7. Environmental Scanning Electron Microscopy (ESEM) of the Enzyme-NP Layers.** After assembly of the enzyme-NP layers, the chip was washed multiple times with  $100\text{ mM}$



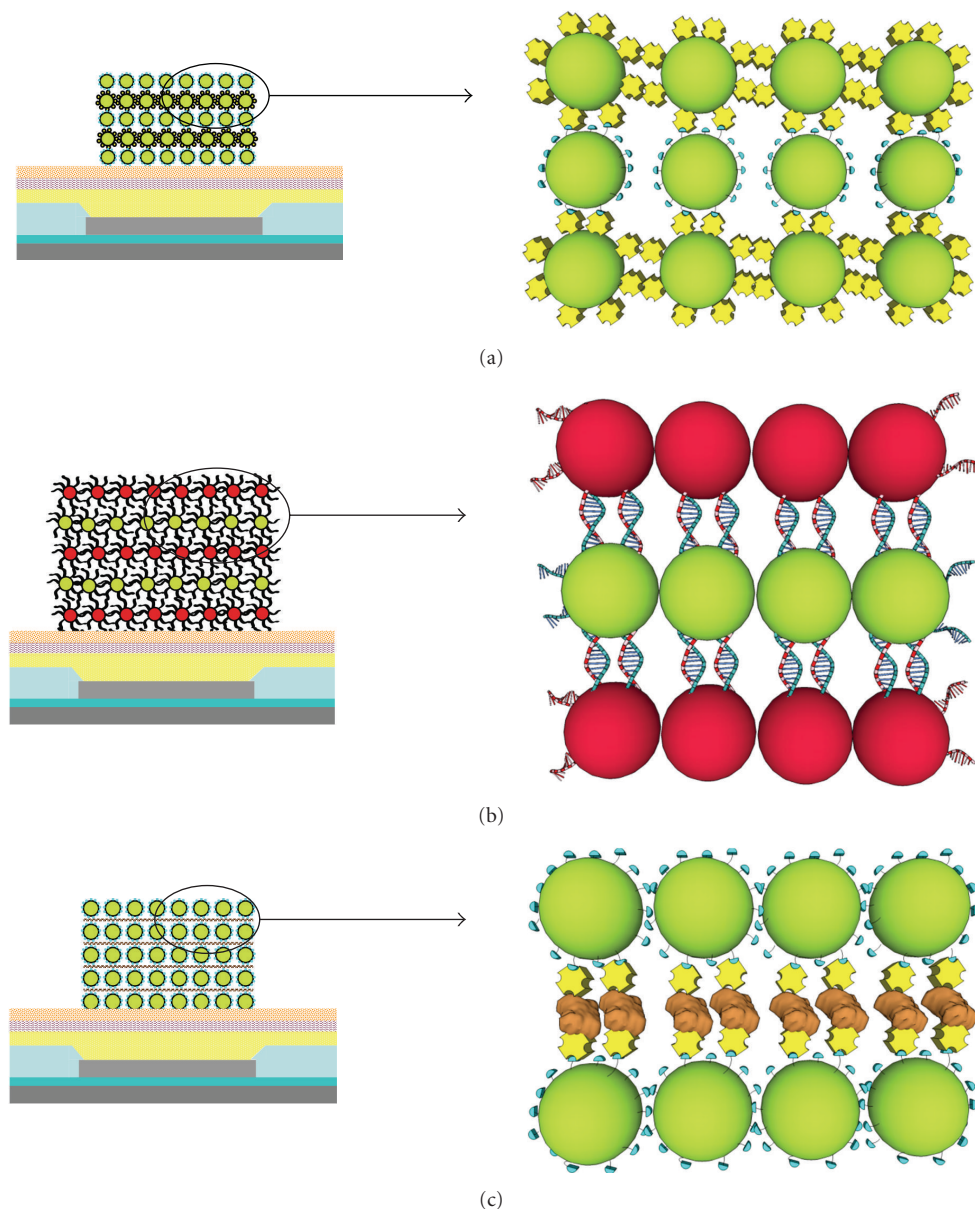


FIGURE 1: Electric-field-directed assembly (layering) of biomolecule NPs by different binding mechanisms: (a) NP layering with alternate biotin (blue)-functionalized NPs and streptavidin (yellow)-functionalized NPs. (b) NP layering by hybridization of complementary DNA sequences. (c) NP layering of biotin-functionalized NPs with streptavidin-functionalized enzymes (brown) (image not to scale).

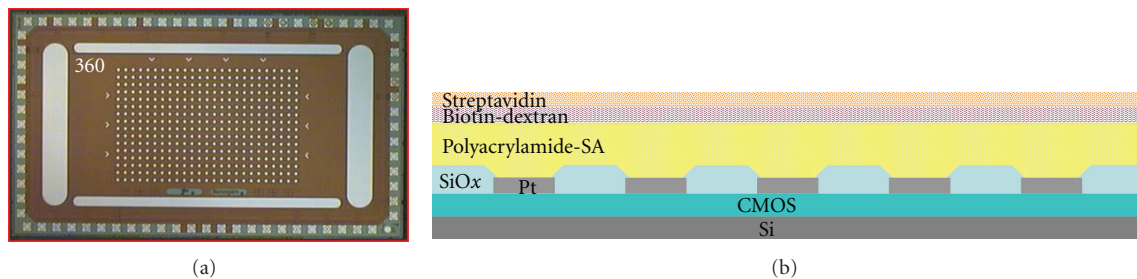


FIGURE 2: Images of the 400 site platinum electrode CMOS microelectronic array and a cross-section of the structure. The microarray is  $4\text{ mm} \times 7\text{ mm}$ , and each microelectrode is  $55\text{ }\mu\text{m}$  in diameter.



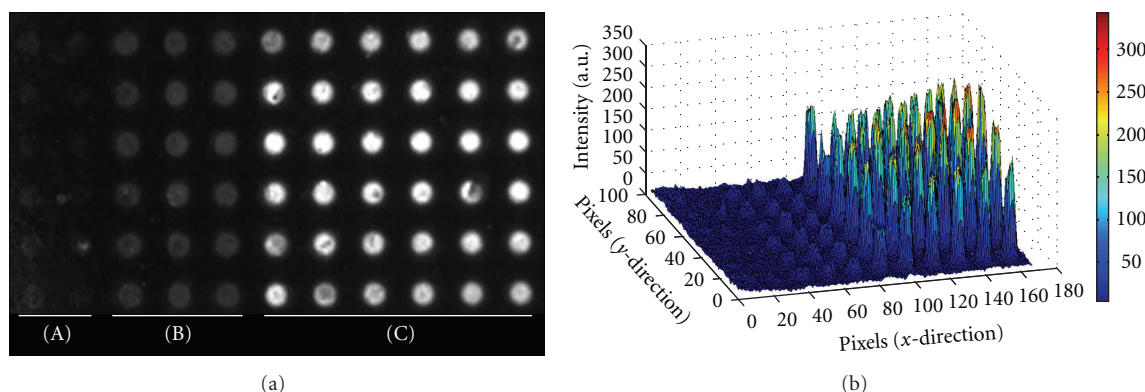


FIGURE 3: (a) Fluorescence image of a section of the CMOS microarray after addressing 39 combined layers of biotin NPs and GOx-avidin. (A) No current applied. (B) Current applied ONLY when biotin NPs were addressed. (C) Current applied when BOTH biotin NPs and GOx-avidin were addressed. (b) Corresponding MATLAB plot of the relative fluorescence intensity (z-axis) of each electrode.

L-histidine buffer and then all solution was removed from the surface to allow the chip to dry. Chips were then coated with either 40 nm of gold sputtered via a Denton Discovery 18 sputter system or 40 nm of chromium via Denton IV desktop sputter coater. Fractures were introduced into the structures by careful cutting with a razor blade. Images were then acquired on a Phillips XL30 ESEM using a 10 kV beam in high vacuum mode.

### 3. Results and Discussion

**3.1. Assembly of Enzyme-NP Layers and Verification of Proper Layer Formation.** The assembly of NP layers was monitored by epifluorescence imaging; however, because only the biotin NPs are fluorescent, it was first important to verify that the NP-enzyme layers were forming as proposed by alternate layering of enzymes and NPs, as opposed to formation due to nonspecific interactions of the biotin NPs to themselves. This was done by organizing the electrodes into three specific regions, as shown in Figure 3(a). Region A consisted of microelectrodes which were never activated. This section served as a negative control to measure the amount of passive binding to the chip surface that would occur simply due to the presence of NPs and enzyme during alternate addressing steps. Region B consisted of microelectrodes only activated when the biotin NPs were addressed. This region served to measure the amount of non-specific binding of the NPs to themselves. Additionally, it served to show the amount of passive assembly that could occur if no enzyme was actively addressed to these microelectrode sites. Finally, region C consisted of microelectrodes which were activated during all addressing steps of NPs and enzymes. Microelectrodes in this region were expected to have proper formation of enzyme-NP layers. The results in Figures 3(a) and 3(b) indicate that the microelectrodes in region A have a fluorescent signal near that of the background, which is the surface of the chip between the electrodes, thus indicating that a very low number of fluorescent biotin NPs passively bound to the streptavidin surface at these sites. Microelectrodes

in region B, which were only activated when biotin NPs were addressed, have a low level fluorescent signal and the microelectrodes in region C, which were activated when both NPs and GOx-avidin were addressed, have a high level fluorescent intensity indicating that multiple layers of NPs formed in region C. Comparison of fluorescence intensities between the three regions suggests that in order to construct higher-order structures both NPs and enzymes must be addressed to the same site, as in region C. If only biotin NPs are addressed, as in region B, the NPs will not bind to one another and no higher-order structures are formed; therefore, there is only low fluorescence intensity from the first layer of biotin NPs assembled onto the streptavidin chip surface. These results were verified with all three enzyme types and with both 200 nm and 40 nm NPs.

To corroborate with the fluorescence data, Figure 4 shows environmental scanning electron microscopy (ESEM) images of three microelectrode sites; one each for region A, B, and C after addressing 31 total layers of 200 nm biotin NPs and streptavidin-AP as well as 21 layers of 40 nm biotin NPs and streptavidin-AP on separate microarray chips. The microelectrodes from region A show only a small number of passively attached biotin NPs. The electrodes from region B show nearly a complete monolayer of biotin NPs, despite being exposed to 16 total addressing steps of biotin NPs. This demonstrates that there is little non-specific binding of the biotin particles to themselves; so despite the electric field directing additional NPs onto the first layer of NPs, they do not stick and are removed during the wash steps. The electrode from region C shows a high number of NPs assembled atop each other. Thus, active directed concentration of both the streptavidin/avidin enzyme and biotin NPs is necessary to assemble the higher-order structures and the layer assembly process does indeed proceed as designed. Additionally, the lack of particles on region A's microelectrodes further verifies that electric-field-directed assembly is efficient and can overcome the diffusion-limited process of passive LBL assembly. Each assembly step only required 15 seconds with NP and enzyme concentrations

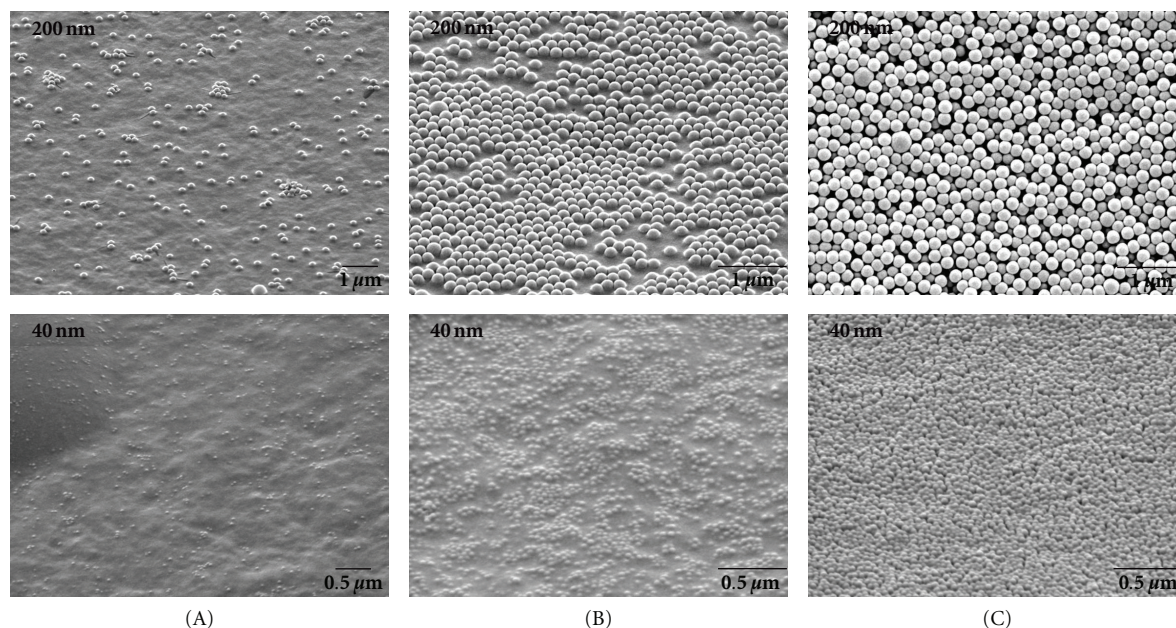


FIGURE 4: ESEM images of a microelectrode in each region (A), (B), and (C) after enzyme-NP assembly. Top row: microelectrodes after assembling 31 total alternating layers of 200 nm biotin NPs and streptavidin-AP. Bottom row: microelectrodes after assembling 21 layers of 40 nm biotin NPs and streptavidin-AP.

in the pM and nM range. At these time scales and NP and enzyme concentrations, no layers could be formed passively on the region A microelectrodes.

These results show that the electric field directed assembly technology is easily scalable to NPs of various sizes. This allows for tuning of the porosity of the final structures which may help control the (enzyme) substrate turnover and reaction kinetics, both of which would play crucial roles in biosensor devices. For drug delivery particles, the porosity will play a paramount role in the drug release profile. Moreover, we believe that integration of various types of NPs with different biomolecules would also be achievable as long as the proper binding elements are in place. Using multiple sized NPs would enable multiple porosities through the structure which may be needed to optimize reaction rates in multienzyme structures. Particles such as quantum dots could be incorporated to enhance detection. Moreover, using other biomolecules such as antibodies or DNA would allow the creation of a wide array of biosensors.

### 3.2. Monitoring NP Layer Assembly and Quality of Layers.

Real-time layer assembly was monitored by visualizing increasing fluorescence intensity atop the microelectrode sites. Figure 5 shows a plot of the mean integrated density of fluorescence per microelectrode for microelectrodes in regions B and C of a microarray after 9, 19, 29, 39, and 47 total layers of 200 nm biotin NPs with alternate addressing of both GOx-avidin and streptavidin-HRP. From the plot, it is evident that the fluorescence for microelectrodes in region B, microelectrodes activated only when biotin NPs were addressed, maintains roughly the same fluorescence intensity throughout the layering experiments. These results further

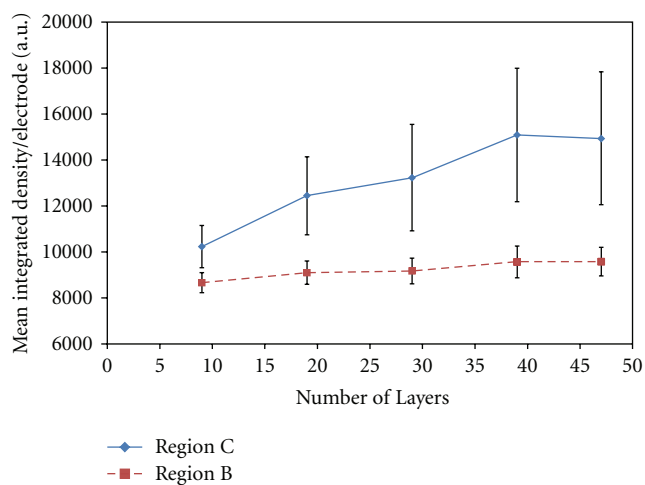


FIGURE 5: Plot showing the calculated mean integrated density per microelectrode for microelectrodes in regions B and C in bienzyme layer structures of 9, 19, 29, 39, and 47 total layers of 200 nm biotin NPs with alternate enzyme layer addressing of GOx-avidin and streptavidin-HRP.

substantiate the results in Figures 3 and 4 that without active electric-field-directed assembly of streptavidin/avidin-conjugated enzymes onto the biotin NPs there is no further layer assembly. Additionally, these results verify that multiple types of enzymes can be incorporated into the same structure as long as they are properly functionalized. In this case, there is a streptavidin-functionalized HRP and an avidin-functionalized GOx, both of which can bind to the biotin on the NPs and facilitate layer formation. The plot shows



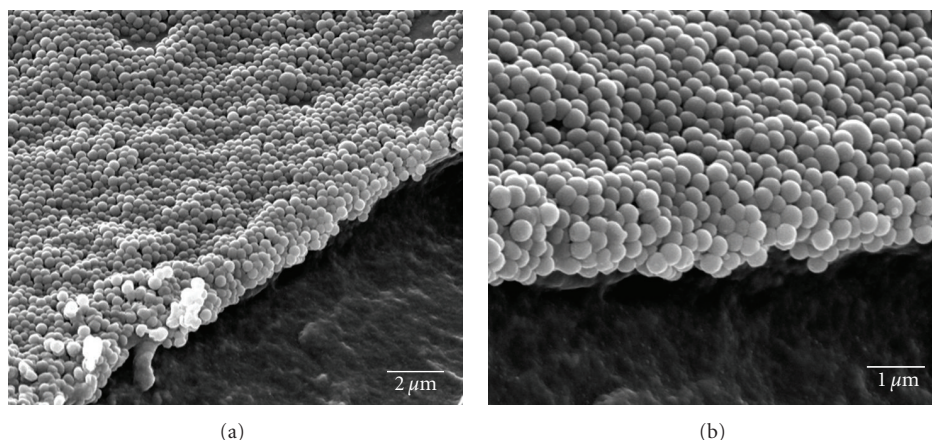


FIGURE 6: ESEM images of 200 nm biotin NPs layered with GOx-avidin at introduced cuts showing the layering of NPs.

a trend of increasing mean fluorescence for microelectrodes in region C as the total number of layers increases. This is what is expected because as the number of layers increases there are more total fluorescent NPs on each microelectrode. The plot in Figure 5, however, does have quite a large amount of variability, which could be attributed to many factors. One factor could be the stoichiometry of the streptavidin conjugation to the enzyme. Streptavidin-HRP was conjugated at a 1:1 ratio and streptavidin-AP at a 2:1 ratio according to the manufacturer's specifications. Streptavidin-AP thus has 4 more available biotin binding sites per enzyme molecule. This increased availability of binding sites makes attachment to biotin NPs more robust and can lead to an increased quality of uniformity of NP layers. Thus, to enhance binding, enzymes can be conjugated with a higher ratio of streptavidin/avidin per enzyme. In addition, as the number of layers increases the stresses on the layer structure increase and the structure could shear or break apart more easily during washes. It is sometimes seen that atop a specific microelectrode the fluorescence intensity would suddenly decrease and this effect was believed to be due to layer fracture and particle loss. Again, a higher stoichiometry of streptavidin to protein would increase the binding interactions between layers and help to prevent structure fracture and NP loss. Finally, another factor could be attributed to nonuniformity in the electric field across the microarray chip or even across an individual microelectrode. This would also lead to variations in NP and enzyme assembly.

ESEM images, as seen in Figure 6, obtained at the edge of introduced fractures reveal the layering of the NPs atop the hydrogel layer. From these micrographs, it is evident that the assembled structures have variability in surface topography making it difficult to clearly distinguish one layer from the next. This is mostly attributed to the particle packing orientation as each additional layer of NPs packs onto the layer below. Additionally, this could be due to NP loss during the introduction of a fracture, during the sputtering of the metal overlayer for ESEM imaging, or even during the imaging process itself. In addition, there may be loss during

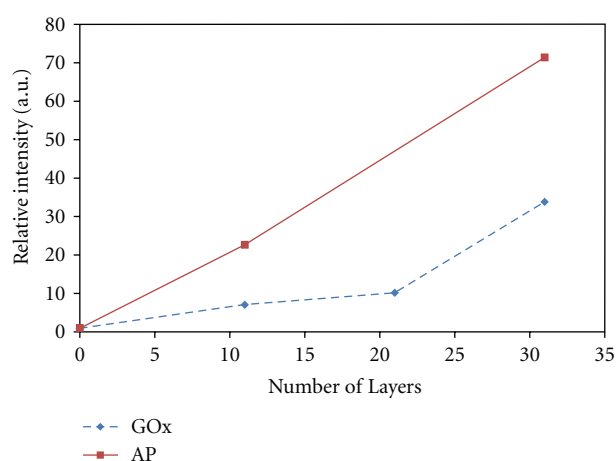


FIGURE 7: Plot of the relative intensity of chemiluminescent signal obtained from chips addressed with 0, 11, 21, and 31 layers of 200 nm biotin NPs and GOx-avidin or 0, 11, and 31 layers with streptavidin-AP.

washes and variations in binding across the electrode during the assembly process.

**3.3. Retention of Enzyme Activity.** Retention of enzyme activity after layer assembly was evaluated by incubating the microarray chips with the appropriate chemiluminescent substrate and then exposing the chips to X-ray film. The results of the scanned and analyzed X-ray film detection of the enzyme-NP layers are shown in Figure 7. Data was collected from chips layered with 200 nm biotin NPs and GOx-avidin with 0, 11, 21, and 31 total layers as well as chips layered with 200 nm biotin NPs and streptavidin-AP at 0, 11, and 31 layers. The results show increasing activity detected with increasing numbers of layers. This trend is seen with both types of enzymes, and this indicates that the total enzyme activity can be tuned simply by altering the number of enzyme layers incorporated into each structure. Similar results could not be obtained from

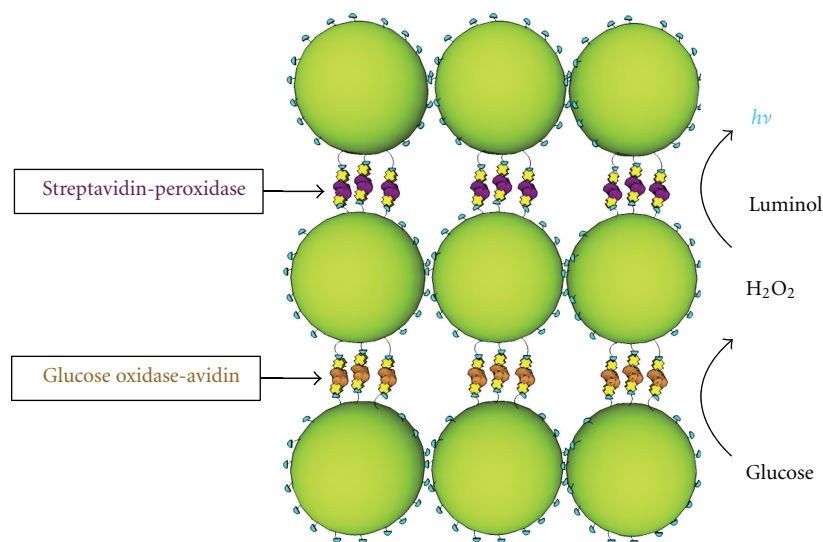


FIGURE 8: Coupling of bi-enzyme NP layers. The incorporation of both streptavidin-HRP and GOx-avidin into the same layer structure may allow for chemical coupling of the layers. The oxidation of glucose by GOx produces hydrogen peroxide which is then a substrate for the chemiluminescent oxidation of luminol, which generates light that can be detected.

bi-enzyme structures, consisting of both GOx-avidin and streptavidin-HRP, as illustrated in Figure 8. This may be due to a number of reasons including poor reagent and substrate quality, poor layer quality, poor structure porosity, insufficient enzyme incorporation into the layers, and a poor detection scheme. A bi-enzyme structure requires optimization due to the coupling of multiple reaction steps. If any one of the reactions is inefficient, then the overall signal may not be detectable. In addition, the products from the first reaction must be able to effectively diffuse to the second set of enzymes; thus, the enzyme layering order may be of importance. Additionally, an important aspect of producing active NP layers is the ability to sensitively detect their activity. The X-ray film used in the detection method verified in proof of principle that the biological activity of the molecules could be retained after assembly. More sensitive methods, including amperometric detection or highly sensitive imaging, beyond the capabilities of the microelectronic array and imaging system we had available, would allow for a better detection scheme to monitor total activity for each fabricated structure. Nonetheless, the presence of a measurable enzyme activity from the single enzyme structures verifies that the application of an electric field is not only efficient for structure assembly but also gentle enough to preserve the functionality of the enzymes.

Altogether the results showing enzyme-nanoparticle layer assembly and enzyme activity retention demonstrate an efficient and effective method of fabricating biological or chemical sensors. Site-specific layer assembly, demonstrated in this study as well as previous studies, means that multiple types of enzyme-nanoparticle structures can be fabricated on each chip in a combinatorial manner [37]. Additionally, various types of enzymes, proteins, or other biomolecules could be used in conjunction with a wide array of particle

types as long as they have complementary binding mechanisms, such as the biotin-streptavidin scheme used here. This would allow for production of high-density microarray sensors capable of analyzing hundreds of analytes at a time.

#### 4. Conclusion

We have successfully demonstrated the ability to fabricate higher-order enzyme-NP structures by electric-field-directed self-assembly. Through the application of electric-field-directed assembly, alternating layers of 200 nm or 40 nm biotin NPs and streptavidin/avidin enzymes have been assembled up to 47 layers. These structures included multilayer structures with 200 nm or 40 nm GOx-avidin-biotin NPs, with AP-streptavidin-biotin NPs, and with HRP-streptavidin-biotin NPs. The electrophoretic assembly method atop a microelectronic array allows for site-specific fabrication from low concentration solutions of enzymes and NPs. The concentration effect due to the electrophoretic deposition results in rapid layer assembly with minimal passive non-specific binding on inactive sites across the chip. Moreover, the enzymatic activity of the biological molecules was preserved in the assembled structures. In addition, we have assembled structures consisting of multiple enzyme types, GOx-avidin and streptavidin-HRP, which demonstrates the potential of multilevel reactions or detection schemes, including chemiluminescence and bioluminescence. This method of fabrication now provides an efficient mechanism of creating biologically and chemically active NP structures from individual components much more efficiently than traditional passive layer-by-layer methods. Assembly of these structures in a combinatorial manner to specific sites on the chip, using a wide array of biomolecules (proteins and DNA) and nanoparticles, would allow for



fabrication of high-density microarray sensors for high-throughput analysis. The ability to incorporate multiple types of molecules along with the potential of liftoff, which enables the detachment of these structures from the surface, renders them more versatile as dispersible biosensors, diagnostic tools, and drug delivery vehicles.

## Acknowledgments

The authors thank Nanogen, Inc. for supplying microelectronic arrays and the Nanochip 400 system, Dr. Dietrich Dehlinger for assistance and training with the system and methods, Juhi Saha for her help in experiments, and the UCSD Nano3 facility and personnel for training and support on the ESEM.

## References

- [1] S. Guo and S. Dong, "Biomolecule-nanoparticle hybrids for electrochemical biosensors," *TrAC—Trends in Analytical Chemistry*, vol. 28, no. 1, pp. 96–109, 2009.
- [2] K. Ariga, Q. Ji, and J. Hill, "Enzyme-encapsulated layer-by-layer assemblies: current status and challenges toward ultimate nanodevices," in *Advances in Polymer Science*, F. Caruso, Ed., vol. 229, pp. 51–87, Springer, Berlin, Germany, 2010.
- [3] N. K. Chaki and K. Vijayamohan, "Self-assembled monolayers as a tunable platform for biosensor applications," *Biosensors and Bioelectronics*, vol. 17, no. 1–2, pp. 1–12, 2002.
- [4] Y. Kobayashi and J. I. Anzai, "Preparation and optimization of bienzyme multilayer films using lectin and glyco-enzymes for biosensor applications," *Journal of Electroanalytical Chemistry*, vol. 507, no. 1–2, pp. 250–255, 2001.
- [5] B. Limoges, J. M. Savéant, and D. Yazidi, "Avidin-biotin assembling of horseradish peroxidase multi-monomolecular layers on electrodes," *Australian Journal of Chemistry*, vol. 59, no. 4, pp. 257–259, 2006.
- [6] Y. Lvov, K. Ariga, I. Ichinose, and T. Kunitake, "Assembly of multicomponent protein films by means of electrostatic layer-by-layer adsorption," *Journal of the American Chemical Society*, vol. 117, no. 22, pp. 6117–6123, 1995.
- [7] M. Onda, K. Ariga, and T. Kunitake, "Activity and stability of glucose oxidase in molecular films assembled alternately with polyions," *Journal of Bioscience and Bioengineering*, vol. 87, no. 1, pp. 69–75, 1999.
- [8] M. Onda, Y. Lvov, K. Ariga, and T. Kunitake, "Sequential actions of glucose oxidase and peroxidase in molecular films assembled by layer-by-layer alternate adsorption," *Biotechnology and Bioengineering*, vol. 51, no. 2, pp. 163–167, 1996.
- [9] K. L. Prime and G. M. Whitesides, "Self-assembled organic monolayers: Model systems for studying adsorption of proteins at surfaces," *Science*, vol. 252, no. 5010, pp. 1164–1167, 1991.
- [10] S. V. Rao, K. W. Anderson, and L. G. Bachas, "Controlled layer-by-layer immobilization of horseradish peroxidase," *Biotechnology and Bioengineering*, vol. 65, no. 4, pp. 389–396, 1999.
- [11] T. Hoshi, N. Sagae, K. Daikuhara, K. Takahara, and J. I. Anzai, "Multilayer membranes via layer-by-layer deposition of glucose oxidase and Au nanoparticles on a Pt electrode for glucose sensing," *Materials Science and Engineering C*, vol. 27, no. 4, pp. 890–894, 2007.
- [12] X. M. Zhao, "Soft lithographic methods for nano-fabrication," *Journal of Materials Chemistry*, vol. 7, no. 7, pp. 1069–1074, 1997.
- [13] S. Bharathi and M. Nogami, "A glucose biosensor based on electrodeposited biocomposites of gold nanoparticles and glucose oxidase enzyme," *Analyst*, vol. 126, no. 11, pp. 1919–1922, 2001.
- [14] D. A. Dehlinger, B. D. Sullivan, S. Esener, and M. J. Heller, "Electric-field-directed assembly of biomolecular-derivatized nanoparticles into higher-order structures," *Small*, vol. 3, no. 7, pp. 1237–1244, 2007.
- [15] S. Dey, K. Mohanta, and A. J. Pal, "Magnetic-field-assisted layer-by-layer electrostatic assembly of ferromagnetic nanoparticles," *Langmuir*, vol. 26, no. 12, pp. 9627–9631, 2010.
- [16] M. Shao, X. Xu, J. Han et al., "Magnetic-field-assisted assembly of layered double hydroxide/metal porphyrin ultrathin films and their application for glucose sensors," *Langmuir*, vol. 27, no. 13, pp. 8233–8240, 2011.
- [17] M. Trau, D. A. Seville, and I. A. Aksay, "Field-induced layering of colloidal crystals," *Science*, vol. 272, no. 5262, pp. 706–709, 1996.
- [18] K. D. Barbee, A. P. Hsiao, M. J. Heller, and X. Huang, "Electric field directed assembly of high-density microbead arrays," *Lab on a Chip*, vol. 9, no. 22, pp. 3268–3274, 2009.
- [19] R. Krishnan, D. A. Dehlinger, G. J. Gemmen, R. L. Mifflin, S. C. Esener, and M. J. Heller, "Interaction of nanoparticles at the DEP microelectrode interface under high conductance conditions," *Electrochemistry Communications*, vol. 11, no. 8, pp. 1661–1666, 2009.
- [20] R. Krishnan and M. J. Heller, "An AC electrokinetic method for enhanced detection of DNA nanoparticles," *Journal of Biophotonics*, vol. 2, no. 4, pp. 253–261, 2009.
- [21] R. Krishnan, B. D. Sullivan, R. L. Mifflin, S. C. Esener, and M. J. Heller, "Alternating current electrokinetic separation and detection of DNA nanoparticles in high-conductance solutions," *Electrophoresis*, vol. 29, no. 9, pp. 1765–1774, 2008.
- [22] R. C. Bailey, K. J. Stevenson, and J. T. Hupp, "Assembly of micropatterned colloidal gold thin films via microtransfer molding and electrophoretic deposition," *Advanced Materials*, vol. 12, no. 24, pp. 1930–1934, 2000.
- [23] L. Besra and M. Liu, "A review on fundamentals and applications of electrophoretic deposition (EPD)," *Progress in Materials Science*, vol. 52, no. 1, pp. 1–61, 2007.
- [24] T. Haruyama and M. Aizawa, "Electron transfer between an electrochemically deposited glucose oxidase/Cu[II] complex and an electrode," *Biosensors and Bioelectronics*, vol. 13, no. 9, pp. 1015–1022, 1998.
- [25] A. L. Rogach, N. A. Kotov, D. S. Koktysh, J. W. Ostrander, and G. A. Ragoisha, "Electrophoretic deposition of latex-based 3D colloidal photonic crystals: a technique for rapid production of high-quality opals," *Chemistry of Materials*, vol. 12, no. 9, pp. 2721–2726, 2000.
- [26] L. Shi, Y. Lu, J. Sun et al., "Site-selective lateral multilayer assembly of bienzyme with polyelectrolyte on ITO electrode based on electric field-induced directly layer-by-layer deposition," *Biomacromolecules*, vol. 4, no. 5, pp. 1161–1167, 2003.
- [27] Y. Solomentsev, M. Böhmer, and J. L. Anderson, "Particle clustering and pattern formation during electrophoretic deposition: a hydrodynamic model," *Langmuir*, vol. 13, no. 23, pp. 6058–6061, 1997.
- [28] M. Trau, D. A. Saville, and I. A. Aksay, "Assembly of colloidal crystals at electrode interfaces," *Langmuir*, vol. 13, no. 24, pp. 6375–6381, 1997.

- [29] S. R. Yeh, M. Seul, and B. I. Shraiman, "Assembly of ordered colloidal aggregates by electric-field-induced fluid flow," *Nature*, vol. 386, no. 6620, pp. 57–59, 1997.
- [30] D. R. Albrecht, V. L. Tsang, R. L. Sah, and S. N. Bhatia, "Photo- and electropatterning of hydrogel-encapsulated living cell arrays," *Lab on a Chip*, vol. 5, no. 1, pp. 111–118, 2005.
- [31] J. Cheng, E. L. Sheldon, A. Uribe et al., "Preparation and hybridization analysis of DNA/RNA from *E. coli* on microfabricated bioelectronic chips," *Nature Biotechnology*, vol. 16, no. 6, pp. 541–546, 1998.
- [32] C. F. Edman, D. E. Raymond, D. J. Wu et al., "Electric field directed nucleic acid hybridization on microchips," *Nucleic Acids Research*, vol. 25, no. 24, pp. 4907–4914, 1997.
- [33] C. Gurtner, E. Tu, N. Jamshidi et al., "Microelectronic array devices and techniques for electric field enhanced DNA hybridization in low-conductance buffers," *Electrophoresis*, vol. 23, no. 10, pp. 1543–1550, 2002.
- [34] A. Kueng, C. Kranz, and B. Mizaikoff, "Amperometric ATP biosensor based on polymer entrapped enzymes," *Biosensors and Bioelectronics*, vol. 19, no. 10, pp. 1301–1307, 2004.
- [35] R. G. Sosnowski, E. Tu, W. F. Butler, J. P. O'Connell, and M. J. Heller, "Rapid determination of single base mismatch mutations in DNA hybrids by direct electric field control," *Proceedings of the National Academy of Sciences of the United States of America*, vol. 94, no. 4, pp. 1119–1123, 1997.
- [36] M. J. Heller, D. A. Dehlinger, and B. D. Sullivan, "Parallel assisted assembly of multilayer DNA and protein nanoparticle structures using a CMOS electronic array," in *International Symposium on DNA-Based Nanoscale Integration*, vol. 859 of *AIP Conference Proceedings*, pp. 73–81, May 2006.
- [37] D. Dehlinger, B. Sullivan, S. Esener, D. Hodko, P. Swanson, and M. J. Heller, "Automated combinatorial process for nanofabrication of structures using bioderivatized nanoparticles," *Journal of the Association for Laboratory Automation*, vol. 12, no. 5, pp. 267–276, 2007.
- [38] D. A. Dehlinger, B. D. Sullivan, S. Esener, and M. J. Heller, "Directed hybridization of DNA derivatized nanoparticles into higher order structures," *Nano Letters*, vol. 8, no. 11, pp. 4053–4060, 2008.

## Methodology Report

# High-Resolution Whole-Mount *In Situ* Hybridization Using Quantum Dot Nanocrystals

**Andriani Ioannou, Iro Eleftheriou, Andrea Lubatti, Anna Charalambous, and Paris A. Skourides**

*Department of Biological Sciences, University of Cyprus, 1678 Nicosia, Cyprus*

Correspondence should be addressed to Paris A. Skourides, skourip@ucy.ac.cy

Received 30 August 2011; Revised 29 September 2011; Accepted 3 October 2011

Academic Editor: P. Bryant Chase

Copyright © 2012 Andriani Ioannou et al. This is an open access article distributed under the Creative Commons Attribution License, which permits unrestricted use, distribution, and reproduction in any medium, provided the original work is properly cited.

The photostability and narrow emission spectra of nanometer-scale semiconductor crystallites (QDs) make them desirable candidates for whole-mount fluorescent *in situ* hybridization to detect mRNA transcripts in morphologically preserved intact embryos. We describe a method for direct QD labeling of modified oligonucleotide probes through streptavidin-biotin and antibody-mediated interactions (anti-FITC and anti-digoxigenin). To overcome permeability issues and allow QD conjugate penetration, embryos were treated with proteinase K. The use of QDs dramatically increased sensitivity of whole-mount *in situ* hybridization (WISH) in comparison with organic fluorophores and enabled fluorescent detection of specific transcripts within cells without the use of enzymatic amplification. Therefore, this method offers significant advantages both in terms of sensitivity, as well as resolution. Specifically, the use of QDs alleviates issues of photostability and limited brightness plaguing organic fluorophores and allows fluorescent imaging of cleared embryos. It also offers new imaging possibilities, including intracellular localization of mRNAs, simultaneous multiple-transcript detection, and visualization of mRNA expression patterns in 3D.

## 1. Introduction

With the advent of cell type specific molecular markers, description and analysis of developmental morphogenesis has become possible in a number of biological systems. Gene-specific RNA probes are now extensively used as they enable visualization of gene expression patterns and thus provide valuable information regarding the role of specific genes during development, as well as regarding positioning and movement of a particular cell type at different stages of development. This technique, known as whole mount *in situ* hybridization (WISH), was initially performed using radioactive probes, but was radically simplified when non-radioactive probes were used successfully [2–4]. It is now widely used in several biological systems, including *Drosophila* [4], *Xenopus* [5], quail [6], *Dictyostelium* [7], and *Zebrafish* [8]. *In situ* hybridization (ISH) is a quite common technique among developmental research labs, yet its uses are quite diverse and include medical and prenatal diagnostics [9–16]. Not long after its introduction, protocols using two

different labels for the RNA probes and two color substrates were described, allowing the detection of more than one transcript simultaneously [17]. However, a major limitation of these chromogenic multilabeling techniques is that the overlapping regions of expression are very difficult to discern. The use of fluorescent methods for detecting transcripts may overcome this limitation; yet fluorophores for single- as well as double-transcript visualization [18] in whole mounts have only been used extensively in the fly and to some extent in the zebrafish [8]. More recently, simultaneous fluorescent detection of three transcripts was reported in the chick, and multiplexing has been used to detect up to seven transcripts in the fly [19–21]. However, successful implementation of current fluorescent protocols is very rare, especially in the mouse or *Xenopus* embryos, and even then the fluorescent images are of insufficient quality and thus cannot rival the staining obtained with normal chromogenic substrates.

In addition, imaging the signal is complicated due to the strong autofluorescence of the embryos [22], which interferes with fluorescent detection of RNA and makes

the use of enzymatic amplification necessary in the *mouse*, *Xenopus*, *chick*, and other embryos. The amplification step is also necessary in the case of chromogenic protocols; however, this step undermines the resolving ability of both methods. Amplification reactions create a precipitate which is deposited in the area surrounding the RNA and then diffuses out. It therefore does not remain localized within the particular intracellular region or compartment where the RNA in question is localized. In fact, it often diffuses throughout the cell and sometimes even leaks outside of the cell being labeled [23]. This problem is less pronounced in the case of tyramide amplification, where the peroxidase reaction produces tyramide radicals that react covalently with proteins at the site of the reaction, reducing the diffusion radius appreciably [24, 25]. However, even in this case, the resolution is still limited by diffusion and depends on the time that the reaction is allowed to proceed [23]. To combat diffusion issues, direct labeling of the probe is required, as this allows single cell, as well as, intracellular resolution of the localization of a particular mRNA. In addition to improved resolution, direct labeling of the probe allows simultaneous hybridization of multiple mRNAs, as long as fluorophores can be spectrally resolved. It is also extremely simple and can be quantitative since the fluorescence of the probe can be calibrated [12]. Despite successful implementation of direct labeling of messenger RNAs in cell culture [26, 27], this has not been possible in embryos due to the low fluorescent intensities of organic fluorophores.

The use of fluorescent methods for detecting transcripts is highly advantageous compared to chromogenic methods, especially because it enables higher quality three-dimensional imaging, multiplexing different RNA species, and covisualization of RNA with proteins. As already mentioned, the major limitations preventing widespread use of fluorescence detection for WISH are the high endogenous background fluorescence of many embryos, as well as the limited brightness and photostability of organic fluorophores. A new type of inorganic fluorophore, namely, Quantum Dots (QDs) have been used recently in several systems *in vitro* for detection of proteins as well as *in vivo* for protein labeling and lineage tracing [28–42]. QDs were also used for *in situ* hybridization in clinical biopsies for the detection of multiple mRNAs with successful conjugation to oligonucleotide probes [43]. QDs have ideal optical properties for use in biology like strong fluorescent signal emission compared to organic and protein fluorophores [44, 45]. In addition, due to their longer excited state lifetime, their fluorescence can be separated from the background fluorescence with time-domain imaging [46]. Using QDs offers a number of other advantages over organic fluorophores including wide excitation spectra (which makes the use of a single excitation filter possible), narrow and tunable emission spectra (which reduces spectral overlap making the simultaneous use of more colors possible), large separation between the excitation and emission (which increases the detection sensitivity), and resistance to photobleaching [47, 48]. Their unique optical properties made QDs an ideal candidate for detecting multiple mRNAs in ISH protocols [49], and their high fluorescence intensity raised the possibility of using

them for RNA detection in whole embryos. Previous efforts to do this met with aggregation issues and were time consuming since detection had to be done with RNA covalently linked to hydroxylated QDs [50]. Since then, we and others have reported new methods of creating hydrophilic QDs and hydrophilic QD conjugates have become commercially available [32, 38, 51]. Studies have also pointed out difficulties in using QDs for FISH experiments [52, 53], including steric hindrance [54], degradation of QD conjugates and adherence to tubes and tips [55].

In this work we explore the use of QDs in WISH experiments. We show that the greatest limitation of these nanocrystals is penetration, since commercially available QDs are quite large and therefore fail to penetrate the many cell layers of an embryo or are significantly trapped if they do. However, we have determined that proteinase K can render *Xenopus* embryos sufficiently permeable to allow QD penetration deep within embryonic tissues. More specifically, we produced fluorescein- (FITC-), biotin-, and digoxigenin (DIG) labeled RNA probes and used QD-antibody and QD-streptavidin conjugates to visualize them. Our experiments show that this is an extremely sensitive assay that significantly improved RNA detection sensitivity. We then employed QDs to visualize several RNA probes that had been used to perform WISH in *Xenopus* embryos. We demonstrate that QD detection of endogenous messenger RNAs is effective and that it can be used to provide WISH data of higher resolution than current techniques. Finally, we show that QDs can be used to carry out two-color *in situ* hybridization simultaneously. Therefore, the use of QDs to perform nonamplified fluorescent whole mount *in situ* in *Xenopus* embryos, one of the most highly autofluorescent (and thus demanding) vertebrate developmental organisms, suggests that QD whole-mount *in situ* will find successful applications in most developmental models.

## 2. Materials and Methods

**2.1. Embryos.** *Xenopus laevis* embryos from induced spawning [56] were staged according to Nieuwkoop and Faber [57]. Operation techniques and buffer (MMR) have been described [56]. *Xenopus* embryos were fertilized *in vitro* and dejellied using 2% cysteine-HCl, pH 7.8, then maintained in 0.1X Marc's Modified Ringer's (MMR).

**2.2. Whole-Mount Immunofluorescence.** *Xenopus laevis* embryos were fixed in 3.7% formaldehyde in MEMFA (2 hours at room temperature), and the vitelline envelope was manually removed with forceps. Permeabilization of embryos was carried out several ways: (1) overnight in 1X PBS supplemented with 0.5% Triton, and 1% DMSO (PBBDT), (2) overnight in 1X PBS supplemented with 5% Triton and 1% DMSO, (3) two hours in 1X PBS supplemented with 0.2% SDS, and (4) for four hours in 1X PBS supplemented with 0.2% SDS or (5) for 25 minutes in 10<sup>-6</sup>g/mL Proteinase K. Embryos were then blocked for 2 hours in 1X PBS with 0.5% Triton, 5% BSA, and 1% Normal Goat serum. Primary antibody staining followed. Embryos were incubated with



biotin-conjugated phosphotyrosine (anti-4G10, Millipore) antibody overnight at 4°C at a dilution of 1:500 (in block solution). Embryos were then washed ( $3 \times 10$  min) in PBDT and incubated for 2 hours at room temperature with streptavidin conjugated Cy3 or QDs 655 nm at 1:500 dilution in fresh block solution. After incubation, embryos were washed in PBDT ( $3 \times 10$  min). For negative control experiments, embryos were blocked and then incubated with secondary conjugates only. Clearing of embryos was performed by immersion of the embryos in two parts benzyl benzoate and one part benzyl alcohol after methanol dehydration (Murray's Clearing Medium, BB:BA). The refractive index of BB:BA closely matches the refractive index of yolk thereby rendering *Xenopus* embryos nearly transparent. The embryos were imaged on a Zeiss Axio Imager Z1 using a Zeiss AxioCam MR3, the Axiovision software 4.7. Optical sectioning was achieved using a Zeiss Apotome structured illumination system.

**2.3. In Vitro Transcription.** Antisense digoxigenin - (DIG-), biotin-, and fluorescein - (FITC-) labeled Xbra (in CS2++), Edd, MyoD (in CS2++), Amylase (in pCR4Blunt-TOPO), Xa-1 (in pBSK+), cardiac actin (in pSP64), and LTBP1 (in CS2++) probes were synthesized by *in vitro* transcription from linearized plasmid using RNA polymerase SP6 or T3 and ribonucleotide mixture which results in RNA transcripts containing bio-UTP, FITC-UTP, or Dig-UTP (Roche). The manufacturer's protocol was followed with a modification in the total reaction volume which was scaled down to 20  $\mu$ L. RNA probes from these reactions was purified using isopropanol/LiCl precipitation.

**2.4. Chromogenic and Fluorescent Wholemount In Situ Hybridization.** Biotin-, FITC-, and DIG-labeled RNA probes (transcribed as described above) were used to perform *in situ* hybridization using the protocol reported by Harland [58], with some modification. Methanol was substituted with ethanol and 4% paraformaldehyde in PBS was used to fix the embryos instead of formaldehyde. After proteinase K treatment (5 min for chromogenic WISH and 25 minutes for QD-based WISH) embryos were blocked with 0.1% BSA, 10% sheep serum in 0.1% Tween in 1 X PBS(PBT) solution, and then washes were performed in PBS. After blocking, embryos were refixed for one hour in 4% paraformaldehyde followed by prehybridization at 65°C. For chromogenic WISH experiments, the original protocol was followed. However, for QD-based fluorescent WISH experiments the protocol was modified. After the last 0.2X SSC wash at 65°C the embryos were blocked with 1 X PBS + 0.1% BSA + 0.1% Tween for one hour and then transferred to a new vial which contained 1 mL of a 1:500 dilution Qdot-streptavidin 705 nm, QD-anti-FITC or QD-anti-DIG 655 nm (Invitrogen) conjugates in blocking solution. The addition of 0.1% BSA and 0.1% Tween into the incubation buffer significantly improved penetration and decreased background without appreciably affecting the QD colloidal stability or the signal intensity. After the incubation, the embryos were washed in PBT ( $4 \times 30$  min) at room temperature. Embryos were then cleared in

BB:BA (as described above). The fluorescent signal remains localized after clearing, and this allows data acquisition from different planes within the embryo without the need for sectioning. The embryos were imaged on an upright Zeiss fluorescent microscope with a Zeiss AxioCam and the Axiovision 4.7 software (using a custom filter set; excitation 300–460 nm, emission 500 nm longpass, dichroic 475 nm). When detecting weak signals, the Axiovision software allowed white balancing of the camera so that the green background (in embryos viewed with a 420 long pass filter due to the bias of the autofluorescence towards shorter wavelengths) appears white, resulting in a major boost of the QD signal (605 peak emission), decrease of the threshold of detection and significantly better contrast. If the calibration of the camera is done properly, control embryos that are not labeled with QDs appear completely white under UV excitation without any traces of red. This color separation method has to be performed carefully and control embryos need to appear white otherwise the risk of generating false staining increases significantly. Due to the fact that the embryo has several distinct regions where the background fluorescence changes not only in terms of intensity but also in terms of spectral balance the region chosen for assignment of “white” was the region in which the background had the longest average wavelength. In this manner we ensured that long-average wavelength background regions would appear white, and shorter average wavelength regions would appear blue.

### 3. Results and Discussion

**3.1. Proteinase K Facilitates QD Penetration in *Xenopus* Embryos.** We first wanted to examine whether QDs could penetrate *Xenopus* embryos to a sufficient depth so as to allow specific deep tissue staining. We initially compared streptavidin-conjugated QDs to streptavidin-conjugated Cy3 in whole-mount immunostaining experiments for their ability to detect a biotinylated antibody against phosphotyrosine. This antibody was purposely selected due to its strong and specific staining pattern of cell-cell boundaries that allows easy visual confirmation upon successful labeling. Not surprisingly, the staining pattern obtained using QDs was very similar to the one obtained using Cy3 in the superficial cell layer of the embryo (upper area of Figure 1(a) showing superficial cells of the fin of a tadpole and data not shown). However, and in contrast to Cy3, QD staining could not be detected beyond the first cell layer indicating that QDs encountered penetration issues, most likely due to size restrictions (Figure 1(a) lower area showing the somites of the tadpole). Several approaches were employed to increase QD embryo permeability, including the use of harsh detergents like SDS, with limited success. However, use of proteinase K treatment enabled penetration of QDs into deep tissues and resulted in specific deep tissue staining (Figure 1(b) and Table 1). However, proteinase K treatment is not suitable for use with most whole-mount immunostaining antibodies as it may lead to degradation of the target antigen.

It should be noted that the best results were obtained using newly opened QD-streptavidin conjugates from Invitrogen. Unfortunately though, the performance of these

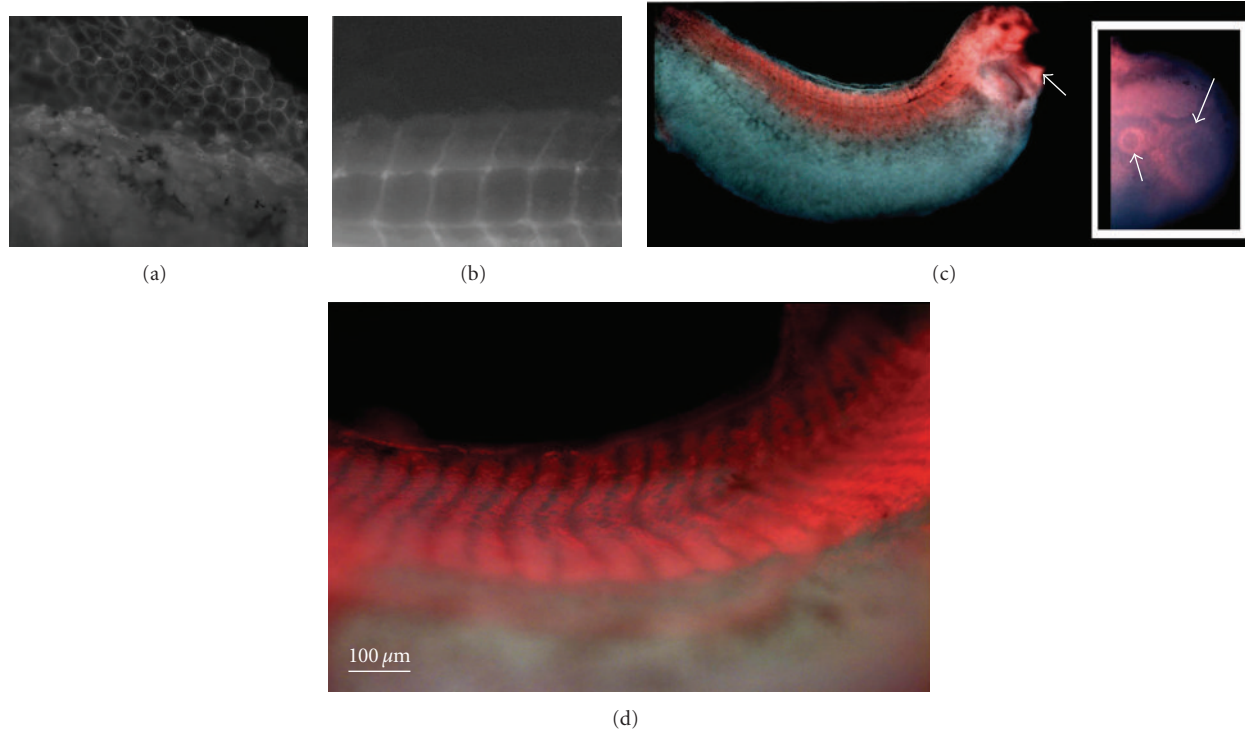


FIGURE 1: Proteinase K treatment is necessary to allow QD penetration and labeling of deep tissues in *Xenopus* and QD705 nm anti-Dig conjugates can be used for the detection of transcripts in wholemount *in situ* hybridization experiments. (a) Detection of biotinylated 4G10 (anti-Phosphotyrosine) antibody using streptavidin conjugated 655 nm QDs in a triton permeabilized embryo. Specific staining can be seen at the cell-cell boundaries of the ectodermal cells of the fin (upper part of the image) but not in the deep tissues (somites at the bottom part of the image). (b) Detection of biotinylated 4G10 (anti-Phosphotyrosine) antibody using streptavidin conjugated 655 nm QDs in a PK permeabilized embryo. Specific staining of the deep intersomitic boundaries can be seen. Superficial cells of the fin cannot be seen due to degradation of this delicate structure by the PK treatment. (c) QD705 nm anti-DIG antibody labeling of the probe for LTBP1 generates a staining pattern that closely matches the published expression for this mRNA [1]. QDs label the somites as well as anterior neural and neural crest tissues including the branchial arches and a region surrounding the eye. (d) Imaging of the QD labeling for LTBP1 in the somites at 10X magnification.

TABLE 1: Comparative chart of different permeabilization approaches used in whole mount immunostaining using a biotinylated anti-phosphotyrosine antibody (4G10 clone) and detected with Streptavidin conjugated QDs. Proteinase K treatment is the only approach which allowed deep tissue staining using QDs.

	Superficial Staining	Deep Tissue Staining
TRITON 1%	+++	—
TRITON 5%	+++	—
0.2% SDS 2 h	+++	+
0.2% SDS 4 h	+++	+
PK 25 min	+++	+++

conjugates was batch dependent and significantly diminished if QD-streptavidin conjugates were stored for more than two-three months, despite a six-month shelf life stated by the manufacturer. In addition, it was evident that use of QDs with emissions in the NIR (700 and 800 nm) provided a big improvement in detection sensitivity due to a significant reduction of tissue autofluorescence in this region of the spectrum. However, commercially available QDs with peak

emissions in these wavelengths are quite large and suffer from even greater permeability problems. Consequently, there is an increased need for more reliable and smaller NIR QDs to become commercially available.

**3.2. QD Labeling of LTBP1 in *Xenopus* Embryos.** Given that proteinase K treatment facilitated QD penetration in *Xenopus* embryos and allowed specific deep tissue staining in whole-mount immunostaining experiments, we wanted to determine whether QDs could be used in WISH experiments in which proteinase K treatment is a standard permeabilization approach. We initially tested whether anti-digoxigenin-conjugated QDs could detect a DIG-labeled RNA probe specific for *Xenopus* Latent Transforming Growth Factor  $\beta$  Binding Protein 1 (LTBP1). As shown in Figure 1, anti-DIG QDs (see Figures 1(c) and 1(d)) gave a similar staining pattern of *Xenopus* LTBP1 to the published pattern obtained using the same probe but developed using a chromogenic reaction [1]. LTBP1 signal was detected in the head region including branchial arches and around the eye (shown as inset of Figure 1(c)) and the somites in agreement with the published expression pattern [1]. Furthermore, QD-labeling of LTBP1

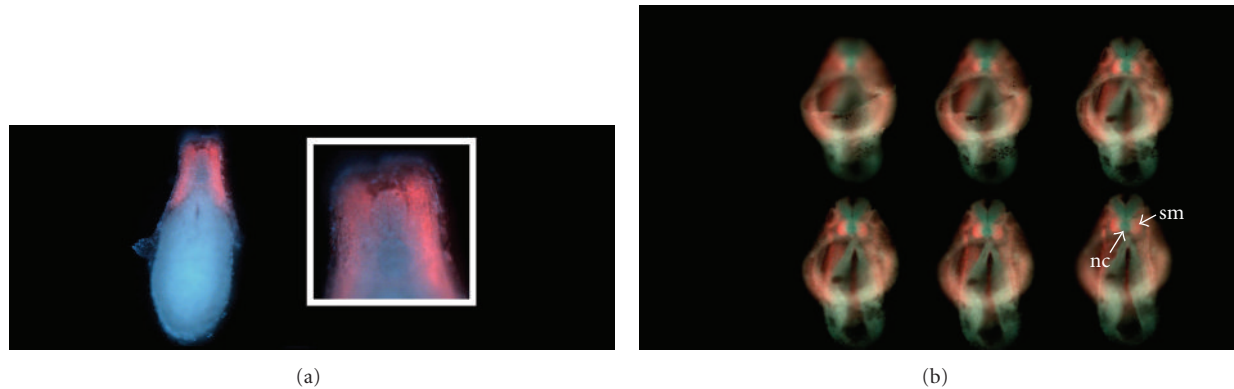


FIGURE 2: QD-streptavidin staining of LTBP1 compares favorably with the published staining achieved using standard chromogenic protocols in the deeper structures of the embryo [1]. (a) A transverse section from a whole mount *in situ* indicating the LTBP1 transcript expression pattern using QD705 nm streptavidin. The somitic staining obtained using QDs is identical to the published data using the chromogenic protocol [1], showing that the QD-streptavidin solution can penetrate and stain the deep areas of the somites. (b) A series of transverse optical sections of a QD-streptavidin-stained embryo for the LTBP1 message. The optical sections reveal that the staining previously identified as notochord by the chromogenic protocol is in fact somitic mesoderm flanking the notochord (nc: notochord, sm: somatic mesoderm).

exhibited high signal intensity and resolution confirming that a regular fluorescence microscope is sufficient for detection (see Figures 1(c) and 1(d)). To further establish that the QD *in situ* protocol is capable of successful and specific staining, we sectioned and imaged whole-mount QD-stained embryos. As shown in Figure 2(a), QDs can penetrate deep into the embryo following proteinase K treatment and stain structures independently of their proximity to the free QDs in solution. Importantly, the use of QDs for *in situ* staining could result in more accurate determination of transcript expression patterns. Figure 2(b) shows a series of optical section images taken from a z-stack movie, using a fluorescence microscope, starting at the head region and moving posteriorly. As indicated, QD labeling survives the clearing protocol used to render *Xenopus* and other embryos transparent. More importantly, however, is that the optical sections demonstrate that the staining does not originate from the notochord as originally published [1], but rather from the somitic mesoderm flanking the notochord. Therefore, the additional spatial cues provided by optical sectioning can lead to a more accurate determination of an expression domain, further emphasizing the advantages of QD *in situ*.

### 3.3. QD Labeling of Specific Transcripts in *Xenopus* Embryos.

The above results suggest that use of anti-DIG conjugated QDs in WISH can give highly specific staining of DIG labeled mRNA probes, even in deep tissues. To further determine the utility of this approach we tested whether QDs could also label alternative modified oligonucleotide probes through biotin-streptavidin and FITC- anti-FITC interactions, using a similar protocol. Figure 3(a) depicts *in situ* staining performed on a dissected *Xenopus* tadpole gut, against a biotin labeled amylase probe using either streptavidin-conjugated QDs or the chromogenic reaction. It is evident, from the images, that similar staining patterns are obtained; both the QDs and the chromogenic staining were restricted to the pancreas, where amylase RNA is expressed. Non-stained areas appear white due to background fluorescence that is

present in all visible wavelengths. Despite high background, we obtained a good signal to noise ratio (sufficient to allow clear visualization and delineation of the expressing region) and excellent contrast in the most highly autofluorescent organ of the *Xenopus* tadpole.

We went on to test three well-known mRNAs, namely, (a) Endoderm (Edd: a pan-endodermal marker), (b) Xbra (an early mesodermal marker), and (c) MyoD (a gene encoding a DNA-binding protein that can activate muscle gene expression), which stain the gut, the mesodermal belt, and the muscle somites, respectively. As indicated in Figures 3(b) and 3(d), the use of QDs in *in situ* gives staining patterns that closely match the ones obtained using standard enzymatically amplified chromogenic reaction methods, while maintaining high resolution. The degree of resolution, however, varies with the transcript of interest and its respective expression pattern. For example, in the case of MyoD (Figure 3(b), FITC-labeled probe used), the posterior somites look fused when using the chromogenic protocol but are clearly distinct when using QDs. In contrast, QD staining of a biotin-labeled probe against Edd, which is expressed in the highly autofluorescent gut appears weak except at the anterior, where the gene is expressed at higher levels (Figure 3(c)). Alternatively, in the case of Xbra (Figure 3(d)), the staining of the chromogenic and the QD (against biotin-labeled probe against Xbra) *in situ* is almost identical. Hoechst was used to counter-stain the nuclei blue in this experiment, and the cleared embryo was visualized from the animal pole.

### 3.4. Simultaneous Labeling of Two Transcripts Using QDs.

The fact that all three common modifications of RNA probes could be detected successfully with QDs raised the possibility that QDs could be used to detect two or more transcripts simultaneously. Achieving multiple transcript labeling using chromogenic protocols is a time consuming, stepwise process which, as explained earlier, results in the inability to distinguish areas of coexpression. In order to determine whether two transcripts can be visualized simultaneously, with the use



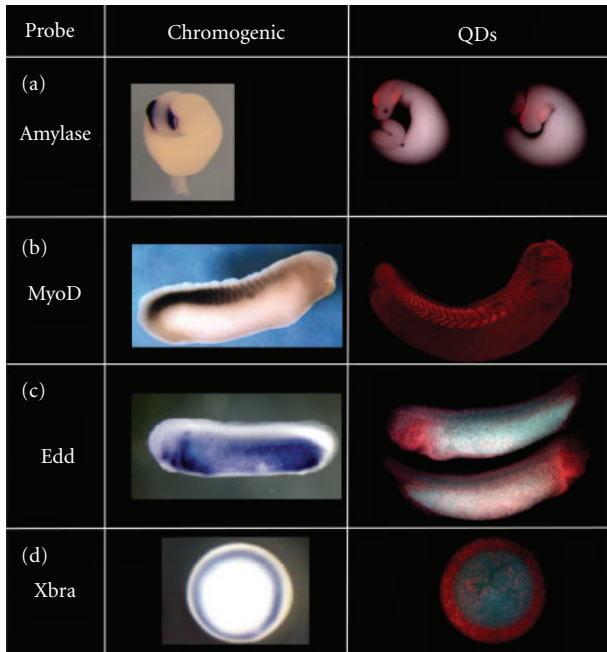


FIGURE 3: *In situ* hybridization using QDs compares favorably with chromogenic *in situ* hybridization staining for a number of well-characterized mRNAs. (a) 705 nmQD-streptavidin staining for amylase on dissected *Xenopus* guts, using a biotinylated amylase probe, is compared to the staining obtained by chromogenic reaction (left). The staining using QDs is identical to that using a chromogenic reaction and restricted to the pancreas, where amylase mRNA is expressed. It is worth noting that the pancreas, a morphologically identifiable organ, is extremely autofluorescent making detection of fluorescent staining difficult. (b) Comparison of the QD and chromogenic staining for MyoD a muscle marker (using a FITC-labeled probe). The 655 nmQD anti-FITC and the chromogenic staining are similar, but the QD staining gives much better resolution of the posterior somites. (c) Comparison of QD versus chromogenic staining for the Edd transcript, an endodermal marker expressed through the tadpoles gut at varying levels (using a Biotin-labeled probe). The staining using a chromogenic protocol is significantly stronger in this case and the 705 nmQD-Streptavidin seems restricted to the high expression regions. Careful observation reveals that the staining is present throughout the gut region but is masked by the intense autofluorescence of the gut. (d) Comparison of the QD staining versus the chromogenic staining for Xbra, a widely used mesodermal marker (using a Biotin-labeled probe). The marker is known to label the mesodermal belt at gastrula stages; both the chromogenic, as well as the QD-streptavidin protocols result in the same staining pattern consistent with the mesodermal belt.

of QDs, we generated two probes; a FITC-labeled probe against Xa-1 and a biotin-labeled probe against *Xenopus* cardiac actin. The two probes were hybridized at the same time and detected using spectrally distinguishable anti-FITC-conjugated and Streptavidin-conjugated QDs, respectively. As seen in Figures 4(a) and 4(b) both probes were visualized successfully demonstrating the ability of simultaneous detection of multiple transcripts using the QD *in situ* protocol.

In addition, due to the lack of enzymatic amplification, the resolving ability of this method is substantially better

than that of amplified protocols. This is evident in Figures 4(c) and 4(d), where we present high-magnification images of whole-mount-stained embryos showing the intracellular mRNA localization for Xa-1 and LTBP1, respectively. As can be seen, QD labeling of transcripts is of extremely high resolution and enables distinction of intracellular localization patterns of mRNA. While LTBP1 localized in the cytoplasm, the Xa-1 transcript appeared to be concentrated near the plasma membrane at the cell-cell contact areas. Even though there is no evidence proving that the presented mRNA distribution coincides with the true intracellular localization of these transcripts, the fact that there are such dramatic differences in the signal patterns from different probes suggests that this is indeed the case. Future work will have to focus on closely examining the resolution of this method in model systems where direct, nonamplified *in situ* can be performed, using traditional fluorophores for comparison. Nevertheless, it is clear that this level of resolution cannot be achieved with existing methods for RNA transcript detection in *Xenopus*, which are mostly based on enzymatic amplification. We thus propose that use of the QD approach can simultaneously give macroscopic and intracellular data regarding the distribution of mRNAs in vertebrate embryos.

#### 4. Conclusions

Herein we describe a new application of QDs in nonamplified whole-mount fluorescent *in situ* detection of endogenous mRNAs. The ideal optical properties of QDs provide unprecedented resolution and strong signal intensities that have not been possible to attain using traditional fluorophores. In fact, even though WISH has been available for more than a decade, the requirement for an enzymatic amplification step significantly limited the resolution of this method. Additionally, limitations of current fluorescent protocols have prevented widespread use of fluorescent *in situ* in most developmental models, with the exception of *Drosophila*, and to some extent zebrafish; direct visualization of highly abundant transcripts is possible in *Drosophila*, but not in most vertebrate models, in which an enzymatic amplification step is required. Fluorescent detection of a messenger RNA opens exciting possibilities in terms of imaging and can eliminate the need for sectioning samples. Optical sectioning provides better spatial cues and ensures correct identification of expression domains. It can also be used to create three-dimensional maps of expression, at a previously unattainable resolution, especially if the amplification step is eliminated. Intracellular localization of mRNA transcripts has only recently been investigated [59–63]. The study of mRNA localization is limited by the current *in situ* methods, both fluorescent and chromogenic, due to their relatively low resolving ability. Chromogenic reactions have been used successfully to localize mRNA transcripts in cultured cells but only for transcripts of very high abundance [60–63]. The method we describe is the first nonamplified fluorescent detection of mRNA *in situ* in *Xenopus*. Our protocol results in signal intensities sufficient for imaging on a regular epifluorescence microscope without the need



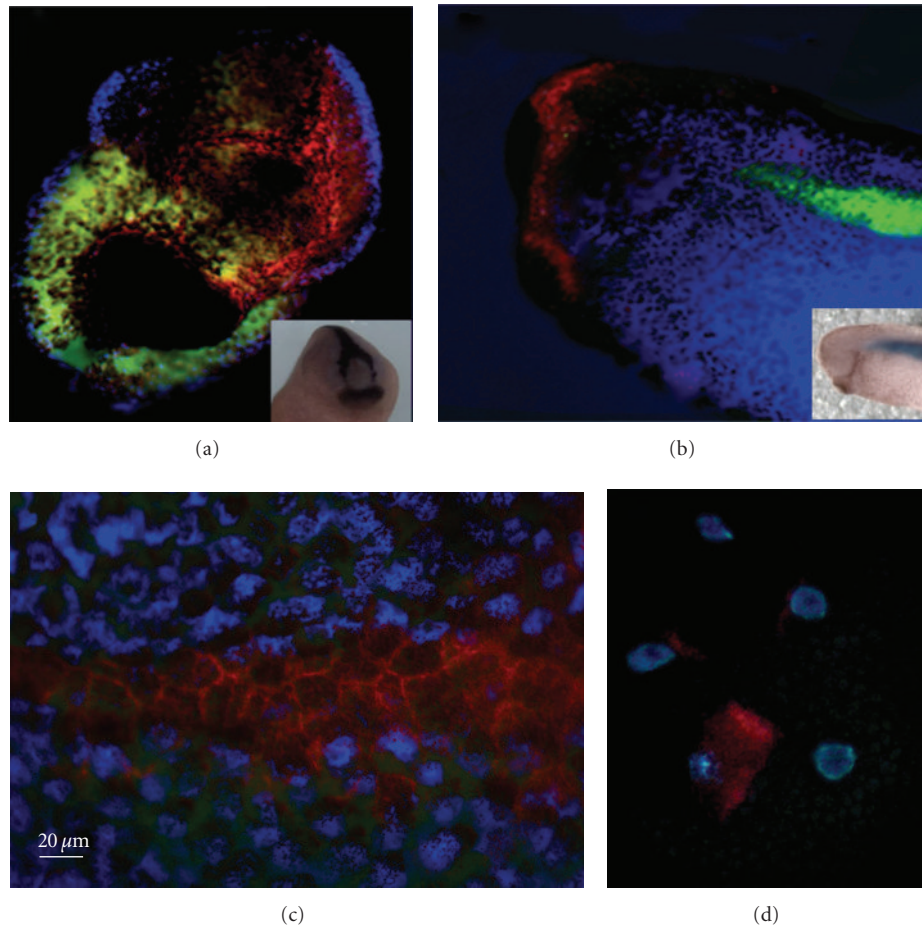


FIGURE 4: Double whole-mount *in situ* hybridization against cardiac actin and Xa-1 and the intracellular distribution of LTBP1 and Xa1. (a) A comparison of the staining pattern between the chromogenic and QD-based visualization of the FITC-labeled Xa-1 probe, shown in red, reveals that the QD staining is identical to that obtained using the standard chromogenic protocol. (b) An embryo processed using Biotin and FITC-labeled probes against cardiac actin (green) and Xa-1 (red), respectively. The two probes were visualized with spectrally resolvable QDs demonstrating that two color fluorescent *in situ* can be performed using QDs. The inset shows the chromogenic staining for cardiac actin for comparison. (c, d) Images of embryos processed for whole-mount *in situ* hybridization and counterstained with Hoechst (blue) at 20X (c) and 40X (d) magnification, showing differences in the intracellular distribution of the transcripts of Xa-1 (c) and LTBP1 (d), both shown in red.

for confocal microscopy. Of great significance, in terms of *Xenopus* and other opaque embryos like the chick, is the fact that the QD *in situ* staining is capable of remaining localized and fluorescent for more than an hour after the embryo is cleared. QD *in situ* also offer the potential for intracellular resolution of mRNA expression. This has not been possible using traditional chromogenic or fluorescent methods. In the case of *C. elegans*, where background is not a major issue, use of fluorescent antibodies to detect labeled RNA probes has to be carried out in conjunction with chromogenic amplified detection of the probes in order to get a comprehensive picture of the overall expression of a gene [64]. The amplified reaction detects low expressing regions and overall expression, whereas the fluorescent antibodies are used to resolve intracellular localization. The fact that our QD *in situ* protocol can do both in the highly autofluorescent *Xenopus* embryo, which is highly demanding, makes us confident that the implementation of QD *in situ* in other less demanding

model systems will be met with equal or more success. More importantly, these results suggest that QDs could be introduced as alternative fluorophores in other fluorescent *in situ* hybridization assays where their spectral properties can offer significant advantages. Overall, our results demonstrate that QD *in situ* are a viable alternative to current ISH protocols, and they expand the uses of QDs in biology.

## Acknowledgments

Funding was provided by the Cyprus Research Promotion Foundation (PENEK/0609/51). The authors thank Dr. Ali Brivanlou for providing the Amylase, LTBP1, Xbra, EDD, and MyoD constructs, Dr. Paul Krieg for providing the Cardiac actin construct, and Dr. Hazel Sive for the Xa-1 construct. I. Eleftheriou and A. Ioannou contributed equally to this work.

## References

- [1] C. R. Altmann et al., "The latent-TGF $\beta$ -binding-protein-1 (LTBP-1) is expressed in the organizer and regulates nodal and activin signaling," *Developmental Biology*, vol. 248, no. 1, pp. 118–127, 2002.
- [2] D. M. Hougaard, H. Hansen, and L. I. Larsson, "Non-radioactive in situ hybridization for mRNA with emphasis on the use of oligodeoxynucleotide probes," *Histochemistry and Cell Biology*, vol. 108, no. 4–5, pp. 335–344, 1997.
- [3] M. L. Pardue and J. G. Gall, "Molecular hybridization of radioactive DNA to the DNA of cytological preparations," *Proceedings of the National Academy of Sciences of the United States of America*, vol. 64, no. 2, pp. 600–604, 1969.
- [4] D. Tautz and C. Pfeifle, "A non-radioactive in situ hybridization method for the localization of specific RNAs in *Drosophila* embryos reveals translational control of the segmentation gene hunchback," *Chromosoma*, vol. 98, no. 2, pp. 81–85, 1989.
- [5] A. Hemmati-Brivanlou, D. Frank, M. E. Bolce, B. D. Brown, H. L. Sive, and R. M. Harland, "Localization of specific mRNAs in *Xenopus* embryos by whole-mount in situ hybridization," *Development*, vol. 110, no. 2, pp. 325–330, 1990.
- [6] L. L. Coutinho, J. Morris, and R. Ivarie, "Whole mount in situ detection of low abundance transcripts of the myogenic factor qmfl and myosin heavy chain protein in quail embryos," *Bio-Techniques*, vol. 13, no. 5, pp. 722–724, 1992.
- [7] R. Escalante and W. F. Loomis, "Whole-mount in situ hybridization of cell-type-specific mRNAs in *Dictyostelium*," *Developmental Biology*, vol. 171, no. 1, pp. 262–266, 1995.
- [8] T. Jowett and Y. L. Yan, "Double fluorescent in situ hybridization to zebrafish embryos," *Trends in Genetics*, vol. 12, no. 10, pp. 387–389, 1996.
- [9] G. W. Dewald, S. R. Brockman, and S. F. Paternoster, "Molecular cytogenetic studies for hematological malignancies," *Cancer Treatment and Research*, vol. 121, pp. 69–112, 2004.
- [10] S. M. Jalal and M. E. Law, "Application of multicolor fluorescent in situ hybridization for enhanced characterization of chromosomal abnormalities in congenital disorders," *Mayo Clinic Proceedings*, vol. 76, no. 1, pp. 16–21, 2001.
- [11] J. W. Vaandrager, E. Schuurin, E. Zwijkstra et al., "Direct visualization of dispersed 11q13 chromosomal translocations in mantle cell lymphoma by multicolor DNA fiber fluorescence in situ hybridization," *Blood*, vol. 88, no. 4, pp. 1177–1182, 1996.
- [12] J. M. Levisky and R. H. Singer, "Fluorescence in situ hybridization: past, present and future," *Journal of Cell Science*, vol. 116, no. 14, pp. 2833–2838, 2003.
- [13] C. M. Ogilvie, "Prenatal diagnosis for chromosome abnormalities: past, present and future," *Pathologie Biologie*, vol. 51, no. 3, pp. 156–160, 2003.
- [14] M. Yver, D. Carles, B. Bloch, P. Bioulac-Sage, and M. L. M. Negrier, "Determination of DNA ploidy by fluorescence in situ hybridization (FISH) in hydatidiform moles: evaluation of FISH on isolated nuclei," *Human Pathology*, vol. 35, no. 6, pp. 752–758, 2004.
- [15] P. Raanani and I. Ben-Bassat, "Detection of minimal residual disease in acute myelogenous leukemia," *Acta Haematologica*, vol. 112, no. 1–2, pp. 40–54, 2004.
- [16] S. Gellrich, R. Ventura, M. Jones, S. Y. Tan, and D. Y. Mason, "Immunofluorescent and FISH analysis of skin biopsies," *American Journal of Dermatopathology*, vol. 26, no. 3, pp. 242–247, 2004.
- [17] J. W. O'Neill and E. Bier, "Double-label in situ hybridization using biotin and digoxigenin-tagged RNA probes," *BioTechniques*, vol. 17, no. 5, pp. 870–875, 1994.
- [18] S. C. Hughes and H. M. Krause, "Double labeling with fluorescence in situ hybridization in *Drosophila* whole-mount embryos," *BioTechniques*, vol. 24, no. 4, pp. 530–532, 1998.
- [19] A. Streit and C. D. Stern, "Combined whole-mount in situ hybridization and immunohistochemistry in avian embryos," *Methods*, vol. 23, no. 4, pp. 339–344, 2001.
- [20] N. Denkers et al., "FISHing for chick genes: triple-label whole-mount fluorescence in situ hybridization detects simultaneous and overlapping gene expression in avian embryos," *Developmental Dynamics*, vol. 229, no. 3, pp. 651–657, 2004.
- [21] D. Kosman, C. M. Mizutani, D. Lemons, W. G. Cox, W. McGinnis, and E. Bier, "Multiplex detection of RNA expression in *Drosophila* embryos," *Science*, vol. 305, no. 5685, p. 846, 2004.
- [22] L. A. Davidson and R. E. Keller, "Neural tube closure in *Xenopus laevis* involves medial migration, directed protrusive activity, cell intercalation and convergent extension," *Development*, vol. 126, no. 20, pp. 4547–4556, 1999.
- [23] R. Krieg and K. J. Halbhauer, "Recent advances in catalytic peroxidase histochemistry," *Cellular and Molecular Biology*, vol. 49, no. 4, pp. 547–563, 2003.
- [24] M. P. C. Van De Corput, R. W. Dirks, R. P. M. Van Gijlswijk, F. M. Van De Rijke, and A. K. Raap, "Fluorescence in situ hybridization using horseradish peroxidase-labeled oligodeoxynucleotides and tyramide signal amplification for sensitive DNA and mRNA detection," *Histochemistry and Cell Biology*, vol. 110, no. 4, pp. 431–437, 1998.
- [25] C. Sardet, H. Nishida, F. Prodon, and K. Sawada, "Maternal mRNAs of PEM and macho 1, the ascidian muscle determinant, associate and move with a rough endoplasmic reticulum network in the egg cortex," *Development*, vol. 130, no. 23, pp. 5839–5849, 2003.
- [26] A. J. Wilson, A. Velcich, D. Arango et al., "Novel detection and differential utilization of a c-myc transcriptional block in colon cancer chemoprevention," *Cancer Research*, vol. 62, no. 21, pp. 6006–6010, 2002.
- [27] A. M. Femino, K. Fogarty, L. M. Lifshitz, W. Carrington, and R. H. Singer, "Visualization of single molecules of mRNA in situ," *Methods in Enzymology*, vol. 361, pp. 245–304, 2003.
- [28] M. E. Åkerman, W. C. W. Chan, P. Laakkonen, S. N. Bhatia, and E. Ruoslahti, "Nanocrystal targeting in vivo," *Proceedings of the National Academy of Sciences of the United States of America*, vol. 99, no. 20, pp. 12617–12621, 2002.
- [29] B. Ballou, B. C. Lagerholm, L. A. Ernst, M. P. Bruchez, and A. S. Waggoner, "Noninvasive imaging of quantum dots in mice," *Bioconjugate Chemistry*, vol. 15, no. 1, pp. 79–86, 2004.
- [30] A. Charalambous, M. Andreou, and P. Skourides, "Intein-mediated site-specific conjugation of Quantum Dots to proteins in vivo," *Journal of Nanobiotechnology*, vol. 7, no. 9, pp. 1–9, 2009.
- [31] M. C. Demetriou et al., "Spatially and temporally regulated  $\alpha$ 6 integrin cleavage during *Xenopus laevis* development," *Biochemical and Biophysical Research Communications*, vol. 15, no. 366, pp. 779–785, 2007.
- [32] B. Dubertret, P. Skourides, D. J. Norris, V. Noireaux, A. H. Brivanlou, and A. Libchaber, "In vivo imaging of quantum dots encapsulated in phospholipid micelles," *Science*, vol. 298, no. 5599, pp. 1759–1762, 2002.
- [33] X. Gao, W. C. W. Chan, and S. Nie, "Quantum-dot nanocrystals for ultrasensitive biological labeling and multicolor optical

- encoding," *Journal of Biomedical Optics*, vol. 7, no. 4, pp. 532–537, 2002.
- [34] X. Gao and S. Nie, "Molecular profiling of single cells and tissue specimens with quantum dots," *Trends in Biotechnology*, vol. 21, no. 9, pp. 371–373, 2003.
- [35] M. Han, X. Gao, J. Z. Su, and S. Nie, "Quantum-dot-tagged microbeads for multiplexed optical coding of biomolecules," *Nature Biotechnology*, vol. 19, no. 7, pp. 631–635, 2001.
- [36] J. K. Jaiswal, H. Mattoussi, J. M. Mauro, and S. M. Simon, "Long-term multiple color imaging of live cells using quantum dot bioconjugates," *Nature Biotechnology*, vol. 21, no. 1, pp. 47–51, 2003.
- [37] Z. Kaul, T. Yaguchi, S. C. Kaul, T. Hirano, R. Wadhwa, and K. Taira, "Mortalin imaging in normal and cancer cells with quantum dot immunconjugates," *Cell Research*, vol. 13, no. 6, pp. 503–507, 2003.
- [38] S. Kim, Y. T. Lim, E. G. Soltesz et al., "Near-infrared fluorescent type II quantum dots for sentinel lymph node mapping," *Nature Biotechnology*, vol. 22, no. 1, pp. 93–97, 2004.
- [39] E. Muro, P. Vermeulen, A. Ioannou et al., "Single-shot optical sectioning using two-color probes in HiLo fluorescence microscopy," *Biophysical Journal*, vol. 100, no. 11, pp. 2810–2819, 2011.
- [40] A. M. Smith, X. Gao, and S. Nie, "Quantum dot nanocrystals for in vivo molecular and cellular imaging," *Photochemistry and Photobiology*, vol. 80, no. 3, pp. 377–385, 2004.
- [41] P. Stylianou and P. Skourides, "Imaging morphogenesis, in *Xenopus* with Quantum Dot nanocrystals," *Mechanisms of Development*, vol. 126, no. 10, pp. 828–841, 2009.
- [42] X. Wu, H. Liu, J. Liu et al., "Immunofluorescent labeling of cancer marker Her2 and other cellular targets with semiconductor quantum dots," *Nature Biotechnology*, vol. 21, no. 1, pp. 41–46, 2003.
- [43] E. Tholouli, J. A. Hoyland, D. Di Vizio et al., "Imaging of multiple mRNA targets using quantum dot based in situ hybridization and spectral deconvolution in clinical biopsies," *Biochemical and Biophysical Research Communications*, vol. 348, no. 2, pp. 628–636, 2006.
- [44] M. Bruchez Jr., M. Moronne, P. Gin, S. Weiss, and A. P. Alivisatos, "Semiconductor nanocrystals as fluorescent biological labels," *Science*, vol. 281, no. 5385, pp. 2013–2016, 1998.
- [45] W. C. Chan and S. Nie, "Quantum dot bioconjugates for ultrasensitive nonisotopic detection," *Science*, vol. 281, no. 5385, pp. 2016–2018, 1998.
- [46] M. Dahan, T. Laurence, F. Pinaud et al., "Time-gated biological imaging by use of colloidal quantum dots," *Optics Letters*, vol. 26, no. 11, pp. 825–827, 2001.
- [47] J. K. Jaiswal and S. M. Simon, "Potentials and pitfalls of fluorescent quantum dots for biological imaging," *Trends in Cell Biology*, vol. 14, no. 9, pp. 497–504, 2004.
- [48] B. O. Dabbousi, J. Rodriguez-Viejo, F. V. Mikulec et al., "(CdSe)/ZnS core-shell quantum dots: synthesis and characterization of a size series of highly luminescent nanocrystallites," *Journal of Physical Chemistry B*, vol. 101, no. 46, pp. 9463–9475, 1997.
- [49] P. Chan, T. Yuen, F. Ruf, J. Gonzalez-Maeso, and S. C. Sealton, "Method for multiplex cellular detection of mRNAs using quantum dot fluorescent in situ hybridization," *Nucleic Acids Research*, vol. 33, no. 18, p. e161, 2005.
- [50] S. Pathak, S. K. Choi, N. Arnheim, and M. E. Thompson, "Hydroxylated quantum dots as luminescent probes for in situ hybridization," *Journal of the American Chemical Society*, vol. 123, no. 17, pp. 4103–4104, 2001.
- [51] A. Watson, X. Wu, and M. Bruchez, "Lighting up cells with quantum dots," *BioTechniques*, vol. 34, no. 2, pp. 296–303, 2003.
- [52] Y. Xiao and P. E. Barker, "Semiconductor nanocrystal probes for human metaphase chromosomes," *Nucleic Acids Research*, vol. 32, no. 3, p. e28, 2004.
- [53] Z. Jiang, R. Li, N. W. Todd, S. A. Stass, and F. Jiang, "Detecting genomic aberrations by fluorescence in situ hybridization with quantum dots-labeled probes," *Journal of Nanoscience and Nanotechnology*, vol. 7, no. 12, pp. 4254–4259, 2007.
- [54] F. Müller, A. Houben, P. E. Barker et al., "Quantum dots—a versatile tool in plant science?" *Journal of Nanobiotechnology*, vol. 4, p. 5, 2006.
- [55] D. Ioannou, H. G. Tempest, B. M. Skinner, A. R. Thornhill, M. Ellis, and D. K. Griffin, "Quantum dots as new-generation fluorochromes for FISH: an appraisal," *Chromosome Research*, vol. 17, no. 4, pp. 519–530, 2009.
- [56] R. Winklbauer, "Mesodermal cell migration during *Xenopus* gastrulation," *Developmental Biology*, vol. 142, no. 1, pp. 155–168, 1990.
- [57] P. D. Nieuwkoop and J. Faber, *Normal Table of Xenopus laevis (Daudin)*, Garland, New York, USA, 1 edition, 1994.
- [58] R. M. Harland, "In situ hybridization: an improved whole-mount method for *Xenopus* embryos," *Methods in Cell Biology*, vol. 36, pp. 685–695, 1991.
- [59] C. Forristall, M. Pondel, L. Chen, and M. L. King, "Patterns of localization and cytoskeletal association of two vegetally localized RNAs, Vg1 and Xcat-2," *Development*, vol. 121, no. 1, pp. 201–208, 1995.
- [60] D. St Johnston, "The intracellular localization of messenger RNAs," *Cell*, vol. 81, no. 2, pp. 161–170, 1995.
- [61] C. Fages, M. Kaksonen, T. Kinnunen, E. L. Punnonen, and H. Rauvala, "Regulation of mRNA localization by transmembrane signalling: local interaction of HB-GAM (heparin-binding growth-associated molecule) with the cell surface localizes  $\beta$ -actin mRNA," *Journal of Cell Science*, vol. 111, no. 20, pp. 3073–3080, 1998.
- [62] K. Yaniv and J. K. Yisraeli, "Defining Cis-acting elements and trans-acting factors in RNA localization," *International Review of Cytology*, vol. 203, pp. 521–539, 2001.
- [63] I. M. Palacios and D. St. Johnston, "Getting the message across: the intracellular localization of mRNAs in higher eukaryotes," *Annual Review of Cell and Developmental Biology*, vol. 17, pp. 569–614, 2001.
- [64] G. Seydoux and A. Fire, "Whole-mount in situ hybridization for the detection of RNA in *Caenorhabditis elegans* embryos," *Methods in Cell Biology*, vol. 48, pp. 323–337, 1995.